Chapter II.9

Beam instrumentation

Peter Forck
GSI Helmholtz Centre for Heavy Ion Research, Darmstadt, Germany

The determination of beam parameters is essential for the operation and development of any accelerator facility. The working principle of frequently used beam instruments for electron and proton beams is discussed. The article includes the beam instrumentation for beam current determination, methods for transverse profile and emittance diagnostics, the usage of beam position monitors for bunched beams, bunch shape measurement and the usage of beam loss monitors. The article also deals with the physical basis of various monitors and applications for beam diagnostics at typical linear and circular accelerators for electrons and protons.

II.9.1 Demands for beam diagnostics

Beam diagnostics is an essential constituent of any accelerator. The "sensory organ" shows the particle beam's properties and behaviour. It deals with the actual beam, including all possible imperfections of an existing technical installation. Without adequate diagnostics, one would "blindly grope around in the dark" for the accelerator settings, and improvements are hardly achievable. There are four categories of diagnostic demands at any facility:

- Reliable, quick measurements to determine the basic parameters of a machine setting used as a fast check of the general functionality. The readings from the instrumentation give a single number or simple plots. These devices should be non-destructive for the beam, yielding online information. A prominent example is a current measurement by a transformer, as shown in Fig. II.9.13 accompanied by the display of the average current in the form of one single number.
- Instrumentation built for a daily check of performance and stability or for controlling necessary parameter changes in the accelerator setting. It can also be used to solve more straightforward machine problems in case of malfunction. An example is the transverse profile determination, in most cases performed by a destructive device as discussed in Section II.9.3; Fig. II.9.48 contains transverse profiles along the beam path as displayed in the control room at the GSI facility during the regular operating procedure.
- Complex instrumentation for the commissioning of a new accelerator component, for the development of increasing performance and for solving more severe problems in case of a malfunction. The devices can be more complex to use and might be destructive for the beam. Creating reliable information about the complex beam behaviour is essential, allowing a clear interpretation. The

This chapter should be cited as: Beam instrumentation, P. Forck, DOI: 10.23730/CYRSP-2024-003.1339, in: Proceedings of the Joint Universities Accelerator School (JUAS): Courses and exercises, E. Métral (ed.),
CERN Yellow Reports: School Proceedings, CERN-2024-003, DOI: 10.23730/CYRSP-2024-003, p. 1339.

determination of the beam emittance is an important example for the commissioning of a LINAC; these methods are discussed in Section II.9.4. For a synchrotron, the measurement of lattice parameters, like the tune, chromaticity or β-function, are required to achieve higher performance and for the comparison to theoretical calculations; related methods are discussed in Section II.9.5.12 and II.9.5.13.

– An additional application is the active influence of the device settings after detecting the beam's properties. Generally, a feedback system concerning a given beam parameter yields an improved beam delivery. An example is the reading of the beam position by beam position monitor, as discussed in Section II.9.5, and the correction of the orbit to its nominal value. Different reaction times are typical, from less than μs to s, depending on the requirement for a given accelerator facility. Such feedback systems involve the beam instrumentation as the input of the correction calculation, as mentioned in Section II.9.5.11. These extensive beam control systems are out of this lecture's scope and will not be discussed here.

The frontiers between these categories are smooth but should give a rough guideline for the design, construction and use of different types of diagnostics.

There is a large variety of beam parameters to be measured. All essential parameters should be controllable for a good alignment of the beam. Table II.9.1 gives an overview of essential beam quantities and the commonly used diagnostic devices and methods. The general properties for most of these devices will be discussed in the following sections without going deeply into details; i.e., the course gives reasonable coverage rather than a detailed description. For some parameters, the type of instrumentation differs for LINACs and synchrotrons due to their different accelerating principles. A prominent example is that in a LINAC or a transfer line, the beam passes only once, while in a synchrotron, the beam evolution of thousands of passages has to be determined. Non-destructive methods are preferred for a synchrotron to monitor the beam behaviour without affecting the circulating beam. Moreover, electron and proton beams have entirely different behaviour. A simple example is that electrons are relativistic just after the first LINAC modules, while for protons, several 100 m long LINACs or even a synchrotron is needed to reach significant relativistic conditions. Another difference is the emission of synchrotron radiation by electrons, while this process occurs for protons only at the highest reachable energies, like in LHC at CERN. Table II.9.1 shows that the same beam quantity can be determined with different devices. Which instrumentation is most suited depends on the various beam parameters themselves. On the other hand, several beam quantities can be determined with the same type of instrument.

Some of the instruments in Table II.9.1 require the insertion of material into the beam, referred to as invasive diagnostics. Synonyms for this word are intersecting or intercepting instruments; the nature of the instrumentation will be discussed in the related sections. The amount of beam influence also depends on the beam properties as related to the beam's energy loss and possible straggling. Non-invasive diagnostics methods are generally preferred for two reasons:

– With non-invasive instrumentation, the beam is not influenced and can be measured simultaneously at different locations within a transfer line. Moreover, for the beam stored in a synchrotron, the evolution of beam parameters over time can be determined; hence, non-invasive instrumentation is regularly used in circular accelerators.

Table II.9.1: Beam parameters and the most commonly used beam diagnostics.

Beam quantity		**LINAC, transfer line**	**Synchrotron**
current I	*general*	transformer (dc, pulsed) Faraday cup	transformer (dc)
	special	particle detector (Scintillator, IC, SEM)	normalized pick-up signal
position $\overline{x}$	*general*	pick-up	pick-up
	special	using profile measurement	cavity excitation (e^-)
profile x_{width}	*general*	SEM-grid, wire scanner scintillation screen, OTR screen	ionization profile monitor synch. radiation (e^-)
	special	grid with ampl. (MWPC)	wire scanner
trans. emittance	*general*	slit grid	ionization profile monitor
$\epsilon_{\mathrm{trans}}$		quadrupole scan	wire scanner
	special	pepper-pot	wire scanner
momentum	*general*	pick-up (ToF)	pick-up
p and $\Delta p/p$	*special*	magn. spectrometer	Schottky noise pick-up
bunch width $\Delta\varphi$	*general*	pick-up	pick-up wall current monitor streak camera (e^-)
	special	secondary electrons arrival arrival at particle detector electro-optical modulation	electro-optical modulation
long. emittance	*general*	magn. spectrometer buncher scan	
ϵ_{long}	*special*	TOF application	pick-up + tomography
tune, chromaticity	*general*	—	exciter + pick-up (BTF)
Q, ξ	*special*	—	transverse Schottky pick-up
beam loss r_{loss}	*general*	particle detector	
polarization P	*general*	particle detector	
	special	Compton scattering with laser	
luminosity $\mathcal{L}$	*general*	particle detector	

– The power released by the beam in intersecting materials might be sufficient for damaging the material. There is a particular risk at high-current proton beam transfer lines and high-intensity LINACs.

Diagnostics are a vital part of any accelerator. About 3 % to 10 % of the total cost of an accelerator facility (without the civil construction costs) is usually related to beam instrumentation. However, due to the complex physics and techniques involved, the personnel involved in the design, operation, and further development of beam diagnostics usually exceed 10 % of the entire personnel of an accelerator facility.

As a first look at "real-life", Fig. II.9.1 shows an instrumental assembly installed behind the heavy ion LINAC at GSI during its commissioning phase. This equipment measured all relevant beam parameters extensively for several weeks for each LINAC module. The beam quantities were: Current, transverse profile, transverse emittance, energy, bunch position, bunch structure, and longitudinal emittance in dependence on various device parameter settings. Now, the equipment is installed behind the

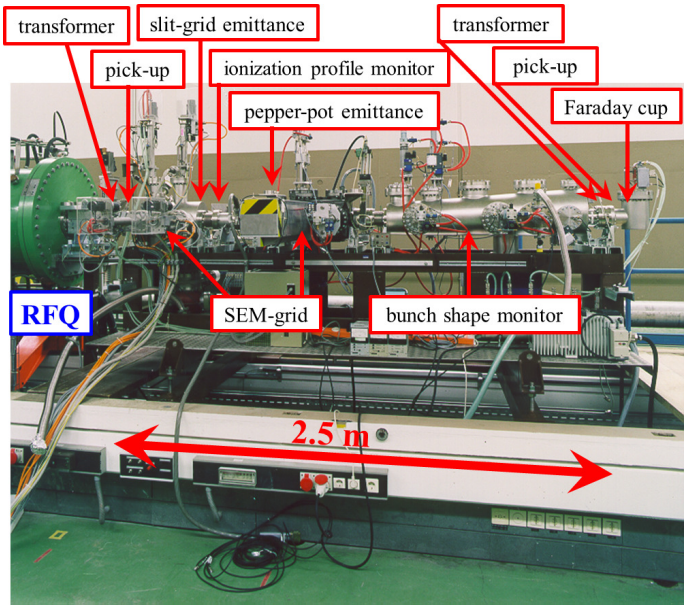

Fig. II.9.1: Photo of a movable test bench provided for commissioning of the high current RFQ of GSI (green tank on the left).

last module for permanent use during operation and for further beam characterisation and improvements.

Most of the diagnostic instrumentation is based on one of the following physical processes with related technical realisations:

- The electro-magnetic influence of moving charges on the environment is described by classical electro-dynamics theory as given by the Maxwell equations. The technique is based on a voltage or current measurement on a low or high-frequency scale. Examples are beam transformers or pick-ups.
- The emission of photons by accelerated charges can be used. This diagnostic is essential for relativistic particles, i.e. electrons or highly energetic protons. The technique is based on optical methods spanning the visible range up to the X-ray region. Examples are synchrotron radiation monitors for transverse beam profile and longitudinally for bunch shape measurements.
- The Coulomb interaction of charged particles penetrating matter is described by atomic or solid-state physics. The energy release due to electronic stopping gives the dominant fraction of the detected signal. The technique is based on current measurements or the observation of light by optical methods. Examples are scintillators, viewing screens, secondary electron emission grids, ionisation chambers, and ionisation profile monitors.
- The nuclear- or elementary particle physics interaction between the accelerated particles and a fixed target or between colliding beams is relevant. From the known cross sections, the beam quantity can be deduced. The technique is based on nuclear- or elementary particle physics detectors. Examples are polarimeters, luminosity monitors, or beam loss monitors used for machine protection and alignment.
- The interaction of the particles with a photon beam can be used. The technique is based on lasers, their associated optics, and detectors for high-energy physics. Examples are laser scanners or Compton polarimeters. These are highly specialised instruments and are not further discussed in

this introduction.

This lecture focuses on the principles of some commonly used devices; not all interesting aspects can be covered. Excellent introductory descriptions for beam diagnostics exist, as well as several books related to various related topics [1]. Information on particular realisations can be found in the proceedings of dedicated beam diagnostics conferences and as a part of the general accelerator conferences [2]. In the literature, one can find extensive descriptions of the full instrumentation used at an ion synchrotron (RHIC at Brookhaven USA [3]) and an electron-positron collider (KEKB in Japan [4]).

Normally, the yield of information from the diagnostic devices follows three successive steps from the measurement up to the display of the quantity of interest, as shown in Fig. II.9.2 for the case of an electro-magnetic beam position monitor:

- Firstly, the beam interacts with the detector. The captured signal has to be amplified and shaped by analogue electronics. Low noise analogue processing is essential at this step. This analogue electronics is usually installed close to the beam pipe.
- The amplified signal is transferred via cables from the accelerator area to a local electronics room. The distance between these two locations can be several 100 m. Further signal conditioning can proceed here, and the signal might be combined with other parameters reflecting the accelerator settings. This is often realised by analogue electronics. The original or modified signal is then digitised and stored by an oscilloscope or a digital bus system. Examples of bus systems are field buses like CAN- or PROFI-bus or crate-based systems like CAMAC, VME, PXI, μTCA, or CompactPCI. Digital signal processing can be applied to the data, which is usually the case in state-of-the-art accelerator facilities as it overtook the role of the previously installed analogue electronics. The control of the electronics is to be performed at this location.
- As the final step, the data, or in most cases a reduced subset, are passed to a PC in the operator's control room. Here, the desired beam properties are visualised. Moreover, the device parameters of the accelerator, such as magnet currents or rf voltages, can be modified from the control room to influence the beam. The resulting effect on the beam is then observed with a new set of measured data.

In this lecture, we focus on the action of the beam on the detector. Raw data are shown for several systems to explain the general detector functionality. The preceding analogue electronics are only discussed briefly. Digitalisation techniques are beyond the scope of this introduction, even though they are essential and require a significant effort. Digital electronics is not a pure diagnostics subject, and the realisation is comparable to many other control applications. From the data analysis on the PC, only typical results are presented; neither details for the realisation of the algorithms nor the associated software at the various steps are described.

Most examples in this lecture are measured at the GSI facility because the author is most familiar with these realisations. It does not mean GSI has the most advanced systems; better installations might exist at other facilities. The GSI accelerator facility, as shown in Fig. II.9.3, consists of two-step pulsed LINACs running on 36 MHz and 108 MHz, respectively, to accelerate all ions from different ion sources up to 12 MeV/u, corresponding to a velocity of $\beta = v/c = 0.15$. This energy is well above the so-called

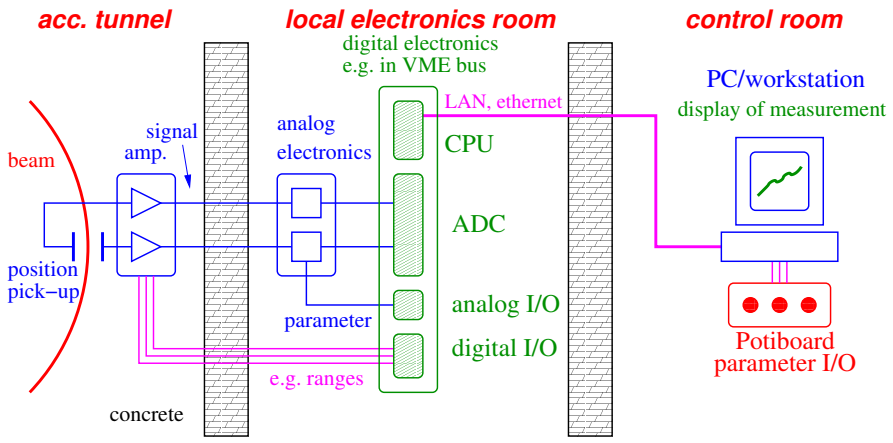

Fig. II.9.2: Schematics of typical beam diagnostics installation using a beam position monitor as an example. The beam signal is captured by analogue electronics and digitised in a local electronics room. The measured parameters and the device setting can be influenced from the control room.

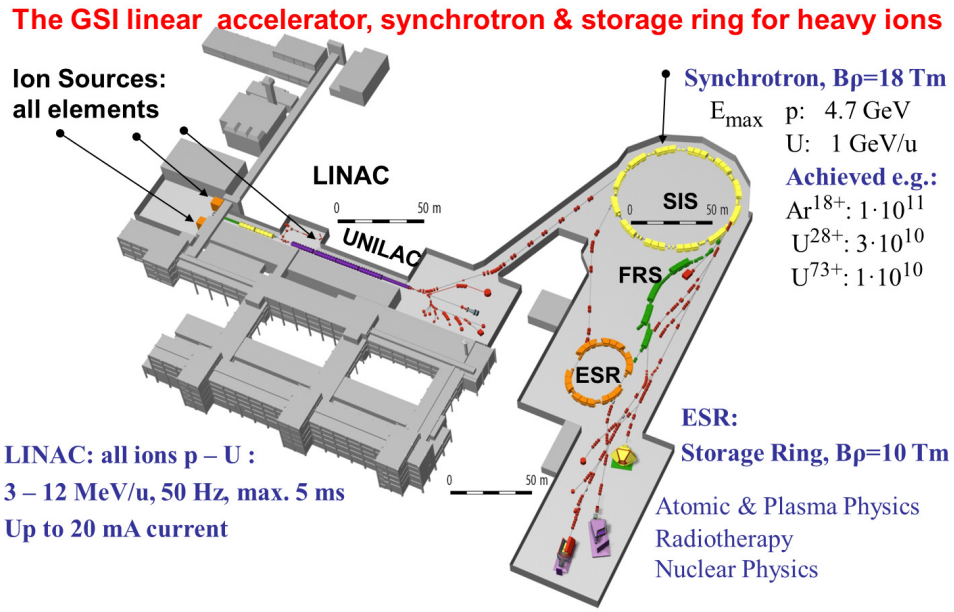

Fig. II.9.3: The GSI heavy ion accelerator facility.

Coulomb barrier, where nuclear reactions are possible. Experiments with these beams are performed in the low-energy experimental hall. For achieving higher energies up to 2 GeV/u, corresponding to $\beta = 0.95$, a synchrotron with 218 m circumference, the SIS (German for Schwerionen-Synchtrotron), is used. The beam can be transferred to the storage ring ESR with a single bunch transfer (so-called fast extraction). Alternatively, it can be sent to fixed target experiments in this fast mode or slow extraction lasting from 1 to 10 s. The scientific investigations at these targets are related to nuclear, atomic or plasma physics and human cancer therapy.

We restrict the lecture to the accelerator instrumentation for stable particles with a moderate current range. Typical applications at these facilities are experiments in atomic, solid state, biological, nuclear, and particle physics, as well as using synchrotron radiation sources. We do not treat the diagnostic needs, e.g., for radioactive beams with low current or the high current beam produced by wake-field

accelerators for short beam durations. Moreover, the special diagnostics for negative H^- beams are not discussed. The measurement of polarisation and luminosity at colliders uses particle detectors and well-known cross-sections for secondary particle production, which is beyond this introduction's scope.

At the end of this introduction, we emphasise that beam diagnostic is essential to achieve stable accelerator operation and the best possible beam quality. It is, hence, of central importance when it comes to scientific advances and applications that benefit society.

II.9.2 Measurement of beam current

The total electrical current is one of the most essential parameters for the operation of a particle accelerator. In daily operation, a first check concerns the current in almost all accelerator laboratories; in most cases, it is measured with a beam current transformer. This device works for electron and proton LINACs and synchrotrons, even for short pulses, like as found for example in the transfer lines between synchrotrons, as well as for un-bunched beams as found for example in proton storage rings. These devices are commercially available [5], even though quite different types are used. A general overview of the current measurement device is presented in Ref. [6]. The principle of current transformers is the detection of the magnetic field accompanied by any beam current. For currents below about 1 μA, transformers cannot be used due to noise limitations. Because of their functioning principle, transformers are always non-invasive devices.

From the first days of accelerators, Faraday cups were used. The cup directly measures the particle beam's charge as it stops all beam particles by the intersecting material of the Faraday cup. For high beam currents, this invasive method can not be applied because the total energy carried by the beam can destroy the intercepting Faraday cup material. The penetration depth reaches more than several cm for particles with energies above some 100 MeV/u for protons and ions; hence the Faraday cups are no longer useful for those beam parameters.

Particle detectors are used for low currents but higher energies above about 100 MeV/u for protons and ions. Here, the energy loss of the charged particle travelling through matter is detected. Either the particles are counted directly, or the particle flux can be calculated with the help of a calibration. For most parameters, this is an invasive method. Slow extraction from a synchrotron within a typical duration of some seconds is an example of typical beam parameters.

Before discussing the different beam current monitors in detail, we define the time structure of a pulsed LINAC according to Fig. II.9.4:

- The average or mean current I_{mean} is the long time average as given in units of A.
- The macro pulse current I_{pulse} is the time average during the beam delivery. In most cases, this is given in units of Ampere [A].
- The current within a bunch I_{bunch}, sometimes also called the micro pulse current. In most cases, the number of particles or charges per bunch is given.

Pulsed LINACs or pulsed cyclotrons can be used as an injector to a synchrotron, where only a typical pulse length of 100 μs is needed for a multi-turn injection. For a single-turn injection, the time is of the order of 10 μs. For other applications, like in atomic or nuclear physics, a cw (continuous

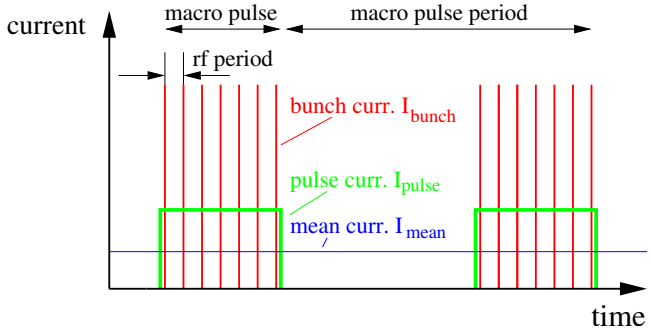

Fig. II.9.4: The time structure of the different currents at a pulsed LINAC.

wave) accelerator is used. Here, the bunches are delivered for an "infinitely" long time. The macro pulse current I_{pulse} then equals the average current I_{mean}, but the bunch structure remains due to the rf acceleration by a LINAC or a cyclotron. There also exist types of accelerators which do not produce bunched beams; examples are Van-de-Graaff- and Cockcroft-Walton accelerator types based on electrostatic acceleration. In this case all three types of currents are equal.

II.9.2.1 Current transformer for pulsed beams

II.9.2.1.1 General considerations and passive transformer

In an accelerator, the current is formed by N_{part} particles of charge state q per unit of time t or unit of length l and velocity $\beta = v/c$. The electrical current passing through a given location is

$$I_{\mathrm{beam}} = \frac{qeN_{\mathrm{part}}}{t} = \frac{qeN_{\mathrm{part}}}{l} \cdot \beta c \tag{II.9.1}$$

with e being the elementary charge. The magnetic field B of a current can be calculated according to the Biot–Savart law

$$d\vec{B} = \mu_0 I_{\mathrm{beam}} \cdot \frac{d\vec{l} \times \vec{r}}{4\pi r^3} \tag{II.9.2}$$

with $\mu_0 = 4\pi \cdot 10^{-7}$ Vs/Am is the permeability of the vacuum, $d\vec{l}$ the length in direction of the beam and $\vec{r}$ the distance between the centre of the beam and the coordinate where the field is determined. Due to the cylindrical symmetry outside of the beam, only the azimuthal component has to be considered along the unitary vector $\vec{e}_\varphi$ as shown in Fig. II.9.5

$$\vec{B} = \mu_0 \frac{I_{\mathrm{beam}}}{2\pi r} \cdot \vec{e}_\varphi \quad . \tag{II.9.3}$$

For a beam current of 1 μA and a distance of 10 cm, the magnetic field has a value of only 2 pT. To put this into perspective, the constant and homogeneous earth magnetic field has a value of about 50 μT.

The beam current can be determined by monitoring the accompanied magnetic field with a current transformer schematically shown in Fig. II.9.6. The beam passes through a highly permeable torus as the "primary winding". An insulated wire wound around the torus with N turns serves as the transformer's "secondary winding" with the inductance L. The inductance L for a torus material of length l in beam direction, inner radius r_{i} and outer radius r_{o} having a relative permeability μ_{r} and N windings is given

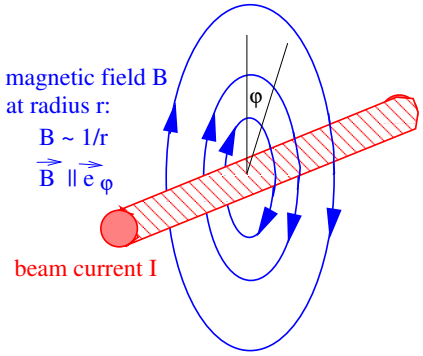

Fig. II.9.5: The magnetic field of around a current.

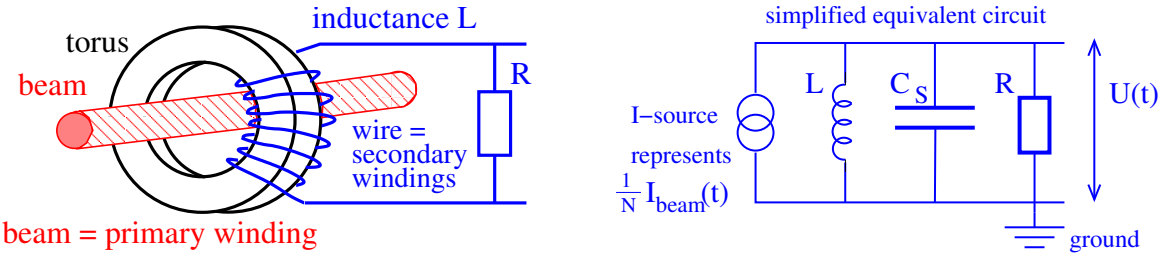

Fig. II.9.6: Scheme of a current transformer built as a ring-core (torus) around the beam (left) and the simplified equivalent circuit (right).

by

$$L = \frac{\mu_0 \mu_\mathrm{r}}{2\pi} \cdot lN^2 \cdot \ln \frac{r_\mathrm{o}}{r_\mathrm{i}} \quad . \tag{II.9.4}$$

The value of the induction can be chosen by the core size (as given by r_i and r_o) and the number of windings N. A further reason for the torus is to guide the field-lines, so only the azimuthal component is measured, and the signal strength is nearly independent of the beam position inside the vacuum pipe.

Generally, for an ideal current transformer loaded with a low value of ohmic resistance R,the relation between the primary current I_prim and secondary current I_sec is given by

$$I_\mathrm{sec} = \frac{N_\mathrm{prim}}{N_\mathrm{sec}} \cdot I_\mathrm{prim} \quad \Longrightarrow \quad I_\mathrm{sec} = \frac{1}{N} \cdot I_\mathrm{prim} \quad \text{due to} \;\; N_\mathrm{prim} = 1 \tag{II.9.5}$$

with N_i the number of winding on the primary side, which is one due to the single pass of the beam through the torus. N_sec is the winding number on the secondary side, called N for simplicity.

For most practical cases, a measurement of a voltage U is preferred, therefore the resistance R is introduced leading to

$$U = R \cdot I_\mathrm{sec} = \frac{R}{N} \cdot I_\mathrm{beam} \quad . \tag{II.9.6}$$

The ratio between the usable signal voltage U and the beam current I_beam is referred to as sensitivity S (or transfer impedance, for a more detailed discussion see Section II.9.5.1)

$$U = S \cdot I_\mathrm{beam} \quad . \tag{II.9.7}$$

To understand the design criteria for the various applications, one has to consider the electrical

properties of the transformer in more detail. With different external electrical elements, the response to a given time structure of the beam can be widely influenced. We first consider the characteristics of a so-called passive transformer or **F**ast **C**urrent **T**ransformer **FCT**, where the voltage across a 50 Ω resistor is recorded. The equivalent circuit of the secondary transformer side is depicted in Fig. II.9.6 on the right side. The beam current is modelled by a current source with a reduction given by the number of windings N according to Eq. II.9.5. One has to take also some stray capacitance C_{S} into account, which is caused by the capacitance between the windings, the windings and the torus and along the shielded cable to the resistor R. To determine the voltage $U(t)$, the impedance of the parallel shunt of the three elements in dependence of the excitation frequency f or the angular frequency $\omega = 2\pi f$ is

$$\frac{1}{Z} = \frac{1}{i\omega L} + \frac{1}{R} + i\omega C_{\mathrm{S}} \quad . \tag{II.9.8}$$

Using some algebra, this is equivalent to

$$Z = \frac{i\omega L}{1 + i\omega L/R - \omega L/R \cdot \omega R C_{\mathrm{S}}} \quad . \tag{II.9.9}$$

This equation can be analysed for three different frequency ranges:

- **Low frequency range assuming $\omega \ll \frac{\mathbf{R}}{\mathbf{L}}$:**
  In this case, the second and third terms in the denominator of Eq. II.9.9 can be neglected. The resulting impedance is then
  $$Z \to i\omega L \quad . \tag{II.9.10}$$
  The meaning of this equation is that the usable signal at the resistor R decreases proportionally to the excitation frequency because the inductance acts as a short circuit for low frequencies. In particular, at $\omega = 0$ no signal can be recorded. It reflects the well-known fact that a transformer can not handle DC-currents.
- **High frequency range assuming $\omega \gg \frac{\mathbf{1}}{\mathbf{RC_S}}$:**
  In this case, the first and second terms in the denominator of Eq. II.9.9 can be neglected. The impedance is then given by
  $$Z \to \frac{1}{i\omega C_{\mathrm{S}}} \quad . \tag{II.9.11}$$
  IT reflects that for high frequencies, the current is mainly flowing through the capacitor; therefore, the voltage drop at the resistor R is low.
- **Working region $\frac{\mathbf{R}}{\mathbf{L}} \ll \omega \ll \frac{\mathbf{1}}{\mathbf{RC_S}}$:**
  For this case, the second term in the denominator of Eq. II.9.9 dominates, and terms one and three of Eq. II.9.8 can be neglected. The impedance is then given by
  $$Z \simeq R \quad . \tag{II.9.12}$$
  This is the usable working region where the voltage drop across the resistor is significant. The working region can be chosen across a wide range as given by the values of the electrical elements L and C. Generally, for a parallel RLC-circuit as shown in Fig II.9.6, oscillations are inhibited if

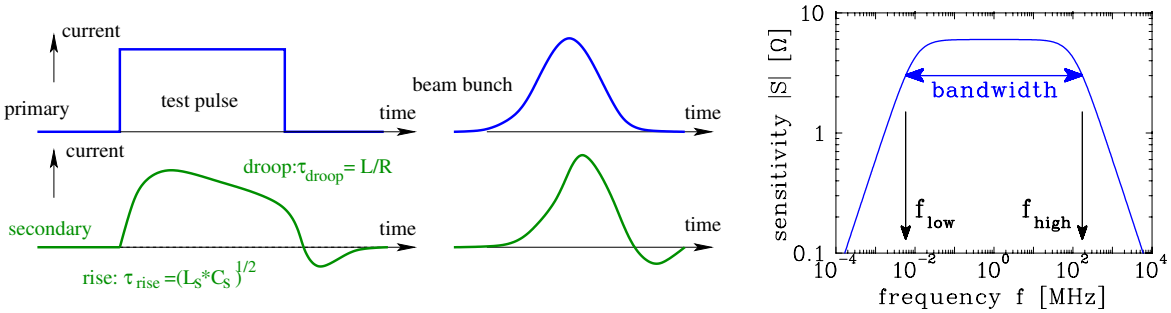

Fig. II.9.7: Left: The response of a transformer to a rectangular pulse and a more realistic beam pulse. Right: The corresponding frequency-domain plot for the sensitivity as a function of frequency.

the condition $R < 1/2 \cdot \sqrt{L/C_s}$ is fulfilled. In particular, the low value of the resistor $R = 50\ \Omega$ to ground allows for a current flow, resulting in an over-damping of possible oscillations.

The frequencies mentioned above restrict the working region with a correct response of the measured signal with respect to the beam current. Fig. II.9.7 depicts the relevant properties: At the lower frequency boundary the signal decreases; the frequency f_{low} for which the signal is decreased by a factor of $e^{-1} = 0.37$ is called the low cut-off frequency f_{low} and is given by $\omega_{\text{low}} = 2\pi f_{\text{low}} = R/L$. At the upper boundary, the corresponding value $\omega_{\text{high}} = 1/RC_{\text{S}}$ is called upper cut-off frequency.

For the following discussion, we are more interested in the time response of the measurement device to a given beam pulse. Therefore, one frequently uses the rise time constant τ_{rise} and the droop time constant τ_{droop} as depicted in Fig. II.9.7 left: If a step-function gives the excitation, the signal amplitude A increases as $A \propto (1 - e^{-t/\tau_{\text{rise}}})$ and τ_{rise} corresponds to the time for an increase by $e^{-1} = 37\%$. It is linked to the upper cut-off frequency by

$$\tau_{\text{rise}} = \frac{1}{\omega_{\text{high}}} = \frac{1}{2\pi f_{\text{high}}} \quad . \tag{II.9.13}$$

Similarly, the droop time constant is linked to the lower cut-off frequency as

$$\tau_{\text{droop}} = \frac{1}{2\pi f_{\text{low}}} \quad . \tag{II.9.14}$$

Both equations have a general meaning and will be used to transfer quantities like bandwidth, as given in the frequency domain of Fig. II.9.7, into the corresponding description in the time domain [1].

For the passive current transformer as described by the equivalent circuit of Fig. II.9.6 (left) the

[1] In the time domain one uses either the rise time constant τ_{rise} or more frequently the rise time t_{rise}, as defined from an amplitude increase from 10 to 90%. It can be written as

$$t_{\text{rise}} = \frac{\ln 0.9 - \ln 0.1}{\omega_{\text{high}}} = \frac{\ln 9}{2\pi f_{\text{high}}} \simeq \frac{1}{3 f_{\text{high}}} \simeq 2.2 \cdot \tau_{\text{rise}} \quad . \tag{II.9.15}$$

Both quantities are therefore connected by $t_{\text{rise}} = \ln 9 \cdot \tau_{\text{rise}} \simeq 2.2 \cdot \tau_{\text{rise}}$.
The same relations hold for the droop time

$$t_{\text{droop}} \simeq \frac{1}{3 f_{\text{low}}} \simeq 2.2 \cdot \tau_{\text{droop}} \tag{II.9.16}$$

.

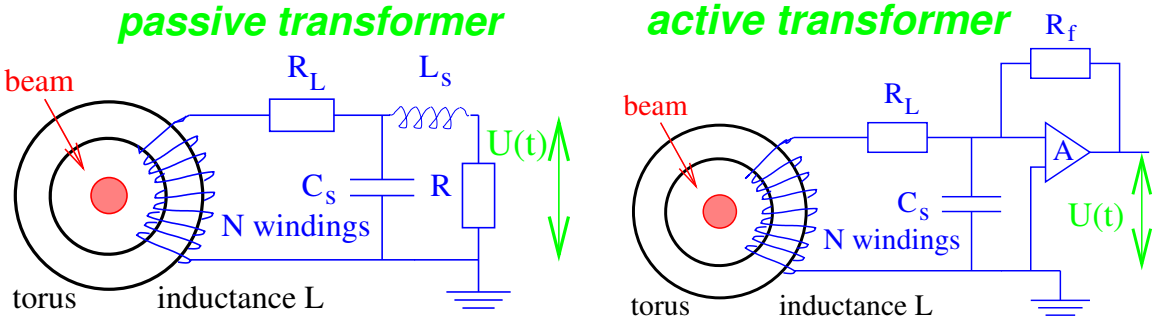

Fig. II.9.8: Equivalent circuits of a passive beam transformer (left) and an active transformer (right).

rise and droop time constants are given by

$$\tau_{\mathrm{rise}} = RC_{\mathrm{S}} \quad \text{and} \quad \tau_{\mathrm{droop}} = \frac{L}{R} \quad . \tag{II.9.17}$$

A more realistic schematic diagram of the passive transformer is shown in Fig. II.9.8. The main difference is the additional loss resistivity in the cables, which is represented by an additional resistor R_{L} included in series in the diagram. Additionally, there is a stray inductance between the windings, best modelled by a serial insertion of an inductance L_{S}. For the higher frequencies response, one has to consider the frequency dependence of the permeability μ_{r} of the torus made of CoFe-based amorphous alloy (so-called Vitrovac©) with $\mu_{\mathrm{r}} \sim 10^5$ for low frequencies. But the permeability decreases above $f \sim 100$ kHz with a scaling $\mu_{\mathrm{r}} \propto 1/f$; hence, the inductance of the torus decreases. For frequencies above ~ 100 MHz, the stray inductance is the dominant contribution. With these two modifications, the rise and droop times are modified to yield

$$\tau_{\mathrm{rise}} = \sqrt{L_{\mathrm{S}} C_{\mathrm{S}}} \quad \text{and} \quad \tau_{\mathrm{droop}} = \frac{L}{R + R_{\mathrm{L}}} \quad . \tag{II.9.18}$$

Passive transformers are used in transfer lines when short beam pulses have to be measured. Fig. II.9.9 shows an example of one bunch extracted from a synchrotron within one revolution, the so-called fast extraction. In the latter case, the passive transformer is installed in the beam pipe outside the synchrotron. The observables are the actual bunch shape, the arrival time with respect to an external reference (e.g. the acceleration frequency) and the total amount of particles gained by integrating the signal. The bunch structure can be observed with a bandwidth of typically 1 GHz, corresponding to a rise time constant of $\tau_{\mathrm{rise}} = 160$ ps [5,8]. As a second example, the observation of the bunch structure during acceleration inside a synchrotron is shown in Fig. II.9.10 for the acceleration of an ion beam injected at a non-relativistic velocity of $\beta = v/c = 15\%$ and accelerated to $\beta = 69\%$. Due to the velocity increase, the bunches approach each other and get smaller as expected from the conservation of the normalised longitudinal emittance, see Section II.9.6. Generally, the observation of the bunches during acceleration and possible bunch merging or splitting is observed by the FCT, and eventually, a feedback system for the control of the acceleration frequency, amplitude and phase is generated from the FCT signal. An innovative diagnostics method has been developed [9, 10] to determine the longitudinal phase space distribution and hence the longitudinal emittance from a measurement of the bunch shape on a turn-by-turn

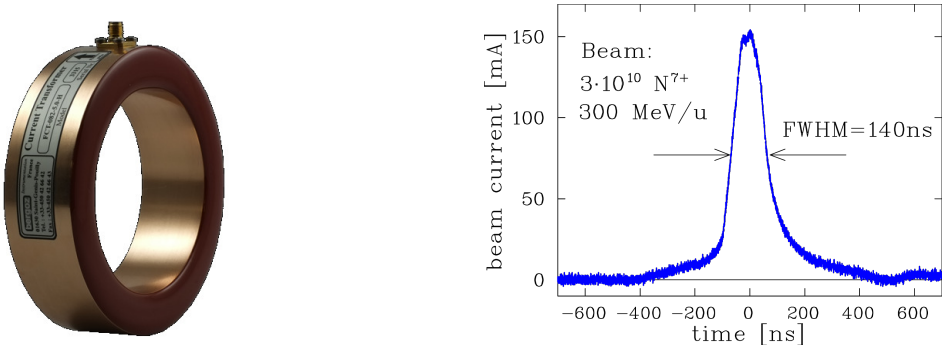

Fig. II.9.9: Left: Photo of a commercially available passive transformer [5]. Right: The signal from a passive transformer for a single beam bunch extracted from the GSI synchrotron at 300 MeV/u.

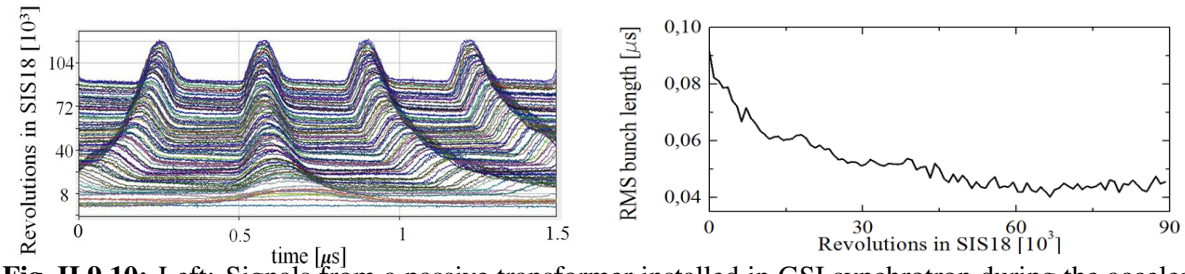

Fig. II.9.10: Left: Signals from a passive transformer installed in GSI synchrotron during the acceleration of a U^{73+} beam. The beam is injected at 11 MeV/u, corresponding to a velocity of $\beta = 15\%$ then four bunches are built and accelerated to 350 MeV/u, corresponding to $\beta = 69\%$ with an accelerating frequency swing from 0.85 MHz to 3.80 MHz within 0.3 s. Each 0.15 ms, a trace of the circulating bunches are shown. Right: The width (one standard deviation) of the bunches during acceleration is shown.

basis. The idea is based on the tomographic reconstruction used as an imaging technique in medicine for X-ray tomography.

An example is the observation of the bunch structure during acceleration inside a synchrotron, as shown in Fig. II.9.10 for the acceleration of an ion beam injected at a non-relativistic velocity of $\beta = 15\%$ of velocity of light and accelerated to $\beta = 69\%$. A second example is shown in Fig. II.9.9 for one bunch extracted from a synchrotron within one revolution, the so-called fast extraction. In the latter case, the passive transformer is installed in the beam pipe outside the synchrotron. The beam pulse length is typically between 1 ns and 10 μs. Moreover, with the passive transformer, the bunch structure in time domain can be observed, and a bandwidth typically of 1 GHz, corresponding to a rise time constant of $\tau_{\text{rise}} = 160$ ps, can be achieved [5, 8]. The specifications of the GSI device are listed in Table II.9.2. Careful matching is necessary between the torus and the 50 Ω resistor R, where the voltage drop is measured.

To get the right choice of the parameters of a passive transformer, we have some requirements:

1. For a high sensitivity, i.e., a large voltage U, a low number of windings is preferred, according to $U(t) \propto 1/N$ in Eq. II.9.6.
2. For a long droop time constant, i.e., the possibility of measuring long beam pulses, a large inductance has to be used. The scaling is $L \propto N^2$ and $L \propto \mu_{\text{r}}$ as given in Eq. II.9.4. Therefore

Table II.9.2: Basic specification of the GSI passive transformer [8].

Parameter	Value
Torus radii	$r_\mathrm{i} = 70$ mm, $r_\mathrm{o} = 90$ mm
Torus thickness l	16 mm
Torus material	Vitrovac 6025: $(\mathrm{CoFe})_{70\%}(\mathrm{MoSiB})_{30\%}$
Torus permeability μ_r	$\mu_\mathrm{r} \simeq 10^5$ for $f < 100$ kHz, $\mu_\mathrm{r} \propto 1/f$ above
Number of windings N	10
Sensitivity S	4 V/A at $R = 50\ \Omega$ (10^4 V/A with amplifier)
Current resolution I_min for $S/N = 1$	40 $\mu\mathrm{A_{rms}}$ for full bandwidth
Droop time constant $\tau_\mathrm{droop} = L/R$	0.2 ms, corresponding to 5% per 10 μs pulse length
Rise time constant $\tau_\mathrm{rise} = \sqrt{L_\mathrm{S} C_\mathrm{S}}$	250 ps
Bandwidth	$f_\mathrm{low} = 0.75$ kHz to $f_\mathrm{high} = 660$ MHz

materials with high permeability are used, e.g., CoFe-based amorphous alloy (so-called Vitrovac©) with $\mu_\mathrm{r} \sim 10^5$. For higher frequencies, μ_r decreases and, therefore, the torus inductance L. A typical cut-off frequency is 100 kHz with a scaling for higher frequencies $\mu_\mathrm{r} \propto 1/f$.

3. To achieve a fast rise time and, therefore, a fast response, the stray capacity C_s should be low due to $\tau_\mathrm{rise} \propto \sqrt{L_\mathrm{s} C_\mathrm{s}}$.

An additional general point is that close to the transformer, the electrical conductivity of the beam pipe has to be interrupted, as schematically shown in Fig. II.9.11. This is done with an insulator, realised by either a ceramic gap or a plastic vacuum seal. The reason is to prevent image current flowing inside the transformer torus. This image current has the opposite sign than the beam current, and without the gap, the field from the image currents add up to zero. Some metallic housing must bypass the image current outside of the transformer torus. It is surrounded by high permeability μ-metal, also used to shield the transformer against external magnetic fields. A general review on transformers is presented in Refs. [6, 7].

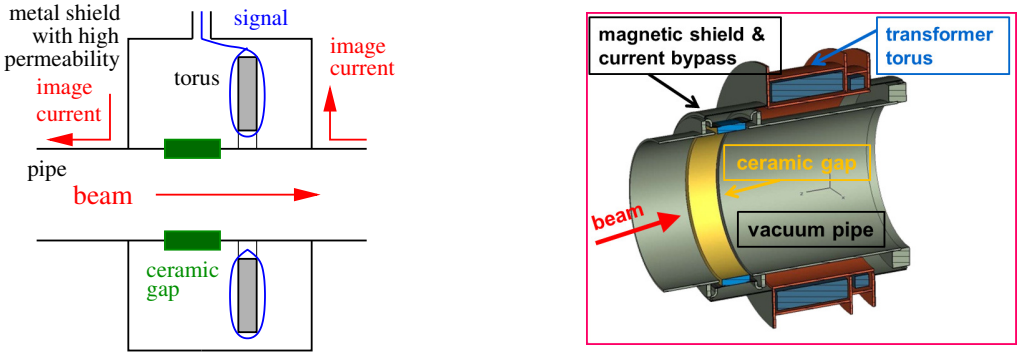

Fig. II.9.11: Left: The schematics show the general scheme beam pipe intersected by a ceramic gap and a transformer housing as used as an image current pass and shielding against external magnetic fields is shown. Right: The technical drawing for a transformer arrangement surrounding a beam pipe, including the gap and magnetic shield, is shown.

Table II.9.3: Some basic specifications of the GSI LINAC active current transformer. Due to the usage of an operational amplifier, the sensitivity is significantly higher than for the passive transformer of Table II.9.2.

Parameter	Value
Torus radii	$r_\mathrm{i} = 30$ mm, $r_\mathrm{o} = 45$ mm
Torus thickness l	25 mm
Torus material	Vitrovac 6025: $(\mathrm{CoFe})_{70\%}(\mathrm{MoSiB})_{30\%}$
Torus permeability μ_r	$\simeq 10^5$
Number of windings N	2×10 with opposite orientation
Maximal sensitivity S	10^6 V/A (with operational-amplifier)
Ranges of the beam current	1 μA to 100 mA
Current resolution I_min for $S/N = 1$	0.2 $\mu\mathrm{A}_\mathrm{rms}$ for full bandwidth
Droop	$< 0.5\%$ for 5 ms pulse length
Upper cut-off frequency f_high	1 MHz (as given by the op-amp property)
Rise time constant τ_rise	160 ns

II.9.2.1.2 Active AC-transformer

For the observation of beam pulses longer than several μs, the droop of a passive transformer leads to significant deformation of the measured signal, as schematically shown in Fig. II.9.7. The droop time constant can be made much longer by using an operational amplifier (op-amp) with a feedback resistor R_f and an open-loop gain A, instead of a constant resistor to measure the voltage. The equivalent circuit is shown in Fig. II.9.8 (right). This scheme is **A**ctive **C**urrent **T**ransformer **ACT**. The effect is the reduction of the operational-amplifier input resistance by a factor of R_f/A. This setup refers to as trans-impedance amplifier or current-to-voltage converter. The remaining resistance is, in most cases, only given by the cable resistivity R_L due to $R_\mathrm{f}/A \ll R_\mathrm{L}$. The droop is now

$$\tau_\mathrm{droop} = \frac{L}{R_\mathrm{f}/A + R_\mathrm{L}} \simeq \frac{L}{R_\mathrm{L}}. \tag{II.9.19}$$

Droop time constants up to 1 second are possible. (Typical cable resistance values are $R_\mathrm{L} \sim 1\ \Omega$.) An additional winding (not shown in Fig. II.9.8 right) can be used to compensate for the "natural" known droop. Moreover, the operational amplifier's feedback resistor R_f can be used for range switching. This principle is called the active transformer or **A**lternating **C**urrent **C**urrent **T**ransformer **ACCT**.

The rise time τ_rise for this active type is much larger than for the passive type. This is mainly due to the choice of low bandwidth (low value of the upper cut-off frequency) of the operational amplifier to reduce the amplifier's high-frequency noise significantly. This results in the high sensitivity of an active transformer.

We discuss here a typical device [8] used at the heavy ion LINAC at GSI with a pulse length of 100 μs (used for the filling of a synchrotron) and 5 ms (used directly by the experiments). The macro pulse current ranges from the low detection threshold of $\sim$ 200 nA up to 100 mA. The extensive dynamic range depends on the operational needs and the maximum current the ion source can deliver. Figure II.9.12 shows the hardware of an ACT and Table II.9.3 contains the parameters for a commercially available type [5].

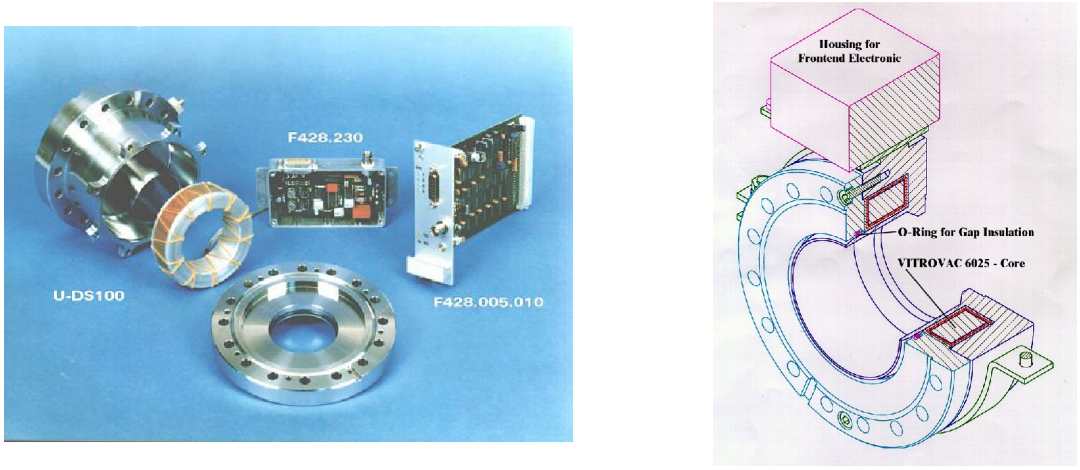

Fig. II.9.12: Left: Photo of an AC-current transformer used at the pulsed heavy ion LINAC at GSI. The torus with the differential winding is shown together with the electronic modules. Right: Technical drawing of the same transformer.

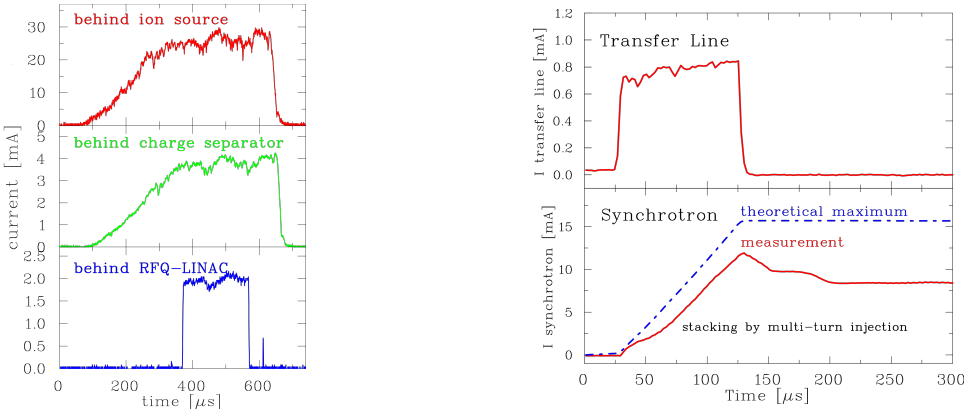

Fig. II.9.13: Left: Transmission determination by AC-transformers at three different locations at the GSI LINAC using a Ni^{2+} beam from a high current source. The upper curve shows the current after the ion source where all charge states are present. The second curve behind a magnetic bend filters the Ni^{2+} ionic state. The third curve is the current after the first LINAC module.
Right: The multi-turn injection at GSI was measured with two AC-transformers. The upper curve is the current delivered by the LINAC, and the lower curve is the stored current in the synchrotron. In this case, 20 turns are used, and 70% efficiency is reached for this Ni^{26+} beam.

The device has a rise time of 1 μs and a maximum droop of only 0.5% for 5 ms long pulses. The torus material is made of amorphous alloy $(CoFe)_{70\%}(MoSiB)_{30\%}$ (Vitrovac©), to enable considerable sensitivity. Besides the high permeability of $\mu_r \simeq 10^5$ it has a high electrical resistance resulting in fast decay of eddy currents. The torus is made of flat strips of 25 μm thickness with a thin insulation and is wound to get the final thickness of $r_o - r_i = 15$ mm. Another essential material constant is the change of the inductance as a function of external stress, the so-called magnetostriction. A low value prevents the micro-phonic pick-up of vibrations produced, e.g., by vacuum pumps.

A measurement done with these types of transformers is shown in Fig. II.9.13 (left), where one macro-pulse is recorded at three locations starting at the ion source until the exit of the first LINAC tank. A high current beam is generated in the ion source with $\sim$ 0.5 ms length. The slow rise of the

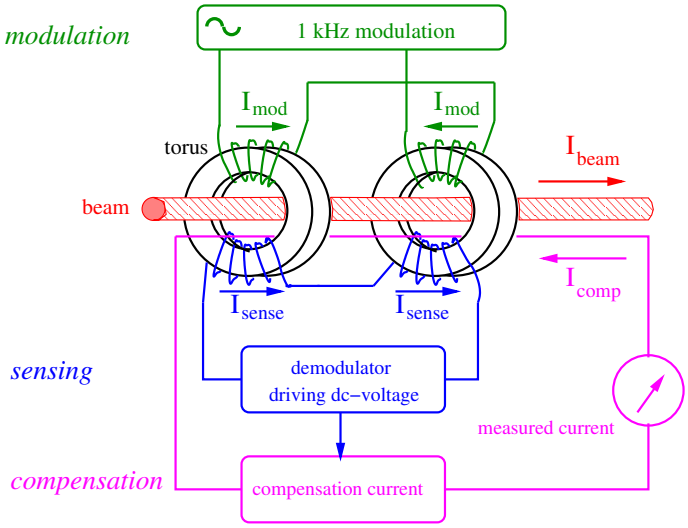

Fig. II.9.14: Schematics of a DC-transformer, see text.

beam current before the LINAC is due to the build-up of the space charge compensation of the unbunched beam. A chopper in front of the LINAC generates the needed pulse length. Transformers are essential to determine and maximise the transmission through the accelerator, particularly if the ion source conditions are unstable. A non-destructive method is needed to follow the beam pulse for its pass through the full accelerator. These transformers are the most frequently used diagnostics for the operation of the accelerator.

To control the filling of a synchrotron by a pulse from a LINAC, transformers of the described type are used. One is mounted in the external beamline, measuring the delivered current, and the other is installed inside the synchrotron to determine the stored current. The multi-turn injection is done with some bumper magnets to fill the horizontal acceptance of the synchrotron by the LINAC pulse, which is much longer than the revolution period. Such a measurement at the GSI facility is shown in Fig. II.9.13 (right): The injection takes place over 20 turns, and accumulation by a factor ~ 15 is achieved. For each beam setting, optimisation of the injection process is an important task to achieve a maximal matching.

II.9.2.2 The DC-transformer

An essential task for beam diagnostics is the measurement of coasting (also refers to as direct current dc) beam current. The application is either a LINAC producing a continuous beam, also referred to as a continuous wave (also refers as to cw) mode, or a synchrotron with storage times from seconds to many hours. The transformers discussed in the previous sections only work for a pulsed beam, even though the droop time constant can be made to be of the order of a second.

The principle of a dc transformer, the so-called **D**irect **C**urrent **C**urrent **T**ransformer **DCCT** [5, 8, 11] is shown schematically in Fig. II.9.14. It consists of two tori with three types of windings, respectively. The first windings of each torus with opposite orientation act as a modulator. The modulation frequency is typically 1-10 kHz. The amplitude of the modulation current is high enough to force the torus into magnetic saturation of $B_{\mathrm{sat}} \simeq 0.6$ T, for positive and negative azimuthal B-field orientation each period. The secondary windings with equal orientation act as a detector for the modulated signal,

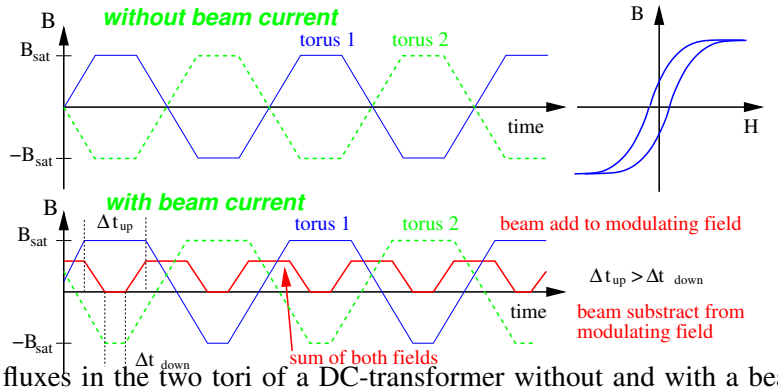

Fig. II.9.15: The fluxes in the two tori of a DC-transformer without and with a beam. The magnetic induction B of the beam adds to the modulated H-field for one modulation phase, and 180^o degrees later, it is subtracted. The sum of the maximum magnetisation gives the measured signal. The scheme is drawn for a triangular modulation; the edges are smoother for a realistic sine modulation.

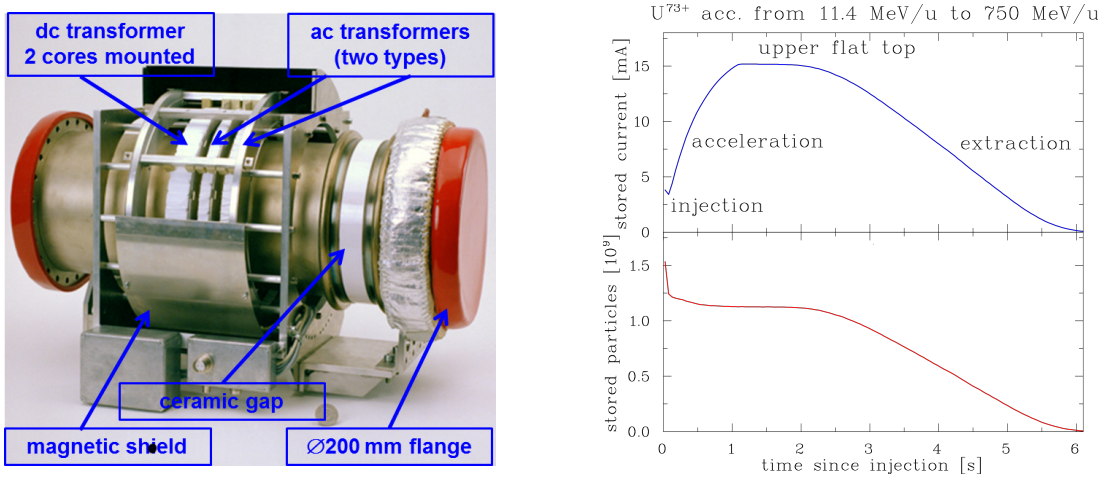

Fig. II.9.16: Left: The DC-transformer installed at the GSI synchrotron. The left torus is the DC-transformer (two tori mounted closely together), the middle is the ac-transformer used for the feedback of the DC-type, and the right one is the AC-transformer for the control of the injection.
Right: The signal of a DC-transformer for a $^{238}U^{73+}$ beam at the GSI synchrotron. The electrical current is shown at the top, and the number of stored particles at the bottom. The acceleration needs about 1 s. After a delay of about 0.5 s, the slow extraction of 4 s length follows.

see Fig. II.9.15. Assuming perfectly identical magnetic characteristics of both tori, the detector signal, as shown in the scheme, should be zero if no beam current flows through the tori. However, an asymmetric shifting of the hysteresis curve results if a DC-beam is fed through the tori, because of the additional magnetic field from the beam. The sum signal U_S is different from zero with a modulation twice the modulation frequency. In the demodulator stage, this signal is rectified. The DC-current is measured by means of the current generated in the feedback compensation circuit, which forces the output signal back to zero flowing through the third winding of both tori. The detector can even be used at even harmonics of the modulation frequency, which results in higher sensitivity and improved signal-to-noise ratio. Due to the precise requirements concerning the matching of the magnetic characteristics for a pair of tori, the design of a magnetic modulator with high resolution and DC-stability is rather complex and depends very much on the selection and treatment of the core material, as discussed in more detail in Ref. [11].

Table II.9.4: The specification of the DC-transformer installed at the GSI synchrotron.

Parameter	Value
Torus radii	$r_{\mathrm{i}} = 135$ mm, $r_{\mathrm{o}} = 145$mm
Torus thickness l	10 mm
Torus material	Vitrovac 6025: $(CoFe)_{70\%}(MoSiB)_{30\%}$
Torus permeability	$\mu_{\mathrm{r}} \simeq 10^5$
Isolating gap	Al_2O_3
Number of windings N	16 for modulation and sensing
	12 for feedback
Ranges for beam current	300 μA to 1 A
Current resolution I_{min} for $S/N = 1$	2 μA
Bandwidth	dc to 20 kHz
Rise time constant τ_{rise}	20 μs
Offset compensation	± 2.5 μA in auto mode
	< 15 μA/day in free run
offset current temperature coefficient	1.5 μA/^{o}C

The applied feedback circuit for the zero flux compensation makes the device sensitive and linear. To achieve a fast response, the signal from an AC-transformer is added into the feedback circuit. With this enhancement, the time resolution of the full device is in the range of 20 μs.

The specification of a typical DC-transformer developed for the heavy ion synchrotron at GSI is given in Table II.9.4 and a photo in Fig. II.9.16 (left). The resolution is about 1 μA. The offset drift, mainly caused by the magnetic properties of the tori, is of the order of 20 μA per day. An automatic zero compensation can improve the offset at times the synchrotron does not contain any beam, e.g., after the ramp-down phase of the magnets. For the parameters of a commercially available type, see [5].

An example of a DC-transformer measurement is shown in Fig. II.9.16 (right). The electrical current and the number of stored particles are shown. A $^{238}U^{73+}$ beam is injected in the synchrotron, and the acceleration starts shortly after the injection. A loss of particles is seen during the rf bunching process due to some misalignment. During the acceleration, the slope of the magnetic field $dB/dt = 1.3$ T/s is constant, resulting in a constant rise of the particle momentum. The current grows linearly only for non-relativistic velocities due to the decrease of the revolution time, inversely proportional to the velocity. For the maximal energy of 750 MeV/u, corresponding to $\beta = 84$ %, the relativistic increase of the mass starts to be significant. After reaching the maximum energy, a ~ 0.5 s flat top is seen for the de-bunching phase. The slow extraction of several seconds is done by changing the tune using a fast quadrupole to get close to a 1/3-resonance to blow up the transverse beam dimension. The resonant beam particles are then separated from the stable circulating beam by an electro-static septum and are extracted.

II.9.2.3 The integrating current transformer

In the past two decades, various electron LINAC facilities came into operation for the production of intense and short light pulses generated by the synchrotron light from high energetic electrons; these are the so-called **F**ree **E**lectron **L**aser **FEL** facilities. In many cases, only one or few bunches are accelerated

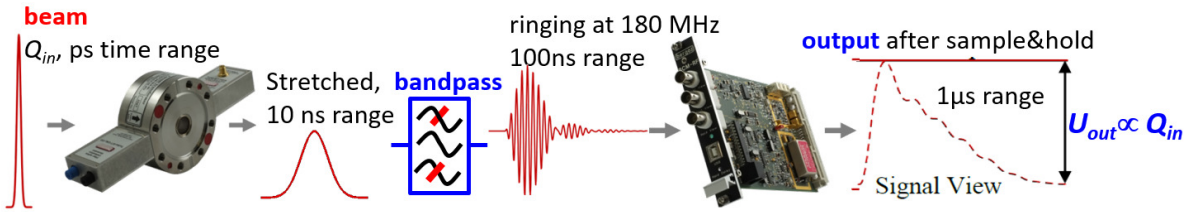

Fig. II.9.17: Functional scheme for ICT showing the short beam bunch of 1 ps duration and its stretching by the ICT. For the so-called turbo-ICT, the signal is filtered with a small bandwidth and the amplitude is detected with an analogue sample&hold circuit. Drawing from company Bergoz [5].

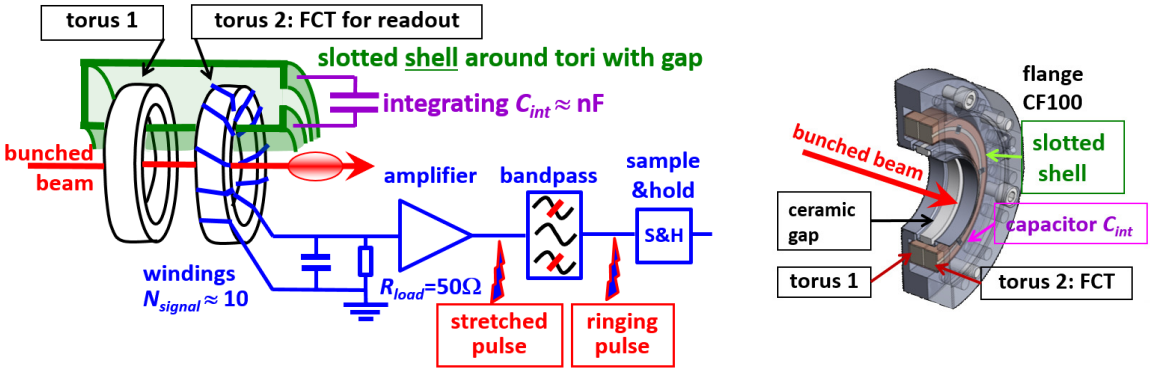

Fig. II.9.18: Left: The general scheme of an ICT. Right: Technical drawing of an in-flange ICT (flange diameter 100 mm) produced by company Bergoz [5].

with a typical bunch length below $t_{\mathrm{bunch}} \leq 1$ ps and repetition periods much longer than $t_{\mathrm{rep}} > 1$ μs. (For comparison, a rise time constant of $\tau_{\mathrm{rise}} = 1$ ps corresponds to a bandwidth of $f_{\mathrm{high}} = (2\pi\tau_{\mathrm{rise}})^{-1} =$ 160 GHz.) A signal for such short bunches cannot be recorded by the transformer type FCT, as its rise time constant is typically much longer and of the order of $\tau_{\mathrm{rise}} \simeq 200$ ps, corresponding to a bandwidth of 0.8 GHz, see Table II.9.2. The usage of an FCT would result in the damping of high frequencies generated by the electrons' magnetic field from the bunches. Instead, another principle referred to as **I**ntegrating **C**urrent **T**ransformer **ICT** is used to determine the number of charges accelerated within the bunch. The related type of signal integration with the typical time scales involved is depicted in Fig. II.9.17.

The general principle of an ICT is based on integrating the image current accompanying the electron bunch. The scheme is depicted in Fig. II.9.18. The electron bunch passes through two tori. These tori are surrounded by a metallic shell made of copper due to its high conductivity. The shell has an interruption at one side coaxially oriented to the beam pipe and bridged with several capacitors with a sizeable total capacitance of typically $C_{\mathrm{int}} \simeq 1$ nF. The image current, as generated by the short passage of the electron bunch, charges these capacitors. In the following time period, the capacitors discharge within a duration much longer than the beam pulse. This discharge-current is sensed by a regular FCT (here called torus 2), as described in Section II.9.2.1.1. The related time constant for the discharge is given by the values of the integrating capacitors C_{int}, the inductance of the transformer tori in connection with the winding number N_{signal} and the load resistor R_{load}, see Fig. II.9.18. Two tori are used for

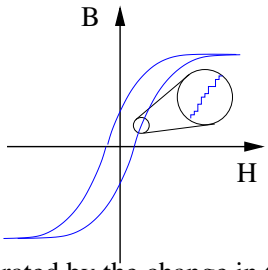

Fig. II.9.19: Barkhausen noise generated by the change in the orientation of the Weiss domains.

the practical realisation to enable better possibilities to match those electrical parameters, in particular, to limit the discharge current sensed by torus 2. An analysis of the equivalent electronics circuit and an example of the realisation is given in Ref. [12]. Beside the usage at electron LINACs, ICTs are installed at synchrotrons providing a precise bunch charge measurement in case the bunch width is significantly shorter than the bunch spacing as, e.g. realised at LHC [12, 13]. In summary, a stretching of the original short pulse is achieved by transferring the signal to a more manageable time range which enables the usage of regular electronics for further signal treatment. A resolution for the single bunch charge down to typically $Q_{\min} \simeq 1$ pC can be reached, corresponding to 10^7 electrons per bunch.

A further increase of sensitivity can be achieved by filtering the signal with a narrow bandpass filter, where the broadband pulse from torus 2 results in a ringing signal shape. Finally, the amplitude of this damped oscillation in the range of 100 MHz is detected by an analogue sample&hold circuit and then digitised. This principle is called Turbo-ICT; a design and its application are described in Refs. [14, 15]. The achievable resolution of a Turbo-ICT is in the order of $Q_{\min} \simeq 10$ fC, corresponding to about 10^5 electrons per bunch. The break between consecutive macro-pulses must be longer than typically 1 μs to allow for the shell discharge and the decay of the filtered signal oscillation. The related beam parameters correspond to the lower operation limit at FEL-based LINAC facilities. The time information related to the bunch shape is lost by this principle but is measured by other means described in Section II.9.6.9.

II.9.2.4 The low current limit of transformers

The very low magnetic field carried by the beam is detected with a transformer; the detection threshold or the signal-to-noise ratio is discussed briefly:

1. A first general limitation is the thermal noise of the load resistor. The effective thermal noise voltage U_{eff} is given by
$$U_{\text{eff}} = \sqrt{4k_{\text{B}}T \cdot R \cdot \Delta f} \tag{II.9.20}$$
where T is the temperature of the resistor R, k_{B} the Boltzmann constant and Δf the required bandwidth. A general rule is that the noise is lower for a smaller bandwidth for a passive transformer $R = 50\ \Omega$ for the load resistor. For an active transformer, the amplifier noise dominates.
2. Regarding the magnetisation of the core material on an atomic scale for solid-state materials Weiss domains develop. The maximum magnetisation is reached in such a Weiss domain, but the different domains' magnetisation does not have the same orientation. By applying an external field the Weiss domains change their orientations in a jerky way. This results in a noisy behaviour, schematically demonstrated in Fig. II.9.19; the effect is called Barkhausen noise. This limitation arises in

the case of the dc transformer due to its operational principle involving modulation, which leads to the saturation of the tori. In contrast, for an ac transformer, the significance of Barkhausen noise diminishes, primarily because of the low-resistive coupling in the secondary winding (50 Ω for the passive type and the low-impedance input of the op-amp for the active type), which effectively prevents the magnetisation of the torus.

3. Selecting the right magnetic core material is crucial to minimize temperature sensitivity and minimize the impact of mechanical vibrations, particularly in terms of reducing magnetostriction.
4. Even when the local magnetic field is accurately measured, it may not necessarily represent the field of the beam. Specifically, the presence of eddy currents within the torus or its vicinity can result in noisy or inaccurate readings. To mitigate eddy currents, a spiral-wound flat ribbon, approximately 25 μm in thickness, featuring high resistivity and insulation between layers, is employed.
5. The transformer has to be well-shielded against external magnetic fields. In particular against the fields from the bending and focusing magnets and the magnetic fields produced by turbo pumps magnetic bearing.
6. It is imperative to control the flow of secondary electrons generated when the beam strikes the vacuum pipe in order to prevent significant inaccuracies in the readings. Shielding within the vacuum pipe is typically a challenging task. Therefore, precise control over beam steering becomes crucial in addressing this issue.

The actual value of the minimum detected beam current depends on the design of the device and the desired time resolution or bandwidth. For most beam current measurements, it is roughly around $I_{\min} \simeq 1$ μA. The ICT measures electrical charges and, hence, does not have a particular time resolution. The detection threshold is $Q_{\min} \simeq 10$ fC.

II.9.2.5 Energy loss and ranges of particles in matter

II.9.2.5.1 Material interaction of protons and ions

For the discussion of all invasive diagnostics, such as Faraday cups, ionisation chambers, wire scanners etc., the energy loss and the related range of the particles penetrating matter serves as the basic physical mechanism. The energy loss of a proton or an ion is mainly due to the collision of the projectile with the electrons of the stopping target, as referred to electronic stopping power.

Due to the different masses of ions and electrons, the energy transfer to the electron per collision is, in most cases, below 100 eV, i.e. only a small fraction of the projectile's kinetic energy. The electronic stopping power $\frac{dE}{dx}$ can be approximated by the semi-classical Bethe-formula which is written in its simplest form as [16–19]

$$-\frac{dE}{dx} = 4\pi N_{\mathrm{A}} r_{\mathrm{e}}^2 m_{\mathrm{e}} c^2 \cdot \frac{Z_{\mathrm{t}}}{A_{\mathrm{t}}}\rho \cdot Z_{\mathrm{p}}^2 \cdot \frac{1}{\beta^2}\left[\frac{1}{2}\ln\frac{2m_{\mathrm{e}}c^2\gamma^2\beta^2 W_{\max}}{I^2} - \beta^2\right] \tag{II.9.21}$$

with the constants: N_{A} the Avogadro number, m_{e} and r_{e} the rest mass and classical radius of an electron and c the velocity of light. The target parameters are: ρ density of the target with nuclear mass A_{t} and nuclear charge Z_{t}; the quantity $\left(\frac{Z_{\mathrm{t}}}{A_{\mathrm{t}}}\rho\right)$ corresponds to the electron density. I is the mean ionisation potential for removing one electron from the target atoms; a rough approximation for a target with nuclear

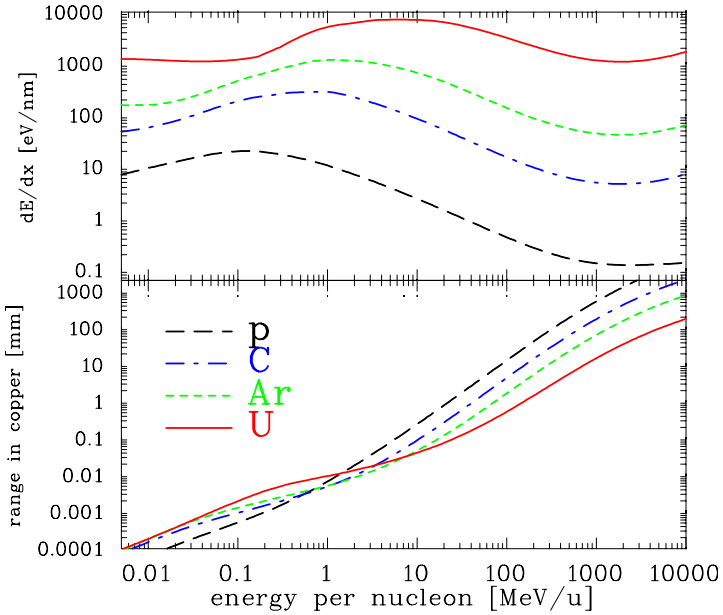

Fig. II.9.20: The energy loss at the surface and the range in copper as a function of the kinetic energy for several ions. The energy interval is plotted from 5 keV/u to 10 GeV/u and the range from 100 nm to 1 m. Electronic and nuclear stopping calculation uses the semi-empirical code SRIM [20].

charge Z is $I \simeq Z_\mathrm{t} \cdot 10$ eV, more precise values are given e.g. in Refs. [19,20]. The projectile parameters are: Z_p nuclear charge of the ion with velocity β and Lorentz factor $\gamma = (1-\beta^2)^{-1/2}$. The maximal energy transfer W_max from relativistic proton or ion projectile of rest mass M to the target electrons of rest mass m_e is given by kinematic considerations for a central collision as [19]

$$W_\mathrm{max} = \frac{2m_\mathrm{e}c^2\beta^2\gamma^2}{1 + \frac{2\gamma m_\mathrm{e}}{M} + \left(\frac{m_\mathrm{e}}{M}\right)^2} \qquad \text{which converges for } \frac{M}{\gamma} \gg m_\mathrm{e} \text{ to} \qquad W_\mathrm{max} = 2m_\mathrm{e}c^2\beta^2\gamma^2. \quad \text{(II.9.22)}$$

The approximation can be interpreted further: For proton or ion impact with non-relativistic energies, i.e. $\gamma \simeq 1$, the velocity of emitted electrons is maximal double of the projectile velocity as expected from classical, mechanical collisions between hard bullets.

The Bethe-formula's dependence on the target charge's square Z_p^2 is remarkable. The Bethe-formula must be modified for ionic projectiles since ions travelling through matter are not always bare nuclei but might still have some inner electrons. The projectile nuclear charge Z_p must be replaced by an effective charge $Z_\mathrm{p}^\mathrm{eff}(\beta)$ in dependence of the velocity β, as calculated by e.g. semi-empirical methods described for the codes SRIM [20] and LISE++ [21].

The result of such semi-empirical calculation for the energy loss by SRIM is depicted in Fig. II.9.20 for different ions into copper as a representative for a medium-heavy metal target. The energy loss is maximal for ions with kinetic energy around 100 keV/u to 7 MeV/u (corresponding to velocities $\beta \sim 1.5$ % to 12 %) depending on the ion species. These are typical energies of a proton or ion LINAC. Below 100 keV/u the energy loss decreases, and nuclear stopping (i.e. the Coulomb collision between the projectile and target nucleus) becomes significant. Energies below 10 keV/u are typical for proton/heavy ion sources mounted on a high-voltage platform. The energy loss is nearly constant for relativistic energies above 1 GeV/u; these are characteristic energies of particles extracted from a syn-

chrotron. Note that the Bethe-formula is valid for any charged projectile with the assumption that its mass is significantly larger than the electron mass as the essential independent variable is related to the projectile velocity β. Frequently, the stopping power is additionally normalised to the matter density as $\frac{dE}{\rho dx}$ is tabulated.

Due to the interaction's statistical nature, fluctuations in the energy transfer occurs, which is generally called straggling. Related to the significant mass difference between the projectile and the target electrons, for the projectile's flight direction, the longitudinal straggling is lower than the range for beam energies above 1 MeV/u and the transverse, refer to lateral straggling, leads only to small variations of the flight path; analytic approximations are discussed in Refs. [16, 17, 19, 20]. Therefore, the projectile path is more or less straight with a defined range; the actual properties are calculated in codes like SRIM or LISE++.

For even lower energies of $E_{\mathrm{kin}} < 10$ keV/u, e.g. at the end of a projectile track, the probability of Coulomb collisions between the projectile and target nucleus dominates the stopping power [16, 20]; this is called nuclear stopping (note that the Coulomb force mediates and not the strong interaction). The energy transfer in this single collision within a crystal material can result in a knock-out of the target nucleus from its lattice position resulting in a displacement. This process leads to radiation damage of materials.

For the consideration of a Faraday cup (see section II.9.2.6), the range inside material is essential. Copper is often used for cups due to its high heat conductivity. The range R of the projectile of kinetic energy E_{kin} is calculated numerically via

$$R = \int_0^{E_{\mathrm{kin}}} \left(\frac{dE}{dx}\right)^{-1} dE \tag{II.9.23}$$

and has an approximate scaling for ions above $\simeq 10$ MeV/u [16]

$$R \propto E_{\mathrm{kin}}^{1.75} \quad . \tag{II.9.24}$$

The results are shown in Fig. II.9.20. For kinetic energies below some 10 MeV/u for protons or ions are shorter than about 1 mm, and a beam particle is stopped in the vacuum tube. But even for higher energies to about several 100 MeV/u, most beam particles are stopped in the vacuum chamber as it collides, in most cases under a grazing incidence. For energies above 1 GeV/u, material outside of the vacuum the beam particle penetrates the vacuum chamber. Nuclear reactions might be possible leading to isotopes with lifetimes above several minutes and, consequently to an activation.

II.9.2.5.2 Material interaction of electrons

The stopping of electrons in matter differs from protons and ions, see Fig. II.9.21 where the sum of the two relevant processes of collisional loss $dE/dx|_{col}$ and radiation loss $dE/dx|_{rad}$ are added. The collisional loss of electrons due to electronic stopping $dE/dx|_{col}$ is also described by a modified Bethe formula; the modification is caused by the equal mass of the projectile and the target electrons and their indistinguishably [16, 19]. This regime dominates for energies below 1 MeV as corresponding to the a velocity of $\beta = v/c = 94$ % and a Lorentz-factor of $\gamma = \left(1-\beta^2\right)^{-1/2} = 2.96$. Even a small

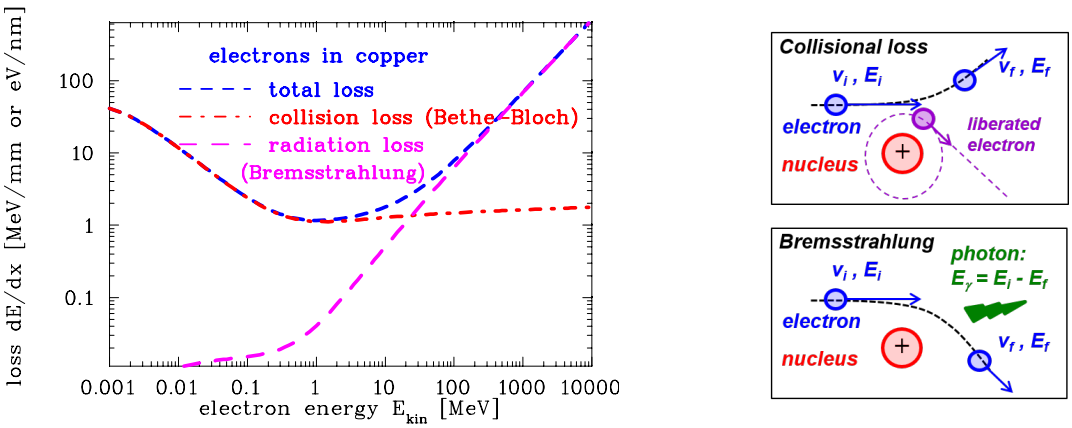

Fig. II.9.21: Left: Energy loss of electrons in copper showing the two regimes for collisional loss and Bremsstrahlung, data calculated in Ref. [22]. Right: Schematics for collisional loss and Bremsstrahlung.

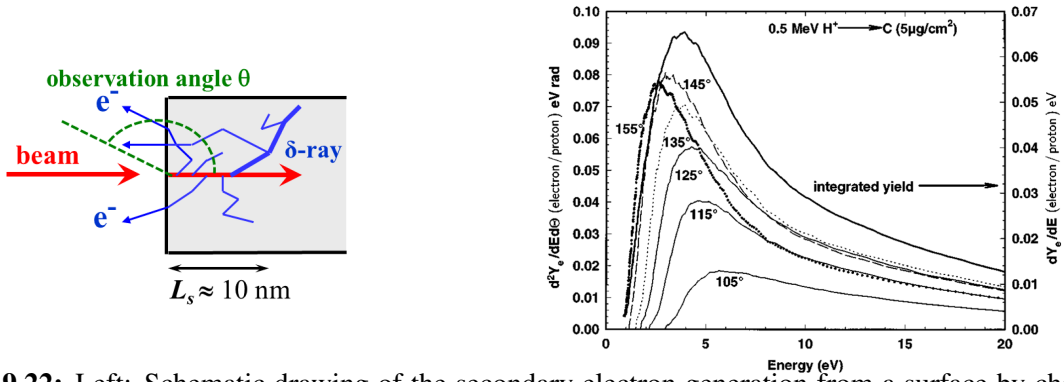

Fig. II.9.22: Left: Schematic drawing of the secondary electron generation from a surface by charged particle impact; L_s is the scattering length from which electrons can reach the surface. Right: A typical measurement of the electron energy spectrum for different emission angles and the total yield in the backward direction by 0.5 MeV proton impact on a carbon foil, from Ref. [24].

electron accelerator reaches higher final energies. For energies above a few 10 MeV, the radiation loss by Bremsstrahlung, i.e. the emission of photons by an acceleration of the electron in the vicinity of the target nucleus, dominant, see, e.g. Ref. [16, 19]. This radiation loss scales roughly linear to the electron energy and quadratically to the target charge Z_t as $dE/dx|_{rad} \propto E \cdot Z_t^2$.

The trajectories of the primary electrons in the target are more curved than for ions due to the possible high energy- and momentum transfer in a single collision, therefore electrons have much larger lateral straggling than ions. Moreover, the longitudinal straggling is more substantial than for ions resulting in a broader range distribution. Due to this extended range and the production of secondary charged particles, Faraday cups for stopping electrons are seldom used at electron accelerators; see Section II.9.2.8.

II.9.2.5.3 Secondary electron generation

When a charged particle, either an ion or an electron, travels through matter, it interacts with the target electrons. In a close, primary collision the target electron can be accelerated to high energies much larger than 100 eV, sometimes these electrons are called δ-rays. The energy distribution depends on the impact parameter and the energy of the incoming particle. In a metallic solid-state material the fast δ-electrons

collide with the surrounding electrons; because both collision partners have equal masses, the energy is transferred efficiently and more electrons are liberated; see the schematics in Fig. II.9.22. This so-called thermalisation of the electrons inside the conduction band is performed in a typical scattering length of some 10 nm, i.e. within the distance of some 100 lattice planes. Due to this many collisions, there is only a weak correlation between the direction of the incoming particle and the scattered electrons. If these electrons reach the surface and still have an energy higher than the work-function (typically 1 to 5 eV), they have a high probability of escaping from the metal. The current of the secondary electrons is given by the so-called Sternglass formula [23]

$$I_{\mathrm{sec}} = Y \cdot \frac{dE}{\rho dx} \cdot I_{\mathrm{beam}} \tag{II.9.25}$$

with I_{beam} being the current of incoming particles and Y being the yield factor describing the amount of secondary emission per unit of energy loss $\frac{dE}{\rho dx}$ at the surface of the metal. The yield Y depends on the metal (via the work-function) and the surface quality, e.g., modified by possible adsorbed gas contamination. The mean kinetic energy of the escaping secondary electrons is in the order of 10 eV and has some dependence on the emission angle; an example of the energy spectrum is shown in Fig. II.9.22 and discussed in more detail in Ref. [24]. To first order the angular distribution $P(\theta)$ of the electron emission can be approximated by a $P(\theta) \propto |\cos\theta|$ law [24], where θ is the angle of the trajectory with respect to the surface ($\theta = 180^\circ$ refers to backscattering, $90^\circ < \theta < 270^\circ$).

II.9.2.6 Faraday cups for low currents

A Faraday cup, designed to measure the electrical current of a particle beam, is illustrated in Fig. II.9.23, with an accompanying photograph in Fig. II.9.24. This instrument consists of an isolated metal cup connected to a current-sensitive pre-amplifier. As in the case of an active beam transformer, the pre-amplifier encompasses a low-impedance input and a subsequent conversion to voltage. Range switching is facilitated by utilizing various feedback resistors in conjunction with the operational amplifier. Faraday cups offer a distinct advantage in their ability to measure significantly lower currents compared to transformers. For instance, with the aid of a low-noise current-to-voltage amplifier and meticulous mechanical design, it becomes feasible to measure currents as low as 10 pA in a dc beam with long integration times up to 1 s. This level of sensitivity surpasses that of a dc transformer by a staggering five orders of magnitude. The capability to perform low-current measurements is of paramount importance, especially in applications such as the acceleration of radioactive beams.

When an accelerated particle hits a surface, secondary electrons are liberated, see also Section II.9.2.5. The flux of these electrons is proportional to $\cos\theta$, where θ is the angle of the electron trajectory with respect to the surface; their average energy is below $\simeq 10$ eV. If these electrons leave the insulated cup, the reading of the beam current is wrong by this amount. A secondary electron suppression has to be foreseen. It can be realised by:

- Very long cups, where the length in beam direction is much larger than the diameter. The contribution of the lost electrons is low for this geometry; this solution is rarely chosen.
- Using a high voltage suppression close to the entrance of the cup. By applying a voltage well above the mean energy of the secondary electrons, these electrons are pushed back to the cup

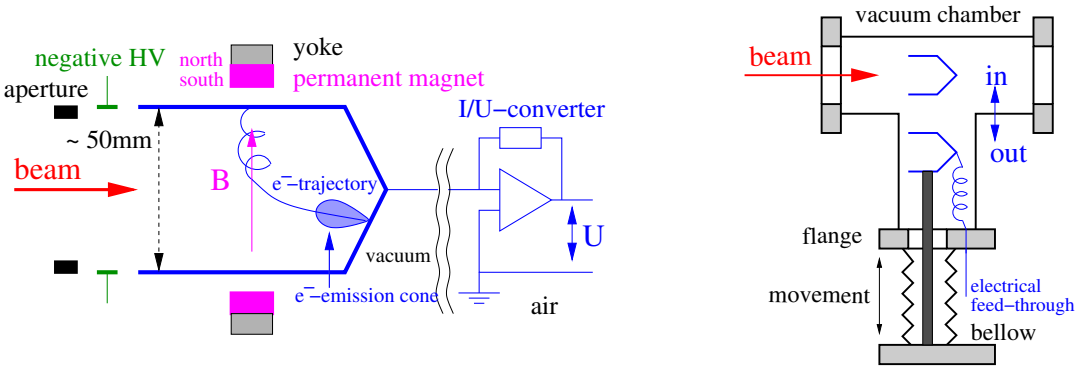

Fig. II.9.23: Left: Scheme of an uncooled Faraday cup with magnetic and electric secondary electron suppression. Right: Scheme depicting the inside and outside position of destructive diagnostics devices.

Fig. II.9.24: Photo of an Ø50 mm uncooled Faraday cup with magnetic and electric secondary electron suppression.

surface; see Fig. II.9.25 (left). For the geometry of a round biased aperture, the electrical field on the beam axis is lower than on the edges; in the depicted case, the maximum potential is about 35 % of the potential applied to the electrode. The emission of the maximal energetic electrons occurred opposite to the beam direction, and the potential has to be chosen to be higher than the kinetic energy of at least 99 % of the electrons. A measurement with varying suppression voltage is shown in Fig. II.9.25 (right).

– By using a magnetic field created by permanent magnets. In this field B, the secondary electrons spiral around the magnetic field lines with the cyclotron radius r_c

$$r_\mathrm{c} = \frac{\sqrt{2 m_\mathrm{e} E_\mathrm{kin}}}{eB} = 3.37 \frac{\sqrt{E_\mathrm{kin}[\mathrm{eV}]}}{B[\mathrm{mT}]}\ [\mathrm{mm}] \tag{II.9.26}$$

where m_e is the electron mass, e its charge and E_kin the kinetic energy component perpendicular to the field lines. For $E_\mathrm{kin} = 10$ V and a field of 10 mT the radius $r_\mathrm{c} \sim 1$ mm. With permanent magnets, field lines perpendicular to the beam axis can be created relatively easily, see Fig. II.9.26. Equation II.9.26 is derived from the equivalence of the Lorentz and centrifugal force $F_\mathrm{L} = F_\mathrm{c} \Leftrightarrow evB = \frac{m_\mathrm{e} v^2}{r_\mathrm{c}}$ and the kinetic energy $E_\mathrm{kin} = \frac{1}{2} m_\mathrm{e} v^2$.

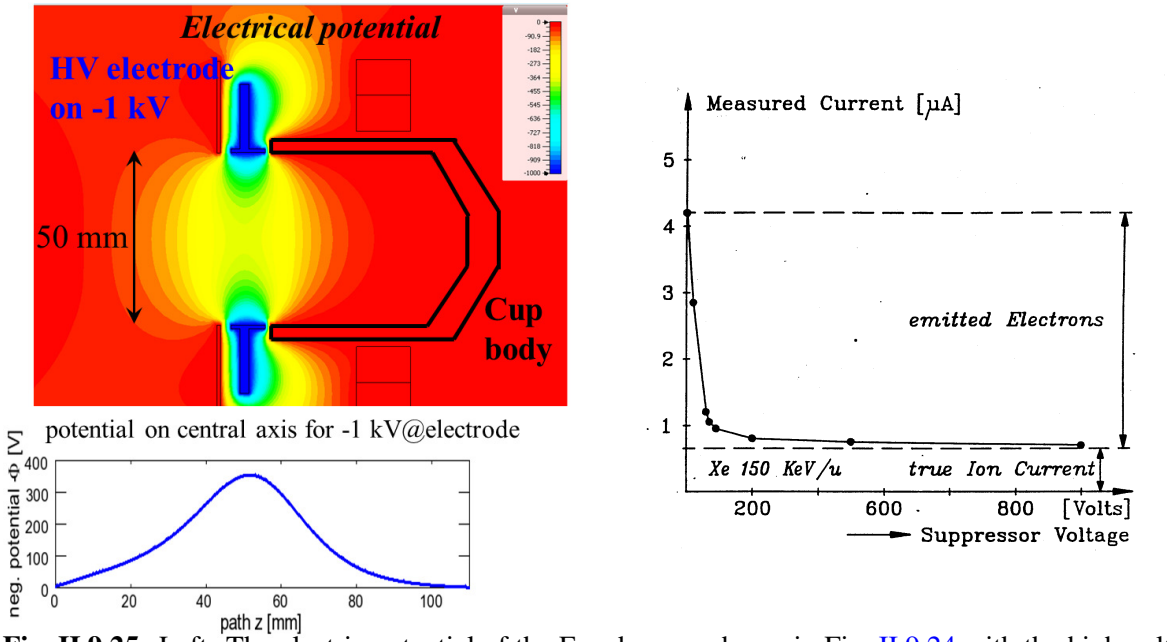

Fig. II.9.25: Left: The electric potential of the Faraday cup shown in Fig. II.9.24 with the high voltage electrode biased by -1 kV is shown at the cylindrical symmetry plane. The beam enters from the left. The negative potential along the central axis is depicted at the bottom. Right: The effect of secondary electrons suppression inside a Faraday cup as determined by the beam current determination as a function of the applied voltage.

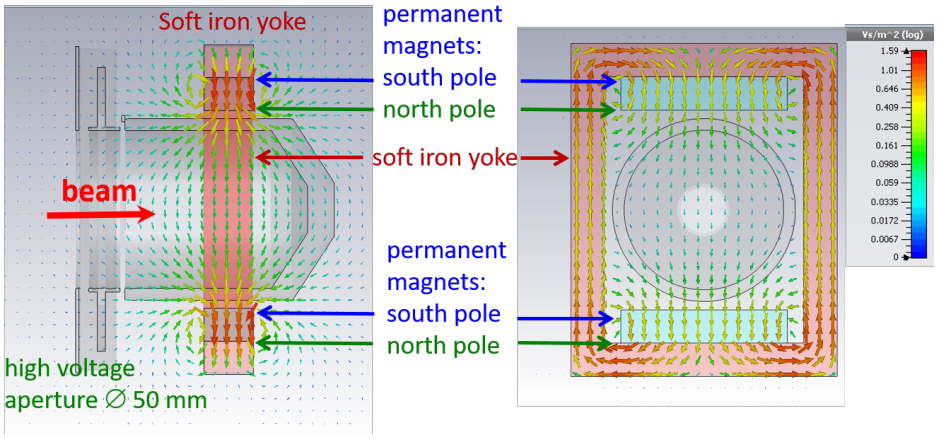

Fig. II.9.26: Magnetic field lines of the arrangement of Co-Sm permanent magnets within the yoke for the Faraday cup of Fig. II.9.24, side (left) and front view (right). At the beam location, the homogeneous field strength is $B \sim 60$ mT.

II.9.2.7 Faraday cups for high current ion beams

Faraday cups are sometimes used for higher beam currents, where measurements are also possible with AC-transformers because they are simpler to realise. In addition, cups serve as beam dumps. For all invasive diagnostic devices, the heating caused by the beam's energy loss must be considered. An example of the temperature rise is shown in Fig. II.9.27, where a pulsed beam (in this case an Ar^{10+} beam with 10 mA electrical current) of pulse length of 1 ms and a repetition time of 20 ms hits an uncooled foil. The heat source is the energy loss of the particles, while the heat sink is the radiation power per area P_r

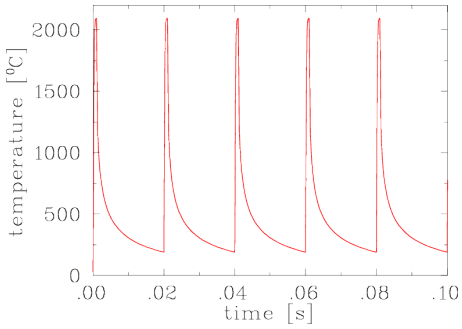

Fig. II.9.27: Temperature increase for a 1 μm thin tungsten foil (emissivity of $\epsilon = 0.49$) irradiated by a 10 mA Ar^{10+} beam of length 1 ms and repetition time of 20 ms with 11.4 MeV/u. The beam size is 5 mm FWHM in both directions and the absorbed power is ~ 40 kW/mm^2.

as described by the Stefan–Boltzmann law

$$P_{\mathrm{r}} = \epsilon \sigma T^4 \tag{II.9.27}$$

where T is the temperature and $\sigma = 5.67 \cdot 10^{-8}$ W/m^{2}K^4 the Stefan–Boltzmann constant. ϵ is the emissivity of the material with typical values $0.1 < \epsilon < 0.8$. Cooling by the emission of electromagnetic radiation is a fast cooling process only for high temperatures due to the T^4 dependence. The heat conductivity is a relatively slow process compared to the heating by a short, intense beam pulse. The foil is heated close to its melting temperature during the pulse (here about 2000 °C). In the intervals between the beam pulses, it cools down to 200 °C again, and the average temperature is only ~ 550 °C. Nevertheless, the material has to survive the high temperature during the beam delivery. The typical beam current needed for a neutron spallation source could easily be higher. A second cooling process is related to the emission of thermal electrons from a hot metallic surface where the electrons' kinetic energy reduces the thermal energy of the solid material. The basic formula for the current density of thermal electrons j_{th} is the Richardson law

$$j_{\mathrm{th}} = A_R T^2 e^{-\Phi/k_B T} \quad , \tag{II.9.28}$$

where $A_R \simeq 120$ AK^{-2}cm^{-2} is the Richardson constant, k_B the Boltzmann constant and Φ the material-dependent work function, which is for typical metals 2 eV $< \Phi <$ 5 eV. The cooling by thermal emission contributes significantly if the surface is close to its glowing temperature. Typical cooling properties are discussed in Ref. [33].

For a quantitative analysis of massive material, the partial differential equation of heat transfer inside the material has to be calculated numerically

$$\frac{\partial T(\vec{x},t)}{\partial t} = \frac{\lambda}{\rho c} \text{div grad } T + \frac{1}{\rho c}\eta(\vec{x},t) \tag{II.9.29}$$

for the temperature T as a function of time t at each position $\vec{x}$ inside the material. λ is the heat conductivity, ρ the density and c the specific heat. The source term $\eta(\vec{x},t)$ is the volumetric power deposition by the beam, which depends on position and time. For a more detailed discussion of an optimised material

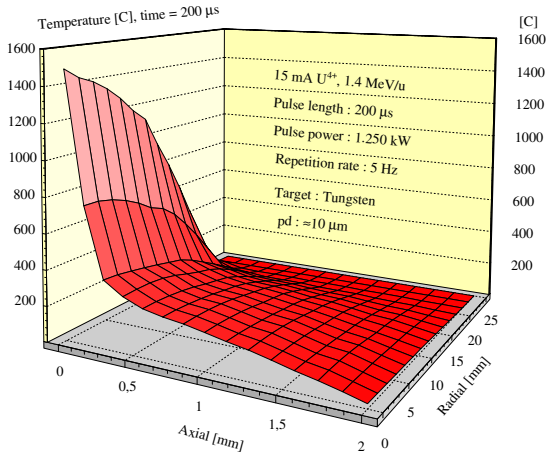

Fig. II.9.28: A 1.4 MeV/u U^{4+} beam of 15 mA electrical current and 0.2 ms pulse length hitting a cooled cylindrical Faraday cup. The distribution of the temperature is calculated by a finite-element method.

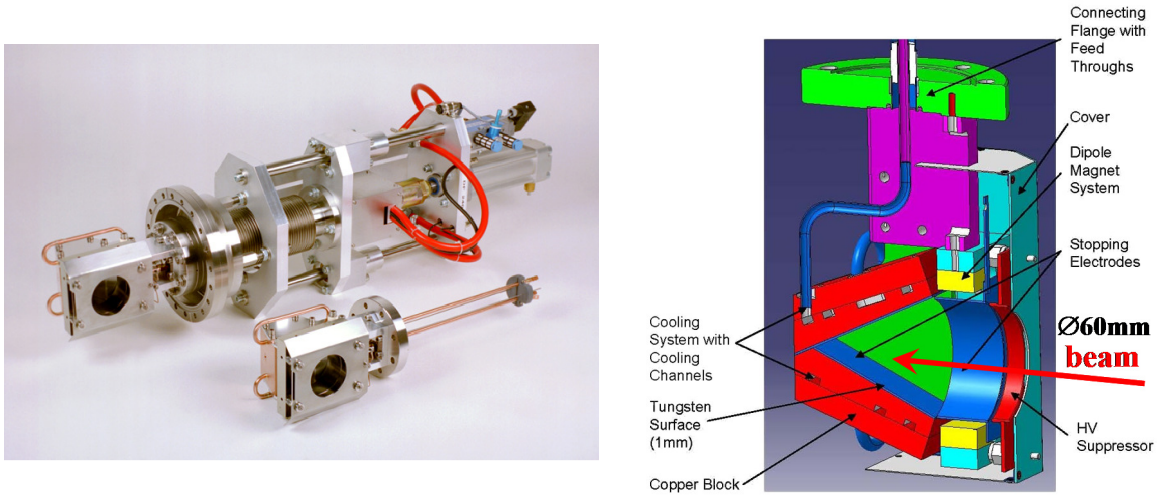

Fig. II.9.29: Left: Photo of a Faraday cup and beam stopper for high intensity beams as installed at the high current LINAC at GSI. The pneumatic drive is mounted on a Ø 150 mm flange. Right: The technical drawing of the same Faraday cup and beam stopper of high intensity beams. The opening of the cup is Ø 60 mm.

and geometric arrangement; see, e.g. Ref. [25].

An example of such a calculation is given in Fig. II.9.28 for a cylindrical cup for a high power Uranium ion beam at the end of the macro pulse. The value is set to the design power of the high current in the 1 MW LINAC at GSI. One solution to dissipate this large power is to increase the surface area of the irradiated material by a cone-like construction, as shown in Fig. II.9.29. The ions at the GSI LINAC have ranges below 1 mm. A 1 mm thin layer of tungsten is used to stop the ions as the melting temperature of tungsten is high as $T_{\mathrm{melt}} \simeq 3380$ °C; while for copper, the melting temperature is significantly lower, $T_{\mathrm{melt}} \simeq 1080$ °C . However, the underlying massive copper block is used for its high heat conductivity. The water cooling can only dissipate the average power, and an equilibrium temperature is reached. For pulsed beams, the maximum value at the surface, or more precisely, close to the range of the particles, is much higher than the equilibrium value. This high temperature is what mainly deteriorates the device. A careful design has to be done, and the beam parameters have to be controlled to prevent the destruction

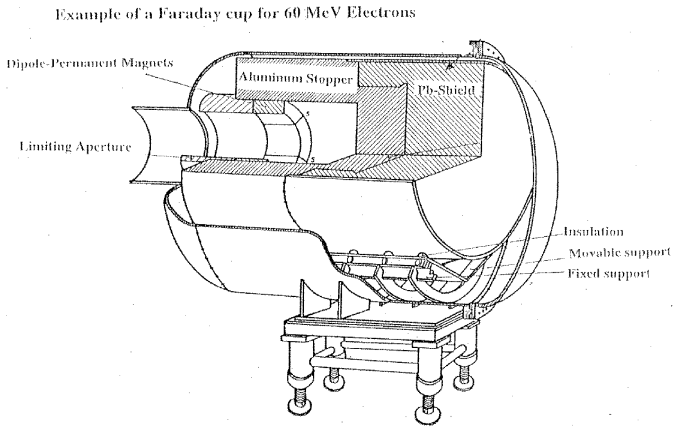

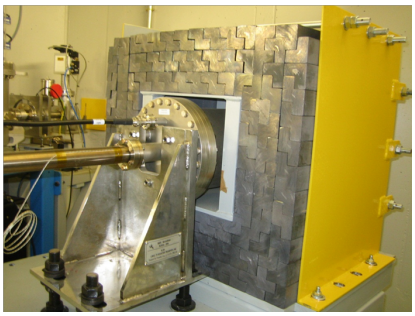

Fig. II.9.30: Left. A drawing of a cup used for 60 MeV electrons. Right. The installation of a Faraday cup used as a beam dump at ALBA, Barcelona.

of cups and beam dumps for higher-power LINACs and cyclotrons.

II.9.2.8 Faraday cups for electron beams

Faraday cups designed for capturing electrons need to be constructed larger in size compared to those intended for ions, as illustrated in Fig. II.9.30. As explained in Section II.9.2.5, where the energy loss of electrons in copper was discussed, a strategic approach is employed to gently decelerate the electrons within the Faraday cup. This is achieved by using low atomic number material such as aluminium. The purpose of this is to minimise the generation of highly energetic Bremsstrahlung photons within the cup which increase roughly with the atomic number Z as $\sigma_{\text{Brems}} \propto Z^2$. Moreover, it is essential to prevent the escape of charged particles, such as electrons or positrons, which may be produced as a result of the Bremsstrahlung photons. To address this concern, a lead shield is incorporated into the setup as an other layer. Because electrons possess a relatively long range within matter, the use of Faraday cups is typically limited to the initial modules of an electron linear accelerator.

Generally, at electron accelerators, Faraday cups are mainly used behind the electron gun for electrons with typically 100 keV energy. In this case, the construction is comparable to the Faraday cups used for proton beams; see Section II.9.2.6. At higher energies, i.e. behind the first few LINAC-modules, the required amount of material to stop the electrons and to absorb secondary charged particles (e.g e^+e^- pair production from the Bremsstrahlung-photons) increases significantly due to this long range. An example of a Faraday cup used for high energies up to some GeV, including the design considerations, can be found in Ref. [26]. In most cases, Faraday cups are used as beam dumps at the end of a transport line.

II.9.2.9 Low current measurement used for slow extraction

Many experiments in particle, atomic or nuclear physics use protons or ions in the energy range as reached in synchrotrons, i.e., higher than some 100 MeV/u. A typical beam current during the acceleration inside the synchrotron, followed by a slow extraction recorded by a DC-transformer was shown in Fig. II.9.16 (right). Typical beam currents, as slowly extracted from a synchrotron, ranges from only

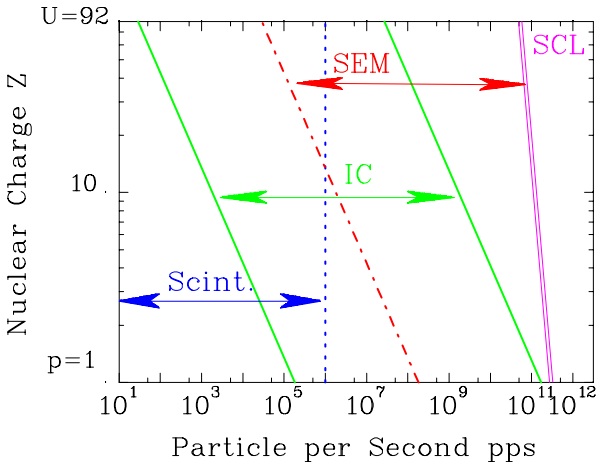

Fig. II.9.31: Overview of the different detector systems used for slow extraction at the GSI synchrotron. The numbers are given for the different ions with a kinetic energy of 1 GeV/u, extracted within 1 s and a spot size of 1 cm^2. With a scintillator up to 10^6 particles can be counted. The lower limit of the IC and SEM corresponds to a secondary current of 1 pA; the upper threshold of the IC is 30 Gray/s. In the figure, SCL refers to the incoherent space-charge limit of the synchrotron at injection energy.

10^3 up to 10^{12} particles per second, which corresponds to an electrical current from 10^{-15} to 10^{-6} A. This is well below the resolution of a DC-transformer. Due to the high energy, the range of the particles is too large for the use of Faraday cups, as shown in Fig. II.9.20 for copper. In addition, a lot of secondary charged particles would be created in the cup material; the techniques of particle detectors are used instead. An overview of the typical dynamic range of detectors is presented in Fig. II.9.31:

- For an ion rate below 10^6 s^{-1}, the individual particles can be counted by scintillators.
- For the medium range from about 10^4 to 10^9 s^{-1}, the energy loss in gas is measured by an ionisation chamber (IC).
- For the higher range from about 10^8 s^{-1}, the emission of secondary electrons from a metal surface liberated by the primary ion's energy loss is determined by secondary electron monitors (SEM).

The design of such a system is described in e.g. Refs. [27–29].

II.9.2.9.1 Scintillation counter

When a charged particle penetrates a scintillating material, the electronic energy loss by the collision of the beam particles with the target electrons creates atomic excitation, which might decay via the emission of fluorescence photons. These photons can be detected and amplified by a photo-multiplier, converted to a logical pulse by a discriminator, and finally counted by a scaler. Scintillators should have some general properties (for more details, see Refs. [16, 17]):

- The light output should be linear to the energy loss.
- The fluorescence should decay as fast as possible to get a high count rate.
- The scintillator material should be transparent for the fluorescence light, and the index of refraction should be around $n = 1.5$ for light guides.

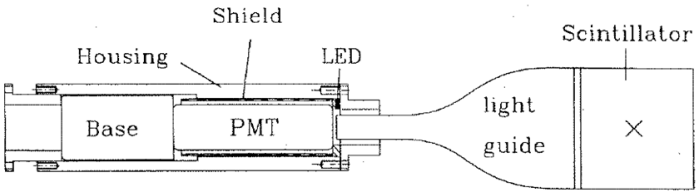

1" Photomultiplier
gain: 10^6
rise time 1.9 ns
max. **average** count rate $3 \cdot 10^6$ 1/s

BC400 Scintillator
75 x 75 mm^2
1 mm thickness

Fig. II.9.32: Left: The scheme of a plastic scintillation counter connected to the photo-multiplier via a plastic light guide. Right: Photo of scintillator wrapped in black tape. The photomultiplier and its base is inside of the metal housing.

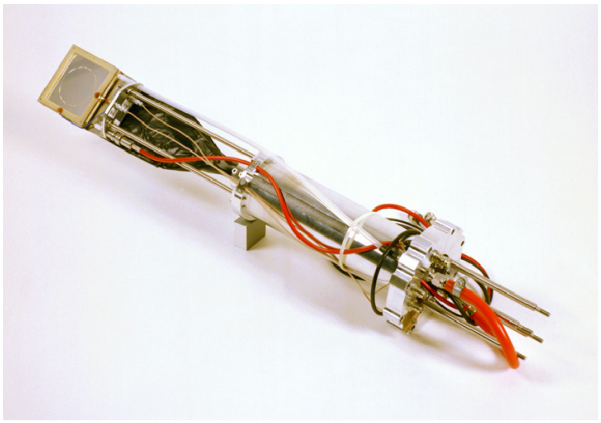

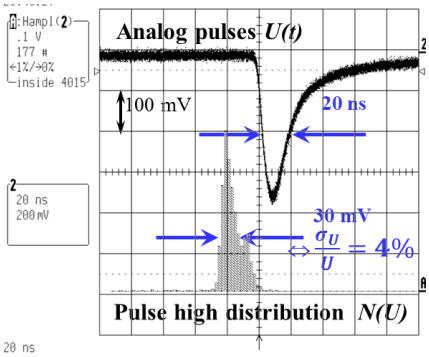

Fig. II.9.33: Left: The hardware of the scintillators (wrapped in black tape) and the IC installed at GSI. Right: Analogue pulses from a plastic scintillator recorded with a low current 300 MeV/u Kr beam; the scaling is 20 ns/div and 100 mV/div. The lower curve is the pulse-height distribution.

- The material should be easy to form and possible to get large sizes, about a factor of two larger than the maximum beam size.
- The wavelength of the light should be within the spectral range of the photo-cathode of the photo-multiplier: 350 nm $< \lambda <$ 500 nm is preferred, i.e., near UV to green light. The photo-cathode of the photo-multiplier converts the light into electrons. These electrons are amplified by $\sim$ 10 stages of so-called dynodes, where electro-static fields are applied to accelerate secondary electrons towards the next multiplication stage.
- The scintillator material should be radiation hard to prevent destruction by the incident particles.

In most cases, plastic scintillators are used. They are cheap and easy to produce in nearly any mechanical shape. As an example, the arrangement used at GSI is shown in Fig. II.9.32 (left) and a photo together with an ionisation chamber in Fig. II.9.33. A large size of 75 $\times$ 75 mm^2 has been chosen with a thickness in beam direction of 1 mm. The plastic scintillator (in this case BC 400) has a short decay time in the range of some ns; see, e.g. Ref. [17]. Typical pulses are displayed in Fig. II.9.33 (right), recorded with a medium energy heavy ion beam. The energy resolution is quite good, which is crucial because it yields good accuracy in this absolute count rate measurement. Due to the several 100

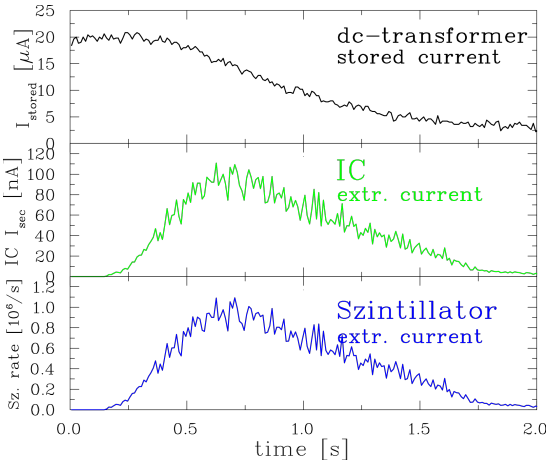

Fig. II.9.34: The extracted current measured by an IC (middle, given in nA for the secondary current) and a scintillator (bottom, given in particles per second) as compared to the current inside the GSI synchrotron determined by a DC-transformer (top, given in μA) for one extraction of a 250 MeV/u $^{208}Pb^{67+}$ beam with a total amount of 10^6 particles.

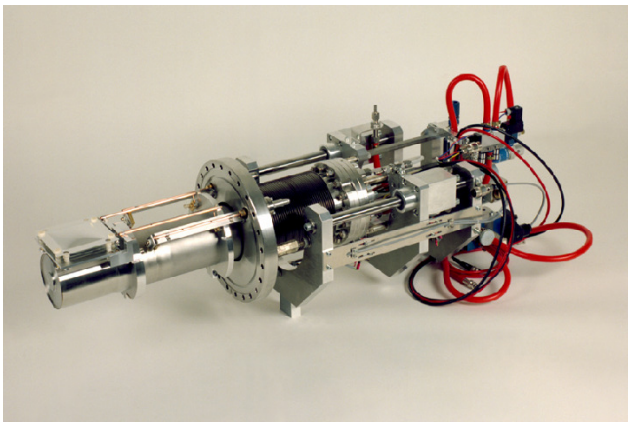

Fig. II.9.35: The pneumatic drive mounted on a Ø200 mm flange containing the scintillator and IC inside the pocket at atmospheric pressure and the SEM in the vacuum.

m long cables between the detector in the beam pipe and the electronic processing, the cable dispersion broadens the peak. Before pile-ups start to play a role, count rates up to several 10^7 s^{-1} can be accepted. A typical measurement of an extracted current is shown in Fig. II.9.34, the particle rate as determined by a scintillator and an ionisation chamber are compared. This is corroborated by the signal of the DC-transformer measuring the stored current in the synchrotron.

The disadvantage of plastic scintillators is the very low radiation hardness due to their complex organic molecular structure. Inorganic crystals have a much higher radiation hardness. In most cases, cerium-activated materials are used [17, 30]. However, these inorganic single-crystal scintillators are challenging to produce in larger sizes.

II.9.2.9.2 Ionization chamber

For the medium particle range, the current is determined by the energy loss of charged particles in a gas inside an **I**onization **C**hamber **IC**. A general description of ICs can be found in Refs. [17,31]. Due to the

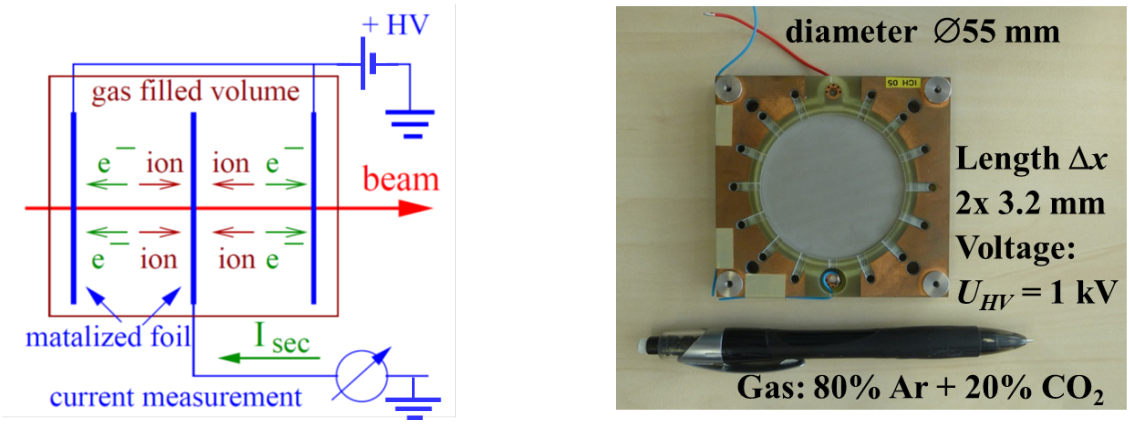

Fig. II.9.36: The scheme of an IC (left) and its realisation with a 2 times 3.2 mm active length in beam direction (right).

Table II.9.5: Specifications of the IC at GSI.

Parameter	Value
Active surface	Ø55 mm
Active length	2 × 3.2 mm
Electrode material	plastic network
Coating	100 μg/cm^2 silver
Gas (flowing)	80 % Ar + 20 %CO_2
Pressure	1 bar
Voltage	500–2000 V

Table II.9.6: Ionisation potential and W-values od some gases.

Gas	H_2	He	N_2	O_2	Ar	CH_4	CO_2
Ionisation potential [eV]	15.6	24.5	15.5	12.5	15.7	14.5	13.7
W-value [eV]	36.4	42.7	36.4	32.2	26.3	29.1	33.0

large statistics, the average energy for the production of an electron-ion pair is an accurate number, the so-called W-values are given in Table II.9.6. The arrangement of an IC is displayed in Fig. II.9.36, and a photo is shown in Fig. II.9.33. For this realisation, the beam passes a 6.4 mm thick active gas volume and creates electron-ion pairs. In most cases, pure argon is sometimes mixed with about 10 % of molecular gases, like CH_4 or CO_2. Metallised plastic foils or networks confine the active gas volume. These metallised electrodes are biased with about 1 kV to separate the charges. The middle electrode measures the number of secondary charges with a sensitive current amplifier. A secondary current down to the pA region can be measured precisely; see, e.g. Ref. [32]. The IC, filled with gas at atmospheric pressure, is separated from the vacuum by a metallic foil of typically 100 μm thickness. The foil thickness must be low to prevent significant energy loss in this foil. The specification of the IC at GSI is given in Table II.9.5.

With the help of the W-values and the calculated energy loss dE/dx within an active length of

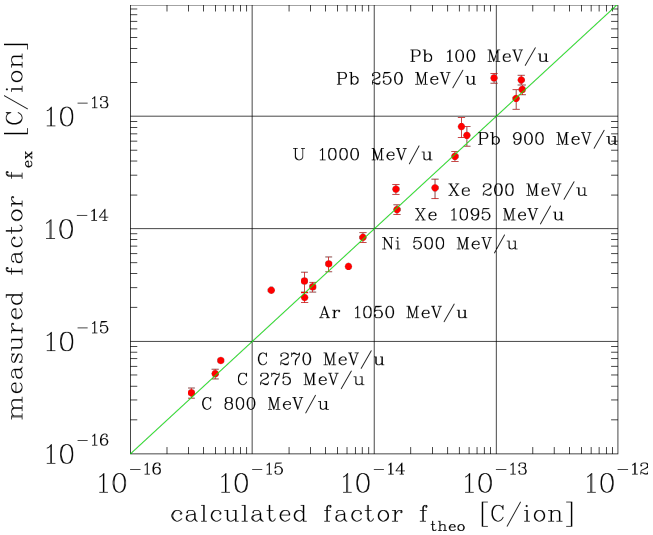

Fig. II.9.37: The measured calibration factor of an IC and calculated value using energy loss for various slowly extracted ions from the GSI synchrotron [29].

Δx, the number of primary ions I_{beam} is determined from the secondary current I_{sec}

$$I_{\text{sec}} = \frac{1}{W} \cdot \frac{dE}{dx} \Delta x \cdot I_{\text{beam}} \quad . \tag{II.9.30}$$

The precision of such a measurement depends mainly on the accuracy of the energy loss calculation. For energies above 1 GeV/u, the value of dE/dx is only weakly dependent on energy E; see Fig. II.9.20. When the energies of the beam particles are lower, calibrations have to be done to reach an accuracy in the range of 1 %. The IC can be calibrated with respect to a scintillator, where an absolute measurement is performed, as shown in Fig. II.9.34. A calibration factor can be determined from the number of counted particles and the secondary current of the IC. The result for different ions and energies performed at GSI [29] is summarised in Fig. II.9.37. Due to the different ions, three orders of magnitude are covered, from 10^{-16} C/ion up to 10^{-13} C/ion. The linearity is excellent.

The lower limit of an IC is given by the minimum measurable secondary current, which is about 1 pA. Taking this minimal current, the lower limit line in Fig. II.9.31 is determined. The upper limit is based on the recombination of the electrons with the ions from the gas, as in the case of Ar working gas, the reaction $\mathrm{Ar}^+ + \mathrm{e}^- \rightarrow \mathrm{Ar}$, which is a sink for the generated charges. This is demonstrated in Fig. II.9.38: We first discuss the characteristic line of the IC with a moderate primary current: The proportional region is reached after applying a moderate voltage of 500 V, corresponding to 1 kV/cm. The output is then independent of the voltage (or the applied electric field). There is no gas amplification, which starts only above $\sim$ 10 kV/cm. The characteristic line is determined by comparison to the SEM (see below) to get the efficiency. For a higher primary current, the plateau is not reached anymore. A higher voltage cannot be applied without the risk of sparks. This decrease concerning efficiency is due to the recombination of the liberated electrons with the positive gas ions, like $\mathrm{Ar}^+ + \mathrm{e}^- \rightarrow \mathrm{Ar}$. The drift time of the ions toward the electrodes depends on the applied electric field, while the drift time for the electrons is nearly constant for the given parameters [17]. The collision frequency of electrons and ions

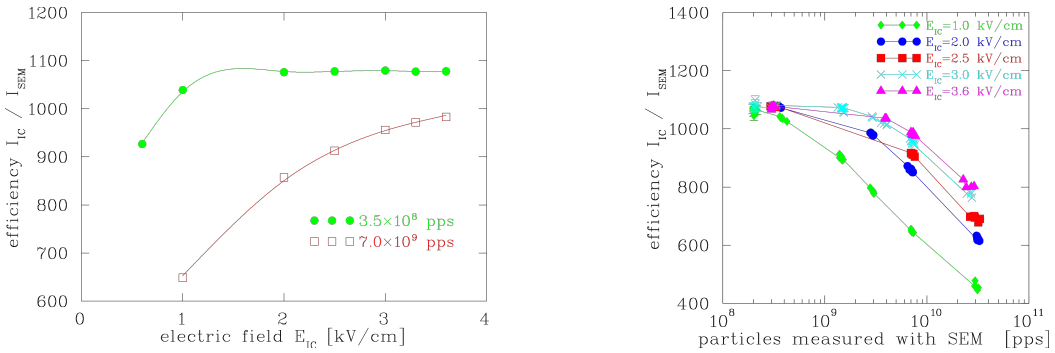

Fig. II.9.38: Left: The characteristic line for the IC as determined of the 300 MeV/u Ne^{10+} beam. The efficiency, as measured by the ratio of the secondary current of the IC and the SEM as a function of the applied electric field [28]. A plateau is reached for a low primary current , while for a high current, the recombination leads to a decrease of the secondary charges. Right: Comparable data shown as a function of transmitted ions per second for different applied electric fields.

Table II.9.7: Properties of the IC close to the saturation point, see text.

Parameter	Ions	Electrons
drift velocity w^{drift}	0.1 mm/μs	20 mm/μs
drift time t^{drift}	50 μs	0.1 μs
saturation density n^{sat}	$2 \cdot 10^9$ 1/cm^3	$4 \cdot 10^6$ 1/cm^3
secondary current I_{IC}	1 μA	
dose rate D_{IC}	30 Gy/s	
aver. rate coefficient α	10^{-9} cm^3/s	

is proportional to their concentration n_e and n_i. The recombination rate is

$$\frac{dn_e}{dt} = \frac{dn_i}{dt} = \alpha \cdot n_e n_i \propto I_{\text{beam}}^2 \tag{II.9.31}$$

with α the rate coefficient. The loss rate is proportional to the square of the primary beam current. Table II.9.7 summarises typical values. One can conclude that the secondary current for the used IC should be below $\sim$ 1 μA for typical parameters, corresponding to a dose rate of about 30 Gray/s [28]. To get the value of the primary beam current the conversion from the energy loss as given in Eq. II.9.30 have to be used.

To achieve a sizeable upper threshold, the use of gases with high electron affinity, like O_2 and H_2O, has to be avoided [17]. The electron affinity describes the probability of an electron capture like $O_2 + e^- \rightarrow O_2^-$. The presence of negative ions enhances the recombination with positive ions, like $O_2^- + O^+ \rightarrow O_3$, resulting in a smaller amount of measured secondary charge. In particular, an IC should not contain any air in case relatively large ion currents should be measured.

II.9.2.9.3 Secondary electron monitor

To cover a high current range (e.g., slow extraction from a synchrotron), the emission of secondary electrons from a metallic surface can be used. Figure II.9.39 depicts a typical setup, where three 100 μm thick Al-foils are visible, installed on the vacuum side of the feed-through. The outer two foils are biased

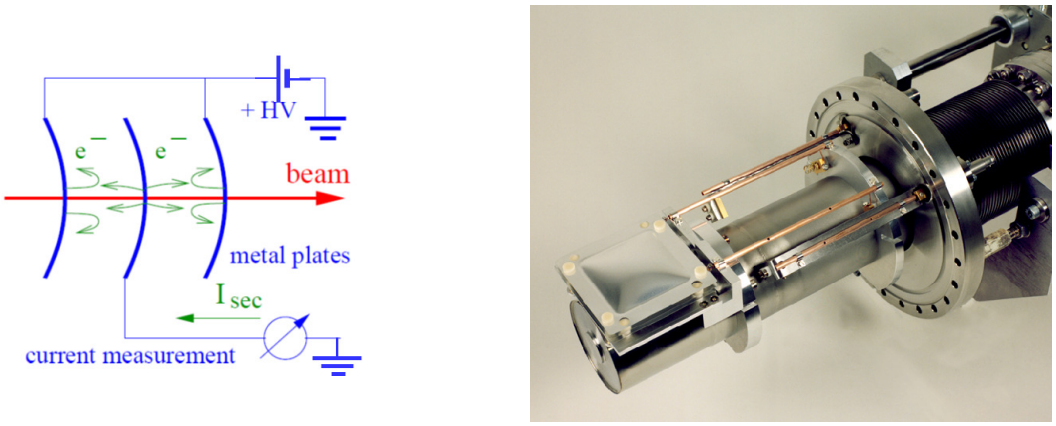

Fig. II.9.39: Left: Scheme of an SEM made of three metal foils. Right: Photo of the SEM part made of 3 Al foils with a thickness of 100 μm of the pneumatic drive used for slow extraction at GSI.

Table II.9.8: Specification of the SEM at GSI.

Parameter	Value
Material	pure Al ($\simeq$99.5%)
Thickness	100 μm
Number of electrodes	3
Active surface	80 $\times$ 80 mm^2
Distance between electrode	5 mm
Voltage	100 V

by typically $+100$ V to sweep out the free electrons. The middle foil is connected to a sensitive trans-impedance amplifier (also referred to as current-to-voltage converter). The secondary emission current depends on the energy loss at the surface $\frac{dE}{\rho dx}$ and is given by the Sternglass formula [23]

$$I_{\text{sec}} = Y \cdot \frac{dE}{\rho dx} \cdot I_{\text{beam}} \tag{II.9.32}$$

with Y being the yield factor describing the amount of secondary emission per unit of energy loss at the surface of the Al foil. A calibration has to be done experimentally to determine the value of Y, yielding a precision of 5%, see Fig. II.9.40. The accuracy is lower than for an IC, because the surface structure determines the actual value of the yield of the material, which might vary depending on the production and cleaning method. Eq. II.9.32 reflects the fact that only electrons are knocked out, which are excited to the conducting band close to the surface of roughly $\simeq$ 10 nm, see Section II.9.2.5 for the discussion of secondary electron emission. The physics of the secondary electron emission is also used for profile measurements; see Section II.9.3.3.

Aluminum, a widely favoured material, is frequently employed in scientific applications due to its exceptional mechanical properties. Its stiffness effectively mitigates susceptibility to external vibrations, such as those originating from turbo vacuum pumps, preventing unwanted micro-phonic interference. However, it is essential to note that the emission yield, denoted as Y can be influenced by irradiation. This phenomenon arises from surface modifications, which, in turn, alter the material's work function, consequently impacting the average yield Y. Experimental data have revealed a significant degradation,

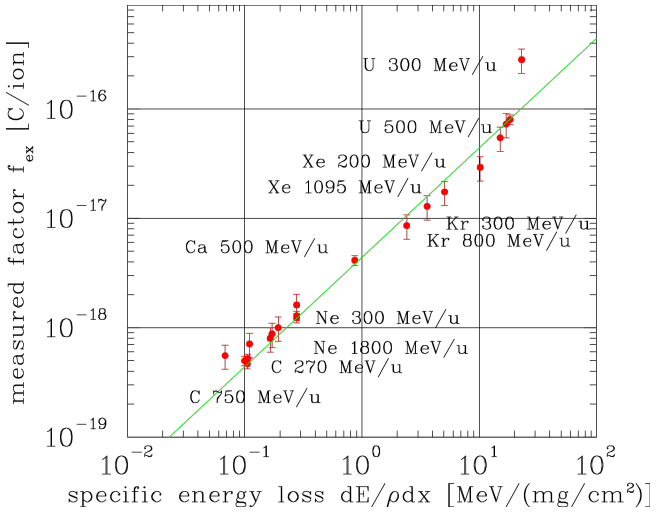

Fig. II.9.40: Measured calibration factor of a SEM and calculated value using energy loss and a fitted value of $Y = 27.4\ e^-$/(MeV/mg/cm^2) for various slowly extracted ions from the GSI synchrotron [29].

amounting to a two-fold reduction in emission yield after exposure to 10^{18} proton/cm^2 at 450 GeV proton energies, as conducted at CERN SPS [34]. Remarkably, titanium foils exhibit considerably lower sensitivity to radiation, rendering them a superior choice for such applications. This enhanced radiation hardness is of paramount importance, given that these devices are often situated at the front of the target, serving as permanent current monitors.

II.9.3 Measurement of beam profile

The transverse beam profile is usually controlled by quadrupole magnets installed in all accelerating sections and transfer lines. Measurements are essential to control the beam width and the transverse matching between different parts of an accelerating facility. The large number of bending, focusing, and correction magnets demand many profile measurement stations. Various instrumentation exists depending on the beam particles, current, and energy. We can only briefly discuss the most popular ones.

The beam spot can be directly observed by intersecting the beam with scintillator screens and viewing the emitted fluorescence with a regular camera. When charged particles with relativistic velocities pass through a metallic foil, radiation is emitted as described by classical electrodynamics; the process is called optical transition radiation OTR. A camera records this light to receive the beam profile comparably to scintillation screens.

Secondary electron emission grids SEM-grids are widely used as an electronic alternative to achieve an extensive dynamic range; a grid of wires with typically 1 mm spacing is inserted into the beam path. Instead of a fixed grid, one single wire can be scanned through the beam which provides a high spatial resolution, called Wire Scanner. Contrary to the previously mentioned invasive methods, a non-invasive approach is frequently installed at high current hadron LINACs and synchrotrons, where the ionization products of the interaction of the beam with residual gas atoms or molecules inside the (non-perfect) vacuum of the tube are detected; this is referred to as ionization profile monitor IPM. In these devices, the resulting electrons or ions are accelerated by an external electrical field to a detector providing a spatial resolution. A profile can also be obtained by observing fluorescence light emitted

by the residual gas molecules excited by the beam interaction, referring to beam induced fluorescence BIF monitor. A sensitive camera is required for single photon detection. IPM and BIF monitors are well suited as non-invasive methods for a synchrotron.

High energy electrons emit synchrotron radiation if their trajectories are curved. Monitoring this light by synchrotron radiation monitors SRM yields direct information about the beam spot.

Normally, the size of an electron beam is less than 1 mm, while proton or heavy ion beams have large diameters, up to some cm. In particular, a beam width several cm can be reached in a synchrotron with multi-turn injection. The beam width is mainly given by the settings of the focusing magnets and the beam emittance ϵ. Knowing the lattice, i.e., the β-function $\beta(s)$ and the dispersion $D(s)$ at the monitor location s, the measured beam width $\sigma(s)$ is given by

$$\sigma_x^2(s) = \epsilon_x \beta_x(s) + \left(D(s) \frac{\Delta p}{p} \right)^2 \qquad \text{and} \qquad \sigma_y^2(s) = \epsilon_y \beta_y(s) \quad . \tag{II.9.33}$$

In a synchrotron, the lattice functions are known from beam optics calculations or can be measured independently. The emittance can be calculated if the momentum spread $\Delta p/p$ is known in addition. (In the vertical direction, the dispersion is zero in most cases, as only horizontal bending magnets are used.) Nevertheless, the contribution due to the dispersion has to be considered to interpret a profile measurement correctly. In a LINAC, the lattice functions are not precisely fixed due to the variable input emittance orientation, leading to a less stringent relation between profile width and emittance.

II.9.3.1 Scintillation screen

The most direct way of beam observation is the recording the light emitted by a scintillation screen intersecting the beam, monitored by a commercial video, CMOS or CCD camera, see e.g. Refs. [35, 36] for an overview. These devices are installed in almost all accelerators from the source up to the target and one example is schematically shown in Fig. II.9.41 together with a realization where the pneumatic drive is mounted on a Ø200 mm flange.

When a charged particle penetrates a material, the energy loss can be transformed to fluorescence light, as discussed in the previous Section II.9.2.9.1. The important properties of such a scintillator are:

- High light output matched to thee camera in the optical wavelength range between $400 \text{ nm} < \lambda < 700 \text{ nm}$ is desired.
- High dynamic range, i.e., good linearity between the incident particle flux and the light output, is desired. In particular, a possible saturation of the light from the beam centre gives rise to a deformation of the recorded profile.
- Absorption of the emitted light should be avoided to prevent artificial broadening by the stray light inside the material should be present.
- A fast decay time is required to enable the observation of possible beam size variations.
- Good mechanical properties for producing large screens up to Ø100 mm lis an important design criterion.
- Radiation hardness is important to prevent permanent damage must be ensured for high intensity

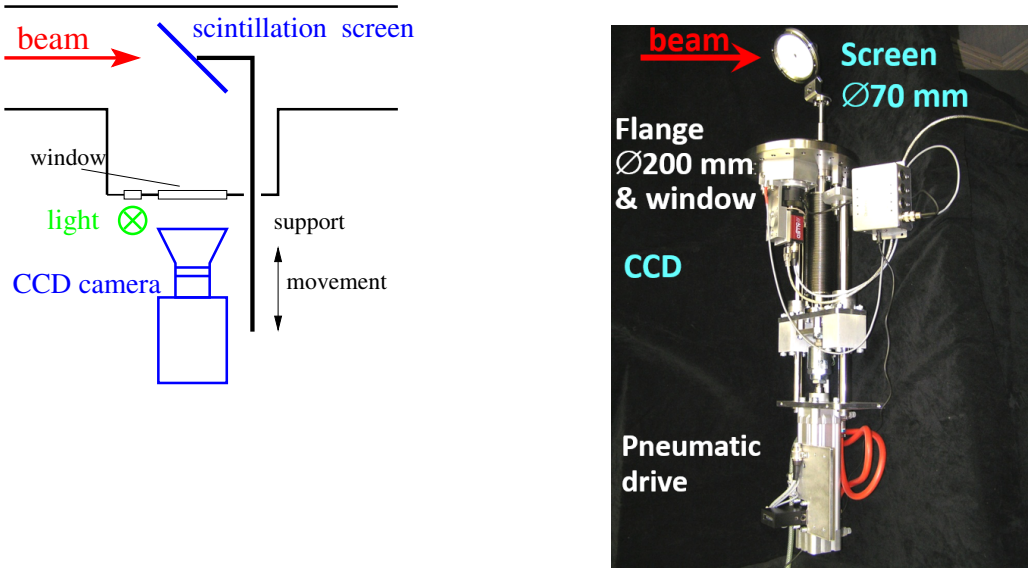

Fig. II.9.41: Left: Schematic drawing of an invasive scintillation screen monitor scheme is shown. Right: A photo of a P43 phosphor scintillation screen of Ø70 mm and the CCD camera mounted on a Ø200 mm flange with a pneumatic drive is depicted.

Table II.9.9: Chemical composition and basic optical properties of inorganic scintillation screens. The matrix Al_2O_3 is used as a ceramic; the last four materials are phosphor screens, where powder is deposited on glass or metal plates.

Abbreviation	Type	Material	Activator	Max. emission	Decay time
Quartz	glass	SiO_2	non	470 nm	$<$ 10 ns
Alumina	ceramics	Al_2O_3	non	380 nm	$\sim$ 10 ns
Chromox	ceramics	Al_2O_3	Cr	700 nm	$\sim$ 10 ms
YAG	crystal	$Y_3Al_5O_{12}$	Ce	550 nm	200 ns
LuAG	crystal	$Lu_3Al_5O_{12}$	Ce	535 nm	70 ns
Cesium-Iodide	crystal	CsI	Tl	550 nm	1 μs
P11	powder	ZnS	Ag	450 nm	3 ms
P43	powder	Gd_2O_2S	Tb	545 nm	1 ms
P46	powder	$Y_3Al_5O_{12}$	Ce	530 nm	300 ns
P47	powder	Y_2SiO_5	Ce and Tb	400 nm	100 ns

applications.

As stated, plastic scintillators have only a low radiation hardness and various kinds of inorganic materials are used instead. In Table II.9.9 some properties are given in Ref. [35]; for more details see Refs. [17,30].

The material Chromox is a ceramic, which can be fabricated like pure Al_2O_3, used widely as an insulating material. The scintillation is due to the Cr activators; chemically, it is comparable to ruby. The disadvantages are its long decay time of $\sim$10 ms and the significant absorption inside the material. Nevertheless, due to its robustness, it is quite often used. The well-known Cerium activated crystal materials like YAG:Ce ($Y_3Al_5O_{12}$:Ce) have better optical properties and are widely used for particle counting applications [17]. However, producing thin crystalline disks of about 10 cm diameter out of this material is cumbersome. In particular, thin disks below a thickness of 100 μm are required for applications at electron LINAC-based FELs due to a typical beam size below 100 μm; see, e.g.

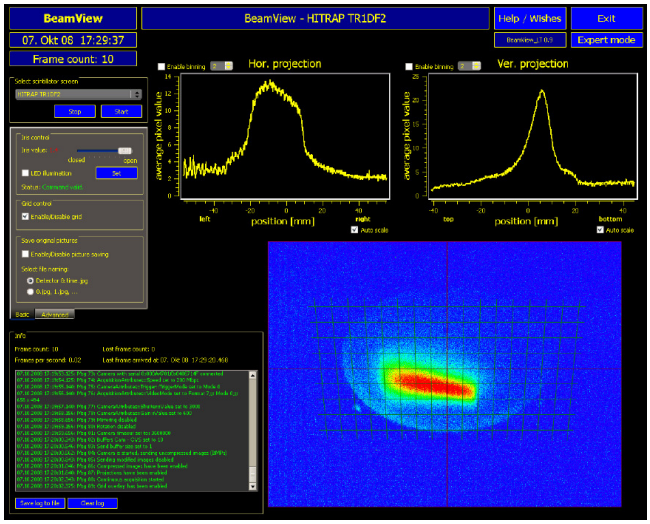

Fig. II.9.42: Beam spot of a low current 4 MeV/u beam at GSI on a YAG:Ce screen recorded with a digital camera. The original black-white image is converted to false-colour for better visibility. The projection on the horizontal and vertical axes are shown in the upper part, from Ref. [43].

Ref. [41]. Instead of the expensive single crystal disk, one can use small grains of $\sim$ 10 μm size, deposited on several mm thick glass or metal disks. These phosphor screens are also frequently used in analogue oscilloscopes, electron microscopes and image intensifiers. P46 is an example of a phosphor screen powder offering lower production costs than the chemically equivalent single-crystal YAG:Ce. The properties of doped materials strongly depend on the activator concentration; Table II.9.9 gives only approximated values.

The beam image from a YAG:Ce screen is shown in Fig. II.9.42 for a low current beam of only $\sim 10^6$ ions at 4 MeV/u, demonstrating the high sensitivity of that material and the good applicability. The sensitivities of the different materials span several orders of magnitude and depend on the particle species, see, e.g. Refs. [36, 37]. Figure II.9.43 shows an example of the light output varying over two orders of magnitude from various scintillating materials [38]. The screens are irradiated with uranium ions leading to a high energy loss and a beam current span of almost two orders of magnitude; however, no signature of saturation was found in any of the materials. Scintillation screens are used in all types of accelerators [36], some examples of investigations are discussed for electron beams [39–41] and proton or ion beams [37, 38, 42] with quite different applications.

For high intensity beams, one has to ensure that the absorbed beam power does not destroy the material. In particular, for slow heavy ions with a range comparable to the screen thickness, this restricts the use, see also the discussion in Section II.9.2.5. A disadvantage of the screen is related to the interception: The used material is so thick (several mm) that it causes a significant energy loss, so it cannot be used to diagnose a circulating beam inside a synchrotron.

The screen is observed with a CCD or CMOS camera with a digital link (such as Camera-link, Gigabit-ethernet etc.). A problem related to digital cameras is the radiation sensitivity of the CCD or CMOS sensor and the related digital electronics. At high levels of radiation, the old-fashioned analogue VIDICON cameras are used; a frame grabber digitizes the analogue video output.

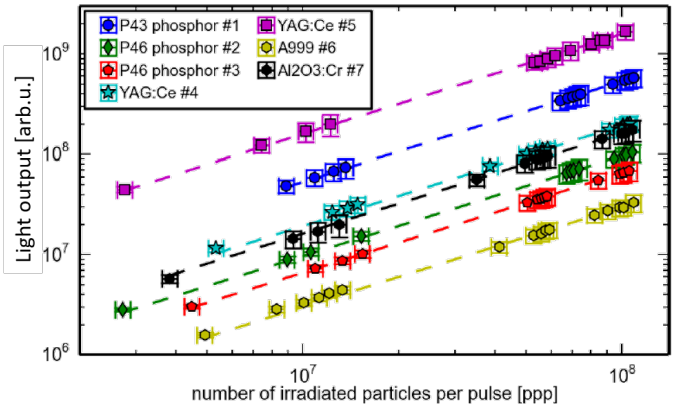

Fig. II.9.43: Example for the relative light output from various scintillation screens (see Table II.9.9) as a function of uranium ion current with $E_{\mathrm{kin}} = 300$ MeV/u as extracted within 1 μs from the GSI synchrotron [38].

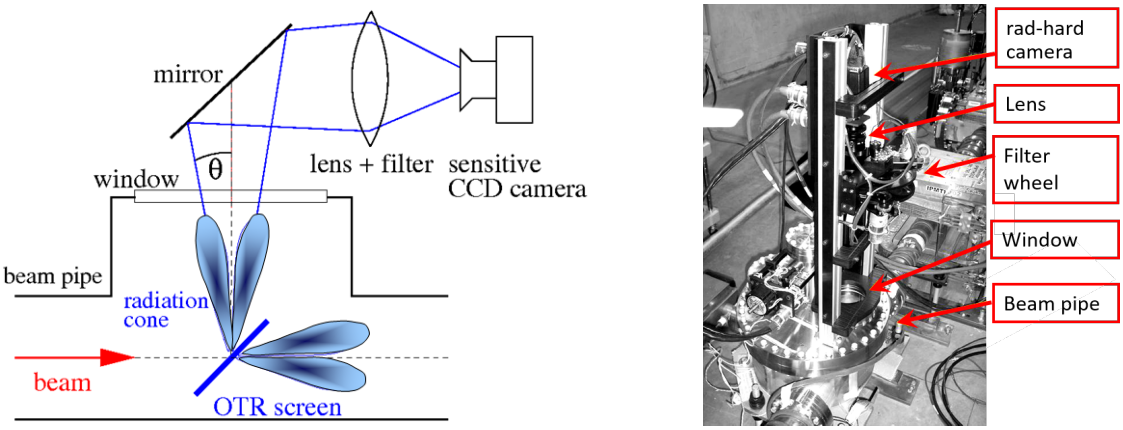

Fig. II.9.44: Left: Schematic drawing of an OTR screen measurement. Right: OTR installation for highly relativistic protons at Fermilab, from Ref. [47].

II.9.3.2 Optical transition radiation screens

At electron accelerators with relativistic particles, the profile is often determined from the electro-magnetic radiation emitted when the beam pass through an intersecting thin metallic foil referred to as **O**ptical **T**ransition **R**adiation **OTR**. The OTR is a pure classical electro-magnetic process, including special relativity, produced when a charged particle passes from one dielectric medium into another. While passing in vacuum in front of the foil, as characterized by the permittivity $\epsilon_r = 1$, the particle has a certain electro-magnetic field configuration. The field distribution differs from the field inside the medium because the foil has a permittivity $\epsilon_r \neq 1$ (a complex number in a mathematical sense), hence different from vacuum field configuration. By approaching the foil, the particle's electro-magnetic field leads to a time-dependent polarization at the foil boundary. When the charged particle transverses the foil, the field configuration is changed suddenly. The change of this polarization at the foil surface generates the radiation with a characteristic intensity and angular distribution.

A typical setup of an OTR measurement is shown in Fig. II.9.44. In most cases, the foil is inserted under 45° with respect to the beam path. The foil is made of Aluminum or Aluminum coated on Mylar with a thickness of 1 μm or less. The light is emitted in the forward direction as well as centred at 90°

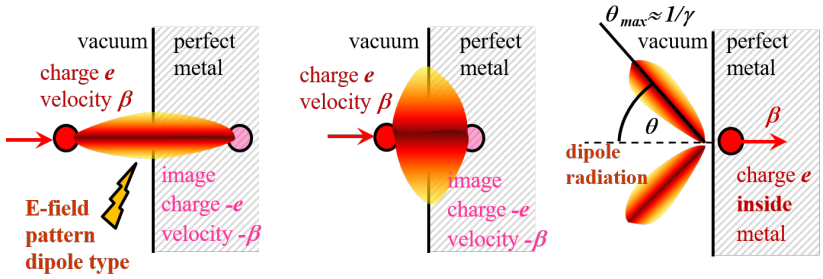

Fig. II.9.45: Schematic electric field distribution for a charge approaching a metal foil with velocity β from left and the resulting dipole radiation after the boundary transfer.

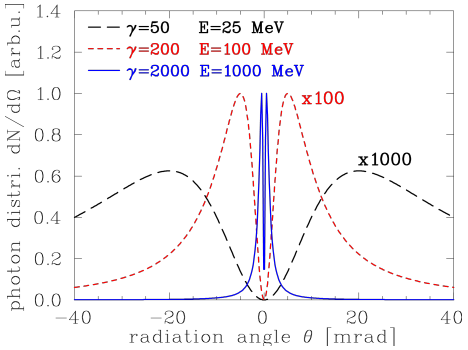

Fig. II.9.46: Intensity distribution of OTR as a function of the emission angle for three different values of the Lorentz-factor γ; the corresponding electron beam energies for electrons are noted. The photon intensity is enhanced by a factor of 1000 for $\gamma = 50$ and 100 for $\gamma = 200$.

because the metallic surface acts as a mirror. Depending on the particle energy, the angular distribution peaks at the angle $\theta = 1/\gamma$ where γ is the relativistic Lorentz factor; see below. For typical values, 100 to 1000 beam particles yield 1 photon in the optical wavelength range. With appropriate optics, an image of the foil is recorded by a regular camera. In some cases, an image-amplified camera is used due to the relatively low number of photons.

The generation of OTR radiation is based on the electro-magnetic field distribution of a charge approaching n ideal metallic surface with velocity β; Fig. II.9.45 depicts the process schematically. Compared to the field distribution of a charge in free space, the field is modified by the specular effect of the metallic surface, as can be described by an image charge. At one instance of time, the moving charge transverses the metallic surface and enters the foil; this leads to a distortion of the electro-magnetic field and the emission of dipolar radiation. The general process is treated in e.g. Refs. [18, 44, 45], leading to a full, closed but extensive mathematical expression. For relativistic beam particles and under some further valid assumptions, the radiated energy dW into a solid angle $d\Omega$ per frequency interval $d\omega$ can be approximated by

$$\frac{d^2W}{d\Omega d\omega} = \frac{2e^2\beta^2}{\pi c} \cdot \frac{\theta^2}{(\gamma^{-2} + \theta^2)^2} \quad , \tag{II.9.34}$$

where c, e, and γ are the velocity of light, the elementary charge and the relativistic Lorentz-factor, respectively. The observation is oriented at an angle θ perpendicular to the beam path, the so-called specular angle, see Fig. II.9.44. There is no difference between the radiation for electrons or protons moving with the same Lorentz-factor, reflecting that only the electro-magnetic fields of the beam particles

contributes to the emission process. The radiated energy does not depend on the frequency ω, i.e., the whole spectrum is covered. This is valid up to the plasma frequency of the metal, which is for most metals in the deep UV at about 10 eV. The radiated energy of Eq. II.9.34 is converted to the number of photons by $W = N_{\mathrm{photon}} \cdot \hbar\omega$ observed within a wavelength interval from λ_{begin} to λ_{end} in the optical region by the camera and integration over the interval λ_{begin} to λ_{end}. This yields the number of photons per solid angle

$$\frac{dN_{\mathrm{photon}}}{d\Omega} = N_{\mathrm{beam}} \cdot \frac{2e^2\beta^2}{\pi\hbar c} \cdot \log\left(\frac{\lambda_{\mathrm{begin}}}{\lambda_{\mathrm{end}}}\right) \cdot \frac{\theta^2}{\left(\gamma^{-2} + \theta^2\right)^2} \quad , \tag{II.9.35}$$

where N_{beam} is the number of beam particles. This function is plotted in Fig. II.9.46 for three different values of the Lorentz factor γ. It is clearly seen that the radiation is more tightly focused for higher energies (more precisely, a high value of the Lorentz-factor γ), having the advantage that a larger fraction of the photon reaches the camera's lens system. At electron accelerators, OTR is used even at moderate energies above $\simeq$ 100 MeV (corresponding to a Lorentz-factor $\gamma \simeq 200$). For proton acceleration, a Lorentz-factor $\gamma \simeq 200$ corresponding to a beam energy above 200 GeV, and is only reached at some high energy proton facilities such as CERN's SPS and LHC where OTR screens are installed [46].

The angular distribution in Eq. II.9.35 is given for a single particle incidence. A real beam has an angular distribution of the beam particles, which must be convoluted to yield a realistic photon distribution. Assuming a Gaussian beam angular distribution with a standard deviation σ_{beam}, the photon angular distribution is modified by the convolution as

$$\frac{dN_{\mathrm{photon}}}{d\Omega} = N_{\mathrm{beam}} \cdot \frac{2e^2\beta^2}{\pi\hbar c} \cdot \log\left(\frac{\lambda_{\mathrm{begin}}}{\lambda_{\mathrm{end}}}\right) \cdot \int_{-\infty}^{\infty} \frac{1}{2\pi\sigma_{\mathrm{beam}}} \exp\left(\frac{-\theta'}{2\sigma_{\mathrm{beam}}}\right)^2 \cdot \frac{(\theta-\theta')^2}{\left(\gamma^{-2} + (\theta-\theta')^2\right)^2} d\theta'. \tag{II.9.36}$$

This integral has to be evaluated numerically and can contribute significantly to the resolution for small beam sizes. In addition, the diffraction by the finite aperture of the optics can limit the resolution, as discussed, e.g. in Refs. [48, 49].

Generally, the technical setup for OTR is comparable to the setup for scintillation screens. For the profile observation, the focus of the camera optics coincides with the OTR screen. In contrast, the focus is set to infinity for the measurement of the photon angular distribution. Using the latter setting, the angular distribution of the beam can be evaluated. Doing both measurements (focus on foils yield the profile, focus on infinity yield the beam angular distribution), a transverse emittance measurement can be performed, see, e.g. Ref. [48]. Note that Fraunhofer diffraction must be considered, limiting the resolution of the emittance measurement.

At modern LINAC-based free electron laser facilities with high energetic beams, the usage of OTR is hindered by the occurrence of so-called coherent OTR emission [50]. For intense, very short bunches (below typically 100 fs duration) with a longitudinal substructure (typically on the fs-scale), photons are emitted during a short time and from a small area. As these are electro-magnetic waves emitted with a phase and angular correlation, interference might occur, leading to an interference pattern at the camera location. The detectable emission characteristic in terms of spatial distribution and wavelength spectrum depends significantly on the longitudinal substructure of the bunch. For those beam parameters, the OTR-foil image does no longer represent the transverse beam distribution and excludes the usage of

OTR for profile measurement. As an alternative, scintillation screens were reverted at those facilities.

The OTR profile determination for non-coherent emission has some advantages and disadvantages compared to a scintillating screen measurement [35, 40]:

- OTR is mainly used for electron beams at energies above 100 MeV. The required Lorentz-factor γ for proton beams is only reached at the very high energy accelerators. Scintillation screens can be used for any beam and energy.
- The usable light emitted from an OTR screen depends significantly on the Lorentz-factor γ; for lower beam energies, several orders of magnitude less light is emitted as compared to scintillation screens. Hence, more sensitive and expensive cameras must be used for an OTR monitor.
- OTR is based on a classical electro-magnetic process leading to linearity between the number of photons and the beam intensity (disregarding the aforementioned coherent photon emission for very short bunches). Scintillation is a more complex process and depends significantly on the material; saturation and radiation damage might occur, falsifying the profile reading.
- For the OTR process, the number of photons and their distribution is independent of the thickness of the foil. Hence, very thin foils of pure Al or Al-coated Mylar foils down to 0.25 μm are used. Scintillation screens are generally thicker to guarantee their mechanical stability. For scintillation screens, the amount of emitted photons scales with the thickness of the material. Hence, they are better suited for low intensity beams.
- OTR and scintillation screens are invasive monitors. However, for OTR, the thin foil minimizes the impact on the beam due to the low scattering probability. It can also be applied at higher beam power because the energy loss is less in the thin, low-Z material leading to a lower influence on the beam. Scintillation screens are thicker, and the heating by the beam might modify the scintillation process. Moreover, most materials contain high-Z material, leading to a larger energy loss.
- Due to the characteristic emission cone of the OTR light, the beam angular distribution can be reconstructed, and, together with the profile reading, the beam emittance can be deduced. Scintillation light is emitted isotropically without any correlation to the particle angle, and, hence, no information about the emittance can be obtained.

II.9.3.3 Secondary electron emission grid

When particles hit a surface, secondary electrons are knocked-out from the surface, as described in section II.9.2.9.3. For profile determinations, individual wires or ribbons interact with the beam; this is called a **S**econdary **E**lectron E**M**ission grid or a harp, as reviewed in Ref. [51]. This is an electronic alternative to a scintillation screen with a much higher dynamic range, i.e., the ratio between minimal to maximum detectable current is orders of magnitude larger. W-Re alloys are often used for their excellent refractory properties for metallic wires or flat ribbons. In particular, at low energy LINACs, this is important because no cooling can be applied due to the geometry. For the analogue electronics processing, each wire has an individual current-to-voltage amplifier (an equivalent name is trans-impedance amplifier). A photo of such a device is shown in Fig. II.9.47, and the specifications are given in Table II.9.10.

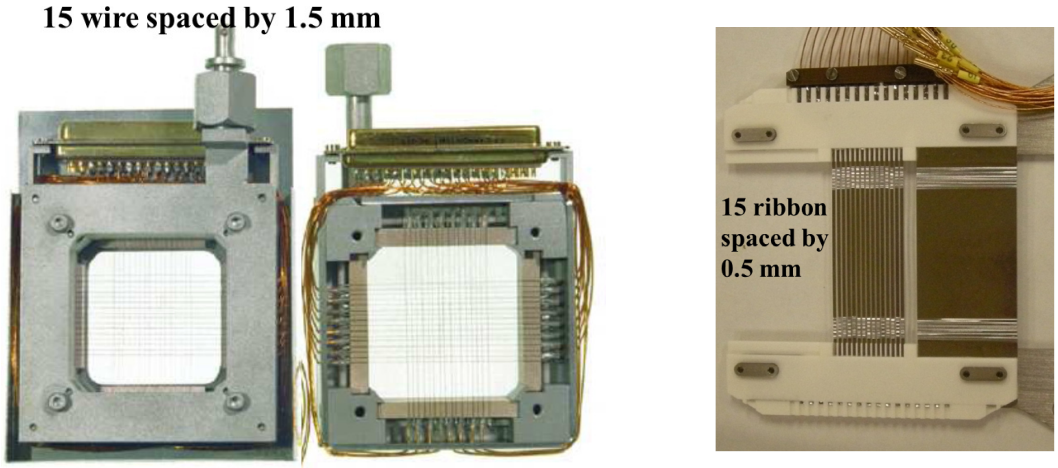

Fig. II.9.47: Left: SEM-grid for both planes with 15 tungsten wires spaced by 1.5 mm as typically used at a proton LINAC. The individual wires are insulated with ceramics. Middle: The same SEM-grid with removed tin cover. Right: SEM-grid based on ribbon made from 25 μm thick aluminium foil by laser cutting; the spacing is 0.5 mm. This type is used for high energetic protons above typically 1 GeV.

Table II.9.10: Typical specification for an SEM-grid used at proton and heavy ion LINACs.

Parameter	Value
Diameter of the wires	0.05 to 0.5 mm
Spacing	0.5 to 2 mm
Length	50 to 100 mm
Material	W or W-Re alloy
Insulation of the frame	Glass or Al_2O_3
number of wires	10 to 100
Max. power rating in vacuum	1 W/mm
Min. sensitivity of I/U-conv.	1 nA/V
Dynamic range of electronics	1:10^6
Integration time	1 μs to 1 s

Generally, SEM-grids are invasive diagnostics; Fig. II.9.49 shows the assembly including the pneumatic drive. For low energies at proton or heavy ion LINACs, the particles are stopped in the material or undergo a significant energy loss. The wires' diameter-to-spacing ratio determines the beam current's attenuation (hence, the signal strength on the individual wires). Typically only 10 % of the beam area is covered by the wires; in this sense, the profile measurement is nearly non-destructive for the beam. For energies above 1 GeV/u, the relative energy loss is negligible, and large size ribbons are used. Figure II.9.48 shows a typical example of profile measurements within a transfer line with several dipoles and quadrupoles between the SEM-grid location used for beam optimization for a transfer line.

Each wire has an individual pre-amplifier; in most cases, it is a trans-impedance amplifier to convert the secondary electron current to a voltage, see Fig. II.9.49. These electronics have to be installed close to the accelerator hardware. A multi-wire cable connects the analogue electronics in the tunnel to a multi-channel ADC outside of the accelerator tunnel. Readout of a full SEM-grid in less than a 1 ms is typical for the use of pulsed or dc beams.

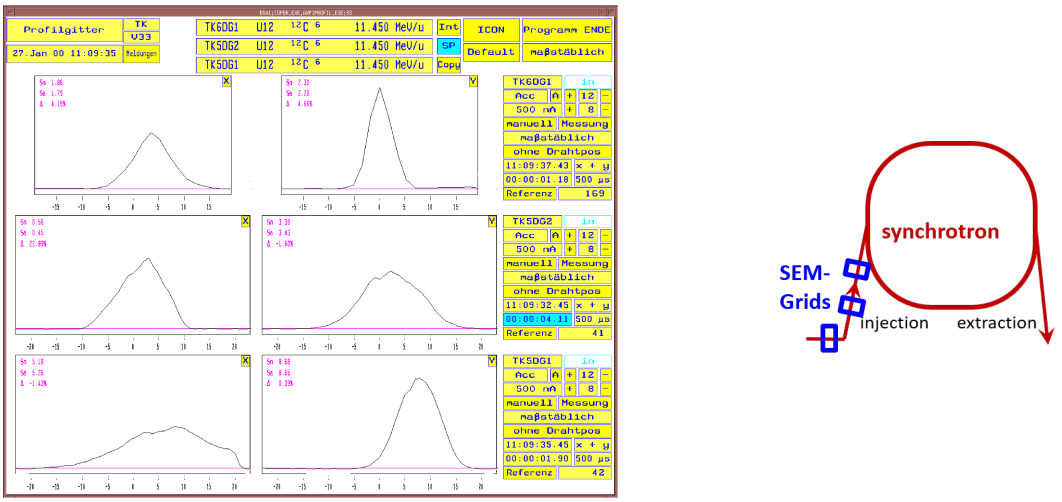

Fig. II.9.48: The measured beam profiles recorded by three SEM-grids in one transfer line at the GSI heavy ion LINAC are displayed; the horizontal profiles are shown left while the vertical peofiles are displayed right. The unit for the plot axis are n units of mm.

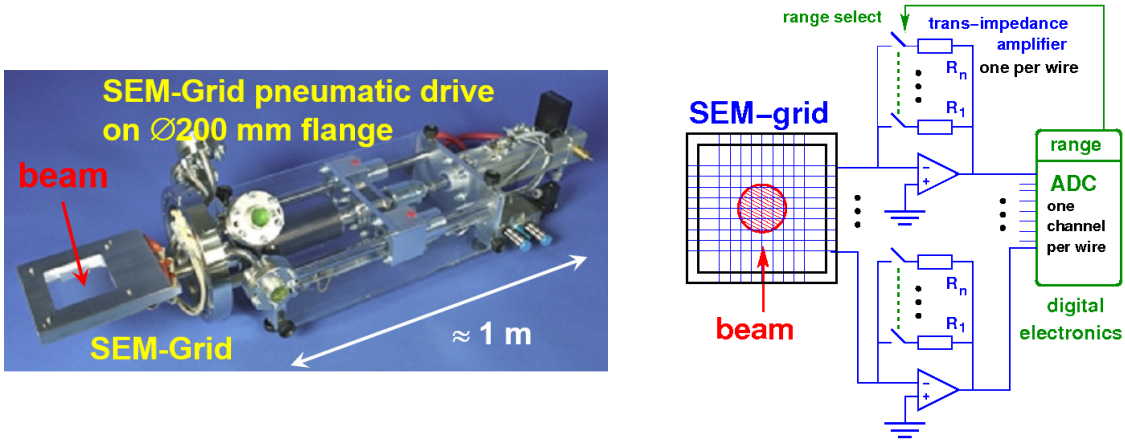

Fig. II.9.49: Left: A SEM-grid mounted on a pneumatic drive for movement in the beam path mounted on a ∅200 mm flange. Right: Typical analogue signal processing for SEM-grids.

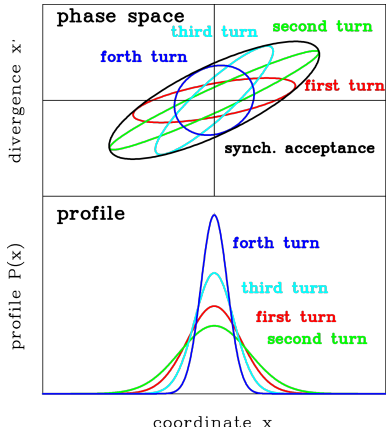

Fig. II.9.50: Illustration for the betatron mismatched injection into a synchrotron. If the orientation of the injected beam emittance does not match the acceptance, variations of the beam profile occur.

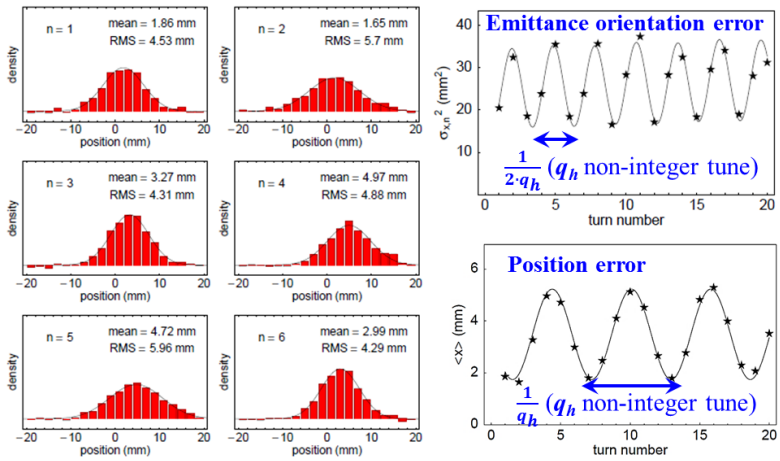

Fig. II.9.51: Left: Profile measurement for a mismatched injection into the CERN PS synchrotron for the first $n = 1...6$ turns. Right: Fitted square of the beam width and centre as a function of time, from Ref. [52].

Application: Betatron mismatch for synchrotron injection

An interesting application for profile measurement is the control of the injection into a synchrotron. If the orientation of the injected beam emittance is wrong due to a misaligned focusing, beam storage is still possible. However, the emittance ellipse starts to rotate with an angle per revolution as given by the fractional part q of the tune Q of the synchrotron as shown in Fig. II.9.50. A rotating ellipse is equivalent to a variation in the beam profile from turn to turn. After several hundred turns, the full synchrotron acceptance is filled due to the de-coherence of the single particle phases, leading to a larger circulating beam and an emittance increase. The mismatch can be determined by recording the profile width turn-by-turn. An example is shown in Fig. II.9.51 for a proton injection into the CERN PS synchrotron at an 1.4 GeV energy and a bunch length of 80 ns [52, 53]. The revolution period is 2.2 μs. Thin SEM grids are used, and the data are digitized each revolution of the short bunch. The energy loss of the protons in the wires is too low to influence this measurement during only a few turns. The oscillation of the profile width is seen, and the fitted Gaussian width is plotted as a function of the turn number. By this avoidable process, the emittance of the stored beam grows by about $\simeq 10$ %. A better injection is created by changing the setting of the quadrupole magnets in the transfer line.

II.9.3.4 Wire scanner

Instead of using several wires with individual, expensive electronics, a single wire can be swept through the beam [51]. The advantage is that the wire spacing does not limit the resolution, and, hence, this technique is often used at electron accelerators with beam sizes in the sub-mm range. Generally, two types of wire scanner are realized, namely the fast and slow type as described below.

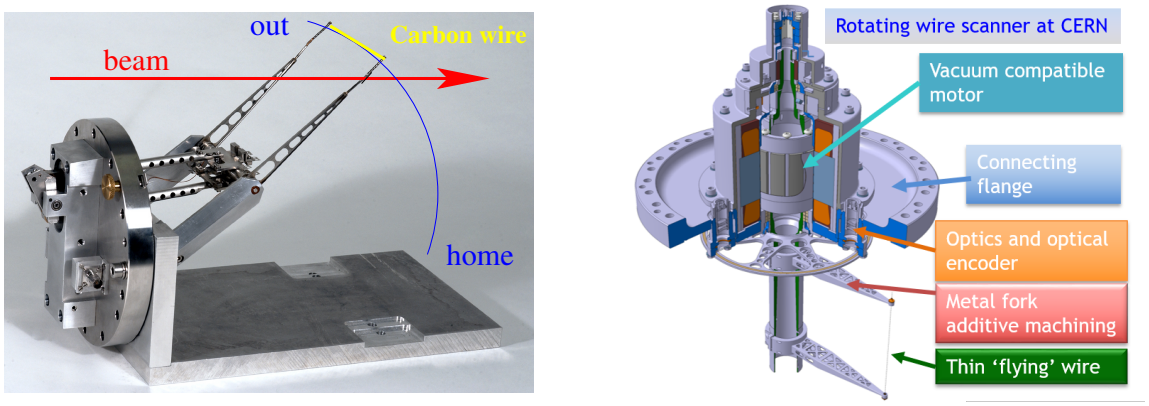

Fig. II.9.52: Left: Fast pendulum scanner or "flying wire" used at CERN synchrotron [54]. Right: The new design used at the CERN synchrotrons relaying on a fast motor inside the vacuum [55].

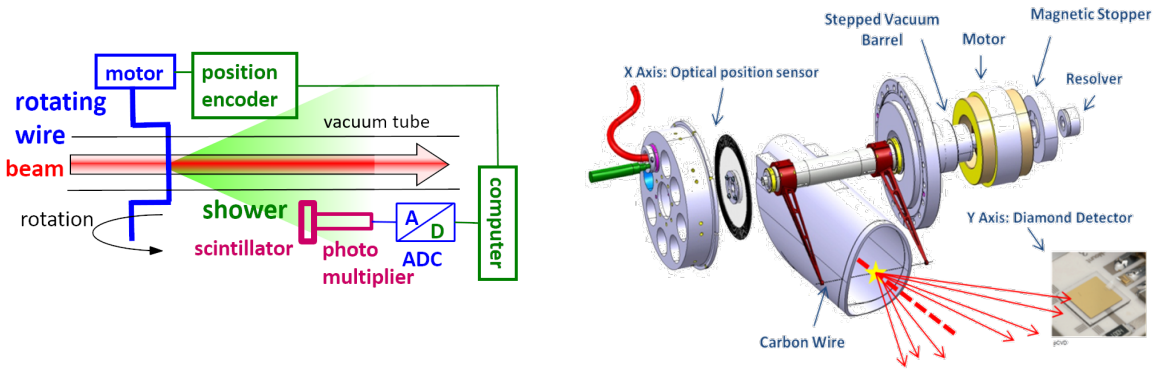

Fig. II.9.53: Left: Scheme of a fast "flying" wire scanner using the production of secondary particles as the signal source. Right: A design drawing for the flying wire and the detector for the shower particle registration, from Ref. [55].

II.9.3.4.1 Fast, "flying" wire scanner

An arrangement with a straight wire on a fast pendulum mechanics is shown in Fig. II.9.52, from Ref. [54]. A purpose build mechanical mechanism can achieve scanning velocities of up to 20 m/s. Sometimes this setup is also called flying wire. As the wire material, carbon or SiC is used due to its low weight and low nuclear charge Z, resulting in a low energy deposition in the wire (Bethe Eq. II.9.21 gives for the stopping power $dE/dx \propto \rho \cdot Z/A$ for a material of density ρ with nuclear charge Z and mass number$A$). Besides, these materials can withstand high temperatures without melting. The thickness can be down to 10 μm. The choice of the wire material is an issue to resist the heating transfer by the intersecting beam and the significant acceleration at begin and end of the scan. The maximum velocity of 20 m/s corresponds to 72 km/h and is reached within $\simeq$ 1 cm. For a typical beam size of 1 mm, the beam is crossed within 1 ms, which should be minimized to enable only a few beam particle passages through the wire to restrict the total energy loss and enable further beam acceleration. On the other hand, the fork and wire material must be stiff enough to prevent significant wire deformation. Choosing novel materials such as nano-wires is an actual research activity; see, e.g. Ref. [55]. Due to the single scanned wire, the profile is not taken in a single instant, even with high scanning velocity. Therefore, only the steady-state distribution can be probed.

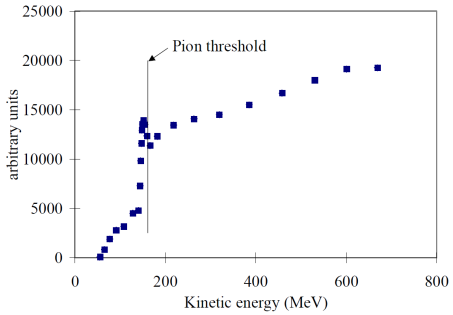

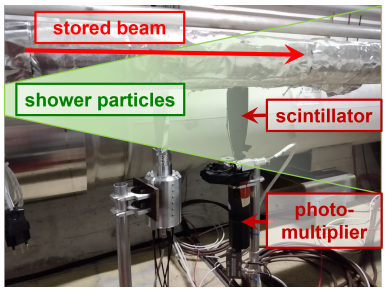

Fig. II.9.54: Left: The total rate from a wire scanner under proton impact at CERN PS-Booster, showing the rate increase above the π-threshold at $\sim$ 150 MeV, from Ref. [56]. Right: Photo of the scintillator used as the detector for the fast wire scanner at LHC; the distance between detector and scanner fork (not depicted) is several meters.

For the profile display, the position of the wire, determined by the position encoder is plotted on the horizontal axis. The beam signal for the vertical axis can be deduced from the current given by the emitted secondary electrons, like for an SEM-grid. In particular, this detection method is used for low energy protons and heavy ions. For beam energies larger than 150 MeV/u for ions or 10 MeV for electrons, the signal is deduced by monitoring the secondary particles outside the vacuum pipe, see Fig. II.9.53. These secondaries might be hadrons created by the nuclear interaction of the proton or ion projectiles and the wire, having enough kinetic energy to leave the vacuum chamber. Figure II.9.54 (left) shows the large signal increase for proton energies above $\simeq$ 150 MeV related to the threshold of π-meson production (the rest masses of π-mesons are $m_{\pi^0} = 135$ MeV/c^2 and $m_{\pi^\pm} = 140$ MeV/c^2). For the case of electron beams, the secondaries are mainly Bremsstrahlung-photons triggering an electro-magnetic shower in the wire and the scintillation detector. The detector is a well-suited beam loss monitor, e.g. a scintillator installed several meters away as shown in Fig. II.9.54 (right) (for the discussion on beam loss monitors see Section II.9.7). The count-rate is plotted as a function of the wire position to represent the beam profile precisely.

II.9.3.4.2 Slow, linear wire scanner

For fast movement, the vibration of the wire restricts the spatial resolution. Much higher precision can be achieved with a much slower movement of typically 0.1 m/s with a linear drive, as shown in Fig. II.9.55 [57]. With these types, a 1 μm resolution is reached in electron accelerators [58]. To get this low beam width σ_{beam} assuming a Gaussian beam, a deconvolution of the contribution of the wire (4μm thick carbon wire in this case) from the measured width σ_{meas} has to be done according to

$$\sigma^2_{\mathrm{beam}} = \sigma^2_{\mathrm{meas}} - 4 \cdot r^2_{\mathrm{wire}} \quad . \tag{II.9.37}$$

In most cases, the wire is mounted on a fork, which is inserted into the beam pass by a mechanical drive mounted on 45°. Then only one drive is sufficient for measuring both transverse planes by mounting the wires in a crossed orientation, as shown in Fig. II.9.55 (right). Due to a beam size $<$ 100 μm at LINAC-based FELs the spatial resolution is a concern and requires a mechanically stable installation; a modern realization is discussed in Refs. [59, 60]. Novel production methods for thin wires are a cutting

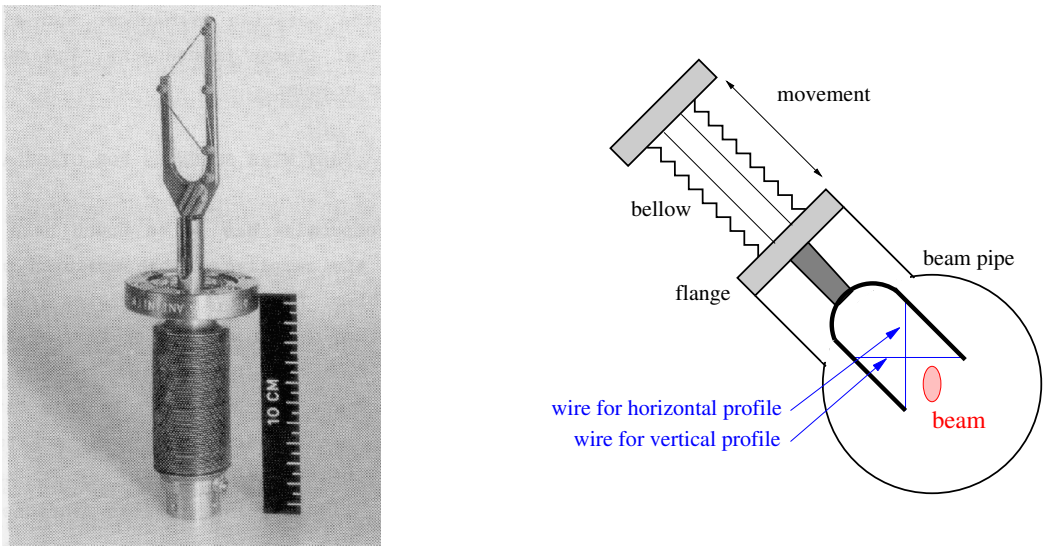

Fig. II.9.55: Left: Linear scanner used at CERN [57]. Right: Typical geometrical installation for a fork with two insulated wires.

edge topic reaching wire diameters below 1 μm [61] with relatively fast scan velocities of up to 1 m/s. If the signal generation is performed by reading the secondary emission current, then two isolated wires can be mounted as a compact arrangement. If the signal is generated by beam loss monitors outside the beam pipe, the two wires are separated (as shown in the Fig. II.9.55 left), so the wires cross the beam one successively.

A comparison of the slow wire scanner and the SEM-grid shows the advantages and disadvantages of both types [51]:

- With a SEM-grid the beam intensity is sampled concurrently, whereas a moving wire samples the parts of the profile at different locations at different times. Therefore, variations of the beam intensity over time will be mixed with transverse intensity variations using a scanning device.
- In the case of pulsed beams, a synchronization between the readout of the electronics and the beam pulse, as well as a movement within the beam pause, is required. The synchronization between readout and beam pulse is easier for an SEM-grid.
- The resolution of a SEM-grid is fixed by the wire spacing (typically 1 mm), while a wire scanner can have higher resolution, down to 10 μm, due to its constant movement. (For high resolution, mechanical vibration must be avoided.)
- The electronics for data acquisition are cheaper for a scanning system. A SEM-grid requires one channel per wire.
- For the cost of the mechanics, it is vice versa: The precise vacuum actuator for the scanner is more expensive than the pneumatic drive needed for a SEM-grid.

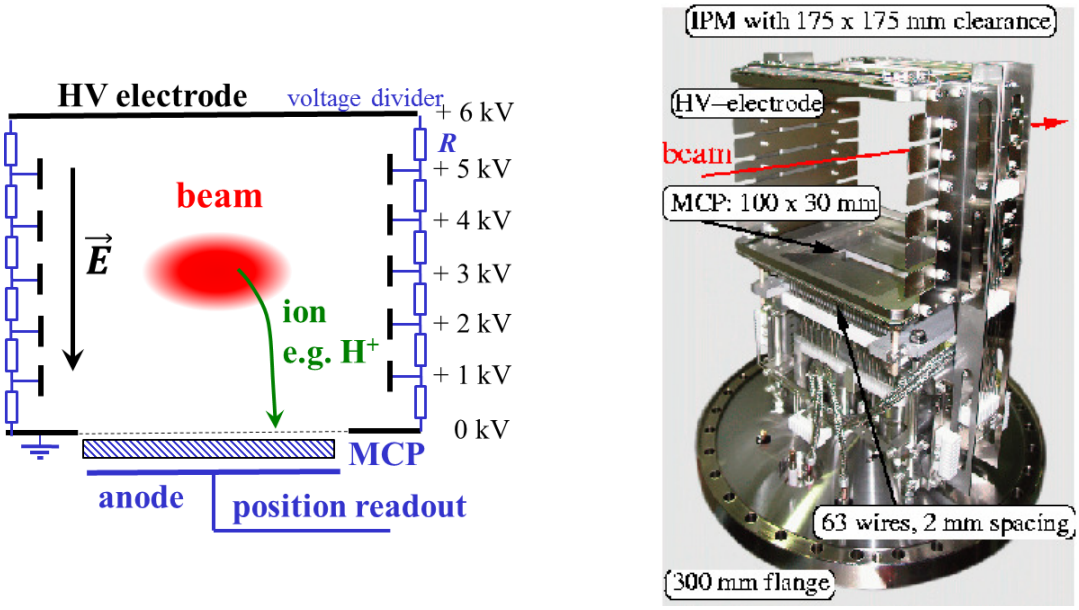

Fig. II.9.56: Left: Scheme of an ionization profile monitor for the horizontal profile determination. Right: The large aperture ionization profile monitor installed at the GSI synchrotron for the horizontal direction, the clearance is 175×175 mm^2. The monitor is mounted on a Ø 300 mm flange. The readout behind the MCP (bottom) is done with an array of 63 wires with 2 mm spacing.

II.9.3.5 Ionization profile monitor IPM

II.9.3.5.1 General method and detection

A frequently used non-destructive method for profile determination is the **I**onization **P**rofile **M**onitor **IPM** sometimes also called **R**esidual **G**as **M**onitor **RGM**. These monitors are installed at most proton synchrotrons to detect beam sizes between some mm and several cm; a review is given in Ref. [62]. They are rarely used for electron synchrotrons due to the smaller electron beam dimensions. The principle is based on the detection of ionized products from a collision between the beam particles and the residual gas atoms or molecules present in the vacuum pipe. A schematic drawing of such a monitor is shown in Fig. II.9.56. Typical pressures for LINACs and transfer lines are in the range $10^{-8} - 10^{-6}$ mbar containing mainly N_2, as well as for synchrotrons $10^{-11} - 10^{-9}$ mbar containing mainly H_2, H_2O and CH_4. The different residual gas composition is related to the different vacuum pumps used to achieve the cited vacuum pressure (such as turbo molecular pumps, ion getter pumps or non-evaporating getter NEG pumps). Due to the electronic stopping process, electrons are liberated, and electron-ion pairs are generated. An estimation of the signal strength can be obtained from the Bethe-formula. However, due to the single collision, W-values (see Section II.9.2.9.2) are only a first-order approximation for the conversion of the energy loss to the number of secondary electron-ion pairs; the ionisation process is better approximated by considering some 100 eV for the creation of one electron-ion pair. To separate the electron-ion pairs, an external electric field is applied in the order of 1 kV/cm by metallic plates installed in the vacuum pipe, but outside the beam path. To get an electric field of high homogeneity, guiding strips are installed at the side to achieve a smooth transition from the HV side to the ground plane. For most applications, the residual gas ions are detected in this setup. A realization from the GSI synchrotron is shown in Fig. II.9.56, providing a large opening of 17 cm [63].

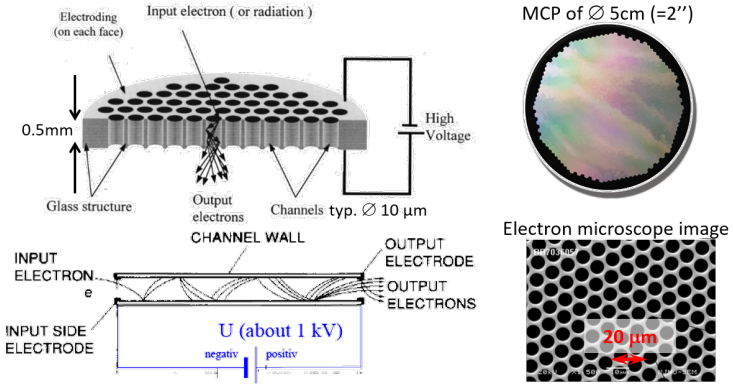

Fig. II.9.57: Illustration of a single MCP made of a glass plate with small channels of typical $\oslash$ 10 μm with the applied voltage for the amplification of secondary electrons; a photo of an MCP and a microscopic image is depicted.

The vacuum pressure is higher at transfer lines at proton LINAC facilities, and, additionally, the energy loss is larger due to the lower beam energy. Enough electron-ion pairs are generated to give a measurable current (down to 0.1 nA per strip) of secondary ions for direct detection by a sensitive SEM-grid like wire array [64].

In a synchrotron, the vacuum pressure and the stopping power are lower. A **M**ulti-**C**hannel **P**late **MCP** single particle detector is used as a "pre-amplifier". An MCP is made of a 1 mm thick glass plate with round channels of $\sim$ 10 μm, see Fig. II.9.57. These channels are coated with high-resistivity materials, and a $\sim$ 1 kV voltage is applied across them. When a residual gas ion (or electron) hits the surface, secondary electrons are liberated, i.e., the ions are converted to electrons. These electrons are multiplied in a similar manner as in a photomultiplier by a factor of typically 10^3 per MCP. Due to the channel diameter, the spatial resolution of a single-step MCP is in the order of 0.03 mm. For higher amplification, a two-step device (referred to as Chevron geometry) with a gain of $\sim 10^6$ is used, resulting in a resolution of about 0.1 mm.

For the detection of the secondary electrons at the MCP output, three types of anodes can be used:

- A SEM-grid made of wires with $\sim$ 0.5 mm diameter and $\sim$ 1 mm spacing. The advantage is the fast readout by appropriate electronics [65]. The disadvantage is the limited spatial resolution.
- An anode type using a particle detection scheme, such as wedge and strip anodes or resistive anodes, see e.g. Ref. [66]. It is based on the detection of single particles, having the advantage that the resolution can be improved by collecting data with high statistics up to the spatial resolution limit of the MCP.
- A scintillation screen (see Section II.9.3.1) is installed close to the MCP backside made of phosphor powder on a glass substrate. The secondary electrons create a light pulse imaged by a CCD or CMOS camera. The advantage is the high resolution due to several hundreds of pixels for one plane and the cheap and direct data acquisition system supplied by the commercial digital camera. However, this technique limits the time resolution and image repetition rate by the camera frame-rate of typically 100 frames per second. For faster readout, the camera is replaced by a

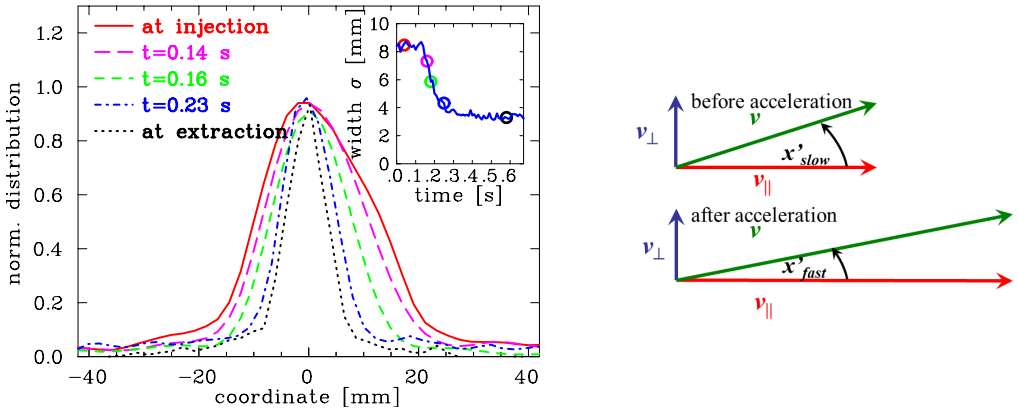

Fig. II.9.58: Left: The evolution of the horizontal beam profile is shown during the acceleration of C^{6+} from 6.7 MeV/u to 600 MeV/u within 0.4 s at the GSI synchrotron. The insert depicts the evolution of the beam width of one standard deviation during the acceleration starting at 0.15 s; the coloured circles indicate beam profiles. Right: Schematic visualization of the transverse $v_\perp$ and longitudinal $v_\parallel$ velocity evolution during acceleration leading to a decrease of the angle x'.

photomultiplier or avalanche diode, see e.g. Ref. [67].

Application: "Adiabatic damping" during acceleration

During the acceleration of a beam inside a synchrotron, the beam width should shrink. This is related to the fact that the emittance is defined in the laboratory frame by the angle between the transverse- and longitudinal velocities. During acceleration, the longitudinal velocity increases (for the non-relativistic beams), while the transverse component remains constant, leading to a decrease in the angle between both vectors as schematically shown in Fig. II.9.58. The process is called transverse adiabatic damping by the conservation of the normalized emittance, see also the discussion in Section II.9.4 and Eq. II.9.60. The normalized emittance is defined as $\epsilon_{\text{norm}} = \beta\gamma\epsilon$ for a beam of velocity β, Lorentz factor γ and actual emittance ϵ. The beam width x_σ scales concerning the emittance as $x_\sigma \propto \sqrt{\epsilon}$.

In Fig. II.9.58, the decrease in the beam width is demonstrated for the acceleration of a C^{6+} ion beam from an kinetic energy of $E_{\text{ini}} = 6.7$ MeV/u, corresponding to a velocity of $\beta_{\text{ini}} = 12$ % and a Lorentz factor of $\gamma_{\text{ini}} = 1.007$, to $E_{\text{final}} = 600$ MeV/u, corresponding to $\beta_{\text{final}} = 79$ % and $\gamma_{\text{final}} = 1.64$. The assumption of normalized emittance preservation would lead to the scaling of the expected beam width as $x_{\sigma,\text{final}} = \sqrt{\frac{\beta_{\text{ini}}\cdot\gamma_{\text{ini}}}{\beta_{\text{final}}\cdot\gamma_{\text{final}}}} \cdot x_{\sigma,\text{ini}} = 0.33 \cdot x_{\sigma,\text{ini}}$ for the depicted case of Fig. II.9.58. The experimental value $x_{\sigma,\text{final}} = 0.37 \cdot x_{\sigma,\text{ini}}$ is close to that theoretical value; the larger value for the experimental case is related to a change in the focusing and further imperfections during the acceleration. An ionization profile monitor as a non-invasive instrument is well suited for long-time observation without any influence on the beam.

Application: Transverse cooling

An example of the importance of a profile measurement is shown in Fig. II.9.59 at the GSI synchrotron with electron cooling is applied. Cooling is often performed to get a high brilliance beam by reducing of the transverse emittance and momentum distribution for high-resolution experiments or to increase the number of stored particles using so-called stacking methods. The reduction of the beam's phase-space volume is achieved by electron cooling (see e.g. Ref. [68]) or stochastic cooling (see e.g. Ref. [69]). In

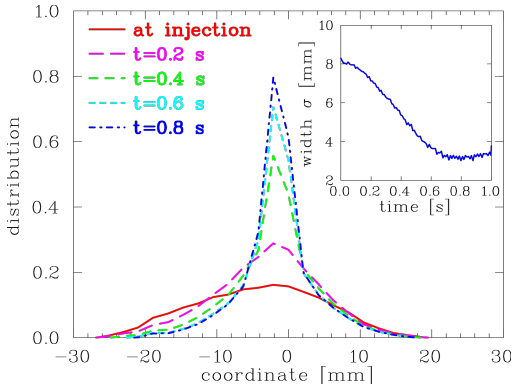

Fig. II.9.59: The profile during an electron cooling process for an 11 MeV/u Ar^{18+} beam stored at the GSI synchrotron. Five profiles from the injection (broad peak) to the coldest profile were recorded at different times during the cycle. The insert shows the standard deviation of the profile as a function of time.

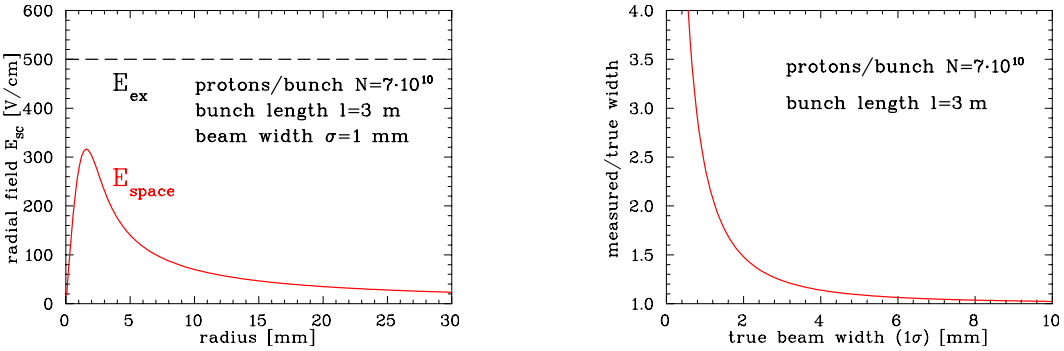

Fig. II.9.60: Left: The space charge field of $7 \cdot 10^{10}$ charges per 3 m bunch length. Right: The resulting broadening using an ionization profile monitor with ion detection is plotted using Eq. II.9.40.

Fig. II.9.59 the effect of transverse cooling is clearly seen.

II.9.3.5.2 Ion detection: Resolution limit by the beam's space charge

The residual gas ions or electrons are accelerated towards the detector by applying an external electric field of typically 0.3 to 3 kV/cm. But the beam, made of charged particles, also carries an electrical field, the space charge field, which influences the trajectory in addition. The radial electric field E_{space} of a round, non-relativistic coasting (un-bunched) beam is given for a Gaussian distribution with standard deviation σ (FWHM=$2.35 \cdot \sigma$) by

$$E_{\text{space}}(r) = \frac{1}{2\pi\epsilon_0} \cdot \frac{qeN}{l} \cdot \frac{1}{r} \cdot \left(1 - e^{-\frac{r^2}{2\sigma^2}}\right) \tag{II.9.38}$$

assuming equal beam size in horizontal and vertical direction, which leads to a radially symmetric field; qeN/l is the number of particles with charge state qe per unit length. For high current operation at a typical proton LINAC or synchrotron, this field strength is comparable to the external field, see Fig. II.9.60 (left). The residual gas ions or electrons are accelerated by both fields, leading to a broadening of the measured profile depicted in Fig. II.9.60 (right) for this beam parameters; a typical trajectory for a residual gas ion is depicted in Fig. II.9.61 (right). To get a first estimation of the real beam size, the correction

can be calculated via

$$\sigma_{\mathrm{beam}}^2 = \sigma_{\mathrm{meas}}^2 - \sigma_{\mathrm{corr}}^2 \quad . \tag{II.9.39}$$

σ_{corr} is given in a first-order approximation by the beam space charge and the external field according to

$$\sigma_{\mathrm{corr}}^2 = \frac{e^2 \ln 2}{4\pi\epsilon_0\sqrt{m_p c^2}} \cdot d_{\mathrm{gap}} \cdot qN \cdot \sqrt{\frac{1}{eU_{ex}}} \quad . \tag{II.9.40}$$

The correction is proportional to the number of beam particles N. It is inversely proportional to the square root of the external field (created by the static voltage U_{ex}) and, therefore, an increase in the external field has only a relatively weak influence on the broadening. A large distance d_{gap} between the two high voltage electrodes result in a longer drift time and therefore in a prolonged influence of the space charge field. The typical time of flight for a single charged H_2^+ molecular ion is of the order of 100 ns. m_p is the mass of the proton. However, the resulting profile broadening is independent of the mass of the residual gas ion, as the trajectory of heavier ions are less influenced, but they need more time to reach the detector plane, and, hence, are influenced by the beam's space charge for a longer duration.

For a Gaussian beam distribution with different extensions in horizontal and vertical direction, an exact analytical formula for bunched beam is derived in Ref. [70]. Moreover, the effect of different masses of residual gas ions are discussed. To calculate this correction for a non-Gaussian cbeam with different horizontal and vertical size and a longitudinal extension within the bunch, numerical simulations are required. Some available codes are compared in Ref. [71] and a versatile numerical code is available, see Ref. [72].

The initial velocity of the residual gas ions right after the ionizin collision between the residual gas molecule and the beam particle (Bethe-regime) is too small to affect the resolution in most practical cases; this is in contrast to the electron detection scheme discussed below.

II.9.3.5.3 Electron detection in the presence of a magnetic field

For the profile measurement of intense beams, the detection of electrons is more suited to overcome the space-charge induced broadening, see Fig. II.9.61. For this, the HV is reversed to accelerate the negative electrons created in the atomic collision toward the detector. If an additional magnetic field B is applied parallel to the external electrical field, the electrons of mass m_e and charge e spiral around the magnetic field lines with the cyclotron radius $r_c = \sqrt{2m_e E_{\mathrm{kin},\perp}}/eB$ where $E_{\mathrm{kin},\perp}$ is the kinetic energy perpendicular to the magnetic field. This transverse kinetic energy is determined by the initial transverse velocity given by the kinematics of the atomic collision. The cross-section depends on the beam and residual gas molecule properties [73], resulting in kinetic energies for the emitted electron with a mean value in the order of $\langle E_{\mathrm{kin},\perp}\rangle \simeq 10$ eV. The cyclotron radius, and, consequently, the detector resolution, is mainly determined by this initial electron energy and is almost independent of the beam's space-charge field. For example, a transverse energy component of $E_{\mathrm{kin},\perp} = 10$ eV and a homogeneous magnetic magnetic field of $B = 0.1$ T results in an cyclotron radius of $r_c = \sqrt{2m_e E_{\mathrm{kin},\perp}}/eB \simeq 0.1$ mm. The projection of the trajectory in the plane perpendicular to the field is a circle with less than 0.1 mm radius; this corresponds to the spatial resolution of the MCP; the magnetic field strength is chosen such that the resolution is mainly determined by the MCP properties. The necessary magnetic field of about 0.1

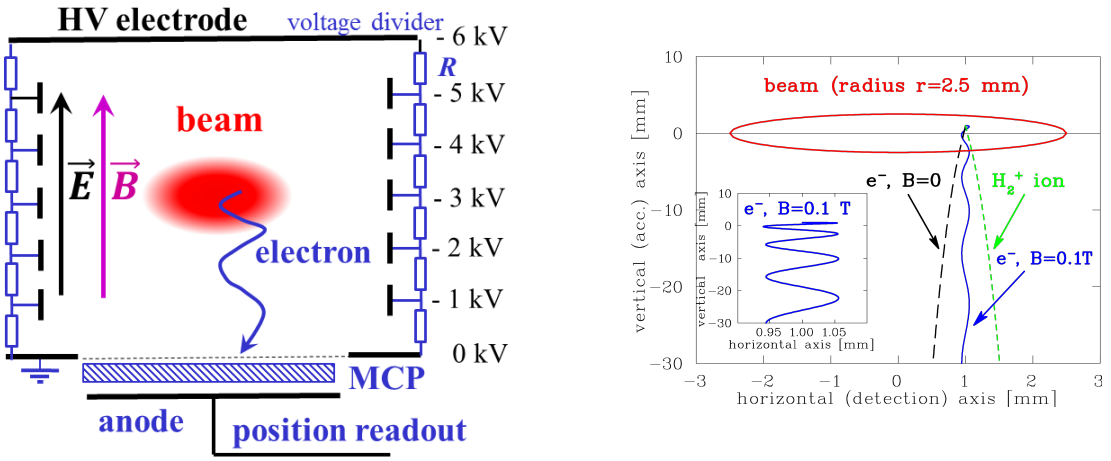

Fig. II.9.61: Left: Schematic trajectory of an electron in an ionization profile monitor in the presence of a homogeneous electric E and magnetic field B. Right: The comparison of the trajectories of an H_2^+-ion and an electron with and without a magnetic field visualizes the broadening due to the beam space-charge field. The electron is fixed to the field line by applying a magnetic field, as shown in the insert. The beam parameters are: $7 \cdot 10^{10}$ protons within a 10 m long bunch with a radius of 2.5 mm.

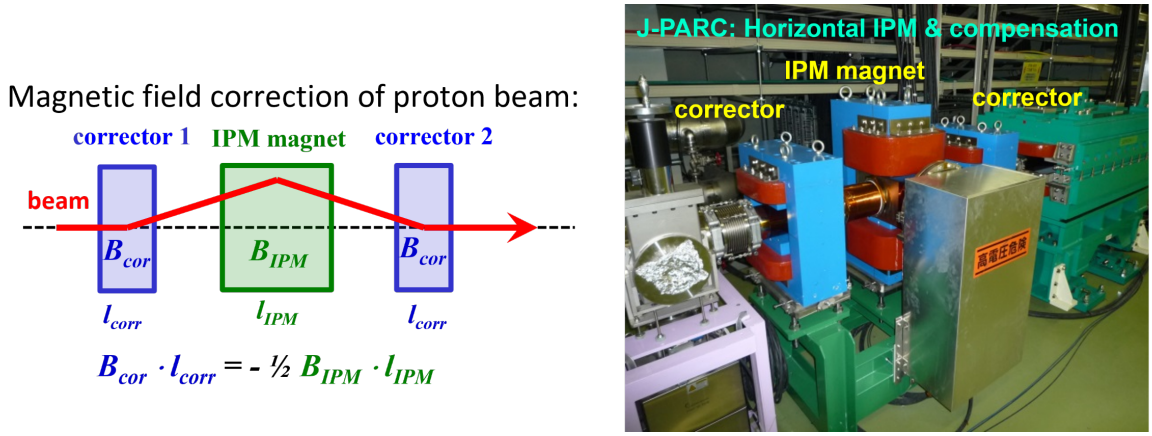

Fig. II.9.62: Left: Schematic trajectory of an ion beam within the main IPM magnet field and the two corrector fields. Right: A photo of the J-PARC IPM realization with a main magnet for the horizontal profile and two corrector dipoles; the dipole field is $B = 250$ mT with a gap of $d_{\rm gap} = 220$ mm, see [74].

T is generated in most cases with a dipole magnet of the same type as used for beam bending, see e.g. Refs. [67, 74, 75]. The movement along the field is a linear acceleration with a typical time of flight of ~ 2 ns as given by the strength of the electric field. An interesting discussion about the required electric and magnetic fields including the remaining distortions can be found in Ref. [76] for the example of LHC beams; in addition, correction algorithms based on machine learning are described in the reference.

To provide a magnetic field of $B \geq 0.1$ T with a gap for the electric field cage of at least $d_{\rm gap} \simeq 20$ cm, a relative long dipole magnet must be installed. Figure II.9.62 shows the realization at the proton synchrotron J-PARC providing a magnetic field of $B = 250$ mT and a homogeneity of about 1 % within at the detection volume [74, 75]. The magnetic field has a significant influence on the proton beam trajectories even for high-energy synchrotrons. To counteract this bend, two corrector magnets with an inverted $B-$field orientation and, in total, the same effective length $2l_{\rm corr}$ as the main dipole

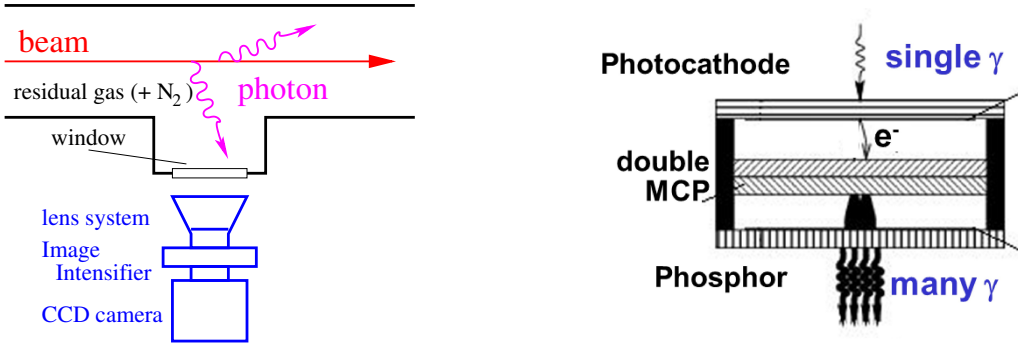

Fig. II.9.63: Left: General scheme of the profile determination via detection of the residual gas fluorescence. Right: Scheme of an image intensifier consisting a photo-cathode, an MCP and a phosphor screen.

l_{IPM} is required as mounted upstream and downstream of the main dipole. The related magnet structure with close fields of opposite orientation must be optimized by numerical field simulations to provide an optimal homogeneity for the electron trajectory and the compensation for the proton beam. The required insertion length in beam direction for the three magnets is typically 1.5 to 2.5 m.

II.9.3.6 Beam induced fluorescence monitor

By the collision of the beam particles with the residual gas, the molecules are not only ionized, but also excitation of internal energy levels can occur. The excitations decay electro-magnetically by light emission leading to fluorescence [77]. In particular, the excitation of N_2 results in transition bands in the optical region. The band originates from the decay of N_2^+ molecular ions excited by the collision with the beam ions in the wavelength range $390\ \mathrm{nm} < \lambda < 470\ \mathrm{nm}$, i.e., in the near UV to blue color. The lifetime is in the range of 60 ns depending on the involved upper and lower molecular levels. About 1 % of the energy loss in N_2 gas is converted to photon emission in the optical wavelength interval [78]. The general scheme of a **B**eam **I**nduced **F**luorescence monitor **BIF** is shown in Fig. II.9.63 and reviewed in Ref. [62].

In LINACs, the most prominent vacuum constituent is N_2; if the signal strength is insufficient, a pressure bump of N_2 gas can be injected into the vacuum pipe with the help of a regulated gas valve. An image-amplified camera can monitor the fluorescence [79]. The advantage of this non-invasive method is that nothing has to be installed in the vacuum pipe and commercially available cameras can be installed. The rate of photons N_{photon} for the detected light is given by

$$N_{\mathrm{photon}} \propto \frac{dE}{ds}\Delta s \cdot p \cdot \frac{f}{\hbar\omega} \cdot \frac{\Omega}{4\pi} \cdot \frac{I_{\mathrm{beam}}}{qe} \tag{II.9.41}$$

where $\frac{dE}{ds}\Delta s$ is the energy loss of ions with charge state q in N_2 for an observation length s and the pressure p, $f \sim 1$ % is the fraction of the conversion from energy loss to a photon of energy $\hbar\omega$ and Ω the solid angle covered by the camera's field-of-view.

In an image intensifier, as depicted in Fig. II.9.63, the photons hit a photo-cathode within a vacuum sealed glass container of typically 18 to 25 mm diameter. With a probability of about 20 %, the photon is converted to an electrons liberated from the photo-cathode by an voltage between the cathode and

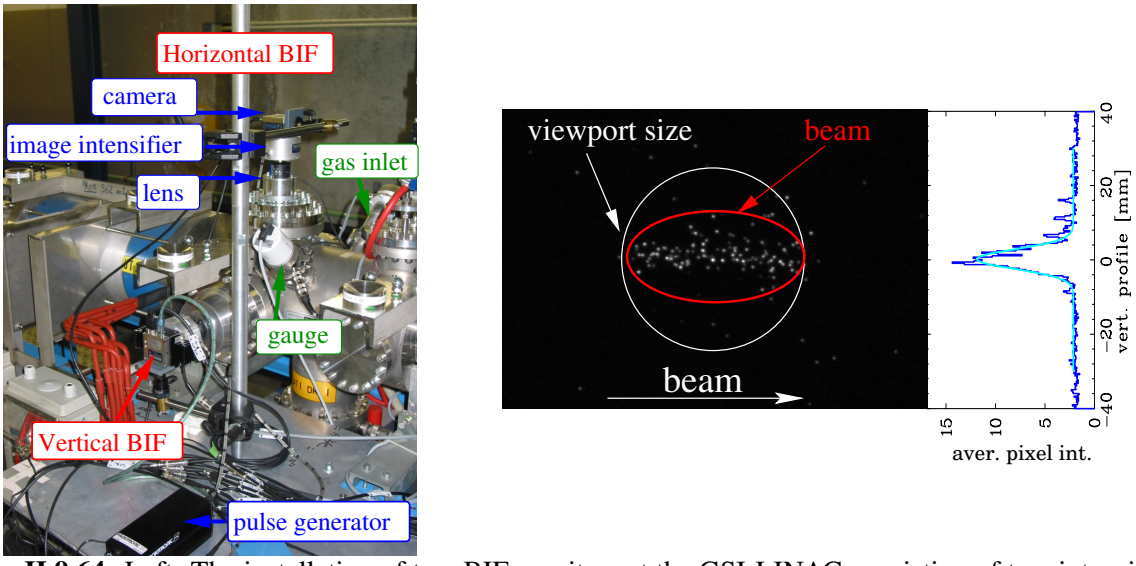

Fig. II.9.64: Left: The installation of two BIF monitors at the GSI-LINAC consisting of two intensified cameras for the horizontal and vertical profile measurement, respectively. Right: Image of a 4.7 MeV/u Ar^{10+} beam of $I_{\mathrm{beam}} = 2.5$ mA and 250 μs duration with a vacuum pressure of 10^{-5} mbar recorded at the GSI LINAC. The original image (recorded with a double MCP intensifier) is shown, as well as the projection on the vertical axis [79].

the MCP front side. As described above, the electrons are accelerated towards an MCP and amplified by a factor of usually 10^6. A phosphor screen converts the electrons back to photons, which are finally imaged by the camera via relay optics or fibres. The total conversion efficiency can be up to 15 %, which characterizes the probability that a single photon is visible as bright light spots in the camera image.

Figure II.9.64 (left) shows the typical installation of a BIF station for horizontal and vertical profile measurement. An example of a related beam image is shown in Fig. II.9.64 (right) recorded at the pulsed LINAC at GSI with an argon beam. Single photon spots are visible on the image, but the projection along the longitudinal direction shows a profile with sufficient statistics [79]. The method is also applied for higher energy beams e.g. at CERN's SPS and LHC [80].

II.9.3.7 Synchrotron radiation monitor

For electron accelerators, the effect of synchrotron radiation, emitted by accelerated electrons can be used for profile determination. As known from classical electrodynamics [18] the radiation power P_{synch} is given for a momentum change dp/dt of a particle with mass m_0 by

$$P_{\mathrm{synch}} = \frac{e^2 c}{6\pi\varepsilon_0 (m_0 c^2)^2} \left[\frac{dp}{dt}\right]^2 . \tag{II.9.42}$$

Taking into account that $dp/dt = p \cdot v/R$, the radiation power from a bending magnet for a beam with kinetic energy E_{kin} is

$$P_s = \frac{e^2 c}{6\pi\varepsilon_0 (m_0 c^2)^4} \frac{E_{\mathrm{kin}}^4}{R^2} \quad . \tag{II.9.43}$$

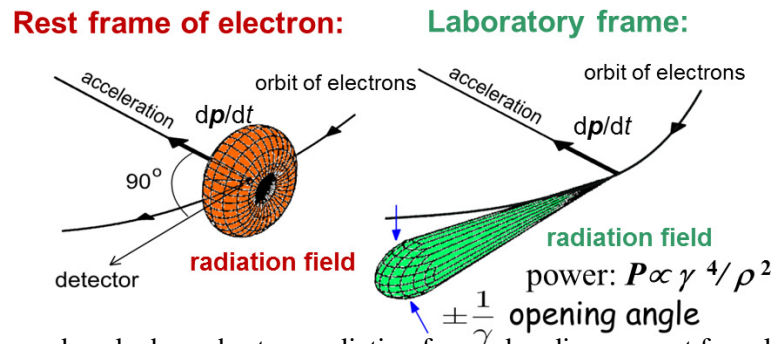

Fig. II.9.65: Forward peaked synchrotron radiation from a bending magnet for relativistic particles.

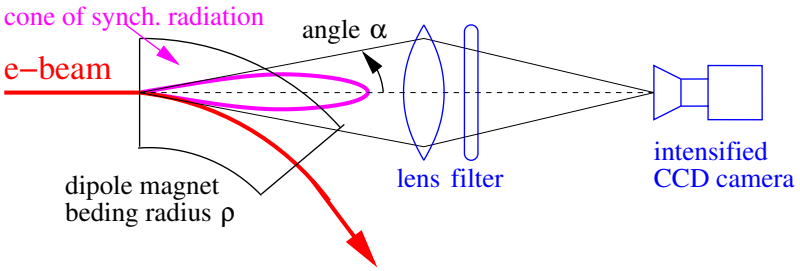

Fig. II.9.66: Sketch of a synchrotron radiation profile monitor observing the radiation from a dipole.

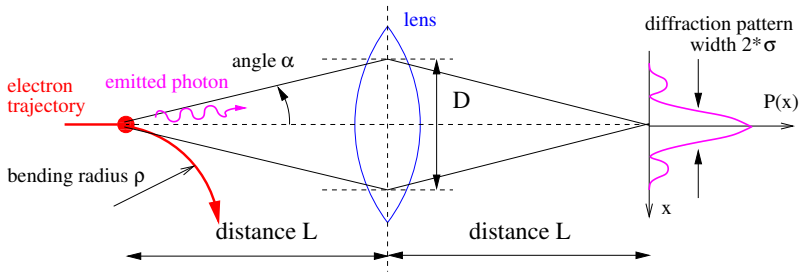

Fig. II.9.67: Sketch of the optical system for synchrotron radiation profile monitors and a 1:1 image visualizes the diffraction limit.

The radiation from electrons and protons at the same kinetic energy compares as

$$\frac{P_{\text{synch}}^{\text{electrons}}}{P_{\text{synch}}^{\text{protons}}} = \left[\frac{932\ \text{MeV}}{511\ \text{keV}}\right]^4 \approx 10^{13}, \tag{II.9.44}$$

which means that the power radiated by electrons is 10^{13} times higher than for protons of the same kinetic energy.

In the centre-of-mass system, the radiation is emitted perpendicular to the momentum change. The Lorentz transformation to the laboratory frame gives a factor of γ, yielding a forward-peaked distribution with an opening cone of half-angle γ, as demonstrated in Fig. II.9.65. The physical principle, achievable resolution, and some applications are reviewed in Ref. [81].

Optical imaging

The light emitted by the electron's bend in a dipole magnet can be used to monitor the beam's horizontal and vertical profile, as schematically shown in Fig. II.9.66. For diagnostic purposes, the visible part of

the emitted spectrum is observed in most cases by using optical band-pass filters. For this wavelength, high-quality optics are available, and standard cameras can be used. For most accelerator applications, the required wavelength is longer than the so-called critical wavelength, where the power spectrum falls off. Due to this approximation, we can apply some approximation; see, e.g. Ref. [82]. For horizontally polarized synchrotron light of wavelength λ the radiation by the electrons is emitted into a cone with an opening angle of

$$\alpha = 0.41\,(\lambda/\rho)^{1/3} \quad , \tag{II.9.45}$$

with ρ being the radius of the bending magnet. For the optical system, a 1:1 image from the beam spot to the camera is obtained by a focusing lens of diameter D, separated by a distance L from the beam and from the camera, see Fig. II.9.67. More precisely, the finite emission angle α results in an image of size D on the lens. From the theory of Fraunhofer diffraction on a round aperture, the pattern on the image plane has a half-width σ of

$$\sigma = \frac{\lambda}{2D/L} \quad . \tag{II.9.46}$$

Combining both equations with the geometrical dependency $D \simeq 2\alpha L$ yields the resolution due to diffraction

$$\sigma \simeq 0.6\left(\lambda^2 \cdot \rho\right)^{1/3} \quad . \tag{II.9.47}$$

A small width of the diffraction pattern and, therefore, a good resolution is achieved for a given optical system by Refs. [83, 84]:

- using dipole magnets with small bending radius ρ; but this radius is fixed by the accelerator construction and
- a short wavelength, but due to technical reasons (optic component & camera), it should not be shorter than near UV i.e. $\lambda > 300$ nm.

Typical limits are about ~ 100 μm, depending on the dipole bending radius. A higher resolution can be achieved by observing the light from wigglers or undulators if they are installed in the synchrotron.

Figure II.9.68 depicts a realization of a synchrotron light profile monitor at CERN LEP [85]. The bending radius is 3.1 km. The diffraction gives the most substantial contribution to the resolution by about $\sigma \sim 300$ μm, which is comparable to the actual electron beam size. The setup consists of a metallic mirror to deflect the light out of the plane of the beam. Due to the high power of the synchrotron radiation, the mirror has to be cooled, and possible deformations can reduce the optical quality. With the help of curved mirrors, the light is focused, and an optical filter selects the wavelength range of blue or UV light; the detector is an image-intensified camera. Even though the resolution is limited, this relatively straightforward system is frequently used l for accelerator operation due to its non-destructiveness. Figure II.9.69 shows an example from the synchrotron light source APS [86].

An example of the application of a synchrotron radiation monitor is shown in Fig. II.9.70 during beam acceleration at the ALBA booster synchrotron [87]. For the two dimensional beam image, the width in the horizontal and vertical direction can be calculated and compared with simulations. At first glance, the adiabatic damping is less pronounced as compared to the example of the hadron beam in Fig. II.9.58: the reason is the contribution to the beam width by the relative momentum spread $\Delta p/p_0$ of the beam

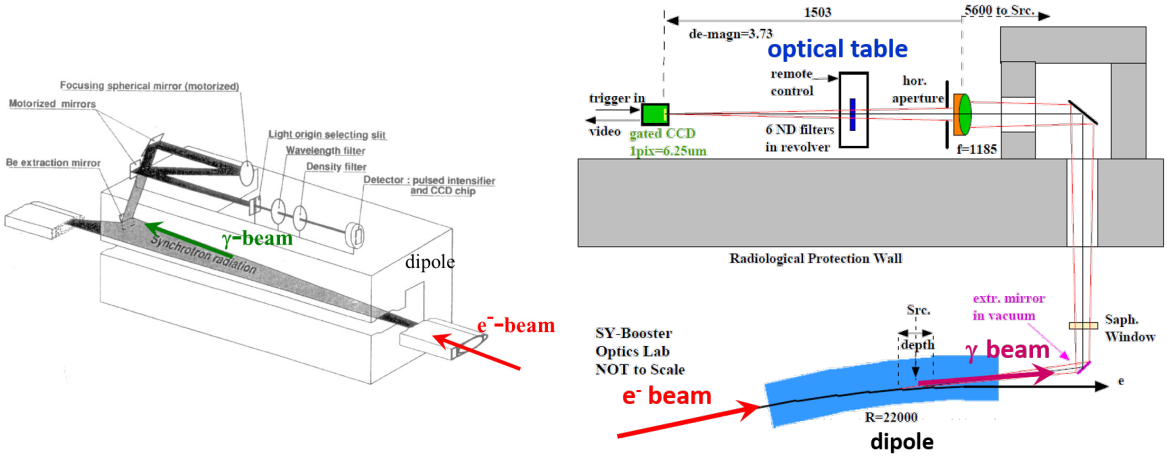

Fig. II.9.68: Left: An early installation of a synchrotron radiation profile monitor at LEP. The optical system is installed close to the 23 m long dipole magnet with a bending radius of 3100 m, from Ref. [85]. Right: The typical monitor installation at a circular light source, from Ref. [88].

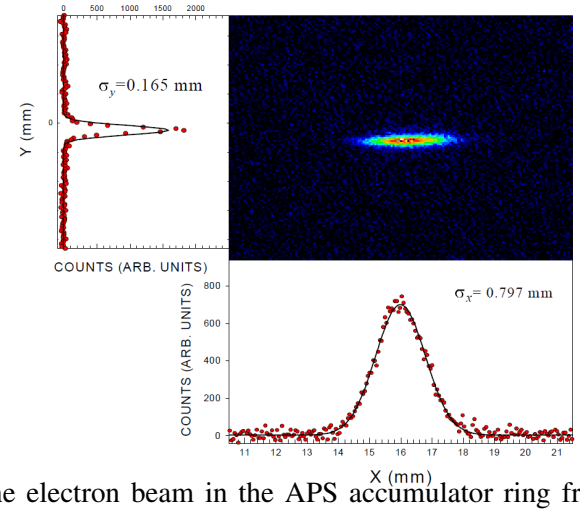

Fig. II.9.69: Image of the electron beam in the APS accumulator ring from a synchrotron radiation monitor at Argonne National Laboratory [86].

particles and non-zero dispersion D at the measurement location as $x_{\mathrm{tot}} = \sqrt{\varepsilon\beta + (D \cdot \Delta p/p_0)^2}$ and the contribution by quantum fluctuations related to the emission of photons [87].

At dipoles in transfer lines such synchrotron light monitors can be installed as well, which is realized at some facilities, e.g. Ref. [88]. However, there might be some technical problems as the amount of light emitted during the single pass of the electrons might be insufficient; instead, OTR screens, due to their simpler technical realization, serve as a frequently used profile diagnostics in transfer lines at light sources or scintillation screens in the case of low beam current applications at other electron accelerators.

X-ray imaging

As stated above, synchrotron radiation monitors for optical imaging have a typical resolution of 100 μm determined by diffraction at aperture limitation and lenses of the optical path from the synchrotron to the optical hutch as well as related to the emission cone of the light; the diffraction pattern depends on the ratio between observation wavelength and aperture. A higher resolution of typically 5 to 10 μm

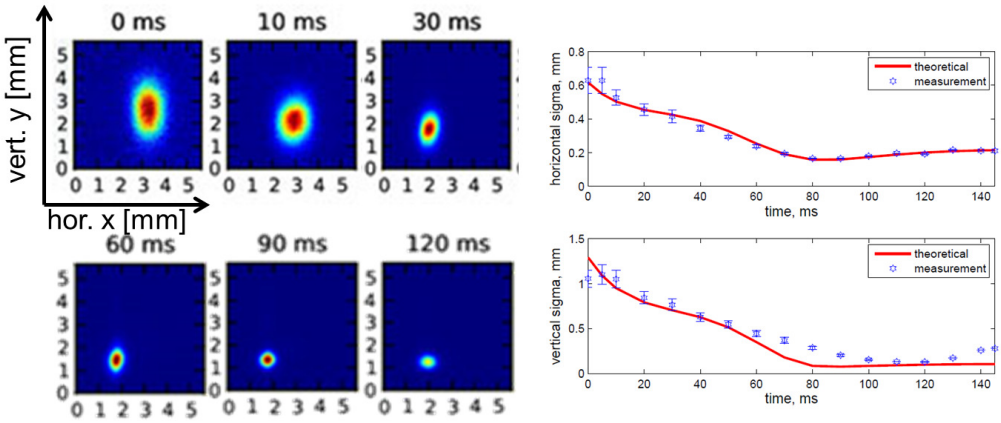

Fig. II.9.70: Left: Examples of a two-dimensional beam image from a synchrotron light monitor at the ALBA booster synchrotron. Right: The fitted horizontal and vertical beam width during the acceleration from 0.1 to 3 GeV within 130 ms, and the comparison with simulations, from Ref. [87].

can be achieved by recording the beam image at shorter wavelengths down to the hard X-ray range of several 10 keV photon energy. Figure II.9.71 compares the schematics of three frequently installed synchrotron radiation monitors. Such X-ray setup is nowadays installed at most circular light sources related to the user requirements for shorter wavelength generation and significantly smaller electron beam emittance. Figure II.9.72 shows one typical realization in more detail where broadband X-rays are recorded using pinhole optics [89]. Most X-ray imaging systems use an image reproduction scale of about 1:1 for a distance of about 10 to 20 m from the source to the optical hutch. The pinhole plate is located mid-way to ensure equal object d and image D distance. The pinhole plate has a hole diameter of typically 10 μm. The plate is made of heavy metal such as tungsten and has a thickness of 1 to 5 mm to attenuate the X-rays outside the hole. A good alignment is required for the optical path of at least 10 m length and a hole of typical 10 μm diameter, in the depicted case realized by an optional laser beam. Upstream of the X-ray beam, a wedge-shaped variable attenuator is used, and a blocking of the optical and UV synchrotron radiation photons by a thin metal window. Downstream of the pinhole, further X-ray shielding is required. As a recording device, a commercially available X-ray camera consists of a scintillator to convert the X-ray photons to optical photons, which are then, as the second step, imaged with a regular camera. A 90^o mirror is used to mount the camera outside the X-ray path. Such pinhole cameras are installed in most light sources as they provide a simple and reliable image method; however, the image quality, particularly the image contrast, is limited. Non-standard X-ray optics have been installed to increase the image quality. Quantitative design considerations, recent developments, and further references are collected in Refs. [90–92].

Optical interference

The resolution limit for the profile measurement is further reduced down to $\simeq 1$ μm by using an interference technique for optical wavelengths created by a double-slit. The scheme is depicted in Fig. II.9.71 (bottom); the general considerations are described in Refs. [92–94] and related formulas are derived. Generally, the coherence of the optical light wavefront approaching the double slit leads to an interference pattern on a distant plane. The interference minima converges to zero intensity for an ideal

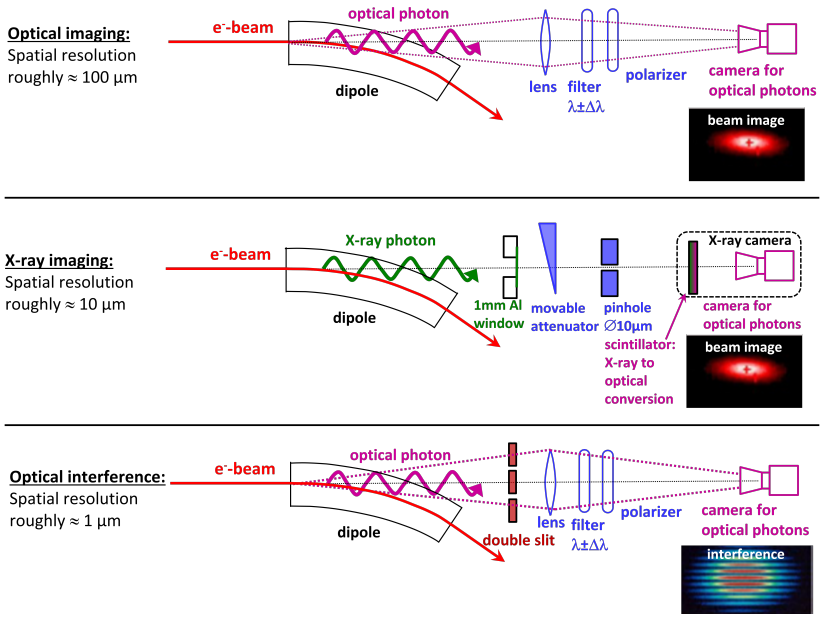

Fig. II.9.71: Schematics of the three methods for profile measurements by synchrotron radiation monitor are shown. Top: optical imaging; middle: X-ray imaging; bottom: optical interference.

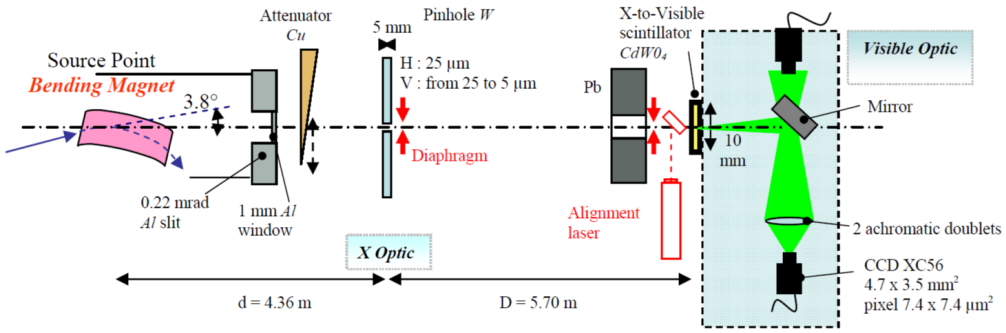

Fig. II.9.72: Schematics of a pinhole X-ray monitor installed at SOLEIL [89].

point-like source and coherent light emission. For an extended source size, the interference pattern is less pronounced and fades out as the minima do not have intensity zero. From this blurring of the interference pattern, the finite electron beam size and its profile distribution can be reconstructed. From the dipole magnet, the light is transported to several 10 m distances to the optical hutch and the slit plus related optics and narrow-band filter installed on a laser table. Beam sizes less than 10 μm were measured; installation examples are described in Refs. [95, 96]. However, the interference methods require very precise alignments of the optical path and are sensitive to environmental disturbances. Hence, its applicability is often restricted to precise machine studies, while for the standard accelerator operation, the X-ray pinhole camera is a more robust instrument.

II.9.4 Measurement of transverse emittance

The emittance describes the quality of a beam by depicting the phase-space distribution with a characterization using statistical moments. Emittance determination are based on profile measurements; it is unimportant what method of profile measurement is used as long as it has an adequate resolution. In the

following, we start with a slit-grid and pepper-pot device, where an aperture fixes the spatial coordinate, and the angle distribution is measured. Those invasive methods are suited for particles having a range in matter below $\sim$ 1 cm, i.e. proton or ions with $E_{\mathrm{kin}} < 100$ MeV/u, see Fig. II.9.20. The emittance can also be determined by fitting the beam envelope, determined by the beam profile at one location with different focusing conditions or at different locations. This can be applied to transfer lines for all beam conditions. However, including emittance growth due to space-charge forces is problematic, i.e., a blow-up of the transverse size due to the forces between the charged particles. The involved physics, technologies, and data acquisition are detailed in Ref. [97].

In a synchrotron, measuring the beam profile at one location is sufficient. For the stationary state of stable storage, the orientation of the ellipse, which is equivalent to the knowledge of the lattice functions dispersion $D(s)$ and β-function $\beta(s)$, is fixed (or can be measured separately). The emittance is calculated from the beam width σ via

$$\epsilon = \frac{1}{\beta(s)} \left[\sigma^2 - \left(D(s) \frac{\Delta p}{p} \right)^2 \right] \quad , \tag{II.9.48}$$

which is valid for the horizontal and vertical plane, respectively. If only horizontal bends occur in a facility, the dispersion in vertical direction is $D_y = 0$, and the equation simplifies to $\epsilon_y = \frac{\sigma_y^2}{\beta_y(s)}$.

II.9.4.1 Definition of the emittance

A linear second-order differential equation can describe the motion of the beam particle. It assumes the absence of any non-linear coupling, like space-charge forces or beam-beam effects as well as coupling between the two transverse and the longitudinal planes. The beam quality is given by the phase-space volume, which is then a constant of the motion. The emittance for one plane is defined by

$$\epsilon_x = \frac{1}{\pi} \int_A dx dx' \quad , \tag{II.9.49}$$

where $A = \pi\epsilon$ is the area of the phase-space occupied by the beam, see Fig. II.9.73. A measurement of the emittance is equivalent to determining the distribution of the spatial coordinate x (i.e., the beam profile), the distribution in angle x', and the correlation between x and x'. The basics of linear beam dynamics are discussed in textbooks on accelerator physics, see Refs. [98–101].

The interpretation of an area assumes a hard-edge, homogeneous distribution. A more realistic case is the Gaussian density distribution $\rho(x, x')$ defined at the position of the vector $\vec{x} = (x, x')$ for each location s along the beam path. The 2-dim density is then (the meaning of the mathematical abbreviations are described below)

$$\rho(x, x') = \frac{1}{2\pi\epsilon_x} \exp\left[\frac{-1}{2} \vec{x}^T \boldsymbol{\sigma}^{-1} \vec{x} \right] \equiv \frac{1}{2\pi\epsilon_x} \exp\left[\frac{-1}{2 \det \sigma} \left(\sigma_{22} x^2 - 2\sigma_{12} x x' + \sigma_{11} x'^2 \right) \right] . \tag{II.9.50}$$

The profile distribution $P(x)$ is obtained by integrating the density ρ over x' as $P(x) = \int \rho(x, x') dx'$ and the parameter $\sqrt{\sigma_{11}}$ is the standard deviation of this distribution. $\sqrt{\sigma_{22}}$ is the corresponding value for the angular distribution $P(x')$ obtained by integrating $\rho(x, x')$ over x as $P(x') = \int \rho(x, x') dx$. σ_{12} is called covariance as it describes the correlation between x and x' and is related to the orientation of

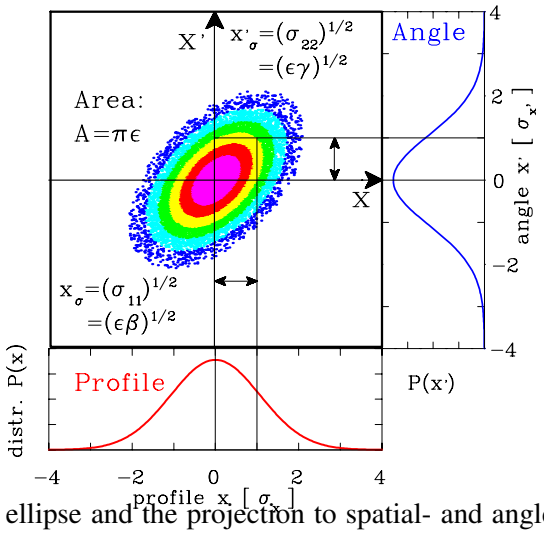

Fig. II.9.73: The emittance ellipse and the projection to spatial- and angle coordinates for a Gaussian density distribution. The values of the independent variables are given in units of the standard deviation.

the ellipse in phase-space; Appendix II.9.10 compiles the required formulas.

With the help of three parameters σ_{ij} the so-called beam matrix $\boldsymbol{\sigma}$ can be defined in the following way:

$$\boldsymbol{\sigma}(s) = \begin{pmatrix} \sigma_{11}(s) & \sigma_{12}(s) \\ \sigma_{12}(s) & \sigma_{22}(s) \end{pmatrix} \tag{II.9.51}$$

at one location s in the beam line. The beam matrix $\boldsymbol{\sigma}$ represents the beam ellipse at this location s and varies along the beam path. It is used in connection with the transfer matrix $\mathbf{R}$, which describes the action of the optical elements along the beam path in a linear approximation with optical elements like drifts, dipoles, quadrupole magnets or solenoids by

$$\boldsymbol{\sigma}(s_1) = \mathbf{R} \cdot \boldsymbol{\sigma}(s_0) \cdot \mathbf{R}^{\mathbf{T}} \tag{II.9.52}$$

from a location s_0 to s_1, see Section II.9.4.4 for a more detailed discussion.

The absolute value of the emittance at each location can be defined using this notation as

$$\epsilon_x = \sqrt{\det \boldsymbol{\sigma}} = \sqrt{\sigma_{11}\sigma_{22} - \sigma_{12}^2} \tag{II.9.53}$$

and corresponds to an occupation of 15 % of the full phase-space area. The unit of this value is m·rad or more frequently mm·mrad. To be consistent with the geometrical interpretation of an area surrounded by an ellipse, the number is multiplied by π; in this case 39 % of the beam is inside the area of $\pi \cdot \sqrt{\sigma_{11}\sigma_{22} - \sigma_{12}^2}$. In other words, the Gaussian beam quality at a given location s is fully described by the beam matrix $\boldsymbol{\sigma}(s)$.

Frequently, the Twiss parameters (better called Courant Snyder functions) are used, which are the beam matrix elements normalized by the emittance as

$$\alpha = -\sigma_{12}/\epsilon \qquad \beta = \sigma_{11}/\epsilon \qquad \gamma = \sigma_{22}/\epsilon \quad . \tag{II.9.54}$$

The beam matrix is then

$$\boldsymbol{\sigma} = \epsilon \cdot \begin{pmatrix} \beta & -\alpha \\ -\alpha & \gamma \end{pmatrix} \tag{II.9.55}$$

and the equation of the beam ellipse can be written as

$$\gamma x^2 + 2\alpha x x' + \beta x'^2 = \epsilon \quad \text{with the normalization} \quad \beta\gamma - \alpha^2 = 1 \quad . \tag{II.9.56}$$

The width of profile and angular distributions is given by

$$x_\sigma = \sqrt{\sigma_{11}} = \sqrt{\epsilon\beta} \qquad \text{and} \qquad x'_\sigma = \sqrt{\sigma_{22}} = \sqrt{\epsilon\gamma} \quad . \tag{II.9.57}$$

Their geometric meaning is one standard deviation of the transverse profile and angular distribution of the beam. The geometrical size of the phase-space ellipse is changed along the beam pass s; therefore, the parameters $\alpha(s)$, $\beta(s)$ and $\gamma(s)$ are functions on the position s. In particular, for a synchrotron $\beta(s)$ is called the beta-function, describing the beam size via $x_\sigma(s) = \sqrt{\epsilon \cdot \beta(s)}$.

For theoretical calculations, one prefers analytical descriptions of the density distribution. One example is the Gaussian distribution of Eq. II.9.50; other functions are discussed, e.g. in Ref. [101]. However, the beam does not always have a Gaussian shape. For any arbitrary phase-space distribution, the beam emittance can be calculated via the statistical moments of a 2-dimensional distribution $\rho(x, x')$. Appendix II.9.10 compiles the definitions for statistical moments.

To describe the beam quality via the emittance the rms value (*r*oot *m*ean *s*quare) can be calculated as

$$\epsilon_{rms} = \sqrt{\det \begin{pmatrix} \langle x^2 \rangle & \langle x x' \rangle \\ \langle x x' \rangle & \langle x'^2 \rangle \end{pmatrix}} = \sqrt{\langle x^2 \rangle \langle x'^2 \rangle - \langle x x' \rangle^2} \tag{II.9.58}$$

and follows the same general mathematical role as Eq. II.9.53.

For a Gaussian distribution, the fraction f of the beam inside the certain value of the emittance can be expressed via the rms value as

$$\epsilon(f) = -2\pi\epsilon_{rms} \cdot \ln(1 - f) \tag{II.9.59}$$

leading to the following table:

factor to ϵ_{rms}	$1 \cdot \epsilon_{rms}$	$\pi \cdot \epsilon_{rms}$	$2\pi \cdot \epsilon_{rms}$	$4\pi \cdot \epsilon_{rms}$	$6\pi \cdot \epsilon_{rms}$	$8\pi \cdot \epsilon_{rms}$
faction of beam f [%]	15	39	63	86	95	98

When a certain emittance value is given for a beam, one has to check its meaning carefully, as there is no standard definition for the emittance to what level of beam fraction this value refers.

The emittance is a quantity defined in the laboratory frame due to the definition of divergence. When a beam is accelerated, the divergence shrinks ("adiabatic damping") due to the changing ratio of longitudinal velocity v_s to transverse velocity v_x: $x' = v_x/v_s$. To compare emittance for different

longitudinal momenta $p_s = m_0 \cdot \gamma_{\mathrm{rel}} \cdot v_s$, the normalized emittance ϵ_{norm}

$$\epsilon_{\mathrm{norm}} = \frac{v_s}{c}\gamma_{\mathrm{rel}} \cdot \epsilon \tag{II.9.60}$$

is referred to a value $v_s/c \cdot \gamma_{\mathrm{rel}} = 1$ (corresponding to $v_s = \sqrt{1/2} \cdot c = 0.71 \cdot c$). c is the velocity of light and $\gamma_{\mathrm{rel}} = 1/\sqrt{1-(v_s/c)^2}$ is the relativistic Lorentz factor. The normalized emittance is constant under ideal accelerating conditions.

A measurement of emittance means a determination of the numerical value of ϵ as well as the orientation and shape of the phase-space distribution.

The above discussion concerns the 2-dimensional horizontal phase-space spanned by the coordinates x and x'; generally, which is not always realistic. Taking all three spatial dimensions into account, a 6-dimensional phase-space must be considered with a 6-dimensional vector $\vec{x} = (x, x', y, y', l, \frac{\Delta p}{p_0})^t$ for the horizontal, vertical and longitudinal direction; l is the bunch length and $\frac{\Delta p}{p_0}$ the momentum spread compared to the reference particle. The beam matrix $\boldsymbol{\sigma}$ and all transfer matrices $\mathbf{R}$ are then 6×6 matrices. However, Eqs. II.9.51 and II.9.52 keep their form also for 6×6 matrices. Using the full 6-dimensional phase-space, correlations between the horizontal, vertical and longitudinal sub-spaces can be described. A dipole magnet is an example of the coupling between horizontal and longitudinal phase-space as it introduces dispersion D for particles of different momentum Δp, leading to an enlarged profile width x_{rms} in terms of addition in quadrature as

$$x_{rms} = \sqrt{\epsilon_{rms}\beta + \left(D\frac{\Delta p_{rms}}{p}\right)^2} \quad . \tag{II.9.61}$$

For simplicity, only the 2-dimensional case spanned by x and x' is considered in the following sections.

II.9.4.2 Slit-grid method

A popular method at proton or ion LINACs is the slit-grid device, where the beam particles have a penetration depth below 1 cm as schematically depicted in Fig II.9.74. Here, the position x is fixed for one direction with a thin slit having an opening of typically 0.1 to 0.5 mm to filter out only a small fraction of the beam at a known location. The full beam is transmitted in the perpendicular direction to get a large signal. The angle x' is determined with a SEM-grid having a distance from the slit of 10 cm to 1 m depending on the ion velocity. In the field-free drift space, the trajectories of the particles, combined in a "beamlet", are straight lines [97, 102–104]. The angular distribution at the slit location gives the contribution to the emittance plot in the phase-space. The slit is then scanned through the beam to get all positions. The data must be normalized to a constant beam current as measured, e.g., by the beam charges hitting the slit. After finishing the full scan, the emittance is plotted, and the rms-value of the emittance ϵ_{rms} is calculated using the statistical moments as given in Eq. II.9.58 from the measured data. A fit with an elliptical shape is extracted from the data, and the Twiss parameters (Courant Snyder functions) can be calculated. An example is shown in Fig. II.9.75 for a low energy ion beam as a contour or three-dimensional plot. As depicted, the slit-grid method can determine more pathological phase-space distributions related to the direct determination of position and angular distribution; it is not restricted to Gaussian distributions. Close to an ion source, this happens often due to the large space-charge forces or

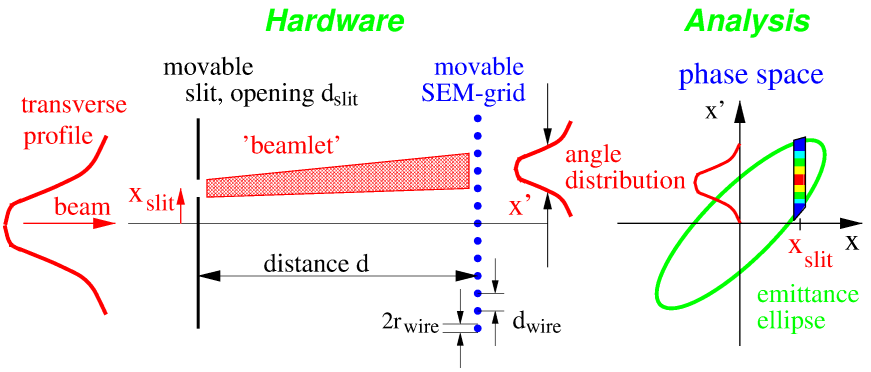

Fig. II.9.74: Scheme of a slit-grid emittance measurement device.

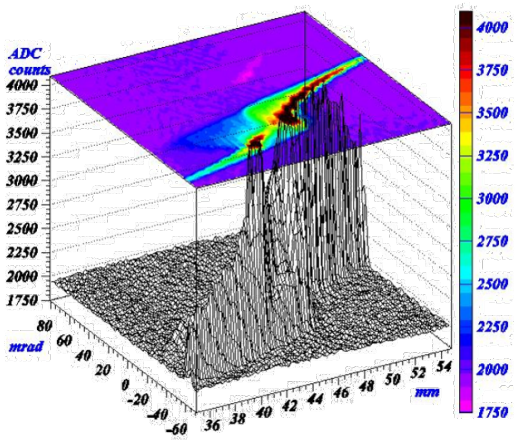

Fig. II.9.75: Emittance measurement using a slit-grid device with a low energy Ar^{4+} ion of 60 keV at the Sprial2 facility depicting a mountain and contour plot [105].

the large profile width, where aberrations of the magnets could be significant.

The resolution concerning the spatial coordinate Δx is limited by the slit width $\Delta x = d_{\text{slit}}$. The angular resolution $\Delta x'$, measured at a distance d, is given by the radius of the wire r_{wire} and the width of the slit resulting in $\Delta x' = (d_{\text{wire}} + 2r_{\text{wire}})/d$. The size of discrete elements in phase-space is given by $\Delta x \cdot \Delta x'$. This leads to a discretization error [106], particularly in the case of small beam sizes (focused beam setting) or small angle distributions (parallel beam setting). The resolution is improved by scanning the SEM-grid in steps lower than the distance of the wires d_{wire}, increasing the density of the discrete elements in the phase-space analysis. Such a case can lead to overlapping elements because their size $\Delta x \cdot \Delta x'$ stays constant. The same holds for a movement of the slit with a step size lower than the slit width. Further error contribution are discussed e.g. in Ref. [107].

II.9.4.3 Pepper-pot device

Using a slit-grid device, the slit and the SEM-grid have to be scanned through the beam, which takes up to several minutes per plane. In particular, for pulsed LINACs, only one step for the slit and the SEM-grid can be performed during a single pulse. Using a slit, the two transverse planes' determinations must be done separately. With a matrix of holes in a plate, such a measurement can be performed within one single beam pulse. Moreover, if the ion sources may have fluctuations from pulse to pulse, the emittance

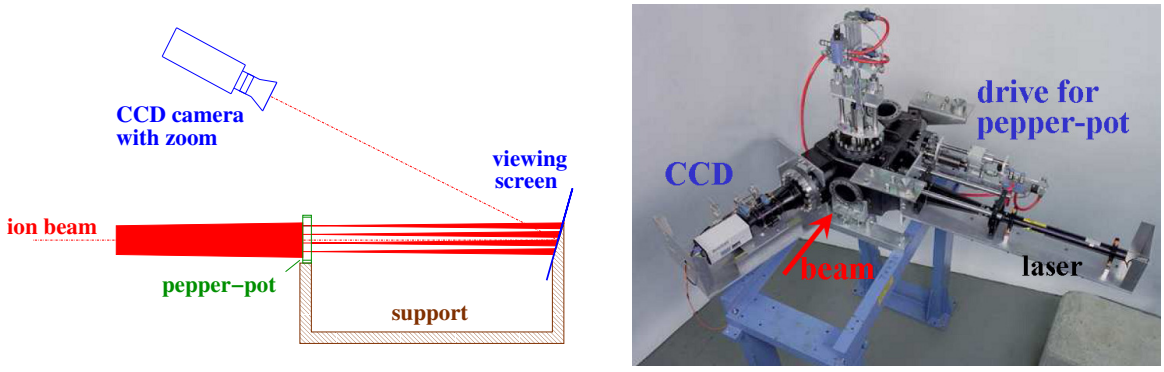

Fig. II.9.76: Left: Scheme of a pepper-pot emittance measurement device. Right: Photo of the hardware of a pepper-pot emittance device, including the laser for calibration (right side), the camera (left), the pneumatic drive for the pepper-pot-screen support (right back) and the drive for the movable mirror for the laser light.

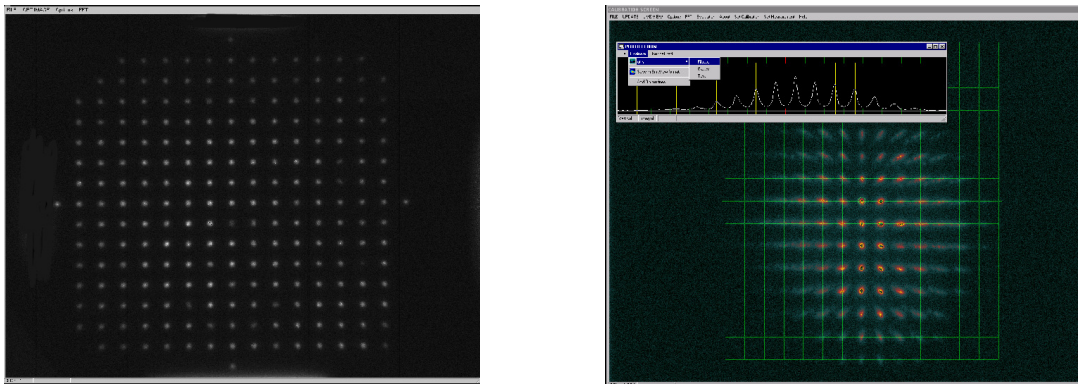

Fig. II.9.77: Left: Screen shots of the pepper-pot device with a laser beam for calibration. Right: A single-shot ion beam, including the projection of the horizontal plane with a high current Ar^{1+} ion beam at 1.4 MeV/u (bottom), from Ref. [110].

is measured for a single beam setting. This is performed with a pepper-pot device [108, 109], Fig. II.9.76 depicts both, a schematic drawing and a photo of an actual realization. As an example, the pepper-pot plate of the GSI device has holes with 0.1 mm diameter and 3 mm spacing. To record a calibration grid on the screen, a HeNe laser beam illuminates the pepper-pot, and the image is recorded with a CCD camera, as shown in Fig. II.9.77 (top). This calibration has to be performed before each beam measurement to prevent errors from probable misalignment. Relative to this, the position and size of the beamlets' spots created by the holes are determined; see Fig. II.9.77 (bottom). For the device used at GSI [108], the size of the pepper-pot is 50×50 mm^2 having 15×15 holes with 0.1 mm diameter. The distance between the pepper-pot and the viewing screen is 25 cm. The screen is made of pure Al_2O_3 due to the high beam intensities. Other materials can be used for the screen, e.g., the phosphor screens discussed in Section II.9.3.1.

The analysis of the emittance plot can be done by evaluating the individual spots' angular distributions; in this case, a possible coupling of the two transverse planes would be detectable. Alternatively, the data are projected to both transverse planes, as shown in the insert of Fig. II.9.77 (bottom). The analysis for the phase-space plot is similar to the slit-grid method. For an estimation of the resolution,

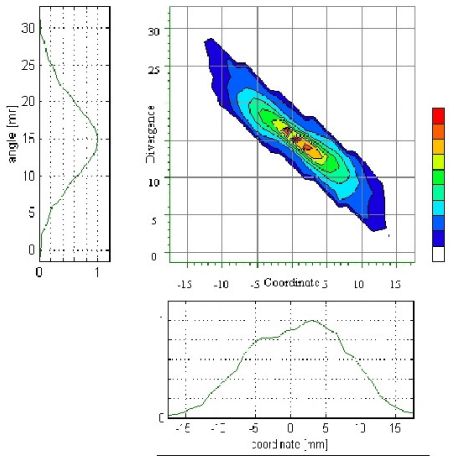

Fig. II.9.78: The horizontal emittance of the data above, including the projection to the axis.

the arguments are comparable to the one for the slit-grid device:

- A good spatial resolution is generated by the illumination of many holes spaced by separated small distances. However, one has to avoid overlapping the beamlets at the screen to distinguish the contributions of the individual holes.
- The diameter of the holes should be small, but in this case, the signal strength goes down.

In general, the resolution is inferior to the slit-grid, where the movable slit can have much smaller increments than the distance between the holes. Like for every destructive measurement, one has to evaluate the total beam power to prevent the melting of the uncooled pepper-pot aperture.

II.9.4.4 Quadrupole variation

The emittance can be determined from a series of profile measurements, either by changing the focusing strength of a quadrupole or by measuring at three or more positions along a transfer line, as schematically shown in Fig. II.9.79 and Fig. II.9.81. To derive the emittance from such a measurement, linear transformations are used. The described measurement is just the reverse of standard transport calculations with codes like MADX: Starting for a given emittance (size and orientation) at the input of a transport line, the beam envelope is calculated along the line. If the profile is measured, one calculates the emittance at the transfer line start location by using the same transformations in reverse (see below).

For a straight, non-dispersive transfer line, the transformation from a location s_0 to s_1 is given by the 2×2 transfer matrix $\mathbf{R}$ (assuming a de-coupling of the directional phase-spaces). Important examples for these matrices are:
Drift with length L:

$$\mathbf{R_{drift}} = \begin{pmatrix} 1 & L \\ 0 & 1 \end{pmatrix} \quad , \tag{II.9.62}$$

horizontal focusing quadrupole with quadrupole constant k and effective length l:

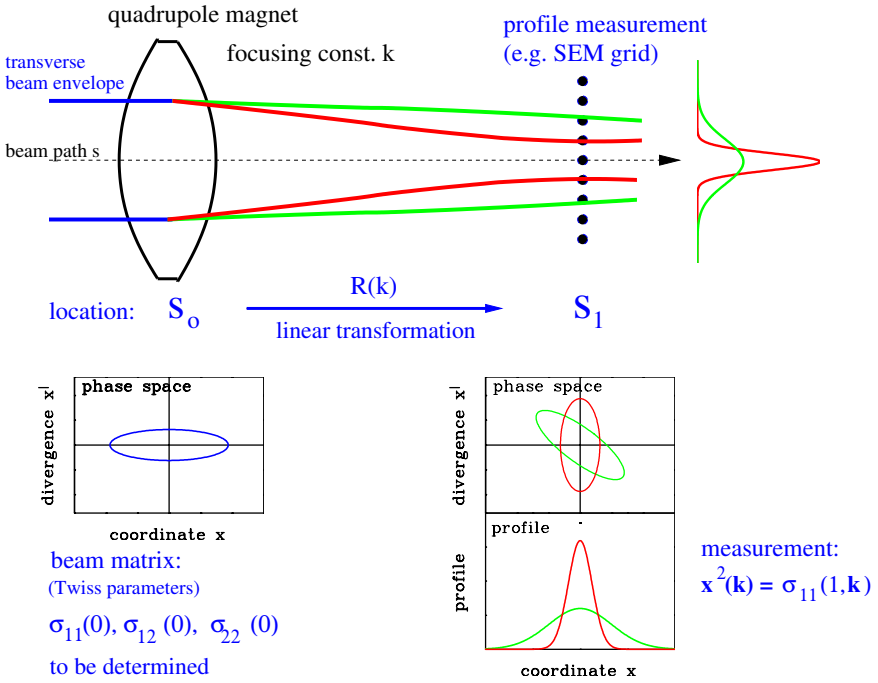

Fig. II.9.79: Variation of a quadrupole strength for the emittance determination at the location s_0.

$$\mathbf{R_{focus}} = \begin{pmatrix} \cos\sqrt{k}l & \frac{1}{\sqrt{k}}\sin\sqrt{k}l \\ -\sqrt{k}\sin\sqrt{k}l & \cos\sqrt{k}l \end{pmatrix} \quad , \tag{II.9.63}$$

horizontal de-focusing quadrupole with quadrupole constant k and effective length l:

$$\mathbf{R_{defocus}} = \begin{pmatrix} \cosh\sqrt{k}l & \frac{1}{\sqrt{k}}\sinh\sqrt{k}l \\ \sqrt{k}\sinh\sqrt{k}l & \cosh\sqrt{k}l \end{pmatrix} \quad . \tag{II.9.64}$$

The quadrupole constant $k = |g|/(B\rho)_0$ is given by the ratio of the field gradient $g = B_{\text{pole}}/a$, with B_{pole} is the field at the pole and a the aperture, and the magnetic rigidity $(B\rho)_0$ within the dipoles of bending radius ρ.

Determining the emittance at the position s_0 is equivalent to evaluating the beam matrix $\boldsymbol{\sigma}$ at this position. The beam matrix transforms to a second location s_1 with the help of the product of transfer matrices for the individual elements $\mathbf{R} = \prod \mathbf{R_{elements}}$ from the quadrupole to the profile measurement location via

$$\boldsymbol{\sigma}(1) = \mathbf{R} \cdot \boldsymbol{\sigma}(0) \cdot \mathbf{R^T} \quad . \tag{II.9.65}$$

The beam width $x_{rms}(1)$ is measured at s_1 and the equation for the element $\sigma_{11}(1)$ is given by

$$x^2_{rms}(1) \equiv \sigma_{11}(1) = R^2_{11}\sigma_{11}(0) + 2R_{11}R_{12}\sigma_{12}(0) + R^2_{12}\sigma_{22}(0) \quad . \tag{II.9.66}$$

This is a linear equation for the unknown three beam matrix elements $\sigma_{ij}(0)$ at location s_0, in Fig. II.9.79 in front of the focusing quadrupole magnet.

To get a solution, we need at least three different settings of the quadrupole strength k_i, and, hence, different transfer matrices $\mathbf{R}(k_i)$ leading to three different readings of the profile width, as depicted

in Fig. II.9.79. Assuming $i = 1, 2...n$ different settings of the quadrupole strength $k_1, k_2...k_n$ and n measurements of the beam width $x^2_{rms}(1, k_i) \equiv \sigma_{11}(1, k_i)$ a redundant system of linear equations is obtained in the form

$$\begin{aligned}
\sigma_{11}(1,k_1) &= R^2_{11}(k_1)\cdot\sigma_{11}(0) + 2R_{11}(k_1)R_{12}(k_1)\cdot\sigma_{12}(0) + R^2_{12}(k_1)\cdot\sigma_{22}(0) \quad \text{focusing } k_1 \\
\sigma_{11}(1,k_2) &= R^2_{11}(k_2)\cdot\sigma_{11}(0) + 2R_{11}(k_2)R_{12}(k_2)\cdot\sigma_{12}(0) + R^2_{12}(k_2)\cdot\sigma_{22}(0) \quad \text{focusing } k_2 \\
&\vdots \\
\sigma_{11}(1,k_n) &= R^2_{11}(k_n)\cdot\sigma_{11}(0) + 2R_{11}(k_n)R_{12}(k_n)\cdot\sigma_{12}(0) + R^2_{12}(k_n)\cdot\sigma_{22}(0) \quad \text{foc. } k_n
\end{aligned} \tag{II.9.67}$$

The solution of this system are the values of the beam matrix $\sigma_{ij}(0)$ (or equivalently the Twiss parameters) at the location s_0, the entrance of the quadrupole magnet. With these values, the size and orientation of the phase-space ellipse are fixed. For three measurements (k_1, k_2, k_3), a unique solution can be obtained, but an error estimation cannot be evaluated. Therefore, more than three measurements must be performed, leading to a redundant system of linear equations. The solution is reached by a least-square fit to the best parameters of $\sigma_{ij}(0)$ or by solving the linear regression problem; the mathematical method is referred to as normal equations. Both algorithms are described in textbooks of Linear Algebra or Numerical Mathematics.

Instead of solving the redundant system of linear equations, one can start from the parabola fit of the beam size squared as a function of the quadrupole strength, as shown in Fig. II.9.80. Most frequently, the transfer line comprises a quadrupole followed by a drift toward the profile measurement location. A quadratic dependence is observed for the following reason: Assuming a thin lens approximation with a focal length f of the quadrupole action, one can write the transfer matrix as:

$$\mathbf{R_{focus}} = \begin{pmatrix} 1 & 0 \\ -1/f & 1 \end{pmatrix} \equiv \begin{pmatrix} 1 & 0 \\ K & 1 \end{pmatrix} \quad . \tag{II.9.68}$$

After a drift of length L, the transfer matrix of the transfer line is

$$\mathbf{R} = \mathbf{R_{drift}} \cdot \mathbf{R_{focus}} = \begin{pmatrix} 1+LK & L \\ K & 1 \end{pmatrix}. \tag{II.9.69}$$

Inserting this matrix into Eq. II.9.65 for the transformation of the beam matrix $\boldsymbol{\sigma}(1) = \mathbf{R}\cdot\boldsymbol{\sigma}(0)\cdot\mathbf{R}^T$, the measured beam matrix element $\sigma_{11}(1) = x^2_{rms}(1)$ can be written as

$$\sigma_{11}(1) = L^2\sigma_{11}(0)\cdot K^2 + 2\left(L\sigma_{11}(0) + L^2\sigma_{12}(0)\right)\cdot K + \sigma_{11}(0) + 2L\sigma_{12}(0) + L^2\sigma_{22}(0) \quad . \tag{II.9.70}$$

This is the expected quadratic function in the quadrupole gradient K. From the beam width measurement for various quadrupole settings, a parabola fit is performed for Fig. II.9.80 with the fit parameters a, b and c (this parametrization is chosen to yield a simple expression for the absolute value of the emittance as shown for Eq. II.9.74 below)

$$\sigma_{11}(K) = a\left(K-b\right)^2 + c = aK^2 - 2abK + ab^2 + c \quad . \tag{II.9.71}$$

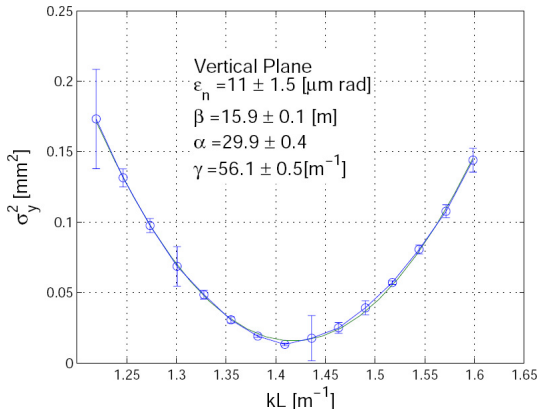

Fig. II.9.80: Profile width (one standard deviation) determined with a YAG:Ce screen at the Elettra electron LINAC for a quadrupole variation and the parabolic fit, from [111].

A comparison of the coefficients of the last two Eqs. II.9.70 and II.9.71 yields

$$\begin{aligned} a &= L^2\sigma_{11}(0) \\ -ab &= L\sigma_{11}(0) + L^2\sigma_{12}(0) \\ ab^2 + c &= \sigma_{11}(0) + 2L\sigma_{12}(0) + L^2\sigma_{22}(0) \quad . \end{aligned} \tag{II.9.72}$$

These linear equations can finally be solved, and the result is the requested matrix elements at the entrance of the optical system:

$$\begin{aligned} \sigma_{11}(0) &= \frac{a}{L^2} \\ \sigma_{12}(0) &= -\frac{a}{L^2}\left(\frac{1}{L} + b\right) \\ \sigma_{22}(0) &= \frac{1}{L^2}\left(ab^2 + c + \frac{2ab}{L} + \frac{a}{L^2}\right) \quad . \end{aligned} \tag{II.9.73}$$

The absolute value of the emittance is calculated from these fit parameters via

$$\epsilon = \sqrt{\det \boldsymbol{\sigma}(0)} = \sqrt{\sigma_{11}(0)\sigma_{22}(0) - \sigma_{12}^2(0)} = \frac{\sqrt{ac}}{L^2} \quad . \tag{II.9.74}$$

Be aware that the fit parameters have some units as given in Eq. II.9.71.

An example is shown in Fig. II.9.80 performed at the electron LINAC at ELETTRA for a beam with 107 MeV using a YAG:Ce scintillation screen for profile determination. To achieve a small error for the emittance determination, it is recommended to pass a beam waist by the quadrupole variation. Only in this case, a parabola can be fitted through the profile data with sufficient accuracy.

The above discussion assumes that the method is performed at sections where no dispersion is present. The dispersion function $D(s)$ gives rise to an additional contribution to the beam width Δx by the momentum deviation Δp of the particles with respect to the mean momentum p as $\Delta x = D \cdot \Delta p/p$ as discussed for Eq. II.9.61. To avoid the measurement of the lattice function $D(s)$ and a longitudinal momentum spread determination, the transverse emittance measurement's location within the transfer

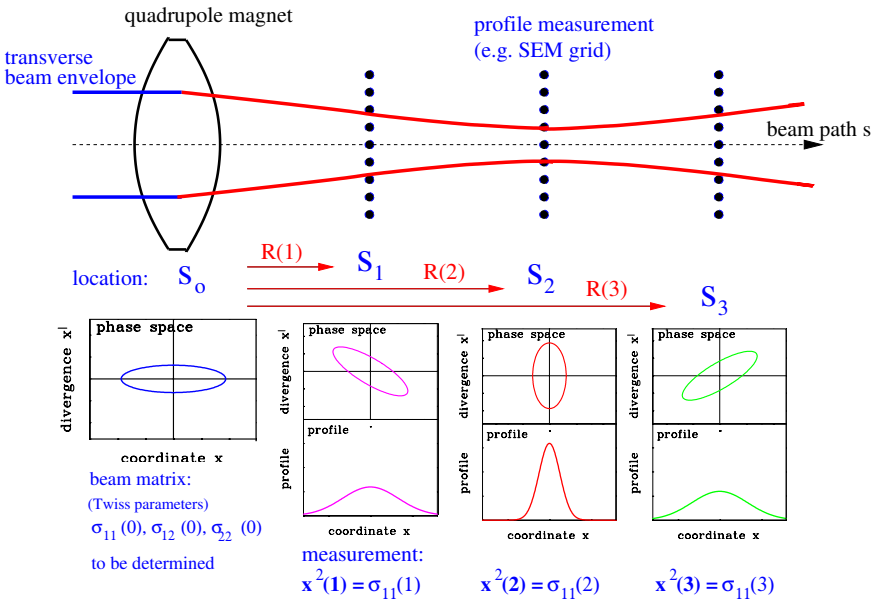

Fig. II.9.81: Scheme for the emittance determination at a transfer line using a profile measurement at three locations.

line should be dispersion free.

The described method is based on linear transformations and conservation of the emittance during the manipulation by the quadrupole. Moreover, an elliptical shape of the emittance is assumed. Depending on the general beam properties, this is a reasonable assumption as long as non-linear effects, such as aberration of magnets by higher-order field contributions or space-charge forces, are low. If the investigations are done with intense beams, an emittance blow-up may occur, depending on the particle density. However, the size is to be changed, and even a waist has to be created. For high intensity beams, self-consistent, iterative algorithms must be applied to estimate the emittance at the quadrupole entrance; see, e.g. Refs. [112, 113]. Using tomographic reconstruction, arbitrary phase-space distributions can be determined from the profiles obtained by the quadrupole variation. Tomography was developed for medical imaging, where a 3-dimensional object is reconstructed from a series of 2-dimensional projects obtained by X-ray or nuclear-magnetic observation. In analogy for the quadrupole scan, the 2-dimensional phase-space distribution is deformed in a well-controlled manner and the 1-dimensional projects to the transverse profile axis is measured. From those profile measurements, the original phase-space distribution is reconstructed; examples are described in Refs. [114–116]. Recently, machine learning algorithms are applied for reconstruction to recues the computing effort and artefact reduction [117].

II.9.4.5 "Three grid" method

Instead of varying a quadrupole, the beam profiles at different locations along a transfer line can be measured with fixed magnet settings. This method is sometimes applied at long transfer lines, where the profile monitors are installed anyhow. There is no general restriction to the involved optics as long as they can be described by linear optics, e.g., dipoles can be included with their known transfer matrix $\mathbf{R}_{\mathbf{dipole}}$ and the related width enlargement as given by Eq. II.9.61.

A profile measurement at least at three or more locations is required, see Fig. II.9.81, for the

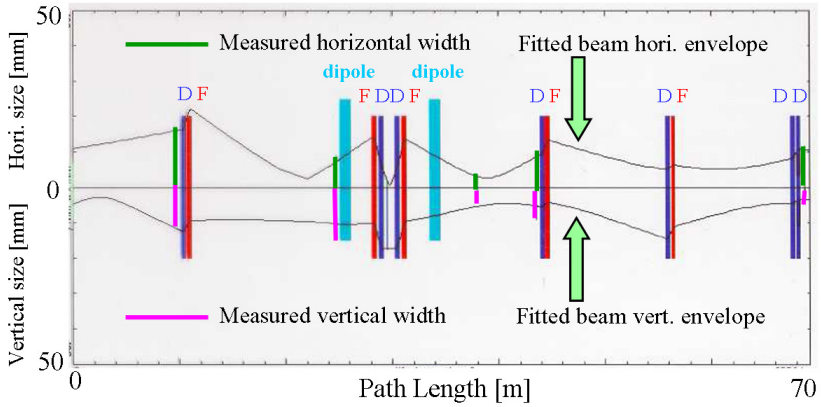

Fig. II.9.82: Determination of the beam envelope by linear transformations in horizontal (top curve) and vertical (bottom curve) direction using different profile measurements. The width of the profile is shown as green lines, performed at a transfer line at GSI.

determination of the three statistical moments of the symmetric beam matrix $\boldsymbol{\sigma}$ assuming a separation of the horizontal, vertical and longitudinal phase-space. However, more measurements are required to enable an error estimation. To achieve good accuracy, one profile monitor should be close to a beam waist. For the determination of the beam matrix elements $\sigma_{ij}(0)$ at the transfer line entrance s_0, the profile widths, and therefore the beam matrix elements $\sigma_{11}(n)$, are determined at n different locations s_n. A system of redundant linear equations for the entrance emittance $\sigma_{ij}(0)$ is given by

$$\begin{aligned}
\sigma_{11}(1) &= R_{11}^2(1)\cdot\sigma_{11}(0) + 2R_{11}(1)R_{12}(1)\cdot\sigma_{12}(0) + R_{12}^2(1)\cdot\sigma_{22}(0) \qquad \mathbf{R}(1): s_0 \to s_1 \\
\sigma_{11}(2) &= R_{11}^2(2)\cdot\sigma_{11}(0) + 2R_{11}(2)R_{12}(2)\cdot\sigma_{12}(0) + R_{12}^2(2)\cdot\sigma_{22}(0) \qquad \mathbf{R}(2): s_0 \to s_2 \\
&\vdots \\
\sigma_{11}(n) &= R_{11}^2(n)\cdot\sigma_{11}(0) + 2R_{11}(n)R_{12}(n)\cdot\sigma_{12}(0) + R_{12}^2(n)\cdot\sigma_{22}(0) \quad \mathbf{R}(n): s_0 \to s_n \quad \text{(II.9.75)}
\end{aligned}$$

This is a comparable formula as derived for the quadrupole variation (Eq. II.9.67), but the transfer matrix $\mathbf{R}(i)$ describes now the beam transport from the starting point of the transfer line s_0 to the location of the individual measurements s_i. The algorithm of the emittance calculation (least-square fit or normal equation algorithm) is the same as for the quadrupole scan. Such a measurement is shown in Fig. II.9.82, compared to the fitted beam envelope, to visualize possible errors. In practice, the parameters of the entrance ellipse are fitted to match the measured profiles using a linear optics code (e.g. MADX) for this transfer line.

To get a reliable measurement, the transfer matrix $\mathbf{R}(n)$ should adequately describe the action by optical elements on the beam. In particular, one has to ensure that the beam centre passes the quadrupoles on their magnetic axes, i.e. no "steering" of the quadrupoles is present. As discussed before, no emittance growth, e.g., due to space-charge forces, is assumed here.

The algorithm is not limited to straight transport lines. If a dipole magnet is present in addition, one has to take its bending and focusing action on the beam into account. This results in a dispersion $D(s)$, i.e., a coupling between the momentum spread $\delta = \Delta p/p$ and the transverse beam size with $\Delta x = D \cdot \Delta p/p$. For this case, the transport matrix contains an additional matrix element R_{13}. Moreover, a dipole

influences the angular distribution called angular dispersion D', resulting in an additional matrix element R_{23}. The single particle trajectory is now described by a 3-dimensional vector $\vec{x} = (x, x', \Delta p/p)^t$ and the transfer matrix $\mathbf{R}$ is now a 3×3 matrix. The effect of momentum spread must be included in the symmetric beam matrix $\boldsymbol{\sigma}$ with three additional elements, the covariances $\sigma_{13} = \langle x, \Delta p/p \rangle$, $\sigma_{23} = \langle x', \Delta p/p \rangle$ and momentum variance $\sigma_{33} = \langle \Delta p/p^2 \rangle$ as a symmetric 3×3 matrix as six independent elements. To determine the values of these beam matrix elements, at least 6 profile measurements have to be done, resulting in at least 6 equations in the system of linear equations for $\sigma_{ij}(0)$ in Eqs. II.9.67 and II.9.75.

II.9.5 Beam position monitors for bunched beams

The central transverse position of the beam as well as the longitudinal bunch shape, is very frequently determined with pick-up plates, refers to as electrodes. The monitor's principle is to measure the image current on an insulated metal electrode as induced by the electro-magnetic field of the beam particles, see Fig. II.9.83. Because the electric field of a bunched beam is time-dependent, a time-varying signal is induced on the electrode. Further signal processing is based on radio-frequency (RF) technologies to determine the beam's horizontal and vertical centre-of-mass. Only time-varying signals can be detected by this principle as generated by a bunched beam. The signal shape, as well as the most frequently used types of pick-ups, are described in this section. The application is the determination of the beam position, i.e., the transverse centre-of-mass of the bunches. To this end, four pick-up electrodes are installed, and the difference of opposite electrode signals yields the centre-of-mass in both transverse planes. The arrangement of electrodes is called **P**ick-**U**p **PU** the corresponding installation for the centre-of-mass determination is referred to as **B**eam **P**osition **M**onitor **BPM**. In all cases, the instrument is non-invasive as the image current of the moving charges is measured. A review of general BPM properties and BPM types is given in Refs. [118] to [122]. In a synchrotron, the closed orbit is determined by the BPMs. Advanced measurements based on position information are discussed at the end of this section, namely the determination of tune, chromaticity and lattice functions of a synchrotron.

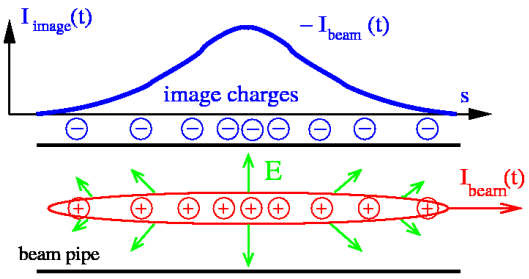

Fig. II.9.83: The beam current induces a wall current of the same magnitude and time structure but reversed polarity.

II.9.5.1 Signal treatment of capacitive BPMs

As shown in Fig. II.9.84, a capacitive pick-up consists of four insulated electrodes or one ring mounted inside the vacuum chamber. Here the induced image charge of the beam is coupled via an amplifier for further processing. The electrode at a distance a from the beam centre has an area of A and a length in longitudinal direction of l. The current I_{im} originated by the image charge Q_{im} as a function of time t is

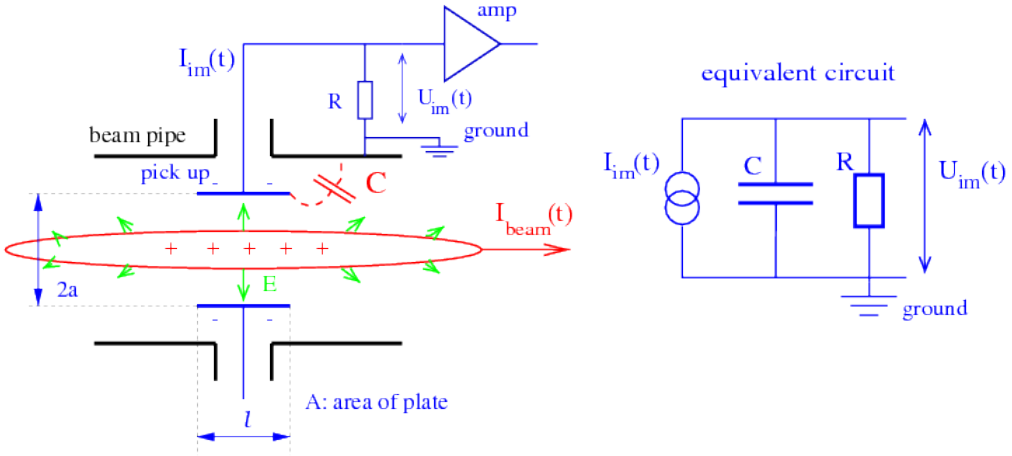

Fig. II.9.84: Scheme of two pick-up electrodes and its equivalent circuit.

the given by

$$I_{\mathrm{im}}(t) = \frac{dQ_{\mathrm{im}}}{dt} = -\frac{A}{2\pi a l} \cdot \frac{dQ_{\mathrm{beam}}(t)}{dt} \quad . \tag{II.9.76}$$

For a beam with velocity β the derivative with respect to time of the beam charge $dQ_{\mathrm{beam}}(t)/dt$ can be reformulated as

$$\frac{dQ_{\mathrm{beam}}(t)}{dt} = \frac{l}{\beta c}\frac{dI_{\mathrm{beam}}}{dt} = -\frac{l}{\beta c} \cdot i\omega I_{\mathrm{beam}}(\omega) \quad , \tag{II.9.77}$$

where the beam current is expressed in frequency-domain using the angular frequency ω as $I_{\mathrm{beam}} = I_0 e^{-i\omega t}$ [2]. Combining Eq. II.9.76 and Eq. II.9.77 the image current can be written as

$$I_{\mathrm{im}}(t) = \frac{1}{\beta c} \cdot \frac{A}{2\pi a} \cdot i\omega I_{\mathrm{beam}} \quad . \tag{II.9.78}$$

As the signal, we use the voltage drop at a resistor R

$$U_{\mathrm{im}}(\omega) = R \cdot I_{\mathrm{im}}(\omega) \equiv Z_t(\omega, \beta) \cdot I_{\mathrm{beam}}(\omega) \quad . \tag{II.9.79}$$

For all types of pick-up electrodes, the general quantity of longitudinal transfer impedance $Z_t(\omega, \beta)$ is defined by Eq. II.9.79 in the frequency-domain according to Ohm's law. For a more detailed discussion of important relations see Refs. [118] to [122]. The transfer impedance describes the effect of the beam on the pick-up voltage, and it is dependent on frequency, the velocity of the beam particles β, and geometrical factors. It is beneficial to use of a description in frequency-domain , where the independent variable is the angular frequency ω. Generally, time- and frequency-domain descriptions are connected by Fourier transformation. Appendix II.9.11 compiles the relevant theorems for the Fourier transformation. A mathematically more stringent derivation of the relevant equations for capacitive BPMs is given in Sections II.9.5.3 and II.9.5.4 below.

The pick-up electrode in Fig. II.9.84 has a certain capacitance C, which is determined by the distance between the electrode and with respect to the beam pipe as well as a capacitance contributed by the cable between the plate and the amplifier input. This amplifier has an input resistor R. Using a

[2] More precisely: The derivative of a function df/dt can be expressed as a multiplication of its Fourier transformation $\tilde{f}(\omega)$ with $-i\omega$, see Appendix II.9.11 with Eq. II.9.165 for the mathematical basis and Section II.9.5.3 for more stringent derivation.

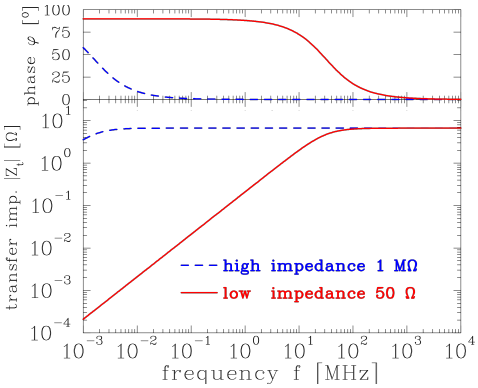

Fig. II.9.85: Absolute value and phase of the transfer impedance for a $l = 10$ cm long cylindrical pick-up with a capacitance of $C = 100$ pF and an ion velocity of $\beta = 50\%$ for high (1 MΩ) and low (50 Ω) input impedance of the amplifier.

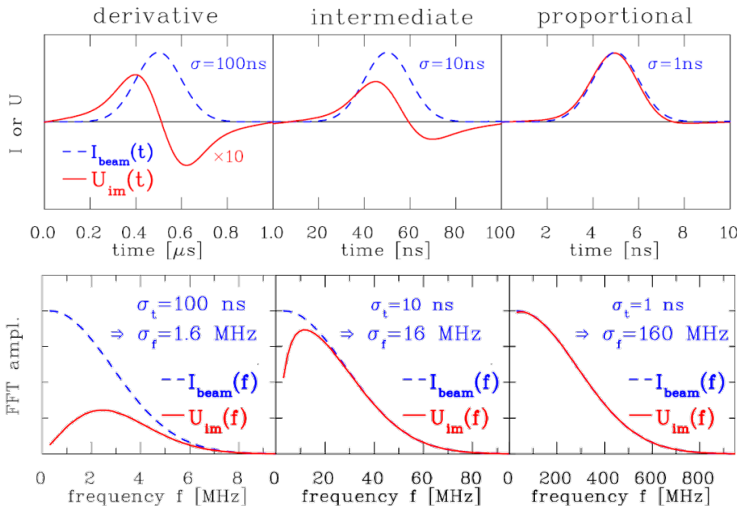

Fig. II.9.86: Simulation of the image voltage $U_{\rm im}(t)$ for the values of the pick-up used in Fig. II.9.85 terminated with $R = 50\ \Omega$ for three different bunch lengths of Gaussian distribution with σ of 100 ns, 10 ns and 1 ns, respectively. The cut-off frequency $f_{\rm cut} = 32$ MHz. Note the different time scales. (The bunch length in the last case is artificially short for a proton synchrotron.) The shape of $U_{\rm im}$ is generated by the following steps: Given $I_{\rm beam}(t) \rightarrow$ FFT yields $\tilde{I}_{\rm beam}(\omega) \rightarrow$ multiplying by $Z_t(\omega)$ yields $\tilde{U}_{\rm im}(\omega) = Z_t(\omega) \cdot \tilde{I}_{\rm beam}(\omega) \rightarrow$ inverse FFT yields $U_{\rm im}(t)$. The Fourier transformations are shown in the lower plots. A Gaussian function in time-domain of width of σ_t has a Fourier transformation described by a Gaussian function of width $\sigma_f = 1/(2\pi\sigma_t)$ centred at $f = 0$.

current source to model the beam and the parallel connection of the equivalent circuit elements, we can write the impedance Z in terms of an equation of complex numbers as

$$\frac{1}{Z} = \frac{1}{R} + i\omega C \quad \Longleftrightarrow \quad Z = \frac{R}{1 + i\omega RC} \quad . \tag{II.9.80}$$

Inserting this impedance in Ohm's law as given in Eq. II.9.79 and using the expression for the image current of Eq. II.9.78, the measurable voltage of the pick-up electrode is then given by

$$U_{\rm im} = \frac{R}{1 + i\omega RC} \cdot I_{\rm im} = \frac{1}{\beta c} \cdot \frac{1}{C} \cdot \frac{A}{2\pi a} \cdot \frac{i\omega RC}{1 + i\omega RC} \cdot I_{\rm beam} \equiv Z_t(\omega, \beta) \cdot I_{\rm beam} \quad , \tag{II.9.81}$$

which results in general transfer impedance

$$Z_t(\omega,\beta) = \frac{1}{\beta c}\cdot\frac{1}{C}\cdot\frac{A}{2\pi a}\cdot\frac{i\omega RC}{1+i\omega RC} \quad . \tag{II.9.82}$$

This is a description of a first-order high-pass filter for the transfer impedance $Z_t(\omega,\beta)$ with a cut-off frequency $f_{\rm cut} = \omega_{\rm cut}/2\pi = (2\pi RC)^{-1}$. For the case of a linear-cut BPMs used at proton synchrotrons (see below), a typical value of the capacitance is $C = 100$ pF with a length of $l = 10$ cm. The high-pass characteristic is shown in Fig. II.9.85 for a 50 Ω and a high impedance 1 MΩ amplifier input resistor. In the figure the absolute value

$$|Z_t| = \frac{1}{\beta c}\cdot\frac{1}{C}\cdot\frac{A}{2\pi a}\cdot\frac{\omega/\omega_{\rm cut}}{\sqrt{1+\omega^2/\omega_{\rm cut}^2}} \quad \text{and the phase relation} \quad \varphi = \arctan\left(\omega_{\rm cut}/\omega\right) \tag{II.9.83}$$

is shown. A BPM must match the interesting frequency range, which is determined by the accelerating frequency and the bunch length. In a typical proton synchrotron typical values of the accelerating frequency are in the 1–10 MHz range, while for LINACs and electron synchrotrons, typically 100 MHz to 3 GHz are applied.

We can distinguish two extreme cases for the transfer impedance in Eq. II.9.82:

– **High frequency range** $\omega \gg \omega_{\rm cut}$**:** Here the transfer impedance converges to

$$Z_t \propto \frac{i\omega/\omega_{\rm cut}}{1+i\omega/\omega_{\rm cut}} \longrightarrow 1. \tag{II.9.84}$$

The resulting voltage drop at R is

$$U_{\rm im}(t) = \frac{1}{\beta cC}\cdot\frac{A}{2\pi a}\cdot I_{\rm beam}(t). \tag{II.9.85}$$

The pick-up signal is a direct image of the bunch time structure with no phase shift, i.e. $\varphi = 0$. To get a low cut-off frequency $\omega_{\rm cut} = 1/RC$, high impedance input resistors are used to monitor long bunches, e.g. in a proton synchrotron. Figure II.9.86 (right) shows the calculated signal shape. Note that in the figure a 50 Ω termination is considered, leading to a large value of the cut-off frequency $f_{\rm cut} = 32$ MHz. In the application of a proton synchrotron, high impedance ($\sim$ 1 MΩ) termination yields a much lower value for the cut-off frequency; for assumed resistivity and capacitance of $f_{\rm cut} = 10$ kHz. The transfer impedance for this case as shown in Fig. II.9.85 where the condition corresponds to the enlarged flat part of the depicted transfer impedance. A typical signal using high-impedance termination is depicted in Fig. II.9.87.

– **Low frequency range** $\omega \ll \omega_{\rm cut}$**:** The transfer impedance is for this case

$$Z_t \propto \frac{i\omega/\omega_{\rm cut}}{1+i\omega/\omega_{\rm cut}} \longrightarrow i\frac{\omega}{\omega_{\rm cut}} \quad . \tag{II.9.86}$$

The voltage across R is in this case

$$U_{\rm im}(t) = \frac{R}{\beta c}\cdot\frac{A}{2\pi a}\cdot i\omega I_{\rm beam} = -\frac{R}{\beta c}\cdot\frac{A}{2\pi a}\cdot\frac{dI_{\rm beam}}{dt} \tag{II.9.87}$$

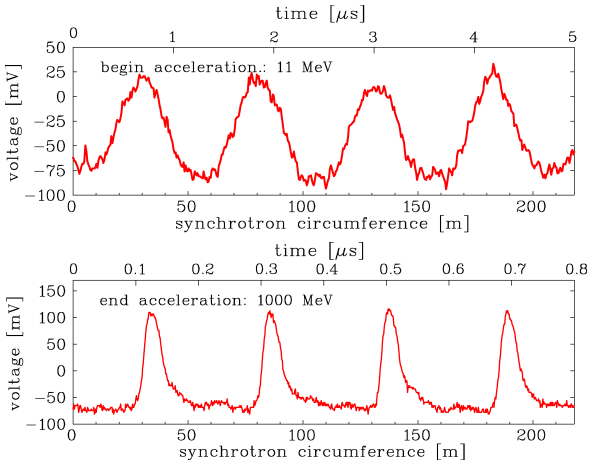

Fig. II.9.87: Bunch signals from a linear-cut BPM for 1 MΩ termination as installed at the GSI ion synchrotron. The upper curve shows the bunches of the proton beam along the synchrotron circumference at the begin of the acceleration and the lower curve after reaching the final energy. Note the different time scales on top of the plots.

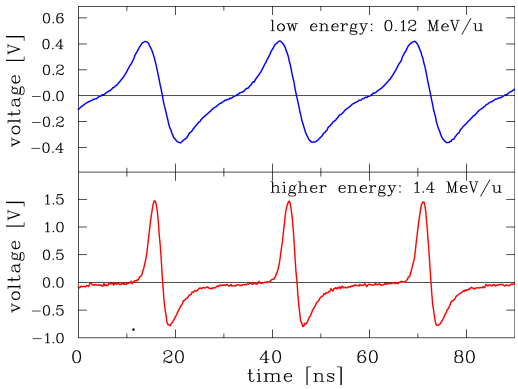

Fig. II.9.88: Bunch signal from a capacitive BPM with 0.12 MeV/u (top) and 1.4 MeV/u (bottom) energy at the GSI ion LINAC. The derivative behaviour is caused by 50 Ω termination to achieve a large amplifier bandwidth. The accelerating frequency is 36 MHz.

using the frequency-domain relation Eq. II.9.165 to substitute the quantity $i\omega I_{\mathrm{beam}}$ with the time derivative $\frac{dI_{\mathrm{beam}}}{dt}$. The measured voltage is proportional to the derivative of the beam current. This can also be seen from the phase relation of the high-pass filter in Fig. II.9.85, where a phase shift of 90° corresponds to a derivative. The signal is bipolar, as shown in Fig. II.9.86 (left). A measurement from the GSI-LINAC is shown in Fig. II.9.88, which fulfils the condition above.

The signal at the amplifier output depends on the frequency range compared to the cut-off frequency. Of course, the bunches are not pure sine waves, and, hence, a mixture of proportional and derivative components contribute to the signal shape in time-domina as presented in Fig. II.9.86 (middle).

With respect to the different limits of the transfer impedance, two important applications are discussed in the following:

– **Range $\omega \gg \omega_{\mathrm{cut}}$ realized by a *low* ω_{cut} due to high impedance:**
In a proton or ion synchrotron, a low frequency is applied for the acceleration in the range of $f_{\mathrm{acc}} = 1$–10 MHz, resulting in bunches of several meters length. In these circular accelerators,

large apertures are necessary of typically $a = 10$ cm lowering the transfer impedance due to $Z_t \propto 1/a$. To achieve a larger sensitivity, the length of the pick-up electrode in beam direction is increased, typically $l \sim 10$ cm due to $Z_t \propto l$. Note that the electrode length is still much shorter than the bunch length. To have a flat sensitivity curve, i.e., a large bandwidth, a low $\omega_{\text{cut}} = 1/RC$ is used by feeding the signal into a high impedance FET transistor as the first stage of the amplifier. A bandwidth of the amplifier circuit of 100 MHz can be reached, but it is difficult to build them with a larger bandwidth. To prevent signal degeneration due to the limited amplifier bandwidth, the application of high-impedance amplifiers is restricted to proton or ion synchrotrons with less than $\sim$ 10 MHz acceleration frequency. Observing the contribution in the bunch spectrum up to the tenth harmonic of the acceleration frequency is sufficient for most applications. As stated above and shown in Fig. II.9.87, a direct image of the bunch is seen in this case.

– **Range $\omega \ll \omega_{\text{cut}}$ realized by a high ω_{cut} due to 50 Ω impedance:**
At proton LINACs and all electron accelerators, the bunches are short, typically in the mm range, due to the higher accelerating frequencies of $f_{\text{acc}} = 100$ MHz to 3 GHz. Firstly, one does not gain signal strength by making the length l larger. Secondly, a 50 Ω termination is used to prevent reflections and to get smooth signal processing with a large bandwidth of up to several GHz. The short l, and, correspondingly, lower capacitance C, and the $R = 50$ Ω lead to a high ω_{cut}. The analog signal comprises the derivative of the bunches as depicted in Fig. II.9.88.

The preceding discussion does not take into account the effect of the frequency response of the associated cables, amplifiers and filters; see Refs. [119, 123] for a more detailed discussion.

II.9.5.2 Signal treatment for a train of bunches

In the previous section, the transfer impedance Z_t was discussed for a single bunch passage, which might be realized at transfer lines between synchrotrons. But most other accelerators deliver a train of bunches separated by the time $t_{\text{acc}} = 1/f_{\text{acc}}$ as given by the acceleration frequency f_{acc}. In Appendix II.9.11 and Eq. II.9.173 the mathematical basis for such a case is briefly discussed. There it is shown that the frequency spectrum for periodic signals is composed of lines at all harmonics h of the acceleration frequency $h \cdot f_{\text{acc}}$ with an envelope function given by the single bunch frequency spectrum.

As an example of transfer impedance properties and the resulting image voltage $U_{\text{im}}(t)$, the application for a typical linear-cut BPM used at proton synchrotrons are discussed here with the same parameter set as in the previous section and the transfer impedance Z_t shown in Fig. II.9.85. The following values for the BPM geometry are used: The electrode length in beam direction is $l = 10$ cm; the distance between the plates and the vacuum pipe centre is $a = 5$ cm covering the full circumference; the capacitance is $C = 100$ pF. For this example, we assume a synchrotron, where the acceleration is performed by $f_{\text{acc}} = 1$ MHz acceleration frequency, a revolution time of 8 μs and an average beam current of 1 mA. The beam has a velocity of $\beta = 50$ % and a bunch duration of $\sigma_t = 66$ ns for a Gaussian distribution, corresponding to a bunch length of $\sigma_l = 10$ m, i.e. much longer than the BPM length of typically 10 cm. The following calculations use the concept of frequency-dependent transfer impedance $Z_t(\omega)$ and the calculation as depicted in Fig. II.9.86.

High impedance termination: In Fig. II.9.89, a high impedance termination of $R = 1$ MΩ is

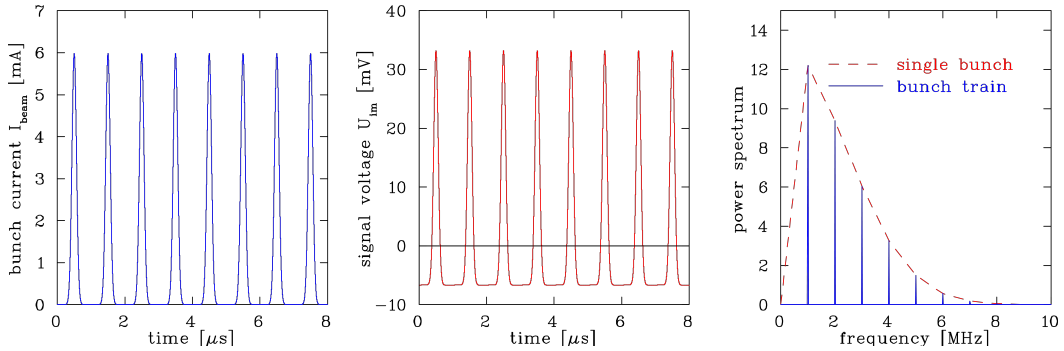

Fig. II.9.89: Signal simulation for 1 MΩ termination of a BPM; see text for further parameters. Left: beam current, middle: signal voltage, right: frequency spectrum of the signal voltage $\tilde{U}_{\mathrm{im}}(f)$.

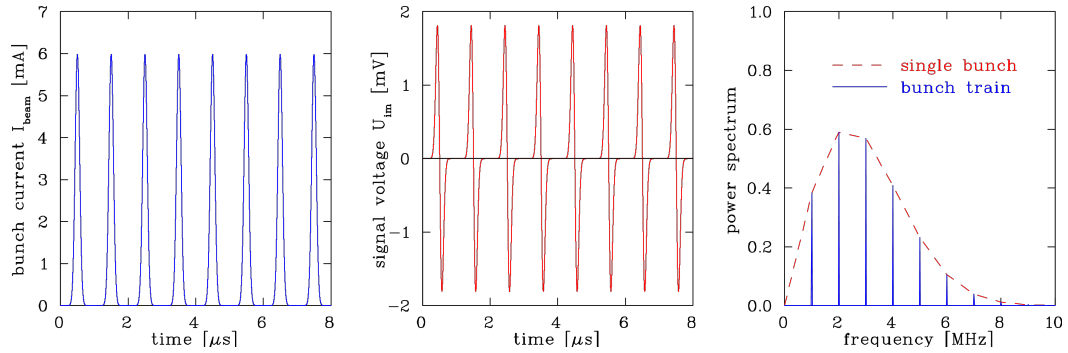

Fig. II.9.90: Signal simulation for 50 Ω termination of a BPM, see text for further parameters. Left: beam current, middle: signal voltage, right: frequency spectrum of the signal voltage $\tilde{U}_{\mathrm{im}}(f)$.

chosen for the BPM signals, leading to the high-pass cut-off frequency $f_{\mathrm{cut}} = (2\pi RC)^{-1} = 1.6$ kHz. The signal shape for $U_{\mathrm{im}}(t)$ is proportional to the beam current $I_{\mathrm{beam}}(t)$ with the proportional constant $Z_t \simeq 5\ \Omega$. However, the signal voltage shows some negative values, the so-called baseline shift. Due to the BPM's high-pass characteristics, any dc-signal part is disregarded by the BPM. Hence, the uni-polar beam current is transformed into an ac-signal with the condition that the integral over one turn is zero, i.e. the baseline is lowered to a value in a way to counteract the positive signal strength; note that the value of the baseline depends on the bunch length. The frequency spectrum of this periodic signal is composed of lines at the acceleration frequency and its harmonics. In other words, the signal power is concentrated in narrow frequency bands, separated by the acceleration frequency. It is common for the position evaluation to use only one of these frequency bands with high power density, e.g. by filtering or narrowband processing to suppress broadband noise contributions, see Section II.9.5.9. The envelope of these lines is given by the Fourier transformation of the single bunch current multiplied by the frequency-dependent transfer impedance. For the bunch duration σ_t of this example, the maximum frequency is about 10 times the acceleration frequency. For the layout of broadband electronics, it is reasonable to enlarge the bandwidth to at least the tenth harmonics to record the full signal shape and its total power spectrum, correspondingly. Using a Gaussian bunch shape, the relation of the Fourier transformation $\sigma_f = (2\pi\sigma_t)^{-1}$ can be used for the bandwidth estimation. Note that the frequency spectrum continues to higher values for non-Gaussian bunch shapes of the same σ_t .

50 Ω termination: It is quite common in RF-technologies to use 50 Ω terminations for signal

transmission. A related impedance for the BPM amplifier input seems to be adequate; the resulting signal shape is depicted in Fig. II.9.90. However, for the parameters of this example, a termination with a 50 Ω resistor leads to a signal of differentiating shape with a drop in voltage by a factor $\simeq 20$ as compared to the high impedance termination. This is caused by the $f_{\mathrm{cut}} = 32$ MHz BPM's high pass characteristic, which is larger than the relevant frequencies as given by the single bunch envelope, see Fig. II.9.90, right. This low signal amplitude is the reason why at proton synchrotrons a higher impedance termination is preferred. As for the high-impedance case, the frequency spectrum contains significant lines up to the tenth harmonics for typical beam parameters. Hence, the electronics bandwidth should be chosen accordingly for a broadband recording. Further examples of signal shapes are presented in Ref. [120].

II.9.5.3 Formal derivation of transfer impedance formula

In this section, a formal derivation of the frequency-domain transfer impedance as of Eq. II.9.82 is discussed using some formulas given in Appendix II.9.11; the related arguments are based on Ref. [124].

The time dependent image current $I_{\mathrm{im}}(t)$ can be written according to Eq. II.9.76 as

$$I_{\mathrm{im}}(t) \equiv \frac{dQ_{\mathrm{im}}}{dt} = -\frac{A}{2\pi a l} \cdot \frac{dQ_{\mathrm{beam}}(t)}{dt} \quad . \tag{II.9.88}$$

for the image charges Q_{im} and beam charge Q_{beam} at an electrode at a distance a from the beam center, an area of A and a length in longitudinal direction of l, see Fig. II.9.84. The Fourier transformation $\tilde{I}_{\mathrm{im}}(\omega)$ of the frequency dependent image current can be expressed using the differentiation law of Eq. II.9.165 as

$$\tilde{I}_{\mathrm{im}}(\omega) = -\frac{A}{2\pi a l} \cdot i\omega \tilde{Q}_{\mathrm{im}}(\omega) \quad . \tag{II.9.89}$$

The related beam charge $Q_{\mathrm{beam}}(t)$ is given by the beam current $I_{\mathrm{beam}}(t)$ in time-domain as a convolution with window function $W(t)$ as

$$Q_{\mathrm{beam}}(t) = \int_{-\infty}^{\infty} I_{\mathrm{beam}}(\tau) \cdot W(t-\tau)\, d\tau \quad . \tag{II.9.90}$$

This window function can be defined by the time t_0 the particles of velocity βc need to pass half of the electrode length $t_0 = \frac{1}{2} \cdot \frac{l}{\beta c}$ as

$$W(t) = \begin{cases} 1 \text{ if } & -t_0 \le t \le t_0 \\ 0 \text{ if } & |t| > t_0 \end{cases} \quad . \tag{II.9.91}$$

The Fourier transformation is given by the law of convolution Eq. II.9.168 and the Fourier transformation of a rectangular window as

$$\begin{aligned} \tilde{Q}_{\mathrm{beam}}(\omega) &= \tilde{I}_{\mathrm{beam}}(\omega) \cdot \tilde{W}(\omega) \\ &= \tilde{I}_{\mathrm{beam}}(\omega) \cdot 2\frac{\sin \omega t_0}{\omega} \end{aligned}$$

$$= \tilde{I}_{\text{beam}}(\omega) \cdot \frac{l}{\beta c} \cdot \frac{\sin \omega \frac{l}{2\beta c}}{\omega \frac{l}{2\beta c}} \tag{II.9.92}$$

with the insertion of the passage time t_0.

For bunches much longer than the pick-up electrode, the sinc-function (see Appendix II.9.11) can be approximated by $\text{sinc}(x) \equiv \frac{\sin x}{x} \approx 1$ for small $|x| \ll 1$. This yield for the frequency dependent beam charge

$$\tilde{Q}_{\text{beam}}(\omega) = \frac{l}{\beta c} \cdot \tilde{I}_{\text{beam}}(\omega) \ . \tag{II.9.93}$$

Inserting this relation in Eq. II.9.89 results in

$$\tilde{I}_{\text{im}}(\omega) = -\frac{A}{2\pi a} \cdot \frac{1}{\beta c} \cdot i\omega \tilde{I}_{\text{beam}}(\omega) \ . \tag{II.9.94}$$

As it is common to measure a voltage across a resistor for the equivalent circuit depicted in Fig. II.9.84, the impedance of the parallel RC-shunt given by Eq. II.9.80 has to be used, which yields with the previous equation the relation for the frequency dependent signal voltage

$$\begin{aligned} \tilde{U}_{\text{im}}(\omega) &= \frac{R}{1 + i\omega RC} \cdot \tilde{I}_{\text{im}}(\omega) \\ &= \frac{i\omega RC}{1 + i\omega RC} \cdot \frac{1}{\beta c} \cdot \frac{1}{C} \cdot \frac{A}{2\pi a} \cdot \tilde{I}_{\text{beam}}(\omega) \\ &\equiv Z_t(\omega, \beta) \cdot \tilde{I}_{\text{beam}}(\omega) \ . \end{aligned} \tag{II.9.95}$$

It is exactly the same formula as Eq. II.9.82, but now derived with a mathematically more stringent argumentation. The assumption that the bunches are much longer than the pick-up electrode is related to a "quasi-static" approach. It is valid at least for most proton synchtrotrons and proton LINACs.

II.9.5.4 Alternative derivation of the transfer impedance

This section concerns an alternative approach to derive the transfer impedance, which points more clearly to the capacitive coupling between the beam and the pick-up electrode as the transfer impedance Z_t of Eq. II.9.82 can be derived directly for the Gaussian Law and the property of the equivalent circuit for long bunches. This description acts as a physical basis of the previously depicted current source used for the description related to the equivalent circuit of Fig. II.9.84. There are only minor changes in the resulting equation; hence, this section acts as an alternative approach.

Assuming a cylindrical pick-up electrode of length l and radius a much shorter than the bunch length and a round beam of radius r_{beam}, then the electric field of the bunch has only a radial component $E_r(r)$ as depicted in Fig. II.9.91 (left). From the Gaussian Law $\oint \mathbf{E} \cdot d\mathbf{A} = \frac{1}{\epsilon_0} \int \rho \, dV$ for the electric field vector $\mathbf{E}$ generated by the charge density ρ within a volume V, the radial electric field $E_r(r)$ can be calculated between the beam edge r_{beam} and the pick-up electrode by integration over the surface vector $d\mathbf{A}$. For the geometry of Fig. II.9.91, the electric field at a radius r between the beam edge and the electrode for a cylinder of length l with a barrel surface of $A_b = 2\pi r l$ is

$$\oint \mathbf{E}_r(r) \cdot d\mathbf{A} = \frac{1}{\epsilon_0} \int \rho \, dV \tag{II.9.96}$$

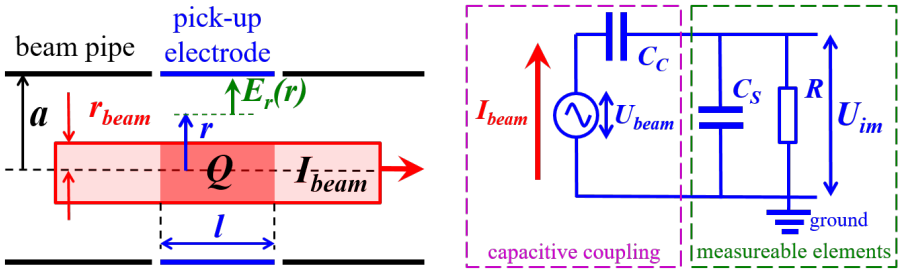

Fig. II.9.91: Left: The cylindrical geometry used to calculate the coupling capacitance for the beam to the pick-up electrodes; see text for the meaning of the symbols. Right: The equivalent circuit for a capacitive pick-up.

$$\implies \quad E_r(r) \cdot A_b \;=\; \frac{Q}{\epsilon_0} \tag{II.9.97}$$

$$\implies \quad E_r(r) \;=\; \frac{1}{2\pi\epsilon_0} \cdot \frac{Q}{l} \cdot \frac{1}{r} \tag{II.9.98}$$

with Q is the total charge within the integration volume. Due to the assumption of a bunch much longer than the pick-up electrode, the electric field $\mathbf{E}_r$ is perpendicular to the surface vector $d\mathbf{A}$ at the end caps and does not contribute to the surface integral and only the barrel surface remains. The induced voltage U_{beam} on the circulating pick-up electrode of radius a by the beam of radius r_{beam} is calculated using the electric field as

$$U_{\mathrm{beam}} \;=\; \int_{r_{\mathrm{beam}}}^{a} E_r(r)\, dr = \frac{1}{2\pi\epsilon_0} \cdot \frac{Q}{l} \cdot \int_{r_{\mathrm{beam}}}^{a} \frac{1}{r}\, dr \tag{II.9.99}$$

$$\;=\; \frac{1}{2\pi\epsilon_0} \cdot \frac{Q}{l} \cdot \ln \frac{a}{r_{\mathrm{beam}}} \quad . \tag{II.9.100}$$

Substituting the line charge density Q/l by the beam current for particles moving with velocity β as $I_{\mathrm{beam}} = Q/l \cdot \beta c$, the induced voltage is written as

$$U_{\mathrm{beam}} = \frac{1}{2\pi\epsilon_0} \cdot \frac{1}{\beta c} \cdot \ln \frac{a}{r_{\mathrm{beam}}} \cdot I_{\mathrm{beam}} \quad . \tag{II.9.101}$$

The coupling between the beam and electrode is modelled electronically as a capacitance C_C as

$$C_C = \frac{Q}{U_{\mathrm{beam}}} = 2\pi\epsilon_0 \cdot l \cdot \frac{1}{\ln \frac{a}{r_{\mathrm{beam}}}} \quad . \tag{II.9.102}$$

As depicted in the equivalent circuit of Fig. II.9.91 (right), the image voltage U_{im} across a resistor R is measured, where R is part of a parallel shunt to the unavoidable stray capacitance C_S. The impedance of the RC_S parallel shunt is

$$\frac{1}{Z_S} = \frac{1}{R} + i\omega C_S \iff Z_S = \frac{R}{1 + i\omega R C_S} \quad . \tag{II.9.103}$$

In general, the whole circuit represents a voltage divider with the input voltage U_{beam} and the measured

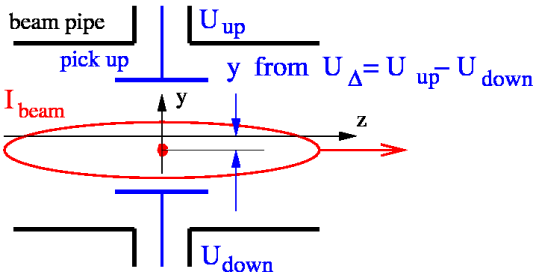

Fig. II.9.92: Schematics of a BPM for the vertical position reading based on the proximity effect.

voltage $U_{\rm im}$. Together with the serial capacitance C_C of impedance

$$Z_C = \frac{1}{i\omega C_C} \tag{II.9.104}$$

and using the relation

$$Z_C + Z_S = \frac{1}{i\omega C_C} + \frac{R}{1+i\omega R C_S} = \frac{1+i\omega R\,(C_C+C_S)}{i\omega C_C(1+i\omega R C_S)} \tag{II.9.105}$$

the image voltage is written as

$$U_{\rm im} = \frac{Z_S}{Z_C+Z_S}\cdot U_{\rm beam} = \frac{C_C}{C_C+C_S}\cdot\frac{i\omega R\,(C_C+C_S)}{1+i\omega R\,(C_C+C_S)}\cdot U_{\rm beam} \tag{II.9.106}$$

$$= \frac{l}{\beta c}\cdot\frac{1}{C_C+C_S}\cdot\frac{i\omega R\,(C_C+C_S)}{1+i\omega R\,(C_C+C_S)}\cdot I_{\rm beam}\quad . \tag{II.9.107}$$

for the last step Eq. II.9.101 and II.9.102 is used. Finally, the transfer impedance Z_t can be written as

$$Z_t(\omega) \equiv \frac{U_{\rm im}(\omega)}{I_{\rm beam}(\omega)} = \frac{l}{\beta c}\cdot\frac{1}{C_C+C_S}\cdot\frac{i\omega R\,(C_C+C_S)}{1+i\omega R\,(C_C+C_S)}\quad . \tag{II.9.108}$$

This is a comparable relation to Eq. II.9.82, but it distinguishes between the stray capacitance C_S and the capacitive coupling between the beam and the pick-up electrodes C_C and justifies the name capacitive pick-up for such an arrangement.

Using as an illustration the previously discussed BPM example with an electrode length $l = 10$ cm, a radius of $a = 10$ cm for a beam of velocity $\beta = 50$ % and radius $r_{\rm beam} = 1$ cm, the value of the coupling capacitance is $C_C = 12.7$ pF as given by Eq. II.9.102. This shows that C_C is significantly lower than the unavoidable stray capacitance $C_S \simeq 100$ pF for a typical technical realization. Hence, the transfer impedance Z_t of Eq. II.9.108 is dominated by C_S and can be approximated by the previously given Eq. II.9.82 for many practical cases.

II.9.5.5 Characteristics for position measurement by BPMs

II.9.5.5.1 Definition and properties of position sensitivity

The deviation of the beam centre from the centre of the vacuum chamber is frequently monitored using four isolated electrodes by determining the voltage difference $\Delta U_x = U_{\rm right} - U_{\rm left}$ or $\Delta U_y = U_{\rm up} - U_{\rm down}$ of opposite electrodes, respectively. The closer distance to one of the electrodes leads to

a higher induced voltage. This is called the "proximity effect" and schematically shown in Fig. II.9.92. Normalizing to the sum signal $\Sigma U_x = U_{\text{right}} + U_{\text{left}}$, the horizontal displacement x can be obtained from

$$x = \frac{1}{S_x} \cdot \frac{U_{\text{right}} - U_{\text{left}}}{U_{\text{right}} + U_{\text{left}}} = \frac{1}{S_x} \cdot \frac{\Delta U_x}{\Sigma U_x} \quad \text{(horizontal)} \quad , \tag{II.9.109}$$

which is independent of the beam intensity. For the vertical plane the position y is given by

$$y = \frac{1}{S_y} \cdot \frac{U_{\text{up}} - U_{\text{down}}}{U_{\text{up}} + U_{\text{down}}} = \frac{1}{S_y} \cdot \frac{\Delta U_y}{\Sigma U_y} \quad \text{(vertical)} \quad . \tag{II.9.110}$$

This position measurement is the most frequent application of pick-ups, hence they are called **B**eam **P**osition **M**onitor **BPM**. The proportional constants S_x respectively S_y between the measured normalized voltage difference and the beam displacement is referred to as position sensitivity expressed in the unit $S = [\%/\text{mm}]$. Sometimes the inverse is used $k = 1/S$ expressed in the unit $k = [\text{mm}]$ and is called BPM position constant or position sensitivity as well. It is possible that the position sensitivity depends on the beam position itself, corresponding to a non-linear voltage response for a large beam displacement and, additionally, on the evaluation frequency; hence, it depends on the horizontal and vertical coordinates resulting in a function $S = S(x, y, \omega)$.

For typical beam displacements of much less than 1/10 of the beam pipe aperture, the difference ΔU is lower by at least a factor of 10 compared to the sum voltage ΣU i.e.

$$\text{typically} \quad \Delta U \ll \frac{\Sigma U}{10} \quad . \tag{II.9.111}$$

Low-noise signal processing is required for the difference voltage to achieve a sufficient signal-to-noise ratio. This concerns the usage of low-noise amplifiers which have to be matched to the signal level. Sometimes difference and sum voltage are generated by analogue means using a so-called $\Delta - \Sigma$ hybrids. In these cases, the difference voltage can be more amplified than the sum signal (typically by 10 dB, which corresponds to a factor of three for the voltage amplification) to match the optimal signal level for the successive electronics or analogue-digital conversion. The most effective noise reduction is achieved by a limitation of the signal processing bandwidth because the thermal noise voltage U_{eff} at a resistor R scales with the square root of the bandwidth Δf as $U_{\text{eff}} = \sqrt{4 k_B T R \Delta f}$ with k_B being the Boltzmann constant and T the temperature. The bandwidth limitation is performed by bandpass filtering at a harmonics of this frequency or mixing with the accelerating frequency in the narrowband processing, as discussed in Section II.9.5.9. A review of general BPM properties and BPM types are given in Refs. [118] to [122].

An example of a capacitive BPM used at the GSI LINAC is shown in Fig. II.9.93. The round electrodes have a diameter of 12 mm and are soldered in a vacuum housing with $a = 50$ mm diameter; the total insertion length is 80 mm and connected by $\oslash 100$ mm flanges; this arrangement is commonly called button BPM. For typical displacements of up to $x < 1/2 \cdot a$, the position sensitivity $S_x(x)$ and $S_y(y)$ is sufficiently constant; Section II.9.5.6 describes the properties of button BPMs. However, the response is non-linear for larger displacements, and a correction algorithm might be applied to the digitized signals.

From a more abstract perspective, we can define the transverse transfer impedance $Z_\perp$ in analogy

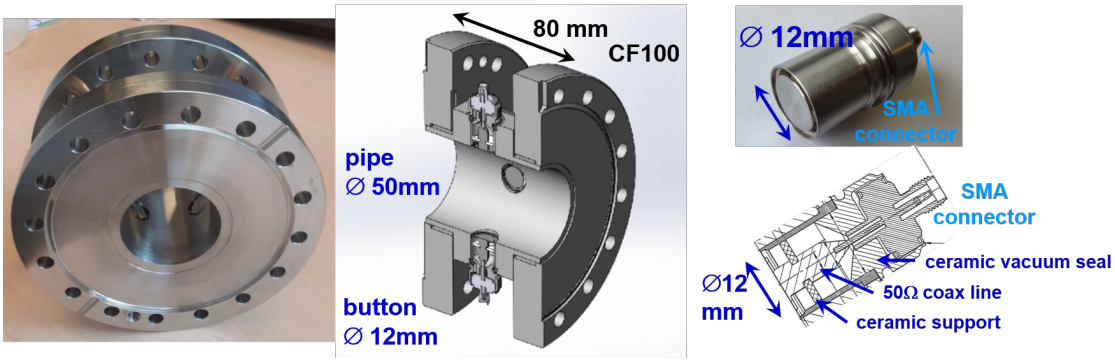

Fig. II.9.93: Left and middle: Photo and schematic drawing of a button BPM at the GSI LINAC mounted on a ⌀100 mm flange. Right: Photo and technical drawing of the button for this BPM.

to the longitudinal case as

$$\Delta U_x = Z_\perp \cdot x I_{\mathrm{beam}} \tag{II.9.112}$$

for an off-centre position x and a beam current I_{beam}; the product xI_{beam} is sometimes referred to as the dipole moment of the beam. $Z_\perp$ can be written as a product of the longitudinal transfer impedance Z_t as of Eq. II.9.82 and a geometric non-linear function $g(x)$ as

$$Z_\perp = \frac{Z_t}{g(x)}. \tag{II.9.113}$$

For some calculations the usage of $Z_\perp$ acts as an alternative to description by the position sensitivity S.

II.9.5.5.2 Characteristic quantities for position measurements

For the characterization of a position measurement system, several descriptors are frequently used, which are compiled for completeness [118]:

Position sensitivity: It is the proportional constant between the beam displacement and the signal strength. It is defined by the derivative

$$S_x(x) = \frac{d}{dx}\left(\frac{\Delta U_x}{\Sigma U_x}\right) = [\%/\mathrm{mm}] \ \text{(linear)} \qquad S_x(x) = \frac{d}{dx}\left(\log\frac{U_{\mathrm{right}}}{U_{\mathrm{left}}}\right) = [\mathrm{dB/mm}] \ \text{(logarithmic)} \tag{II.9.114}$$

for the horizontal direction and the vertical direction, respectively. The unit is $S = [\%/\mathrm{mm}]$ for linear processing or $S = [\mathrm{dB}/\mathrm{mm}]$ for logarithmic processing [118]. For small displacements, a constant value is expected. For larger displacements, the horizontal sensitivity S_x might depend on the beam position in the horizontal direction, referred to as non-linearity. Additionally, it might depend on the beam's vertical position, referred to as horizontal-vertical coupling. Moreover, it might depend on the evaluation frequency. Hence, in the most general case, the position sensitivity $S(x, y, \omega)$ is a function of horizontal x and vertical y displacement as well as frequency ω. Sometimes the inverse of S is used abbreviated as $k = 1/S$ and is given in the unit of $k = [\mathrm{mm}]$.

Accuracy: It refers to the ability of position reading relative to a mechanical fix-point or any other absolutely known axis , e.g. the symmetry axis of a quadrupole magnet. The accuracy is mainly influenced by the BPM's mechanical tolerances, as well as the long-term stability of the mechanical alignment. For cryogenic installations, the mechanical position reproducibility after cool-down cycles influences

the accuracy. Besides these mechanical properties, it is also influenced by electronics properties such as amplifier drift, noise and pick-up of electro-magnetic interference. Long-term drifts can be compensated by calibrating the electronics at regular intervals. The digitization leads to a granularity of values, which might limit the reachable accuracy. For modern installations, this limitation is compensated by enhanced ADCs with a high number of bits.

Resolution: It refers to the ability to measure small displacement variations; relative values are compared here contrary to the accuracy. In most cases, the resolution is better by a factor of two to five as compared to the accuracy. The resolution depends strongly on the measurement time because averaging procedures can exceed the accuracy by a factor of 100. A typical value for the resolution for a broadband, single bunch reading is 10^{-3} of the beam pipe radius or roughly $\simeq 100$ μm for a beam pipe of 10 cm as assumed in Section II.9.5.7. For averaged readings on a typical time scale of 10 to 1000 ms, a resolution of 10^{-5} of the beam pipe radius or roughly $\simeq 1$ μm can be reached. As for the accuracy, the resolution depends on the electronics noise contribution as well as short-term and long-term drifts.

Analogue bandwidth: The lower and upper cut-off frequency of the analogue electronics must be matched to the frequency spectrum delivered by the bunched beam. For noise reduction, the bandwidth can be limited by analogue filters.

Acquisition bandwidth: It refers to the frequency range over which the beam position is recorded and should be matched to the analogue bandwidth. A much larger bandwidth is required to monitor fast changes of beam parameters , resulting in a lower position resolution. The same is true for short beam deliveries, as found in transport lines as averaging is not meaningful. The bandwidth can be restricted to achieve a high resolution for slow varying beam parameters which is similar to analogue narrowband processing described in Section II.9.5.9.

Real-time bandwidth: The quantity characterizes the data rate of producing an analogue or digital position signal with predictable latency to be used, e.g. by an orbit feedback system.

Dynamic range: It refers to the beam current range for a reasonable system response. In most cases, the signal adoption is done by a variable gain amplifier at the input stage of the electronics processing chain. Within the dynamic range, the position reading should have a negligible dependency with respect to the input level.

Signal-to-noise ratio: It refers to the ratio of the wanted signal to unwanted noise. An unavoidable contribution is given by thermal noise. Cooling of the first stage amplifier reduces this thermal noise. Other sources, such as electro-magnetic interference or ground-loops can contribute significantly to an unwanted signal disturbance. The related signal deformations are frequently incorporated in this quantity even though they are not caused by noise. Careful shielding and grounding are required to suppress these disturbances.

Detection threshold: It refers to the minimal beam current for which the system delivers usable information. Noise contributions limit the detection threshold. Sometimes this quantity is also called signal sensitivity.

II.9.5.6 Position measurement using button BPMs

For a round arrangement of buttons and a beam with a longitudinal extension much larger than the button diameter, a simple 2-dimensional electrostatic model can be used to calculate the voltage difference as a

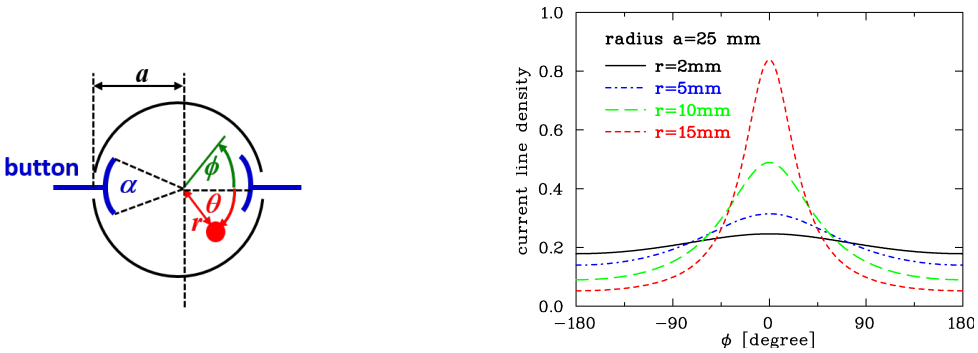

Fig. II.9.94: Schematics for a button BPM and the image current density generated by a "pencil" beam at different displacements r for an azimuth $\theta = 0$.

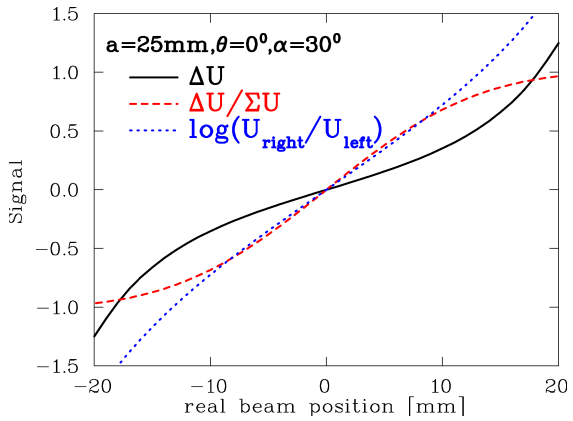

Fig. II.9.95: Difference voltage, normalized difference and logarithmic ratio for a button BPM arrangement of angular coverage $\alpha = 30^o$ as a function of horizontal beam displacement, i.e. $\theta = 0$ for a beam pipe radius $a = 25$ mm.

function of beam displacement reflecting the cylindrical symmetry. According to Fig. II.9.94 we assume a thin, "pencil" beam with a transverse extension much smaller than the beam pipe radius of current $I_{\rm beam}$ located off-centre by a displacement r at an angle θ. The wall current density $j_{\rm im}$ at the beam pipe of radius a is given as a function of the azimuthal angle ϕ as

$$j_{\rm im}(\phi) = -\frac{I_{\rm beam}}{2\pi a} \cdot \left(\frac{a^2 - r^2}{a^2 + r^2 - 2ar \cdot \cos(\phi - \theta)} \right) \qquad \text{(II.9.115)}$$

and is depicted in Fig. II.9.94. A mathematical derivation of this electrostatic formula is given in [18,127] where a point-like charge located at the coordinates r and θ is assumed.

As discussed above, this represents the proximity effect, where the current density depends on the distance with respect to the beam centre. For button-type BPM electrodes covering an angle α, the image current $I_{\rm im}$ is given by:

$$I_{\rm im} = a \int_{-\alpha/2}^{+\alpha/2} j_{\rm im}(\phi)\, d\phi \quad . \qquad \text{(II.9.116)}$$

The resulting signal difference for opposite electrodes as a function of horizontal beam displacement, corresponding to $\theta = 0^o$, shows a significant non-linear behaviour, as depicted in Fig. II.9.95. The signal

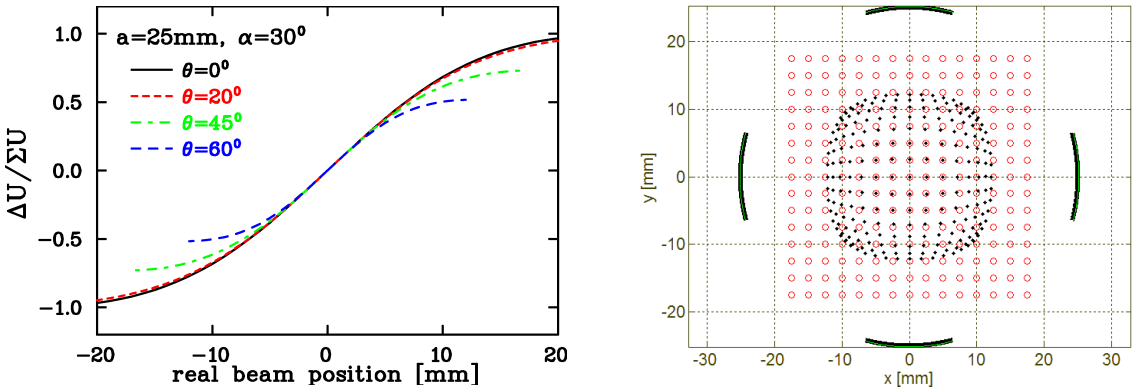

Fig. II.9.96: Left: Horizontal position calculation for different azimuthal beam orientation θ for the parameters of Fig. II.9.95. Right: In the position map, the open circles represent the real beam position, and the dots are the results of the $1/S \cdot \Delta U/\Sigma U$ algorithm with $S = 7.4$ %/mm for the central part.

voltage is calculated according to Eq. II.9.79 as $U = R \cdot I_{\mathrm{im}}$. The linear range for the normalized difference $\Delta U/\Sigma U$ continues to larger beam offsets. The non-linearity increases if the beam centre moves outside of the horizontal axis as shown in Fig. II.9.96 for different values of the azimuthal orientation θ as a function of horizontal displacement $x = r \cdot \cos\theta$ according to Eqs. II.9.115 and II.9.116. For an orientation along the diagonal line $\theta = 45°$, a significant deviation from linearity starts at about 1/4 of the beam pipe radius for this example. This non-linearity can be influenced by the button size represented by the angle α. However, in the central part, the reading is nearly independent of the orientation leading to a universal position sensitivity S. The dependency between the horizontal and vertical plane is better depicted in the position map of Fig. II.9.96 (right): Here, the real beam positions with equidistant steps are plotted as well as the results using $1/S \cdot \Delta U/\Sigma U$ calculations with S fitted at the central part. The previously described 2-dimensional electrostatic model delivers satisfying results for typical electron beams of relativistic beam velocities i.e. TEM-like field pattern; only minor corrections are necessary for a circular BPM arrangement.

If the beam is accelerated only to a non-relativistic velocity $\beta \ll 1$, as for proton LINACs and cyclotrons, the electric field cannot be described as a TEM wave any more. Instead, the field pattern, as originated by the charged particles, has a significant longitudinal extension because the electric field propagation is faster than the beam velocity; see the discussion in Section II.9.6.1. Moreover, this field pattern and, therefore, the wall current depends strongly on the beam displacement for opposite BPM electrodes, resulting in a velocity dependence of the position sensitivity $S(\beta)$. This is discussed analytically in Ref. [128] and a numerical example is given in Ref [129].

A BPM arrangement obeying the circular beam pipe geometry is installed at CERN LHC and depicted in Fig. II.9.97. Due to the size and the round electrodes, this arrangement is commonly called button BPM. The reason for such installation is to ensure a smooth transition from the regular beam pipe to the BPM region and to prevent for an excitation of stationary electro-magnetic fields by the beam, referred to as wake-fields. In most other cases, planar buttons are used due to their more straightforward mechanical realization as shown in Fig. II.9.93.

Button BPMs are the most popular devices for electron accelerators. They consist of a circular plate of typically 10 mm diameter, mounted flush with the vacuum chamber as shown in Fig. II.9.98.

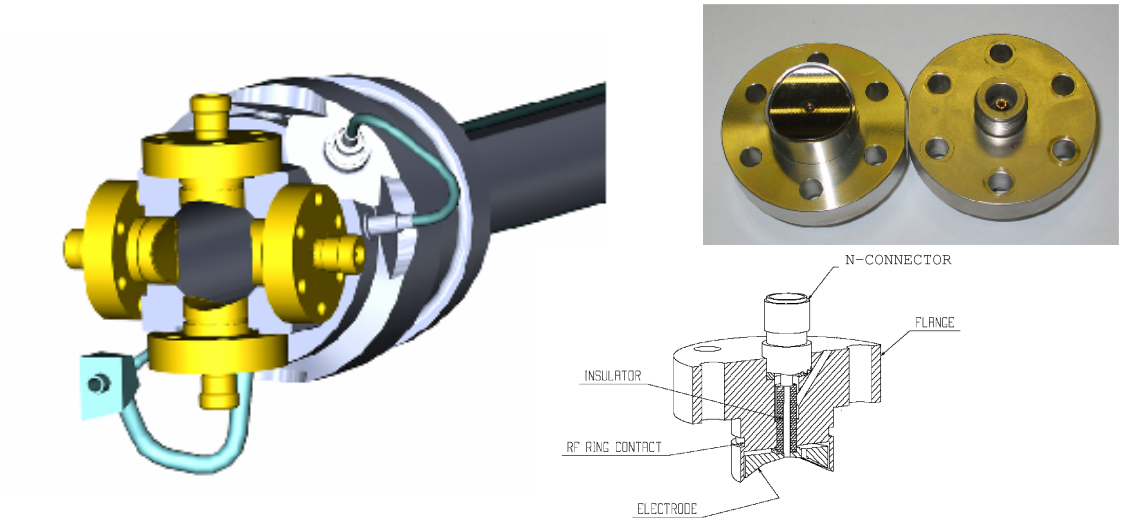

Fig. II.9.97: Left: The installation of the curved Ø 24 mm button BPMs at the LHC beam pipe of Ø 50 mm, from Ref. [130]. Right top: Photo of a BPM used at LHC; the air side is equipped with an N-connector. Right bottom: Technical drawing for this type.

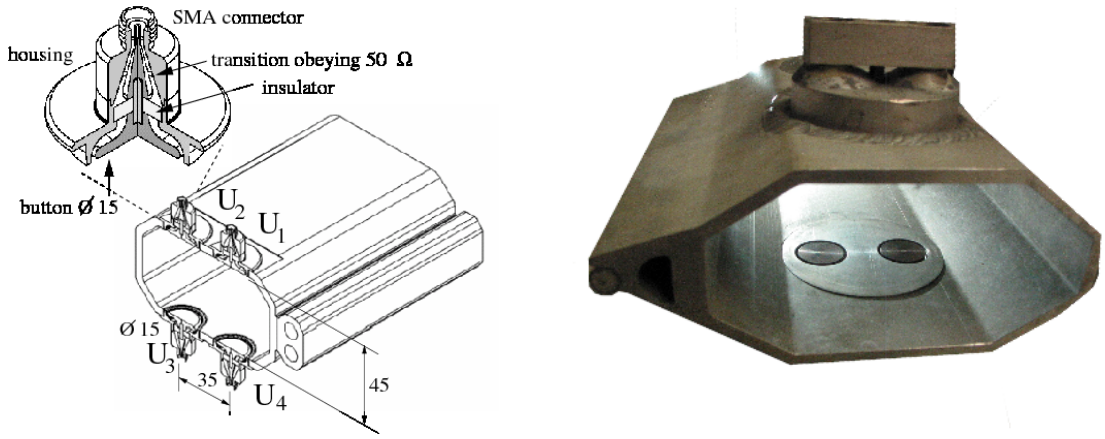

Fig. II.9.98: Left: Typical button BPM arrangement within a vacuum chamber at a synchrotron light source, from Ref. [131]. Right: Photo of the realization at HERA, DESY.

This insertion does not change the cross-section of the chamber and avoids the excitation of wake-fields by the beam. The button should have a short vacuum feed-through with a smooth transition to a 50 Ω cable to avoid the excitation of standing waves and reaches a bandwidth of up to 10 GHz.

Fig. II.9.98 shows a typical setup used at the storage ring of a synchrotron light source within a planar arrangement, where the buttons are not mounted in the horizontal plane to avoid synchrotron light hitting the feed-through. According to Fig. II.9.98 (left), the position is evaluated via

$$\text{horizontal: } x = \frac{1}{S_x} \cdot \frac{(U_1 + U_4) - (U_2 + U_3)}{U_1 + U_2 + U_3 + U_4} \quad \text{vertical: } y = \frac{1}{S_y} \cdot \frac{(U_1 + U_2) - (U_3 + U_4)}{U_1 + U_2 + U_3 + U_4} \tag{II.9.117}$$

using all four electrode voltages for the position determination. An appropriate size and location for the buttons for a linear sensitivity within a certain range at the central part and comparable values of the related horizontal and vertical position sensitivity has to be calculated numerically, see e.g. Refs. [132–

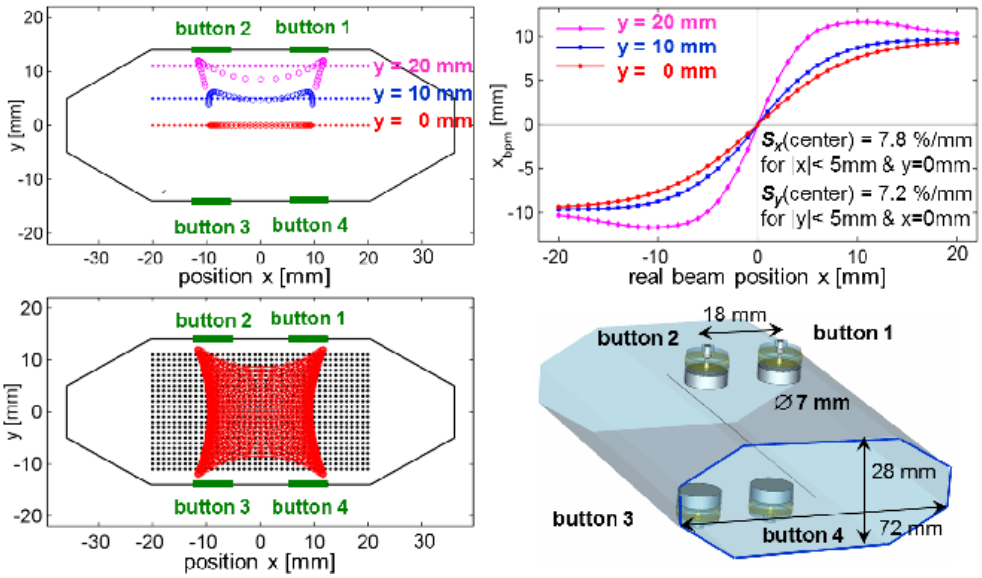

Fig. II.9.99: Numerical calculation of the position map for the arrangement at the synchrotron light source ALBA. Top left: Results of position calculation for a horizontal scan from -20 mm $< x <$ 20 mm for three vertical offsets using constant horizontal $S_x(\text{centre})$ and vertical $S_y(\text{centre})$ position sensitivities. Top right: The calculated position for the horizontal scan for these three vertical offsets; the horizontal position sensitivity $S_x(\text{centre})$ at the central part is determined from the slope of the curve with zero vertical offset. Bottom left: Position map for the entire horizontal and vertical range. Bottom right: The geometry of the Ø 7 mm button electrodes of 18 mm horizontal distance within the chamber; from Ref. [134].

134]. The optimized location depends on the size and distances of the electrodes, as well as the chamber cross-section. A result for such an optimized setting is shown in Fig. II.9.99 for the typical geometry of the storage ring at a synchrotron light source. The inherent geometry of the vacuum chamber leads to a non-linear position sensitivity and a strong coupling between horizontal and vertical displacements (i.e. non-linear position sensitivity $S(x, y)$ in Eq. II.9.114). In case only one value for position sensitivity is given it concerns the central part of the BPM arrangement, as e.g. shown in Fig. II.9.99 (top right) for the curve $y = 0$ mm. The vertical position sensitivity $S_y(\text{centre})$ is calculated from a corresponding (but not shown) diagram. After optimization, the values of the position sensitivity at the central part, in this example $S_x(center) = 7.8$ %mm for $y = 0$ and $S_y(\text{centre}) = 7.2$ %/mm for $x = 0$ are nearly equal and comparable to the values one would obtain for a circular beam pipe. But in contrast to the circular arrangement, even in the central part the horizontal position sensitivity $S_x(x, y)$ depends significantly on the vertical displacement y as well and a corresponding dependency for the vertical direction $S_y(x, y)$. The related non-linearity and horizontal-vertical coupling is visualized in Fig. II.9.99 (bottom left) by a complete position map using constant values for the sensitivity $S_x(\text{centre})$ and $S_y(\text{centre})$. However, in case the beam diameter is much smaller than the chamber size, numerical corrections can be applied to compensate for the non-linearity and coupling via polynomial interpolation incorporated in the analysis software, see, e.g. Ref. [134].

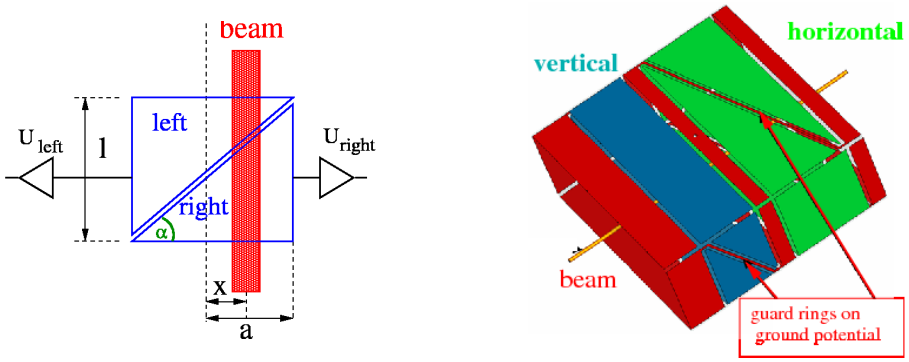

Fig. II.9.100: Left: Scheme of the position measurement using the so-called linear cut and an example of an electrode arrangement for the horizontal plane. Right: Schematic drawing for a linear cut BPM for both planes.

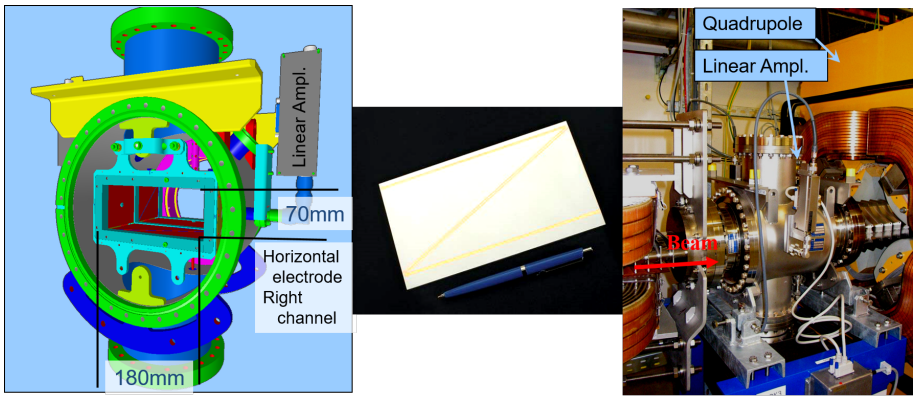

Fig. II.9.101: Linear-cut BPM installed at the medical synchrotron HIT with an aperture limitation of 180×70 mm^2.Left: technical drawing, middle: the bottom plate for the horizontal position, right: installation at the synchrotron.

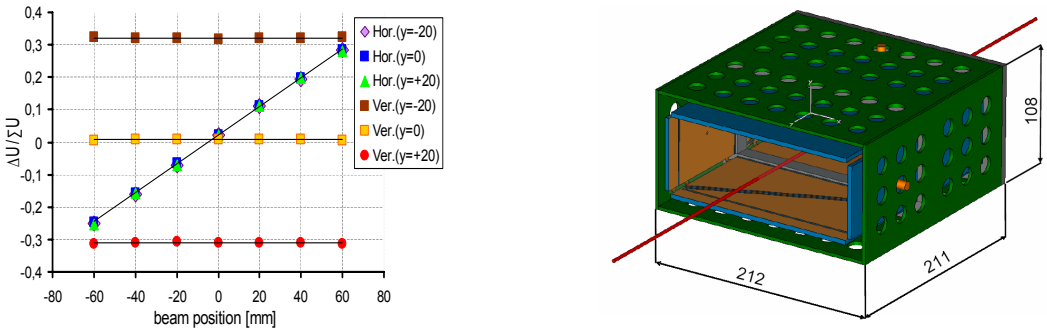

Fig. II.9.102: Left: Numerical calculation of the position reading $\Delta U/\Sigma U$ as a function of beam displacement for the horizontal plane. The simulated beam is swept in horizontal direction (curves with constant slope) and vertical direction (constant functions) and proves the decoupling of both planes [135]. Right: The BPM geometry for these calculations.

II.9.5.7 Linear-cut BPMs for proton synchrotrons

Due to the long bunches at proton or ion synchrotrons, long electrodes of typically 10 cm are installed to enhance the signal strength. A box-like device is used frequently to achieve linear response with respect to the beam displacement, see Figs. II.9.100 and II.9.101. For the previously discussed button BPM

Table II.9.11: Simplified comparison between linear-cut and button BPM.

	Linear-cut BPM	**Button BPM**
Precaution	bunches longer than BPM	bunches comparable to BPM
BPM length (typ.)	10 to 20 cm per plane	Ø 0.5 to 5 cm
Shape	rectangular or cut cylinder	orthogonal or planar orientation
Mechanical realization	complex	simple
Coupling	often 1 MΩ, sometimes 50 Ω	50 Ω
Capacitance (typ.)	30–100 pF	3–10 pF
Cut-off frequency (typ.)	1 kHz for $R = 1\text{M}\Omega$	0.3 to 3 GHz for $R = 50\ \Omega$
Usable bandwidth (typ.)	0.1 to 100 MHz	0.3 to 5 GHz
Linearity	very linear, no x-y coupling	non-linear, x-y coupling
Position sensitivity	good	good
Usage	at proton synchrotron, $f_{\text{acc}} < 10$ MHz	proton LINAC, all electron acc. $f_{\text{acc}} > 100$ MHz

geometries, the signal from the electrode closer to the beam's centre-of-mass is larger than that of the more distant electrode, is referred to as proximity effect. Contrary, the linear-cut BPMs follow another principle: The induced signal is proportional to the electrode length at the beam centre. For a given beam displacement x, the electrode's image voltage U_{im} is proportional to the length l_{left} and l_{right} of the beam projected on the electrode surface as shown for the horizontal direction in Fig. II.9.100 (left). For triangular electrodes with half-aperture a one can write:

$$l_{\text{right}} = (a + x) \cdot \tan\alpha \quad \text{and} \quad l_{\text{left}} = (a - x) \cdot \tan\alpha \quad \Longrightarrow \quad x = a \cdot \frac{l_{\text{right}} - l_{\text{left}}}{l_{\text{right}} + l_{\text{left}}} \quad . \tag{II.9.118}$$

The position reading is linear and can be expressed by the image voltages as

$$x = a \cdot \frac{U_{\text{right}} - U_{\text{left}}}{U_{\text{right}} + U_{\text{left}}} \equiv \frac{1}{S_x} \cdot \frac{\Delta U_x}{\Sigma U_x} \quad \Longrightarrow \quad S_x = \frac{1}{a} \quad , \tag{II.9.119}$$

which shows that the position sensitivity for this ideal case is simply given by the inverse of the half-aperture. Compared to other types of BPMs, the position sensitivity is constant for nearly the full range of displacements, i.e. no significant corrections due to non-linearity is required [135]. This fact is demonstrated in Fig. II.9.102 where the result of numerical simulations show a linear scaling of the difference voltage ΔU_x of opposite plates normalized to the sum voltage ΣU_x as a function of beam offset up to about 2/3 of the half aperture. Moreover, the position reading in the horizontal plane is independent of the beam position in the vertical plane. Due to the linearity, the position reading is additionally independent of the beam size, which is of important for the relatively large beam size compared to the chamber aperture for low energy proton or ion synchrotrons. This position linearity is the main advantage of the linear-cut type as compared to the button BPM type. Sometimes linear-cut BPMs are called "shoe-box" BPMs due to the rectangular arrangement and much larger size compared to the button type. An analogue signal from such a linear-cut BPM used at an ion synchrotron is shown in Fig. II.9.87.

As a summary, the basic parameters for linear-cut and button BPMs are compared in Table II.9.11; this table contains significant simplifications and serves as an overview only.

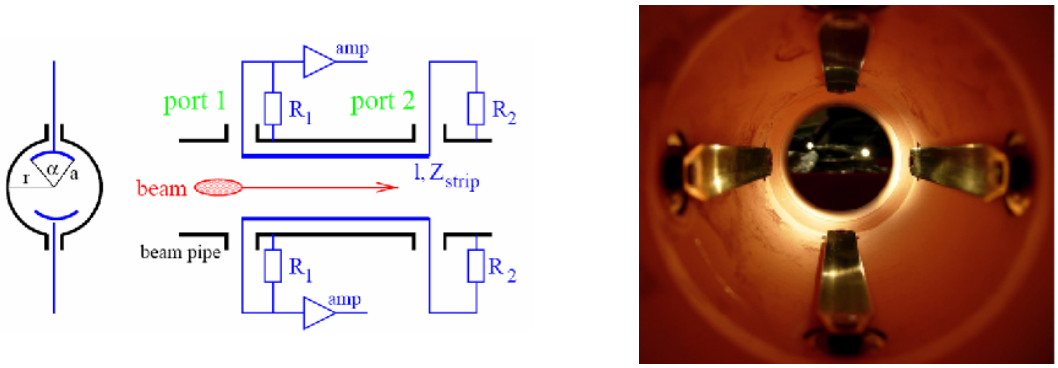

Fig. II.9.103: Left: Scheme of a stripline BPMB. Right: Photo of the LHC stripline BPM of 12 cm length, from Ref. [130].

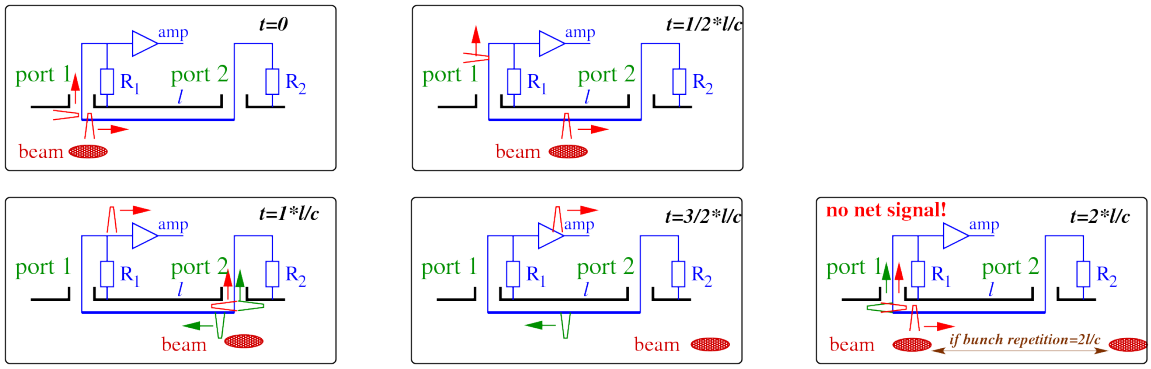

Fig. II.9.104: Four plots visualize the signal generation at a stripline electrode for a single bunch propagating with velocity of light and in phase with the signal propagation. The plot on the lower right shows the signal cancellation in case of a bunch repetition by $t = 2l/c$.

II.9.5.8 Signal treatment of a stripline BPM

In the above discussion of capacitive BPMs, a quasi-electrostatic approach was used, disregarding effects based on the signal propagation. If the bunch length becomes comparable to the size of the BPM, the final propagation time leads to a signal deformation or in other words: For short bunches, button BPMs have to be small and can deliver only a low signal strength. Stripline BPMs are well suited for short bunch observation because the signal propagation is considered in the design like for transmission-lines in microwave engineering. The azimuthal coverage of the stripline BPM can be larger than for a button type yielding an increased signal strength. Moreover, stripline BPMs have the characteristic of a directional coupler, which is of great importance for the installation in a collider of counter-propagating beams within the same beam pipe: Stripline BPMs can distinguish between the directions of beam propagation and can record only the position from one beam by suppressing the signal from the counter-propagating beam, as explained below. The electrical properties of such a BPM are comparable to a directional coupler used for microwave devices [136].

A stripline BPM consists of four transmission lines of several cm length, having at both ends a feed-through with an impedance of R_1 and R_2 matched to 50 Ω, see Fig. II.9.103. The stripline electrode of length l is installed at a distance a from the beam centre, covering an angle of α within a cylindrical vacuum chamber of radius r. The characteristic impedance Z_{strip} of this strip depends on the parameters

r, a and α, like for a micro-strip line on a printed-circuit board [136]. It is chosen to be $Z_{\mathrm{strip}} = 50\ \Omega$ for matching the characteristic impedance at the two ports, i.e. the condition $Z_{\mathrm{strip}} = R_1 = R_2 = 50\ \Omega$ is fulfilled. Further on, we assume that the beam is relativistic and can be approximated by a travelling TEM wave with velocity v_{beam}, which equals the signal propagation on the strip $c_{\mathrm{strip}} = v_{\mathrm{beam}} = c$. The bunch length should be shorter than the strip length to prevent signal overlapping. The signal generation at the upstream port 1 during the bunch passage is visualized in Fig. II.9.104 and described in the following:

- At $t = 0$, the bunch passes the front edge of the strip. The wall current is divided into two parts due to the matching of the voltage divider $Z_{\mathrm{strip}} = R_1 = 50\ \Omega$. Half of this signal travels towards port 1 and half travels downstream along the stripline.
- During $0 < t < l/c$, the beam and the signal travel in phase according to the condition $c_{\mathrm{strip}} = v_{\mathrm{beam}} = c$.
- At $t = l/c$, the bunch reaches the upstream port 2. Here the image charge leaves the stripline, generating an equal amplitude but opposite sign of current, which is split into two halves according to $Z_{\mathrm{strip}} = R_2 = 50\ \Omega$. However, the image current is leaving the detector and has the opposite sign to that generated at the upstream port. Therefore, half of the signal cancels the initially generated signal at port 1. The other half travels now back towards the upstream port 1.
- At time $t = 2 \cdot l/c$, the back travelling signal generated at port 2 reaches the upstream port 1.
- If the bunch repetition time of the bunches is $t_{\mathrm{acc}} = 2 \cdot l/c$ the reflected, inverted signal from the first bunch cancels the signal from this second bunch.

This ideal behaviour has two important consequences: Firstly, there is no signal at the upstream port 2 for a beam propagating in the described direction. For a second beam travelling in opposite direction, the roles of the ports are interchanged, which enables the separation of signal from counter-propagating beams like in colliders; this is not possible for other types of BPMs. However, due to imperfections of the mechanical and electrical realization, the suppression of the counter-propagating signals (i.e. signal strength at port 2 compared to strength at port 1) is typically 20 to 30 dB, i.e. the voltage at port 2 is lower by a factor 10 to 30. Secondly, the voltage signal for the ideal case at port 1 is given by

$$U_1(t) = \frac{1}{2} \cdot \frac{\alpha}{2\pi} \cdot R_1 \left(I_{\mathrm{beam}}(t) - I_{\mathrm{beam}}(t - 2l/c) \right) \quad . \tag{II.9.120}$$

Inserting a Gaussian bunch distribution as $I_{\mathrm{beam}}(t) = I_0 \cdot \exp(-t^2/2\sigma_t^2)$ this equation can be written as

$$U_1(t) = \frac{Z_{\mathrm{strip}}}{2} \cdot \frac{\alpha}{2\pi} \left(e^{-t^2/2\sigma_t^2} - e^{-(t-2l/c)^2/2\sigma_t^2)} \right) \cdot I_0 \quad . \tag{II.9.121}$$

This voltage signal at port 1 is shown in Fig. II.9.105 (left) for several bunch durations σ_t.

The related transfer impedance Z_t is obtained from the Fourier transformation of such a stripline BPM to be

$$Z_t(\omega) = Z_{\mathrm{strip}} \cdot \frac{\alpha}{4\pi} \cdot e^{-\omega^2\sigma_t^2/2} \cdot \sin(\omega l/c) \cdot e^{i(\pi/2 - \omega l/c)} \tag{II.9.122}$$

and is shown in Fig. II.9.105 (right). For a short bunch it shows the following features:

- $|Z_t|$ is composed of a series of maxima for $f_{max} = \frac{c}{4l} \cdot (2n - 1)$ for $n = 1, 2, ...$

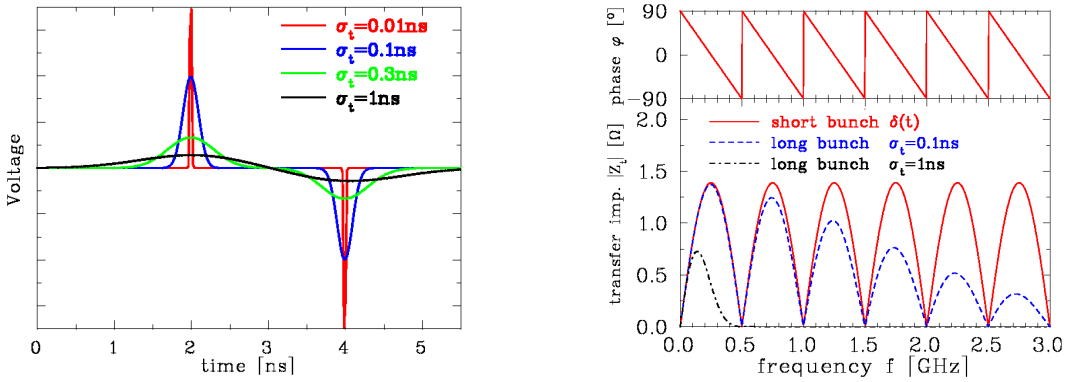

Fig. II.9.105: Left: Calculation of a voltage signal at the upstream port of a stripline BPM of $l = 30$ cm and a coverage of $\alpha = 10^o$ for different bunch durations σ_t. Right: The corresponding transfer impedance.

- For a given acceleration frequency f_{acc}, the length l must be chosen to work close to the maximum. The first maximum is located at $l = \frac{c}{4f_{\mathrm{acc}}} = \lambda/4$, with λ being the "wave length" of the bunch repetition. Due to this behaviour, such BPMs are also called quarter-wave couplers.
- The sensitivity is zero for $l = n \cdot \lambda/2$. This means no signal is present when the spacing between bunches equals $2l$ due to the destructive interference between consecutive bunches.
- The phase φ as a function of frequency is built of straight lines with a zero phase shift at the maxima locations for $l = (2n-1) \cdot \lambda/4$. The recorded signal is a direct image of the bunch for those frequencies. Contrary to capacitive pick-ups, short bunches can be monitored without significant signal deformation close to these frequency locations.

For a finite bunch duration σ_t, the transfer impedance decreases for increasing frequencies as given by the term $|Z_t| \propto e^{-\omega^2\sigma_t^2/2}$ in Eq. II.9.122. This is related to the overlap of direct and reflected signals leads to destructive interference. Even the first maximum of the transfer impedance can be effected for a bunch length comparable to the stripline length. However, in most cases, the length of the stripline can be chosen to avoid signal damping.

The position sensitivity of the four strips of such BPM can be calculated in the same way as for button types, see Eqs. II.9.115 and II.9.116. In the case of low beam current, the azimuthal coverage α can be enlarged to intercept more image current, leading to an increased signal amplitude without too much signal distortion. However, the characteristic impedance of the strips has to be kept to $Z_{\mathrm{strip}} = 50\ \Omega$, resulting in an increased mechanical size of the beam pipe. Moreover, the signal propagation towards the feed-through has to fulfil this matching condition. Even for smaller azimuthal coverage, the electrical transition for the strips to the coaxial vacuum feed-through has to be designed carefully, obeying sensitive radio-frequency and mechanical requirements. The realization of a stripline BPM is more complex compared to the button type. An example of the technical design [137] for the electron LINAC at TTF2 is shown in Fig. II.9.106. The striplines can be installed inside a quadrupole magnet, reducing the BPM insertion length.

The basics of stripline BPMs are summarized in Table II.9.12 and compared to the button type. Due to the precise matching condition required for the stripline type, the technical realization is complex.

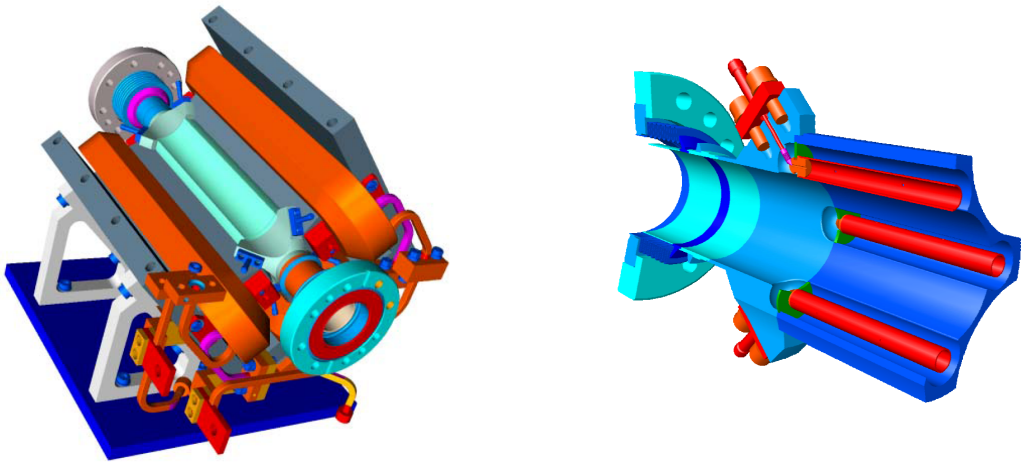

Fig. II.9.106: Technical drawing of the stripline BPM installed inside a quadrupole magnet at TTF2 (left) and the design of the transition for the strip to the feed-through (right). The beam pipe has Ø 34 mm, from Ref. [137, 138].

Table II.9.12: Simplified comparison between stripline and button BPM.

	Stripline BPM	**Button BPM**
Idea for design	traveling wave	electro-static
BPM size (typical)	length: 5 to 30 cm per plane transverse coverage up to $\alpha \simeq 70^0$	Ø 0.5 to 3 cm signal deformation for larger Ø
Signal quality	minor deformation	possible deformations due to finite size and capacitance
Signal strength	large depending on trans. coverage	small
Bandwidth	nearly broadband with well defined minima	high-pass with $f_{\mathrm{cut}} \simeq 3$ GHz
Requirement	careful 50 Ω matching	50 Ω more easy achievable
Mechanical realization	complex	simple
Installation	inside quadrupole possible	compact due Ø $\leq$ 3 cm
Directivity	**yes**	no

Besides the possibly larger signal strength and bandwidth, the main advantage of stripline BPMs is their directivity, which is necessary at any collider with counter-propagating beams in a common beam pipe.

For the position measurement, other techniques are used in addition, including monitors measuring the magnetic field with so-called inductive BPMs or the excitation of cavity modes within a so-called cavity BPM. Further descriptions and citations can be found in Refs. [118, 120–122, 139].

II.9.5.9 Electronic treatment for position determination

To determine the beam's position, the electrodes' signals have to be compared. The signal shape (differentiation or proportional behaviour) is of minor importance for this comparison. This contribution describes the electronics used for this purpose only briefly; a detailed review is given in Refs. [140, 141]. For the position resolution, the signal-to-noise ratio is essential. Besides the stray fields from the RF

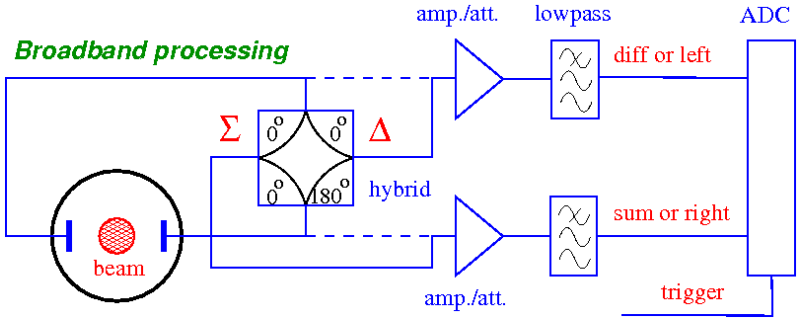

Fig. II.9.107: Schematic illustration of a broadband signal processing. The plate signals are either fed directly to the amplifier (dashed line) or via a hybrid where the sum and difference is generated in an analogue manner (solid line).

cavities, the broadband amplifier noise and the electronic noise of the following devices contribute. Therefore, a minimum bunch current is needed for a reliable position measurement. Different principles are commonly used based on analogue electronics referring to broadband and narrowband processing, respectively. Both methods can be realized with analogue electronics or digitally.

II.9.5.9.1 Broadband processing

In the broadband case, as shown in Fig. II.9.107, the signals from the individual electrodes are amplified (or even attenuated) to adapt the signal strength to the ADC input level. The sum and difference signal is then calculated from the digitized values. For noise reduction and alias-product suppression, a low-pass filter is used matched to the sample rate of the ADC. In some installations, an external trigger, as generated from the acceleration frequency, forced the digitalization: For acceleration frequencies above several 100 MHz, the technology of under-sampling is used, followed by an adequate digital signal processing [120]. In some applications, the sum and difference voltages are analogously generated by a 180° hybrid or a differential transformer. Because they are purely passive devices, they can be mounted close to the BPM plates even in case of high radiation. The resulting sum and difference signals are then stored in the ADC. The difference signal, which is usually lower by at least a factor of 10, can be amplified by a higher amount than the sum signal to exploit the entire ADC range. (An overview of standard RF components can be found in Refs. [122, 142].) The analogue electronics is required to match the signal shape to the properties of the ADCs, and an appropriate trigger are is used for the digitalization.

Modern installations do not use these types of analogue electronics. Instead, the signals are directly digitized by fast ADCs or digital receivers, which are even commercially available [143]. With the help of high-speed digital signal processing, the bunch signal is then reduced to one value per bunch, and the beam position is calculated from the sum and difference value; see, e.g. Ref. [144]. The precision of this method is lower as compared to the narrowband processing described below. For electron accelerators with small beam sizes, a resolution of typically 10 μm can be achieved by this broadband processing. The advantage is the possibility of performing a bunch-by-bunch analysis (i.e. measuring the position of always the same bunch rotating in a synchrotron) using an appropriate trigger setting or precise digital signal processing.

The broadband scheme is installed at transfer lines between synchrotrons where only one or few

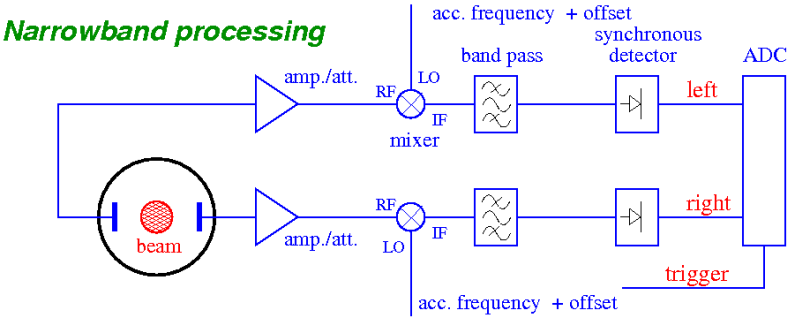

Fig. II.9.108: Schematic illustration of an analogue signal chain for a narrowband treatment.

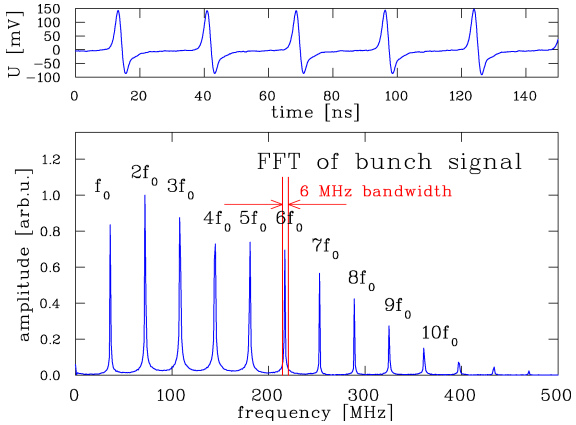

Fig. II.9.109: Bunch signal (top) and its Fourier transformation (bottom) at the GSI-LINAC of a 1.4 MeV/u beam. In the Fourier spectrum, each line corresponds to the indicated harmonics of the 36 MHz accelerating frequency. The position evaluation is done at $6f_0 = 216.8$ MHz by a 6 MHz narrowband processing as indicated by the red lines.

bunches are transferred. A further modification often installed at transfer lines uses logarithmic amplifiers where an order of magnitude increase of input signal is converted to a linear increase of the output signal; they are commercially available, e.g. Ref. [5]. The advantage is an extensive dynamic range covered by a single amplifier stage without range switching. The disadvantage is the lower achievable accuracy, which is often acceptable at transfer lines.

II.9.5.9.2 Narrowband processing

The narrowband processing is used to get a higher precision of the position reading, attaining 1 μm in electron machines by this electronics scheme. The better signal-to-noise ratio is achieved by reducing the signal processing bandwidth by several orders of magnitude. As an illustrative example, the Fourier transformation of the signal from the GSI LINAC BPM is shown in Fig. II.9.109. The spectral power of the signal is mainly available at the bunch repetition harmonics nf_0. The position evaluation uses only this large signal power within the band of frequency span Δf, while the thermal noise is reduced as $U_{\text{eff}} \propto \sqrt{\Delta f}$. Technically, the pick-up signal is mixed with the accelerating frequency.

A mixer is a passive RF-device multiplying the two waves at the port RF (for radio frequency) and LO (for local oscillator). The product is available at port IF (for intermediate frequency). From a mathematical perspective, the mixer multiplies the two waves at LO and RF, and we get from a trigonometric

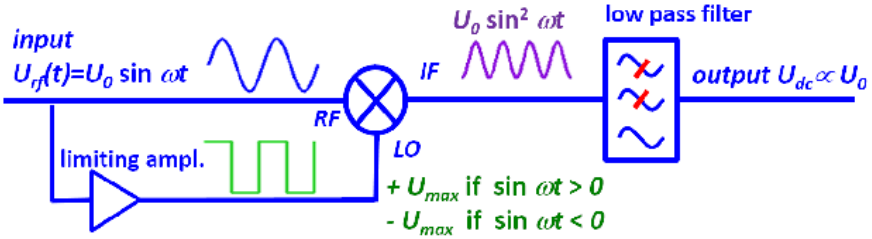

Fig. II.9.110: Scheme of a synchronous detector to rectify an RF signal.

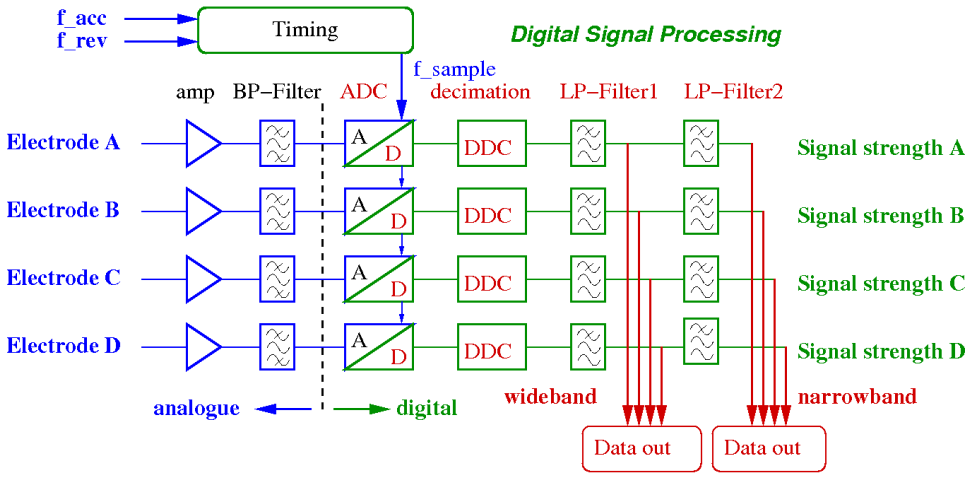

Fig. II.9.111: Scheme of digital BPM electronics as typically used at the storage rings of synchrotron light sources.

theorem [3]

$$A_{\mathrm{IF}}(t) = A_{\mathrm{RF}} \cdot A_{\mathrm{LO}} \cos \omega_{\mathrm{RF}} t \cdot \cos \omega_{\mathrm{LO}} t = \frac{1}{2} A_{\mathrm{RF}} \cdot A_{\mathrm{LO}} \left[\cos(\omega_{\mathrm{RF}} - \omega_{\mathrm{LO}})t + \cos\left(\omega_{\mathrm{RF}} + \omega_{\mathrm{LO}}\right) t\right]. \tag{II.9.123}$$

Typically 10.7 MHz, or one of its harmonics (due to its extensive use in telecommunication), is filtered out by a narrow bandpass filter.

In the next processing stage, the signal is rectified by a so-called synchronous detector, for which the schematics are shown in Fig. II.9.110 having the following functionality: The RF signal is split, and one branch is fed into a limiter amplifier driven into saturation, which transforms the signal to a bipolar rectangular pulse. This signal is mixed with the original signal to yield a unipolar waveform (corresponding to the square). It is passed then through a low-pass filter. An ADC then digitizes the resulting quasi-dc signal, and the position is calculated via software. In general, this technique is called heterodyne mixing, and the same principle is used in an analogue spectrum analyser. The mixing is equivalent to an average over many turns, leading to higher precision in the position reading. However, this method does not allow a turn-by-turn observation. This method can also be applied for a synchrotron with varying acceleration frequency, e.g., a proton synchrotron for non-relativistic velocities, because the varying accelerating frequency is changed in phase with the bunch signal, resulting in a constant intermediate frequency. Such a system is commercially available [145].

[3] $\cos x \cdot \cos y = 1/2 \cdot [\cos(x-y) + \cos(x+y)]$

II.9.5.9.3 Digital signal processing

The methods discussed above perform the BPM signal conditioning in an analogue manner; for most cases, it leads to a low bandwidth output, which is then digitized with a slow sampling ADC. Motivated by the intensive use in telecommunication, the properties of ADCs in terms of sampling rate and voltage resolution were significantly improved during the last decade; an overview of ADC technologies can be found in Refs. [146, 147]. Additionally, the digital signal processing capabilities were enhanced. Modern technologies tend to digitize the signal at an early stage of the signal path and replace the analogue conditioning with digital signal processing, e.g. performing the narrowband treatment in the digital domain. In most cases, the required parallel processing is realized on an FPGA basis (Field Programmable Gate Array) to ensure fast, real-time response [148]. On this digital basis, versatile treatments can be implemented without any hardware exchange [149], leading to higher flexibility for the application. An example is filtering one data set with different bandwidths to match the position and time resolution to the requirements; such digitalization and processing units are commercially available [143]. A simplified scheme of a typical electronics board designed for usage at synchrotron light sources is shown in Fig. II.9.111. The general functionality is described in the following:

- The analogue signal from the BPM electrodes (A to D in the figure) is conditioned by a linear amplifier with switchable gain adjustments to ensure a constant input level to the ADC.
- Analogue bandpass filtering is performed with a relatively small bandwidth of about 10 MHz at the acceleration frequency of typically 352 or 500 MHz, as used at most circular synchrotron light sources.
- The analogue signal, conditioned in the described manner, is digitized with a fast, high resolution ADC with a typical sampling rate of 200 MS/s and a nominal resolution of 16 bit. The sampling frequency f_{sample} is locked to the acceleration frequency f_{acc} using the principle of under-sampling [150] as discussed below.
- A Digital Down Converter DDC demodulates the digital data to a lower frequency range resulting in a data reduction. The DDC is the corresponding digital device to the analogue mixer [150].
- A digital filter increases the accuracy of the data. They are provided for external readout at the so-called wideband port with a bandwidth of typically 10 kHz. The difference over sum algorithm is performed digitally using the data from this port.
- Further filtering, required for precise closed-orbit determination at a rate of typically 100 Hz, is performed, and the result is provided at the narrowband port.

Due to the digital realization of the filter functions, the parameters can be adapted to the requirements of FPGA programming. The digital data can be used simultaneously for monitoring and feedback systems. If a turn-by-turn measurement is demanded, a single bunch is chosen as derived from the revolution frequency f_{rev} of typically 1 MHz to trigger the ADC. The advantage of digital signal processing is the excellent variability without hardware modification. Using digital filters, the bandwidth and, hence, the data rate and position resolution can be varied over a wide range and provided for different applications. There is no significant disadvantage of such systems; however, their versatile usage requires a large amount of engineering power for FPGA programming and matched data exchange and analysis.

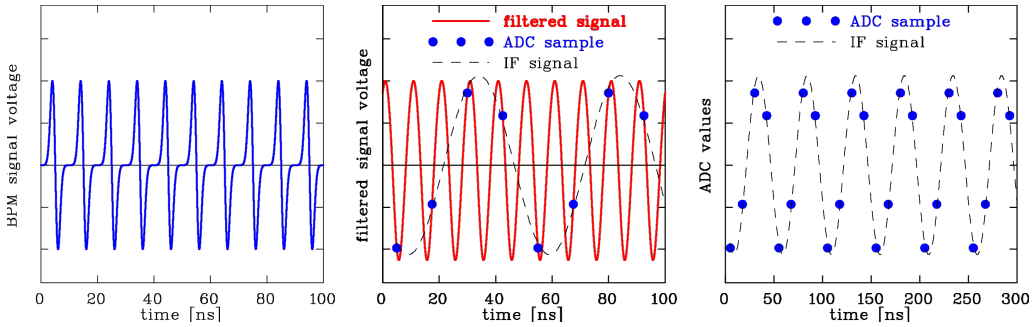

Fig. II.9.112: The schematic shows the principle of under-sampling as performed for a BPM signal (left) filtered at the acceleration frequency (middle). The right plot shows the resulting digital values on an enlarged time scale. For this example, the acceleration frequency is chosen as $f_{\mathrm{acc}} = 100$ MHz, and the sampling frequency is $f_{\mathrm{sample}} = 4/5 \cdot f_{\mathrm{acc}} = 80$ MHz, corresponding to four samples distributed over five bunches. The periodicity of the digital data is 50 ns corresponding to a bandwidth of 20 MHz for the reconstructed IF signal.

Principle of undersampling: Fig. II.9.112 depicts the general functionality of undersampling [150, 151]: Since a sine wave can be reconstructed from 4 values, a periodicity of the digitized values is achieved if the sampling frequency fulfils the condition $f_{\mathrm{sample}} = \frac{4}{4n+1} \cdot f_{\mathrm{acc}}$ with $n = 1, 2, 3....$ The value of n is chosen in such a way that f_{sample} has the closest value below the maximal sampling rate of the ADC. In time-domain, one can describe under-sampling in a way that a periodic signal is reconstructed from 4 digital values equally spaced over $4n + 1$ periods. The resulting reconstructed sine-wave is called IF signal for intermediate frequency, according to its analogue counterpart. For the typical case of a synchrotron light source with an acceleration frequency of $f_{\mathrm{acc}} = 500$ MHz, the ADC is sampled at $f_{\mathrm{sample}} = \frac{4}{4 \cdot 4+1} \cdot f_{\mathrm{acc}} = 117.6$ MHz corresponding to $n = 4$. This means that the signal is mirrored to a band from zero to $f_{\mathrm{acc}} - 4 f_{\mathrm{sample}} = 32$ MHz. This case can be described in the time-domain such that 4 ADC values are equally distributed over 17 bunches.

II.9.5.9.4 Comparison of BPM electronics

Table II.9.13 summarizes the advantages and disadvantages of the usual implementation of the discussed electronics schemes. All electronics methods can be adapted to the requirements in a flexible manner to compensate the related disadvantages partly. Analogue narrowband processing gives a high accuracy but cannot be adapted to requirements for bunch-by-bunch evaluation. For slow readout, digital signal processing delivers the same accuracy. The flexibility without hardware exchange is the key advantage of this modern scheme, which opens the possibility of versatile usage of position data. The BPM readout is realized in such a way at all new accelerators. For a proton synchrotron with an acceleration frequency $f_{\mathrm{acc}} \leq 10$ MHz, the BPM signal is amplified on a broadband basis preserving the bunch structure and the sampling is even performed in the baseband; the position is then calculated by digital signal processing. The discussed and further methods are reviewed in Refs. [120, 141].

II.9.5.10 Trajectory measurement

The term trajectory describes the position of a single bunch during its transport through the accelerator. It is the basic information of the initial alignment of the accelerator setting. Because the single bunch

Table II.9.13: Simplified comparison between various electronic processing schemes.

Type	Usage	Precaution	Advantage	Disadvantage
Broadband (analogue)	p-acc.	f_{acc} < 300 MHz	bunch monitoring post processing possible required for fast feedback	resolution limited by noise broadband hardware
Narrowband (analogue)	all	stable beams ≥ 10 μs	high resolution low detection threshold	no turn-by-turn complex analogue electronics
Digital Signal Processing	all	some bunches ADC with $\simeq 200$ MS/s	very flexible high resolution modern technology for future demands	limited time resolution due to under-sampling extensive digital hardware

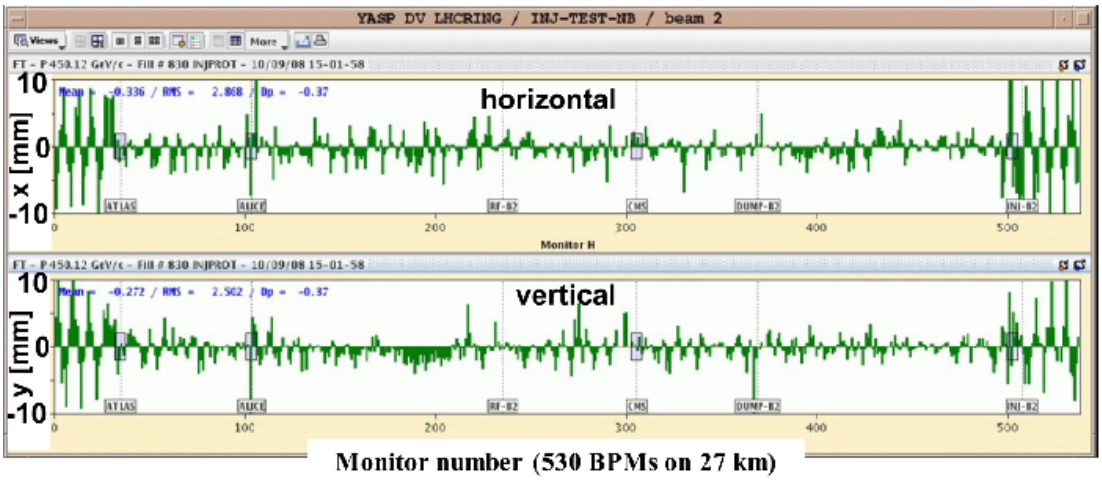

Fig. II.9.113: Measurement of the trajectory of a single bunch injected in the LHC with a position display at the 530 BPMs around the synchrotron, from Ref. [152].

position is monitored, broadband processing for the BPM electronics is used; the reduced position resolution is of minor concern for this measurement. As an example Fig. II.9.113 depicts the measurement of the trajectory of a single bunch injected into the LHC at the first days of its commissioning [152]. The position reading at each of the 530 BPM on the 27 km long synchrotron is displayed, showing some oscillations caused by mismatched injection parameters, which could be aligned later on with the help of this diagnostics. The same type of measurement can be done at transport lines in case an appropriate electronics chain is installed. For the transfer between synchrotrons, only a few bunches are transferred, and a broadband processing chain is applied.

II.9.5.11 Closed orbit measurement at a synchrotron

In a synchrotron, several BPMs are installed to determine the closed orbit. As a rule of thumb, an appropriate choice is to have four BPMs per tune value separated approximately by about $\mu \simeq 90^{\circ}$ betatron phase advance. The BPMs should be located at positions with a large value of the betatron function to have a reasonable spatial resolution even for small average beam excursions. The closed

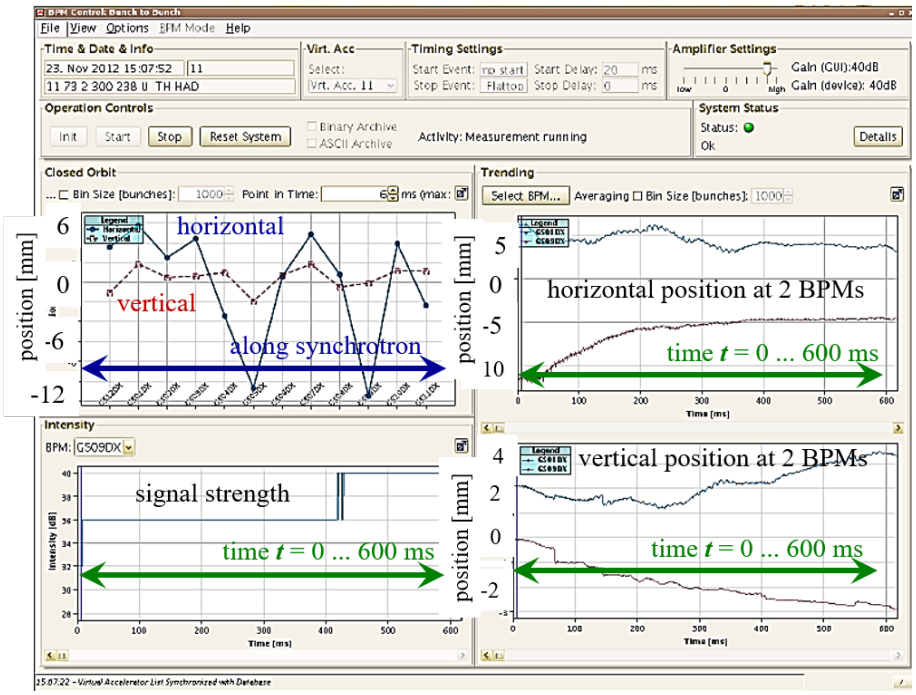

Fig. II.9.114: Example of a position measurement done at the GSI synchrotron for a partly misaligned beam during a 0.6 s long acceleration. The upper left top plot shows the position around the ring at 12 locations at the begin of the ramp; the upper right plot shows the horizontal position during the acceleration ramp for two BPM locations, the lower right plot the vertical position for these BPMs; the lower left plot is a signal power $\propto U_\Sigma^2$ during the ramp for a single BPM. The panel at the top is used for the control of pre-amplifiers and timing.

orbit is the central beam path along the circular accelerator, taking existing imperfections into account. The closed orbit might differ from the ideal path, defined by the centre of the quadrupole magnets. Only for a good alignment, the actual beam behaves as expected from beam optics calculations, e.g. no beam steering by the quadrupole magnets occurs. An example of position measurement is displayed in Fig. II.9.114 during the acceleration in the GSI synchrotron.

The position reading of the BPMs around the ring can be used as the input of a feedback loop to do an active beam correction, see, e.g. Refs. [153–155]. Such a feedback system is installed in most synchrotrons, but a description is out of the scope of this lecture.

II.9.5.12 Tune measurement

One essential parameter of a synchrotron is its tune. For synchrotrons operating at high currents, the tune shift and tune spread is of interest to find a large stable region in the working diagram. BPMs measure the centre of the bunched beam; hence, the beam must be excited to coherent betatron oscillations. First we define the betatron frequency f_β as

$$f_\beta = Q \cdot f_0 \tag{II.9.124}$$

as the tune Q expressed in relation to the revolution frequency f_0. The tune itself is the number of betatron oscillations per turn. The principle of a tune measurement related to position determination by BPMs is to excite a coherent transverse betatron oscillation, whose frequency gives the value of the tune.

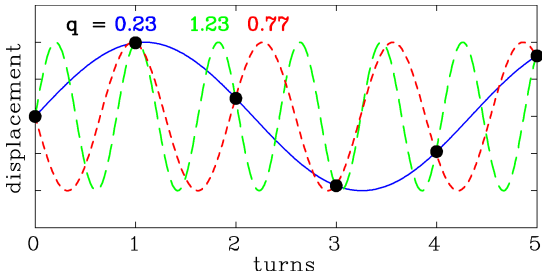

Fig. II.9.115: Schematic of the tune measurement for six subsequent turns determined with one BPM and the three lowest frequency fits.

The tune value can be split in two parts as $Q = Q_n + q$ with Q_n is the integer part and q fractional part; most measurement methods determine the fractional part q. The integer number of oscillations Q_n cannot be seen, but this is normally of no interest, as it is known from calculations. This behaviour is schematically shown in Fig. II.9.115 for the case of a turn-by-turn reading of one BPM: Using the position reading, a sine function can be fitted through the data, but one cannot distinguish between the lowest frequency (here $q = 0.23$) and higher values, leading to the fact that the fractional part is only uniquely defined for $0 < q < 0.5$. To distinguish between a value below or above 0.5, the focusing by the quadruples (i.e. the tune) can be slightly changed, and the direction of the shift of q can be observed. The calculation of q is done by a Fourier analysis of the time-domain data.

Most current methods are based on a frequency-domain treatment [156, 157]. Before discussing this, a more straightforward excitation method is described first, using a time-domain point-of-view.

II.9.5.12.1 The kick method, time-domain method

For this method, coherent betatron oscillations are excited by a fast kick. This kick has to be much shorter than the revolution time $1/f_0$ and is provided in most cases by the injection or extraction kicker installed in the machine anyhow. The strength of the kick has to be chosen sufficiently low to prevent beam losses. To achieve a reasonable resolution, the BPM should be located at a lattice point with a large value of the betatron function. The beam position is monitored turn-by-turn (broadband processing only) and it is stored as a function of time. The Fourier transformation of the displacements gives the fractional part q of the tune. An example from the GSI synchrotron is shown in Fig. II.9.116.

To understand the limitation of this method, one has to look at the single particle behaviour. At the time of the kick, the particles start a free betatron oscillation with the same phase, but each particle has a slightly different betatron frequency due to the tune spread. Even if the individual oscillations last for a long time, the coherent motion detected by a BPM is damped as a consequence of the de-coherence of the individual motion given by the time of the inverse betatron frequency spread, see Fig. II.9.117. A description is given in the frame of Landau damping. This damping, as given by the detuning of the transverse oscillation, limits the observation time and, correspondingly, the precision of the tune determination by this method. The tune is calculated from the position reading via Fourier transformation: A limited series of position measurements $x_1, x_2, ..., x_N$ of N consecutive turns with non-vanishing displacements are taken into account. The distribution function of the tune $P(q_i)$ is calculated via discrete

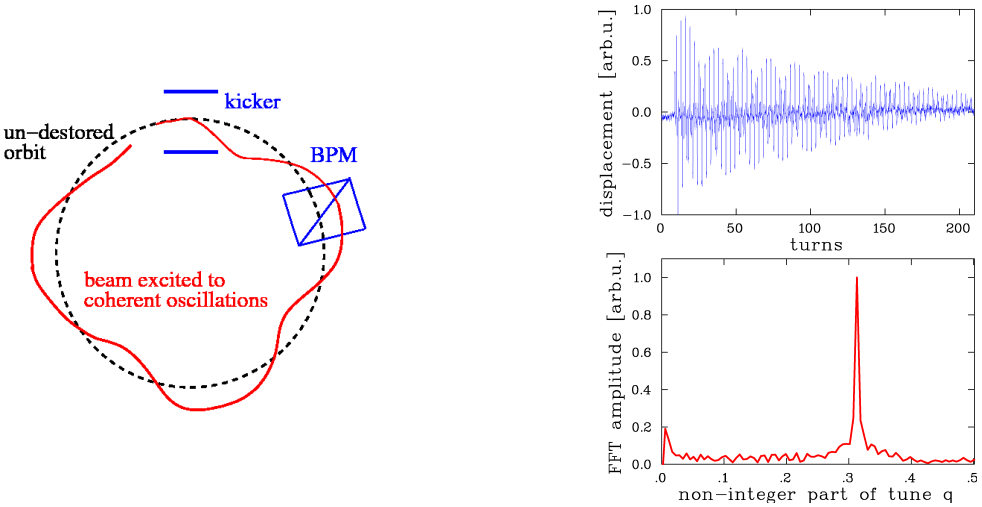

Fig. II.9.116: Left: Scheme of the beam excitation and detection of coherent bunch oscillations by a BPM. Right: Beam oscillations after a kick excitation recorded in time-domain for 200 turns (top) and its Fourier transformation for q determination (bottom) at the GSI synchrotron.

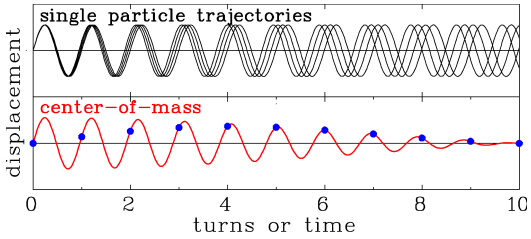

Fig. II.9.117: Plot of the individual trajectories of four particles after a kick (top) and the resulting coherent sum signal as measured by a BPM (bottom). (The tune spread is much too large for a real machine.)

Fourier expansion from the displacement reading via [151]

$$P(q_i) = \frac{1}{N}\sum_{n=1}^{N} x_n e^{-2\pi i n q_i} \quad . \tag{II.9.125}$$

As given by the properties of Fourier transformations, the discretisation of the obtained peak is generally related to the number of position samples N by [151, 156]

$$\Delta q = \frac{1}{2N} \quad . \tag{II.9.126}$$

Therefore, the peak in the distribution function $P(q_i)$ has at least this width. To achieve an adequate resolution of typically $\Delta q \simeq 10^{-3}$, at least $N = 500$ turns of non-vanishing displacements are needed. In a lot of practical cases, the de-coherence time is shorter than this border, as demonstrated in Fig. II.9.116. The described straightforward method is not very precise. However, some improved analysis methods using digital filters exist to achieve better precision; see, e.g. Ref. [158].

An additional drawback of such a measurement is a blow-up of the transverse emittance of the stored beam because the excitation of the individual particles are damped much slower than the coherent

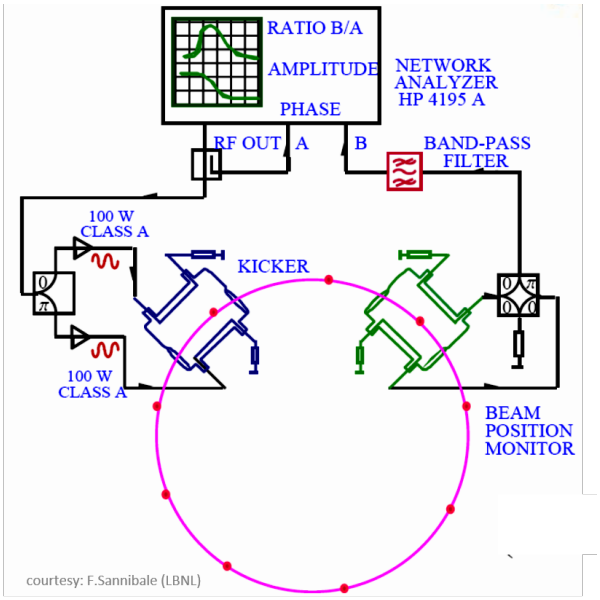

Fig. II.9.118: Scheme of a beam transfer function (BTF) measurement.

motion, as depicted in Fig. II.9.117. This method can thus be used for electron synchrotrons, where the particle's motions are damped relatively fast by synchrotron radiation (typical time scale of seconds), and the tune resolution requirement is not more than typically 10^{-3}.

II.9.5.12.2 Beam transfer function measurement by a frequency chirp

An RF method for tune determination uses a beam excitation driven by a continuous sine wave stimulus. This wave is swept slowly, within typically one second over a certain band, and the beam response is measured in coincidence. The device used in RF engineering for this purpose is a network analyser; see e.g. Ref. [159]. It provides a frequency scan over a user-given range, amplified and applied to the beam via an RF exciter. Generally, an exciter is constructed comparable to a BPM but fed with the external RF-signal to excite the beam to coherent oscillations. The normalised difference signal U_Δ/U_Σ from the BPM is fed to the input of the network analyser, as shown in Fig II.9.118. Here the amplitude and phase relative to the excitation are measured precisely and displayed. The horizontal axis of the display corresponds to the frequency band for the beam excitation. The displayed spectrum represents the **B**eam **T**ransfer **F**unction **BTF**, which can be defined as the transverse velocity response to the given transverse kick. Besides the name BTF measurement, this method is sometimes called "beam excitation by a frequency chirp". Modern installations use a performant frequency generator associated with a matched ADC with a recording in time-domain; for the analysis, data are digitally Fourier transformed.

Due to practical reasons, a harmonic of the revolution frequency f_0 is used for the excitation and the resulting resonance line is expressed in terms of these harmonics. An example of such a measurement with an excitation around the $h = 25^{th}$ revolution harmonics is shown in Fig. II.9.119. The beam reacts as a driven oscillator with a resonance as given by the tune value. Because only the fractional part can be measured, this resonance is located at $f_h^{\pm} = (h \pm q)f_0$ on both sides of the revolution frequency and are called lower and upper sideband. From the distance of the sidebands, the fractional part of the tune q is determined. The resonance nature of the BTF measurement can also be seen from the phase shift of

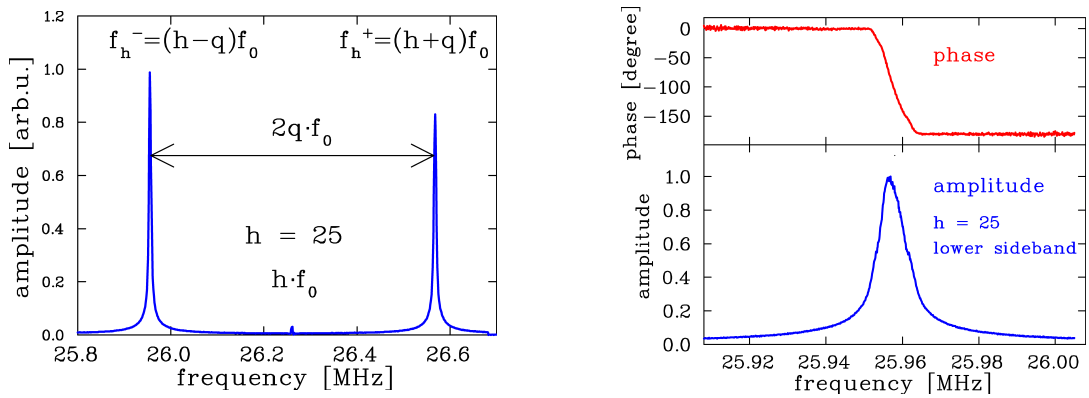

Fig. II.9.119: BTF measurement at the GSI synchrotron with a 500 MeV/u U^{73+} beam having a revolution frequency of $f_0 = 1.048$ MHz. The wide scan around the $h = 25^{th}$-harmonics is shown left, and a scan around a lower sideband centred at f_{25}^- on the right for amplitude and phase. The fractional tune is $q = 0.306$ for these data.

180^o during resonance crossing, as shown in on the right side of Fig. II.9.119. An analytic expression for the BTF can be found in Ref. [160] based on the theory of a driven oscillator including Landau damping. From the width of a sideband, the tune spread can roughly be estimated as $\Delta q \simeq \frac{\Delta f}{h f_0}$. For a more detailed evaluation of the sideband-width for beams with low space charge contributions, i.e. for the validity of linear beam optics, one has to take the longitudinal momentum into account, resulting in a more complex description of the sideband width (see Eq. II.9.128) as discussed below.

With this method, a high precision of the tune value q up to 10^{-4} can be reached. Such a measurement might take some time (up to several minutes) because the frequency has to be swept, the response to one single frequency is measured at a given time. The sweep velocity determines the resolution, i.e., a slow sweep yields a better resolution. In addition, the sweep velocity has to be slow enough to allow the transient beam response to die out and a steady-state response to be attained. The measurement can also be done using sensitive BPM electronics with an un-bunched beam.

From the width of the sidebands, the chromaticity can be deduced for low current beams, assuming that the tune spread ΔQ is mainly determined by chromaticity ξ in connection with momentum spread $\frac{\Delta Q}{Q_0} = \xi \frac{\Delta p}{p_0}$ and not by space charge effects. (The related formulas are collected in Appendix II.9.12.) From the position of the sidebands $f_h^{\pm} = (h \pm q) f_0$ and the product rule of the frequency derivative for the frequency distribution and the tune q one gets

$$\Delta f_h^{\pm} = \Delta f_0 (h \pm q) \pm \Delta q f_0. \tag{II.9.127}$$

Inserting the definition of frequency dispersion η Eq. II.9.180 and chromaticity ξ Eq. II.9.182 leads to

$$\begin{aligned} \Delta f_h^- &= \eta \frac{\Delta p}{p} \cdot f_0 \left(h - q + \frac{\xi}{\eta} Q \right) \quad \text{lower sideband} \\ \Delta f_h^+ &= \eta \frac{\Delta p}{p} \cdot f_0 \left(h + q - \frac{\xi}{\eta} Q \right) \quad \text{upper sideband.} \end{aligned} \tag{II.9.128}$$

First, one can see that the sideband widths are unequal. Which band is broader, depends on the sign of the chromaticity ξ (in most case negative), on q and the harmonic number. In Fig. II.9.119 this is not

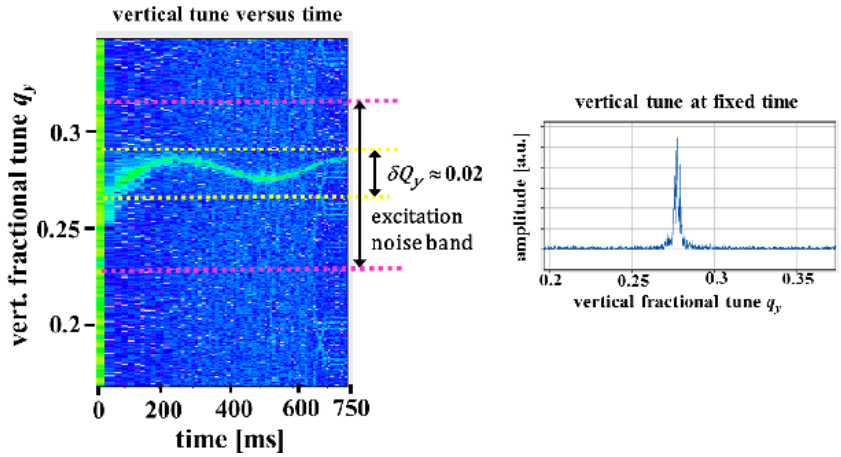

Fig. II.9.120: Left: Measurement of the tune at the GSI synchrotron for an Ar^{10+} beam accelerated from 11 to 300 MeV/u within 0.75 s [161]. Displayed is the Fourier transformation of displacements of successive individual bunches over 4096 turns excited by the depicted noise band during acceleration as a function of time. The maximum of the Fourier transformation is colour-coded in a linear manner; δQ_y is the variation of the tune value. Right: Single tune spectrum 110 ms after the ramp start averaged over 4096 turns corresponding to $\sim$ 15 ms.

clearly seen due to the large scale, but the height is lower for the left sideband corresponding to a large width because the integral power is equal for both sidebands. From the width of the sideband, we have a measurement of the chromaticity without any beam excitation. Of course the other parameters $\Delta p/p$, η (or γ_{tr}) and q have to be measured independently.

II.9.5.12.3 Noise excitation of the beam

Instead of a frequency scan excitation, a wide-band RF signal can be applied. The beam is excited by the same frequency spectrum as delivered by a network analyser. However, here the excitation takes place for all frequencies simultaneously, using white noise of adequate bandwidth being wider than the tune variation. The position reading is done in the time-domain using a fast ADC recording each bunch. The position data for each bunch are Fourier-analysed, and the spectrum is drawn corresponding to the tune value. An example is shown in Fig. II.9.120 from the GSI synchrotron during acceleration [161]. The resolution for the tune is given by the inverse of the averaging time for one FFT calculation (for the data in Fig. II.9.120 in the order of some ms, corresponding to 4096 turns), leading to about $\Delta Q \sim 3 \cdot 10^{-3}$ for one single scan. Due to the band excitation a time-resolved observation of the tune is possible during the entire acceleration ramp.

II.9.5.13 Measurement of lattice functions

The technique of beam excitation can also be used to determine the parameters of the lattice functions as calculated by the beam optics. In particular, local values of dispersion and β-function as well as the global quantity chromaticity has been measured with this technique. Knowledge of these parameters is important during the commissioning of a new machine, the control of mechanical misalignment, and a check of critical settings, e.g. close to a low-beta insertion. If required, the values of the local lattice function can be corrected by applying correction magnets inside the synchrotron. Only the basics of these

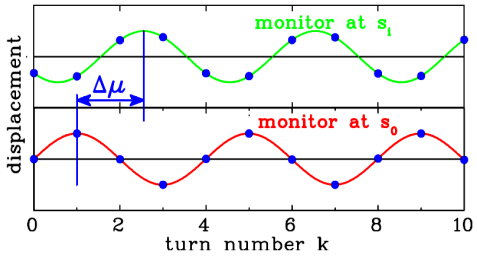

Fig. II.9.121: Scheme of the individual measurements at two BPMs for a phase advance $\Delta\mu$ determination. A sine function can be fitted through the data points.

regularly applied measurements are discussed here; further descriptions can be found in Refs. [154–157].

The dispersion function $D(s)$ at a position s in the synchrotron is defined as

$$x(s) = D(s)\frac{\Delta p}{p} \tag{II.9.129}$$

with $x(s)$ being the displacement for a given momentum deviation Δp from the nominal momentum p. The dispersion function $D(s)$ can be determined at the BPM location s by a slight momentum change of the beam with the help of a frequency detuning of an accelerating cavity while keeping the setting of all magnets constant, which leads to a small acceleration or deceleration of all particles. For several momentum settings Δp, a position measurement x with the BPM is performed. The resulting position measurements x are then plotted as a function of the momentum deviation $\Delta p/p$; the dispersion D at the BPM location is the slope of this curve.

Having a turn-by-turn readout of several BPMs, the coherent betatron oscillation of a single bunch can be monitored. The position reading at a BPM i located at s_i for turn number k is given by

$$x_{ik} = \hat{x}_i \cdot \cos\left(2\pi Qk + \mu_i\right) = \hat{x}_0 \cdot \sqrt{\frac{\beta(s_i)}{\beta(s_0)}} \cos\left(2\pi Qk + \mu_i\right) \tag{II.9.130}$$

with $\hat{x}_i$ the amplitude at the BPM i, $\hat{x}_0$ the amplitude at a reference BPM at s_0, $\beta(s_i)$ and $\beta(s_0)$ the β-functions at these BPMs, Q the tune and μ_i the betatron phase at s_i with respect to the reference location.

The ratio of the β-functions can be determined by a comparison of the amplitudes at these two locations

$$\frac{\beta(s_i)}{\beta(s_0)} = \left(\frac{\hat{x}_i}{\hat{x}_0}\right)^2. \tag{II.9.131}$$

The accuracy of such a measurement might not be high, because the absolute calibration of the BPM enters the calculation.

Alternatively, a β-function measurement is based on the determination of the phase advance between two BPM locations as

$$\Delta\mu = \mu_i - \mu_0 \tag{II.9.132}$$

with high accuracy by fitting a sine function to the measured data, as schematically plotted in Fig. II.9.121. It leads to another way of β-function measurement, using the betatron phase difference

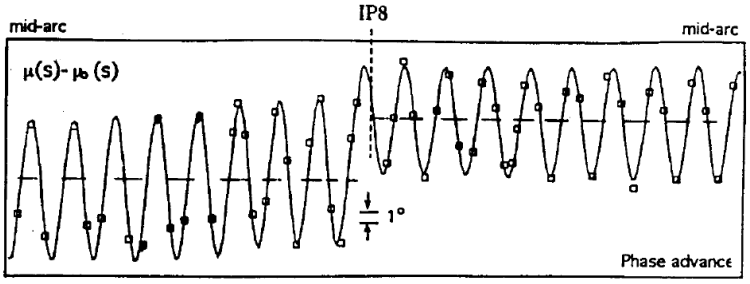

Fig. II.9.122: Result of a betatron phase measurement at LEP. The difference between the measured phase $\mu(s)$ and the calculated phase $\mu_0(s)$ for the linear optics model is shown for each BPM location around the interaction point IP, from Ref. [162].

$\Delta\mu$ between the two locations s_0 and s_i as

$$\Delta\mu = \int_{s_0}^{s_i} \frac{ds}{\beta(s)} \quad , \tag{II.9.133}$$

where the measured value $\Delta\mu$ is compared to the result using the theoretical β-function for the optical model of the synchrotron.

In Fig. II.9.122, such a measurement is shown as recorded at the e^+e^- collider LEP previously in operation at CERN [162]. The difference between the theoretical phase as calculated by the optical model using MAD code and the measured phase determined from 1024 turns for each BPM is plotted. The deviation is in the order of 10^o with an additional shift related to the strong focusing close to the interaction point to achieve the luminosity at the collision point of the e^+ and e^- beams. Such deviations are caused by the magnets' unavoidable mechanical and electrical misalignments; for the depicted case, it corresponds to less than 1 % of the nominal quadrupole settings. With the help of the correction dipoles and separately controllable quadrupoles, the betatron phase advance can be adjusted, and, hence, the β-function and the related beam size is controlled. Such measurements are of great importance to control the corrector setting and achieve the nominal beam parameters, particularly at circular colliders and synchrotron light sources. Advanced measurement techniques and analysis methods for determining β-functions and further optics parameters are summarised in Refs. [154, 155, 163].

The focusing of a quadrupole depends on the particle momentum, resulting in a change of the tune for different momenta. It is described by the chromaticity ξ defined as

$$\frac{\Delta Q}{Q} = \xi \frac{\Delta p}{p} \quad . \tag{II.9.134}$$

This value can be determined directly by a slight momentum change using a detuned RF-frequency, i.e. the same procedure described above for the dispersion function measurement. The tune is then measured as discussed above and plotted as a function of the momentum deviation; the value of ξ is given by the slope, as shown in Fig. II.9.123. A linear behaviour between $\Delta p/p$ and $\Delta Q/Q$ is only valid in a small momentum interval (here $\Delta p/p = \pm 0.1\%$). For larger deviations, non-linear forces from the synchrotron magnets contribute significantly. Instead of changing the RF-frequency, one can also change the magnetic field of the main dipole magnets because this type of measurement is based on the detuning between ideal closed orbit and revolution frequency. The chromaticity can also be determined locally by

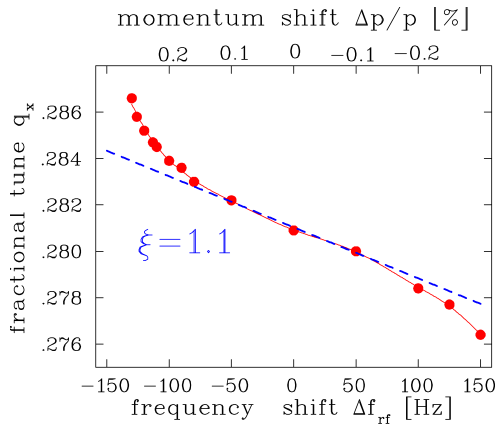

Fig. II.9.123: Measurement of the chromaticity at LEP. The horizontal tune is determined for different settings of the acceleration frequency and, therefore, of the momentum of the circulating beam. The chromaticity is fitted through the linear part of the data [164].

comparing the measured betatron phase advance using Eq. II.9.130 with the tune Q as a fit parameter (the β-function has to be known). These measurements have to be repeated for different Δp. Examples of measurements and further references are given in Ref. [154].

II.9.6 Measurement of longitudinal parameters

Longitudinal parameters are described comparably as the transverse parameters. The longitudinal phase-space, as depicted in Fig. II.9.124, is spanned by two variables:

- The longitudinal spread of the bunch l is determined in units of length [mm], time [ns] or phase [° degrees with respect to the accelerating frequency f_{rf}]. The mean value is the centre of the bunch relative to f_{rf} or relative to the ideal reference particle. The corresponding transverse value is the transverse beam profile. The quantity has no meaning for a coasting beam, e.g., in a proton storage ring.
- The momentum spread $\delta = \Delta p/p$ is the deviation relative to the momentum p of the ideal reference particle. Instead of the momentum, it is sometimes common for proton LINACs and cyclotrons to relate the quantity beam energy $\Delta E_{\mathrm{kin}}/E_{\mathrm{kin}}$ or even only ΔE_{kin} is given. The corresponding transverse value is the beam divergence.

The value of longitudinal emittance ϵ_{long} is given by the product of the two above mentioned quantities

$$\epsilon_{\mathrm{long}} = \frac{1}{\pi}\int_A dl d\delta. \tag{II.9.135}$$

where A is the area of the phase-space occupied by the beam particles, see Fig. II.9.124. Linear transformations can be applied similarly to the transverse case; see Section II.9.4.1. The normalised longitudinal emittance

$$\epsilon_{\mathrm{long}}^{\mathrm{norm}} = \frac{v_s}{c}\gamma_{\mathrm{rel}} \cdot \epsilon_{\mathrm{long}} \tag{II.9.136}$$

is preserved under ideal conditions where v_s is the longitudinal velocity and γ_{rel} is the relativistic Lorentz factor.

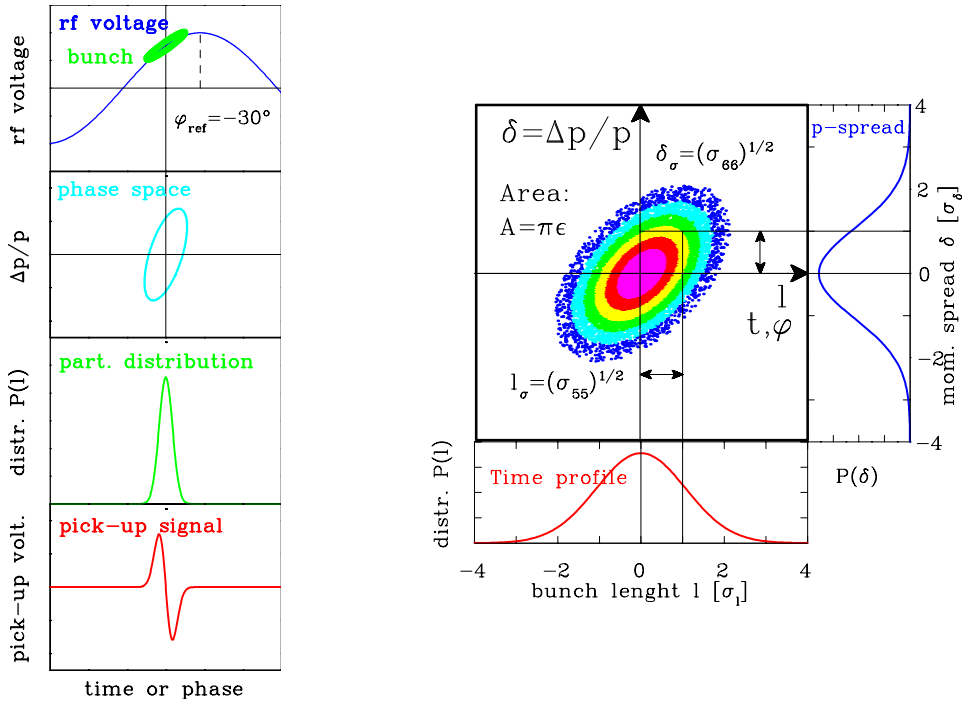

Fig. II.9.124: Left: The relation between the accelerating voltage and the longitudinal emittance, as well as the time distribution of the bunches as measured with the differentiated pick-up signal. Right: The longitudinal phase-space plot of a Gaussian distribution.

Using BPM electrodes as monitors, the projection of the phase-space distribution on the time axis is determined, resulting in the bunch position and width. A determination of the emittance by linear transformation is possible. Some conditions must be fulfilled for a capacitive pick-up to guarantee an adequate interpretation: Firstly, the bunch has to be much longer in the longitudinal direction than the BPM electrode. For bunches with a length comparable to the electrode, a second condition is that the beam must be sufficiently relativistic to ensure that the beam's electric field is essentially transverse. For the transverse electric field component $E_\perp$ for a cylindrical symmetry, Lorentz transformation [18] gives an enhancement in the laboratory frame compared to the rest-frame of moving charge by

$$E_{\perp,lab}(t_{\rm lab}) \simeq \gamma \cdot E_{\perp,rest}(t_{\rm rest}) \quad , \tag{II.9.137}$$

see the more detailed discussion in Section II.9.6.1, in particular concerning the transformation of the time $t_{\rm rest}$ to $t_{\rm lab}$, which is important for non-relativistic particle velocities, e.g. at proton LINACs. In this case, the second condition is not fulfilled, and other methods have to be applied. The signal does not reflect the longitudinal bunch shape for bunches shorter than the capacitive BPM electrodes. For electron beams, the bunch length is so short that the bunch structure is smeared out by integration on the BPM capacitance, i.e. expressed in terms of electrical parameters by the limited bandwidth. Here the monitoring of synchrotron radiation is used in connection with the fast optical method using streak cameras.

A measurement of the energy- or momentum spread $\delta = \Delta p/p$ is not discussed in detail here. A magnetic spectrometer can be used for this purpose, having a point-to-point focus in connection with

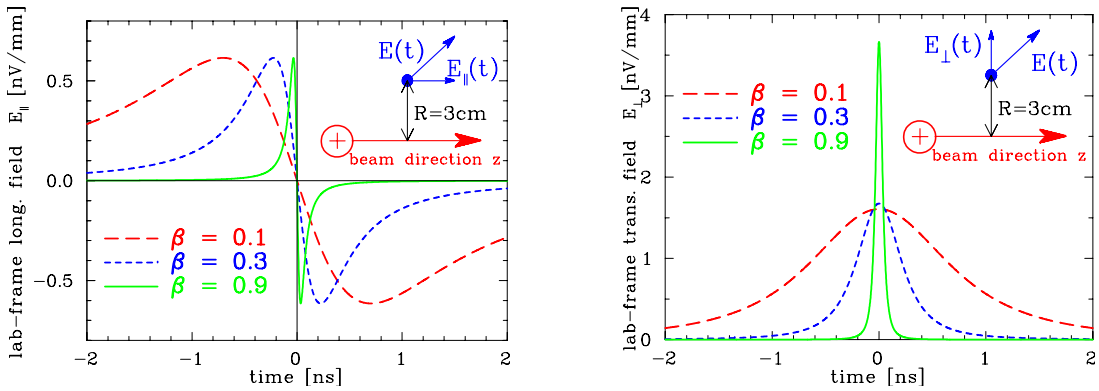

Fig. II.9.125: Effect of the advanced longitudinal (left) and transverse (right) electric field at an observation location $R = 30$ mm from the beam axis for different velocities of a point-like charge. For $t_{\mathrm{rest}} = t_{\mathrm{lab}} = 0$ the closest approach is reached.

small slits located at appropriate locations. The beam's momentum distribution leads to an additional profile width $\sigma_p = D(s) \cdot \Delta p/p$ with the dispersion function $D(s)$ along the transfer line, which can be determined by a profile measurement. The related optical setup is discussed in textbooks on beam optics, e.g. Ref. [167].

II.9.6.1 Electric fields of a relativistic charge

Due to the finite velocity of light, the electric field of a moving charge is modified as given by the Lorentz transformation. Figure II.9.125 shows the electric field of a single moving charge for different velocities β: The longitudinal electrical field $E_{\parallel}(t)$ in the lab-frame has been calculated for a single particle with a charge of $1e$, travelling in empty space, measured according to the time in the lab-frame, i.e. $t_{\mathrm{lab}} \equiv t$. It is calculated by the relativistic Lorentz-boost, including the transformation of the time coordinate [18] to be

$$E_{\parallel,lab}(t) = -\frac{e}{4\pi\varepsilon_0} \cdot \frac{\gamma\beta ct}{\left[R^2 + (\gamma\beta ct)^2\right]^{3/2}} \quad . \tag{II.9.138}$$

R is the distance of closest approach and $\gamma = \left(1-\beta^2\right)^{-1/2}$ the relativistic Lorentz factor. The transverse field component $E_{\perp}$ in the lab-frame is given by

$$E_{\perp,lab}(t) = \frac{e}{4\pi\varepsilon_0} \cdot \frac{\gamma R}{\left[R^2 + (\gamma\beta ct)^2\right]^{3/2}} \quad . \tag{II.9.139}$$

The above formulas are valid for a free particle and are modified by the boundary condition of the metallic surface, e.g. of the beam pipe or the BPM electrodes. A beam bunch consist of many particles distributed within a certain volume; to calculate the accompanying electric field, one has to integrate over the bunch volume. For non-relativistic velocities, the electric field arrives earlier at the electrodes and does not reflect the charge distribution of the bunch, see Section II.9.6.7 for more details.

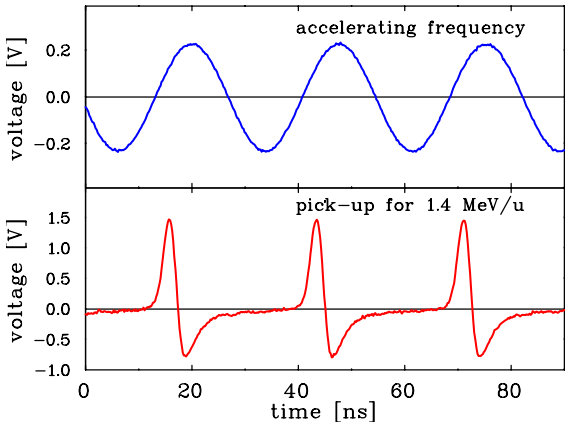

Fig. II.9.126: The LINAC cavity accelerating frequency (top) and the corresponding BPM signal recorded by a capacitive pick-up (bottom) for the determination of the bunch zero crossing from a 1.4 MeV/u ion beam.

II.9.6.2 Determination of phase position

For the matching of beam parameters at successive LINAC cavities, the correct phase relation between the accelerating frequency and the bunch arrival has to be determined by beam-based measurements. Figure II.9.126 shows a typical measurement for a slow 1.4 MeV/u ion beam recorded by a capacitive BPM as depicted in Fig. II.9.93. Due to the differentiated beam signal, the centre of the bunch is well determined. Due to the different cable lengths, there is an arbitrary but fixed phase shift between the BPM signal and accelerating frequency f_{rf}. The corresponding transverse quantity is the horizontal or vertical beam position.

II.9.6.3 Determination of non-relativistic mean energy

The final beam energy of a LINAC cavity is sensitive to the actual setting of the RF amplitude and the phase relative to the preceding cavities. Therefore, energy determination is important for beam transmission optimisation. A measurement can be performed for non-relativistic energies using two BPM electrodes separated by the distance L and a **T**ime-**o**f-**F**light **ToF** measurement; see, e.g. Refs. [64, 165]. As displayed in Fig. II.9.127, two BPM electrodes are installed in a straight section with a typical distance of several meters. This distance L has to be known precisely to an accuracy of typically 1 mm. The bunch centre-of-mass can be read from the oscilloscope, or the correlation function between the two signals can be calculated. Figure II.9.128 depicts a typical measurement. As shown in the schematic, several bunches are between the BPMs, and an estimate of the velocity is needed to determine the number of bunches for a unique solution. The beam's mean velocity is calculated for the measured time t_{scope} via

$$\beta c = \frac{L}{NT + t_{\mathrm{scope}}} \tag{II.9.140}$$

with N bunches between the BPMs and the bunch repetition time $T = 1/f_{\mathrm{rf}}$.

The accuracy of such a velocity measurement $\Delta\beta/\beta$ is given by the uncertainty of the distance

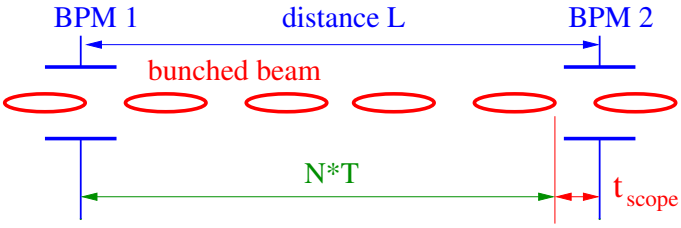

Fig. II.9.127: Principle of a ToF measurement using two pick-ups.

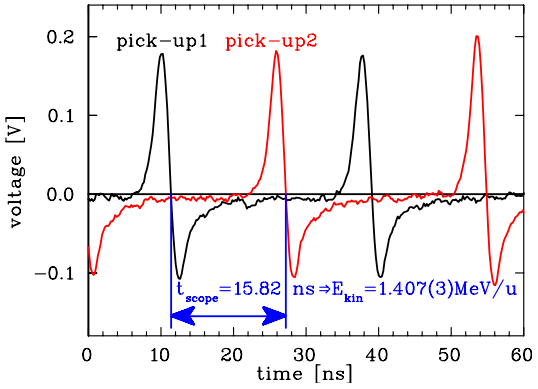

Fig. II.9.128: Time-of-flight signal from two pick-ups with $E_{\mathrm{kin}} \simeq 1.4$ MeV/u at the GSI-LINAC. The frequency is $f_{\mathrm{rf}} = 36.136$ MHz $\Leftrightarrow T = 1/f_{\mathrm{rf}} = 27.673$ ns. For the distance $L = 1.629$ m between the pick-ups $N = 3$ bunches are between the pick-ups. Inserting the time difference of $t_{\mathrm{scope}} = 15.82$ ns in Eq. II.9.140, the velocity $\beta = 0.05497(7)$ and the corresponding beam energy $E_{\mathrm{kin}} = 1.407(3)$ MeV/u are calculated. The error is given by Eq. II.9.141 inserting the uncertainties of $\Delta t = 0.1$ ns and $\Delta L = 1$ mm.

Table II.9.14: The energy resolution for a ToF measurement with a pick-up distance of 3.25 m for some GSI LINAC modules (GSI-internal LINAC module names are given). The RF-frequency is $f_{\mathrm{rf}} = 36.14$ MHz, and the assumed time accuracy is 100 ps.

Physical parameter	Units	RFQ	IH1	IH2	AL4
energy E_{kin}	[MeV/u]	0.12	0.75	1.4	11.4
velocity β	%	1.6	4.0	5.5	15.5
total ToF	[ns]	677	271	197	70
bunch spacing $\beta c/f_{\mathrm{rf}}$	[cm]	13	33	45	129
resolution $\Delta E_{\mathrm{kin}}/E_{\mathrm{kin}}$	%	0.07	0.10	0.12	0.22

ΔL and the scope reading Δt to be

$$\frac{\Delta\beta}{\beta} = \sqrt{\left(\frac{\Delta L}{L}\right)^2 + \left(\frac{\Delta t}{NT + t_{\mathrm{scope}}}\right)^2} \quad . \tag{II.9.141}$$

An accuracy better than 0.1 % for the energy spread $\Delta E_{\mathrm{kin}}/E_{\mathrm{kin}} = 2\Delta\beta/\beta$ can be reached, assuming an accuracy for the distance of $\Delta L = 1$ mm and $\Delta t = 100$ ps for the time measurement. Those parameters used at the GSI-LINAC are summarised in Table II.9.14. The ToF measurement resolution should be of the same order as the momentum (or energy) spread of the bunched beam, which for typical cases at proton LINACs is in the order of 0.1 to 0.3 %

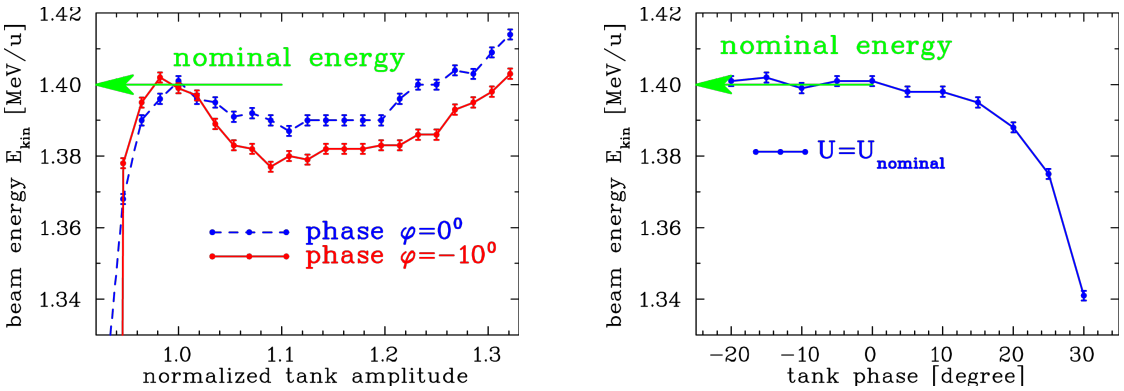

Fig. II.9.129: Left: The output energy of the GSI-LINAC is depicted as a function of the applied RF-amplitude inside the cavity for the parameter in Fig. II.9.128. Right: The phase for the nominal amplitude is shown. The required energy of this module is 1.400 MeV/u. The distance between the BPMs is $L = 1.97$ m with $N = 4$ bunches between subsequent monitors.

The procedure depicted in Fig. II.9.128 is executed by a time-domain processing with a broadband analogue electronics chain and a recording by a fast-sampling oscilloscope. Frequency-domain processing is preferred in recent applications as it is more common for today used electronics. One of the acceleration frequency harmonics is chosen, and digital signal processing methods calculate the phase of this narrowband processing; it corresponds to the phase of the Fourier transformation at the chosen frequency for the arrival of the bunch at the BPM locations. The phase difference with respect to the acceleration frequency's phase acts as the reference value. Assuming a comparable bunch shape at the two BPM locations for the ToF measurement, the difference between those two phases can be converted to a time scale for the velocity calculation.

A LINAC cavity's final beam energy depends on the accelerating RF amplitude and phase. Figure II.9.129 shows a measurement for an ion beam of 1.400 MeV/u nominal energy. This nominal energy is reached only in a small interval; for the displayed case, the allowed amplitude range is below ± 2 %, and the phase should be aligned within $\pm 10^o$. This corresponds to a relatively small range and calls for a precise beam alignment and substantial accuracy in the ToF measurement, as demonstrated by the small error bars in Fig. II.9.129. Matching the nominal beam energy of a LINAC module is an essential task because the energy acceptance of the following module is typically restricted within several percent, and a sufficient beam transmission through a chain of LINAC modules is only achieved if all modules produce the right energy increase. Moreover, the longitudinal emittance depends strongly on the correct RF amplitude and phase setting.

Even though the ToF method is commonly called energy measurement, it is basically a velocity determination. This method can not be applied to electron beams because electrons are relativistic after the first LINAC modules. Acceleration of electrons is more related to an increase in their momentum; consequently, the energy determination by the bending of a dipole magnet is more appropriate in this case. Because of the dependence of the bending radius on the particle momentum Δp with respect to the reference particle of momentum p_0, the momentum distribution is transferred to a distribution in the horizontal plane. This is described by the optical parameter dispersion $D(s)$ as the additional beam offset is $\Delta x(s) = D(s) \cdot \Delta p/p_0$. However, the resulting profile is a mixture of the transverse and longitudinal

parameters, and transverse collimation is required at the entrance of the optical system; see the discussion in textbooks on beam optics, e.g. Ref. [167].

II.9.6.4 Longitudinal emittance from linear transformation

In some cases, the length of the bunches fits the length of the capacitive or stripline electrodes of a BPM to get reliable information on the bunch structure. The longitudinal emittance can then be determined from linear transformations, similar to the transverse case described in Sections II.9.4.4 and II.9.4.5. The quadrupole variation corresponds to the change of the longitudinal focusing performed by a buncher; see Fig. II.9.130. The phase of a buncher is adjusted to 0^o, so no acceleration for the central reference particle is present. By varying the amplitude, the bunch can be longitudinally focused, i.e. compressed at the measurement location. The action is described in the longitudinal sub-space ($l, \delta = \Delta p/p$), which is a part of the entire 6-dimensional phase-space describing both transverse and the longitudinal planes [4]. The general transfer matrices $\mathbf{R}$ for the transverse and longitudinal phase-space have 6×6 elements, as does the beam matrix $\boldsymbol{\sigma}$. Disregarding any transverse-longitudinal coupling (e.g. by a dipole magnet), the longitudinal phase-space corresponds to the "lower right" part of the full 6×6 matrices, having the indices 5 and 6. The reduced 2×2 transfer matrix of a buncher $\mathbf{R}_{\mathrm{buncher}}$ is given in thin lens approximation by [99, 166]

$$\mathbf{R}_{\mathrm{buncher}} = \begin{pmatrix} 1 & 0 \\ -1/f & 1 \end{pmatrix} \quad , \tag{II.9.142}$$

where the focal length f is given by

$$\frac{1}{f} = \frac{2\pi q U_0 f_{\mathrm{rf}}}{A p v^2} \tag{II.9.143}$$

with the voltage amplitude U_0 of the accelerating wav e with frequency f_{rf} for a particle of charge q and mass number A with velocity v and momentum p. The transfer matrix for a drift space of length L is given by

$$\mathbf{R}_{\mathrm{drift}} = \begin{pmatrix} 1 & L/\gamma_{\mathrm{rel}}^2 \\ 0 & 1 \end{pmatrix} \quad , \tag{II.9.144}$$

where γ_{rel} is the relativistic Lorentz factor. As for the transverse case, the emittance can be determined by an amplitude variation U_0 of the buncher leading to different longitudinal focusing. A measurement of the bunch length at location s_1 has to be performed for at least three settings of the buncher. The beam matrix $\boldsymbol{\sigma}(0)$ at the buncher location s_0 has to be determined. For the bunch width $l_{\max}(1, f_k) = \sqrt{\sigma_{55}(1, f_k)}$ at location s_1, a system of linear equations for $\sigma_{ij}(0)$ in the form

$$\begin{aligned}
\sigma_{55}(1, f_1) = &\quad R_{55}^2(f_1) \cdot \sigma_{55}(0) + 2R_{55}(f_1)R_{56}(f_1) \cdot \sigma_{56}(0) + R_{56}^2(f_1) \cdot \sigma_{66}(0) \quad \text{focusing } f_1 \\
\sigma_{55}(1, f_2) = &\quad R_{55}^2(f_2) \cdot \sigma_{55}(0) + 2R_{55}(f_2)R_{56}(f_2) \cdot \sigma_{56}(0) + R_{56}^2(f_2) \cdot \sigma_{66}(0) \quad \text{focusing } f_2 \\
&\quad \vdots \\
\sigma_{55}(1, f_n) = &\quad R_{55}^2(f_n) \cdot \sigma_{55}(0) + 2R_{55}(f_n)R_{56}(f_n) \cdot \sigma_{56}(0) + R_{56}^2(f_n) \cdot \sigma_{66}(0) \quad \text{focusing } f_n
\end{aligned}$$

[4] The 6-dim phase-space is spanned by the vector $\vec{x} = (x, x', y, y', l, \delta)^t$ and with the help of the 6×6 transport matrices $\mathbf{R}$ the linear behaviour of the accelerator can be described including the coupling between the horizontal, vertical and longitudinal degree of freedom. For the formula used here, the bunch length l is given a unit of spatial length in [m] to have the same units for all three degrees of freedom.

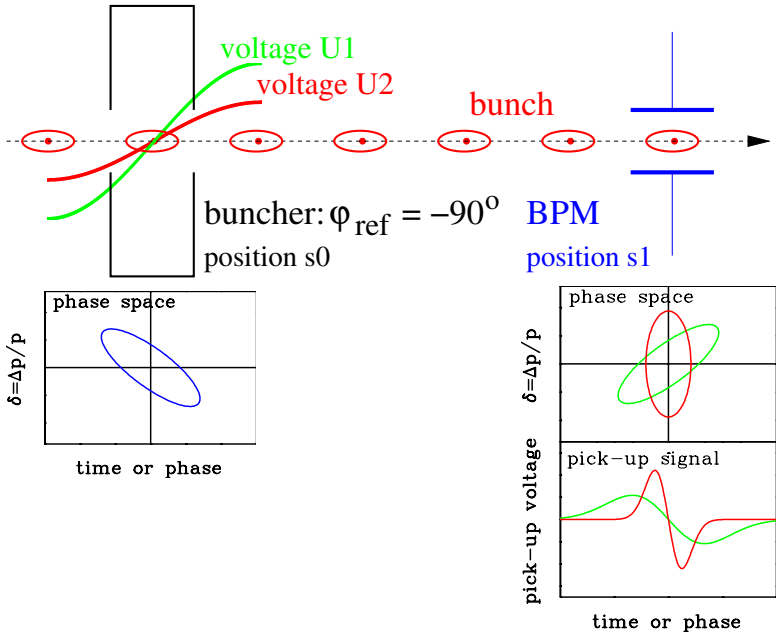

Fig. II.9.130: Scheme for a longitudinal emittance measurement using a buncher and one bunch shape monitor.

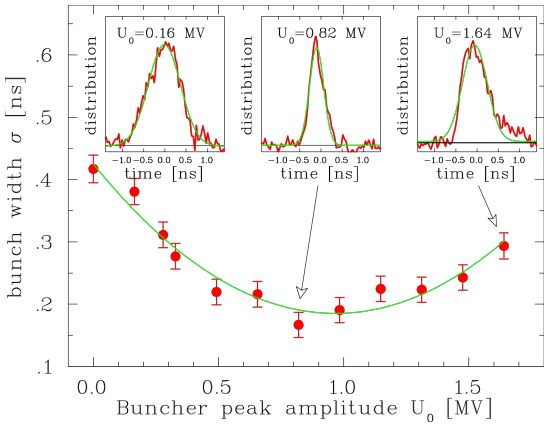

Fig. II.9.131: Measurement of the bunch width (one standard deviation) as a function of the buncher voltage 31 m upstream. The bunch shape is not measured by a BPM, but a specially designed monitor for low energetic beams [168].

is obtained for $k = 1, 2...n$ measurements with $f_k = f_1, f_2...f_n$ different settings of the buncher. This redundant system of linear equations has to be solved as discussed in Section II.9.4.4. A measurement is shown in Fig. II.9.131. For the method, it is of no importance which instrumentation device is used as long as it reflects the actual bunch shape of the beam.

Corresponding to the "three grid method", the bunch width can also be determined from a series of measurements along a transfer line, see Fig. II.9.132. As in the transverse case Section II.9.4.5, we get a redundant system of linear equations for the transformation $\mathbf{R}(k)$ from the buncher to the BPM at

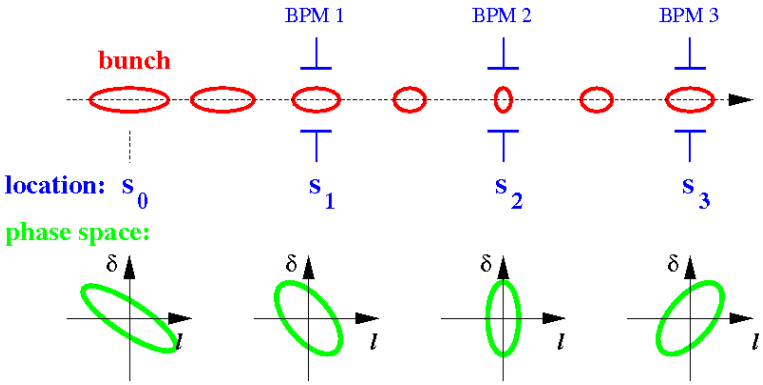

Fig. II.9.132: Scheme for a longitudinal emittance measurement using several BPMs in a transfer line.

s_k of the form

$$\begin{aligned}
\sigma_{55}(1) = &\quad R_{55}^2(1)\cdot\sigma_{55}(0) + 2R_{55}(1)R_{56}(1)\cdot\sigma_{56}(0) + R_{56}^2(1)\cdot\sigma_{66}(0) \quad \mathbf{R}(1): s_0 \to s_1 \\
\sigma_{55}(2) = &\quad R_{55}^2(2)\cdot\sigma_{55}(0) + 2R_{55}(2)R_{56}(2)\cdot\sigma_{56}(0) + R_{56}^2(2)\cdot\sigma_{66}(0) \quad \mathbf{R}(2): s_0 \to s_2 \\
&\vdots \\
\sigma_{55}(n) = &\quad R_{55}^2(n)\cdot\sigma_{55}(0) + 2R_{55}(n)R_{56}(n)\cdot\sigma_{56}(0) + R_{56}^2(n)\cdot\sigma_{66}(0) \quad \mathbf{R}(n): s_0 \to s_n
\end{aligned}$$

As discussed for the transverse case, the restrictions are the presence of simple, e.g. Gaussian phase-space distributions, linear beam manipulations and the lack of non-linear space-charge forces. Moreover, one has to underline that the above methods are only used at LINACs. In most cases, the BPM resolution is insufficient, and special detectors are used as discussed in Section II.9.6.7 for proton beams and Section II.9.6.8 for electron beams.

For beams extracted from a synchrotron, the variation of the bunch length within the beam transfer line is negligible in most cases due to the low momentum spread $\Delta p/p$ of the circulating beam and the short flight time t_{drift} to the target or a subsequent synchrotron as the increase of the bunch length is $\Delta t = \Delta p/p \cdot t_{\mathrm{drift}}$. As an example, the following number can be inserted: For a relativistic beam of velocity $\beta = 0.90$ and a distance of $L = 100$ m from synchrotron to target, the drift time is $t_{\mathrm{drift}} = L/\beta c = 370$ ns; assuming a momentum spread of $\Delta p/p = 10^{-3}$ the resulting lengthening of the bunch is $\Delta t = \Delta p/p \cdot t_{\mathrm{drift}} = 0.37$ ns, which is shorter than the typical bunch length of $\sigma_{\mathrm{bunch}} > 10$ ns in a proton synchrotron. Therefore, the measurement inside the synchrotron is sufficient, and a fast current transformer (as discussed in Section II.9.2.1.1 and depicted in Fig. II.9.10) mounted in the synchrotron can be used for monitoring.

II.9.6.5 Longitudinal emittance using tomographic reconstruction

In a proton synchrotron, the bunch length is much longer than the typical BPM electrode or the gap of a resistive wall current monitor, see Section II.9.6.6. It allows the recording of an accurate image of the bunch shape. Observation and control of the longitudinal behaviour at injection, acceleration and possible bunch manipulations, such as combining or splitting of bunches, can be performed.

An analysis method has been developed at CERN [9] to determine the longitudinal phase-space distribution and hence the emittance from a measurement of the bunch shape on a turn-by-turn basis. The

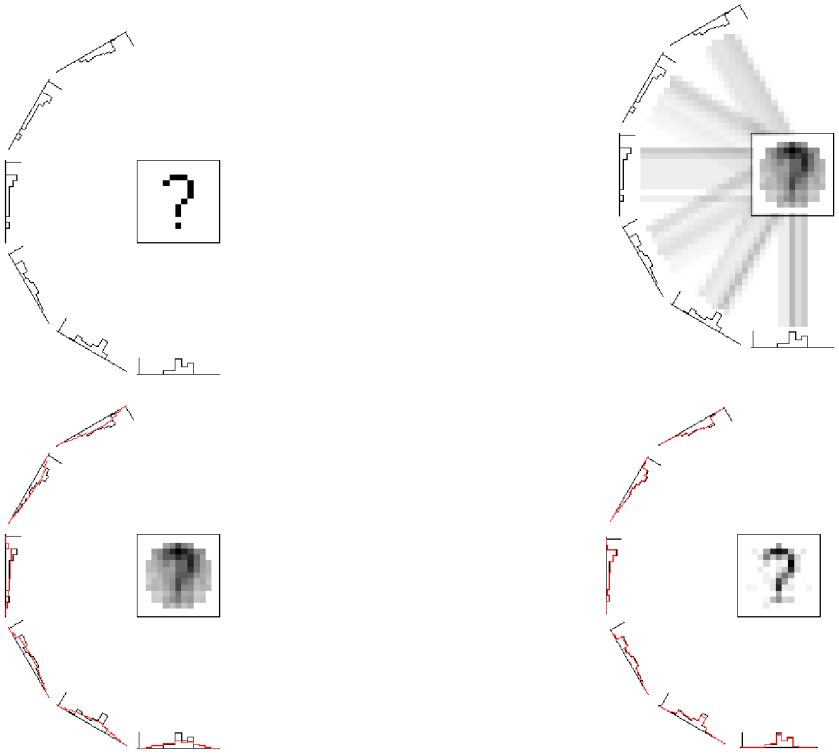

Fig. II.9.133: Schematic plots for the tomographic reconstruction technique [9]. The original 2-dimensional image and the 1-dimensional projections are shown at the left side. A first back projection is shown top right. The first iteration step for generating the differences in the projected data is plotted bottom left. After ~ 50 iterations, the original image can be reconstructed.

idea is based on the well-known tomographic reconstruction used as an imaging technique in medicine for X-ray tomography and nuclear magnetic resonance (NMR) tomography and described in textbooks on medical physics. The underlying principle of tomography is to combine the information from a sufficiently large number of projections to unambiguously reconstruct a more complete picture with the extra dimension reinstated. The application of tomography to longitudinal phase-space in an accelerator becomes evident once it is realised that a bunch of particles performing synchrotron motion is analogous to a patient rotating in a stationary body scanner. On each turn around the machine, a longitudinal pick-up provides a "snapshot" of the bunch projected at a slightly different “angle”, i.e. the oscillation of the bunch shape as given by the inverse of the synchrotron frequency f_{synch} is in nearly all cases much lower than the revolution frequency $f_{\mathrm{rev}} \gg f_{\mathrm{synch}}$. It suffices to combine such profiles tomographically to obtain a two-dimensional picture of phase-space density. Moreover, non-linear emittance growth can be included [9]. A general, well-fulfilled condition is that the synchrotron frequency is much lower than the revolution frequency. At least half a synchrotron period has to be recorded, corresponding to a 180° degree image of the patient body in the medical imaging applications.

The general idea for tomography is based on algebraic reconstruction techniques, described in textbooks on medical physics, as depicted in Fig. II.9.133 from Ref. [9]. The contents of the bins of a 1-dimensional histogram are redistributed over the 2-dimensional array of cells which comprise the reconstructed image. Assuming no a-priori knowledge of the original two-dimensional distribution, the contents of one bin are spread over all the cells that could have contributed to that bin. The back-

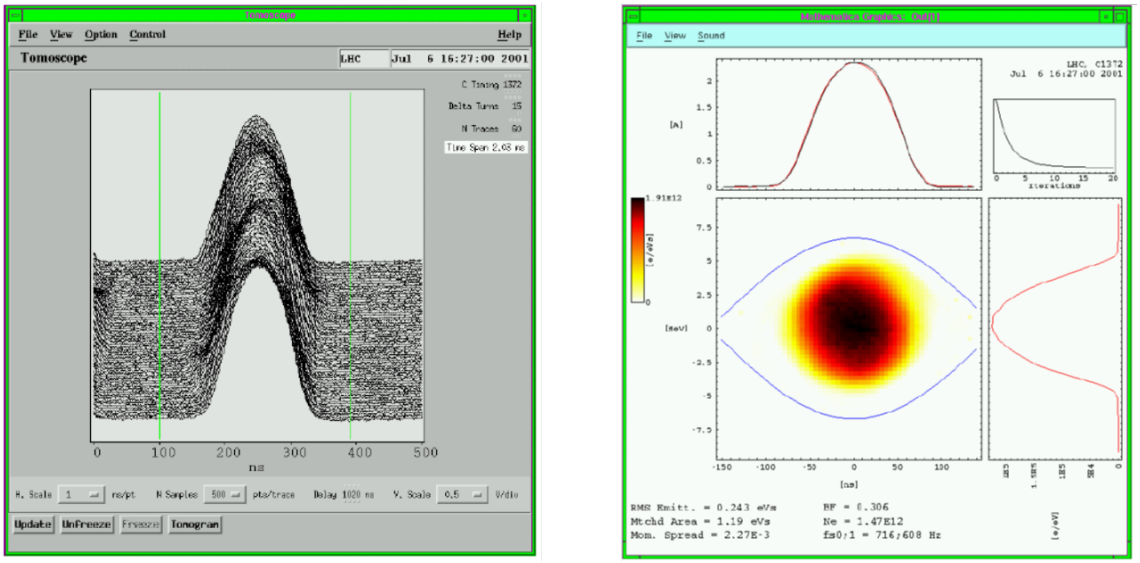

Fig. II.9.134: The recorded bunch shape at the CERN PS using a resistive wall current monitor for 500 turns (left) and the reconstructed longitudinal phase-space. The bucket size is shown in phase-space, and the projections to the time axis (top) and energy (right) are displayed, from Ref. [10].

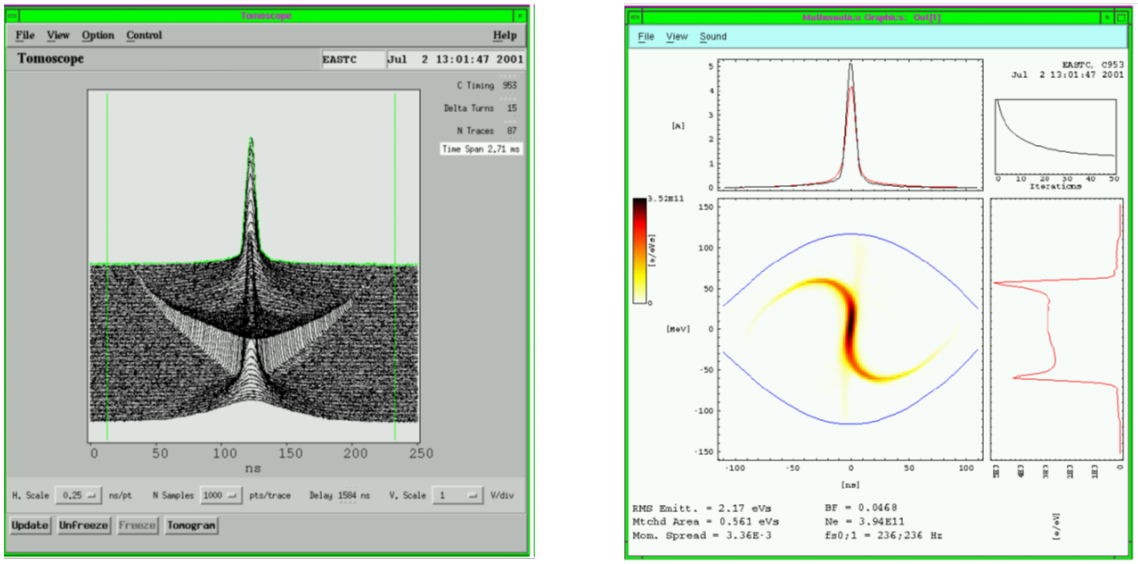

Fig. II.9.135: Same as Fig. II.9.134 but for a mismatched bunch. The complex rotation of the bunch width is seen on the left, and the reconstructed phase space density for one specific time slice on the right. The filamented distribution rotates to yield varying bunch shapes, from Ref. [10].

projection of all bins of all profiles yields a first approximation to the original distribution. Back projection of the bin-by-bin difference between the original set of profiles and this new one yields an improved approximation. Further iterations converge more rapidly if any cell with negative contents is reset to zero. A more detailed description is found in Ref. [9].

Two examples [10] demonstrate the high analysing power of tomography. The first example, displayed in Fig. II.9.134, is a standard, constant bunch shape recorded with a digital scope. The reconstruction of the first time slice shows a good bucket filling. The second example in Fig. II.9.135 is related to a particular bunch manipulation. In phase-space (as shown for a small bunch width), the distri-

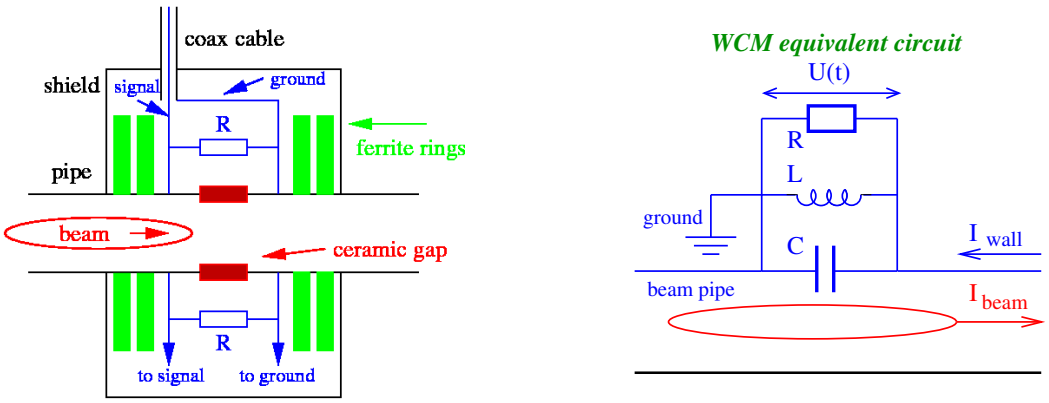

Fig. II.9.136: Schematic of a wall current monitor (left) used for fast bunch observations and its equivalent circuit (right).

bution rotates at the synchrotron frequency, resulting in varying bunch shapes as a function of time. This compact bunch is created to fulfil the user demands of short bunches for dedicated experiments. The observation inside the synchrotron has the advantage of observing the entire creation process of bunch rotation and enabling the correct trigger timing for the extraction of this bunch.

II.9.6.6 Resistive wall current monitor

A large bandwidth for the device itself and the associated electronics is required to observe the bunches and their structure. With a resistive **W**all **C**urrent **M**onitor **WCM**, a bandwidth up to several GHz can be reached [169]. The beam always induces an image current flowing along the vacuum pipe, having the same magnitude and a comparable time structure. To measure this image current, the vacuum pipe is interrupted by a ceramic gap, as displayed schematically in Fig. II.9.136. The gap is bridged by typically n =10 to 100 resistors with a low resistivity of the order of R =10 to 100 Ω leading to a total value of $R_{\mathrm{tot}} = R/n \sim 1\ \Omega$. The resistors are azimuthally distributed on a printed circuit board so that the signal amplitude is independent of the actual beam position. At several locations, the signal is connected to a coaxial cable, feeding an amplifier. The voltage across the resistors U_{tot} is given by

$$U_{\mathrm{tot}} = \frac{R}{n} \cdot I_{\mathrm{beam}} \quad . \tag{II.9.145}$$

The resistors must be carefully shielded against noise from the surroundings as caused, e.g., by ground currents from the RF-system. The shield also acts as a short circuit for low frequencies. In addition, ferrite rings are mounted around the vacuum pipe to force the image current through the resistors by damping the high frequencies penetrating the rings. Using ferrites with a high permeability μ resulting in a large value of inductance $L \propto \mu$, the lower cut-off frequency $f_{\mathrm{low}} = (2\pi)^{-1} \cdot R_{\mathrm{tot}}/L$ can be decreased. Values of about $f_{\mathrm{low}} \sim 10$ kHz are typical and allow un-differentiated bunch structure observation. The upper cut-off frequency is given by the capacitance C of the gap to be $f_{\mathrm{high}} = (2\pi)^{-1} \cdot (R_{\mathrm{tot}}C)^{-1}$. Several GHz are realisable with a careful design of all RF components. The equivalent circuit is similar to a passive transformer, as discussed in Section II.9.2.1.1, leading to comparable electrical properties. The only exception is that the capacitance for the WCM is given by the ceramic gap, which is larger than any stray capacitance. The wall current monitor is well suited for broadband bunch shape observations

Fig. II.9.137: Photo of the wall current monitor used at Fermilab for protons, from [169]. The ceramic gap is shown separately. The ferrite rings and the printed circuit with the resistors are visible.

at proton synchrotrons with bunch lengths down to the ns region.

II.9.6.7 Bunch structure for non-relativistic energies

For a beam with non-relativistic velocity, the electric field of a bunch has a significant longitudinal component, as calculated for Fig. II.9.125. This longitudinal field seen by the BPM electrode leads to a signal smearing. The structure of a bunch cannot be monitored with a pick-up, as demonstrated in Fig. II.9.138 for a 1.4 MeV/u ion beam corresponding to $\beta = 5.5$ %. Moreover, the required resolution of 1° in phase, or less than 50 ps in time, corresponds to a bandwidth of more than 10 GHz, which is hardly achieved by RF technologies. Other methods have to be applied for such a measurement. The result is essential for the adjustment of the LINAC modules, including bunchers for the injection to subsequent accelerators, and the comparison of measurements and beam dynamics calculations, e.g. required during a commissioning phase of a new accelerator. The bunch width and structure enter the numerical codes in the same manner as the transverse parameters, e.g., for estimating emittance growth by space charge forces. Moreover, as is shown below, a Gaussian distribution is not a good approximation for the bunch structure at these low energies. Three different devices are discussed in the following.

II.9.6.7.1 Coaxial Faraday cups for bunch shape observation

Faraday cups, as described in Section II.9.2.6, are used to monitor the structure of bunches for non-relativistic protons or ions at LINACs up to an energy of about 100 MeV/u and a bunch length of down to 100 ps. It is a direct measurement of the beam particle arrival at the metallic surface of the cup. The electric signal is then guided to a broadband amplifier by a 50 Ω matched transition line. All components of this electrical chain must have a bandwidth of several GHz for an undistorted image of the bunch shape, which is not easily achievable. Figure II.9.139 depicts the schematics of a coaxial Faraday cup: The beam hits a collector, which is mounted in a rotational symmetric configuration inside an outer conductor leading to a 50 Ω transmission line. To ensure the large bandwidth of several GHz and prevent signal reflection, it is necessary to keep a constant ratio of the collector radius r_{coll} and the outer radius of the shield r_{shield}. The impedance Z of a coaxial transmission line should be 50 Ω everywhere and is

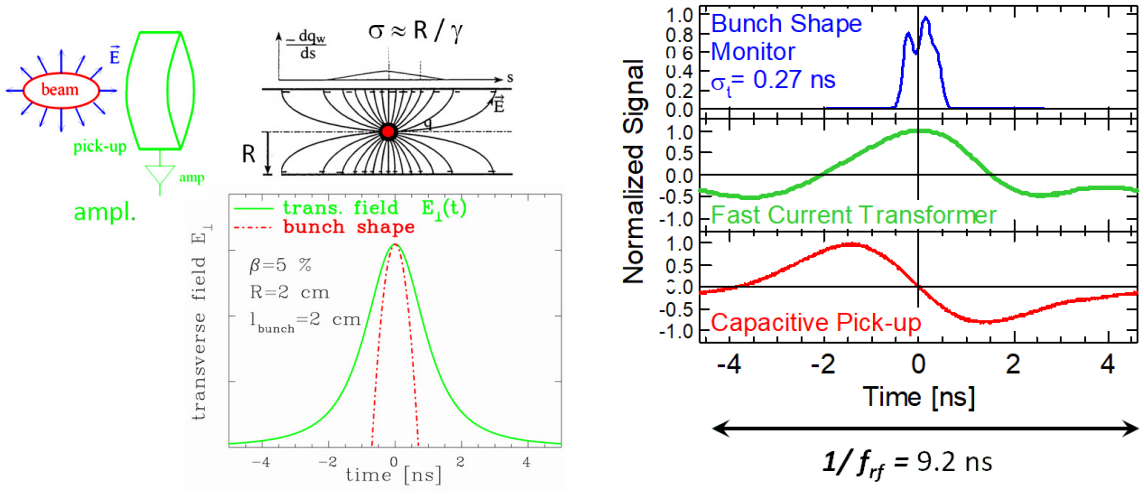

Fig. II.9.138: Left: Time evolution of the transverse electric field as seen by the pick-up is simulated for a bunch with a $\cos^2$-distribution. Right: The comparison of a pick-up and FCT signal to the bunch structure measured with a BSM (see below) at the GSI LINAC for a beam of 1.4 MeV/u corresponding to a velocity of $\beta = 5.5$ %.

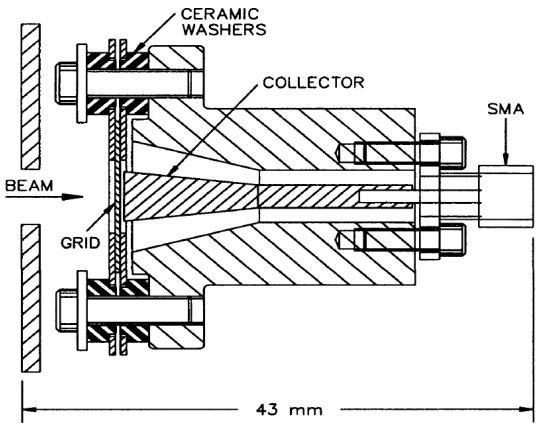

Fig. II.9.139: Schematic drawing of a 50 Ω Faraday cup. A smooth transition to the SMA connector, maintaining 50 Ω impedance, is used. The grid for minimising the advanced electrical field component is mounted close to the collector [170].

determined via

$$Z = \frac{Z_0}{2\pi} \cdot \ln \frac{r_{\text{shield}}}{r_{\text{coll}}} \quad . \tag{II.9.146}$$

The constant Z_0 is the "impedance of the vacuum" and is given by $Z_0 = \sqrt{\mu_0/\epsilon_0} = 377\ \Omega$. If the impedance is not constant, part of the signal is reflected, leading to a deformation of the beam image [5].

[5] A general measure of the matching quality is the voltage reflection coefficient Γ of a transmission line, defined by

$$U_{\text{back}} = \Gamma \cdot U_{\text{forward}} \tag{II.9.147}$$

with U_{forward} the input voltage and U_{back} the reflected voltage. Expressed in terms of the transmission line impedance Z_1 and the impedance of the load Z_2 the voltage reflection coefficient Γ is

$$\Gamma = \frac{Z_2 - Z_1}{Z_2 + Z_1} \quad . \tag{II.9.148}$$

There are three extreme cases:

Most coaxial Faraday cups have a relatively small collector area, comparable with the size of the transmitting coaxial cable; in Fig. II.9.139, it is only a few mm [170, 171]. In this case, only the central part of the beam hits the collector, which is acceptable if no dependence of the bunch shape on the position exists. However, dispersive optical elements in a transfer line, such as dipole magnets, lead to a correlation between the transverse and longitudinal phase-space. In this case, it must be ensured that the effect is small, or a more detailed analysis of the measurements is required.

Due to the creation of secondary particles, Faraday cups can only be used for protons or ions with energies below about 100 MeV/u. For those non-relativistic velocities of about $\beta \leq 50\%$, the advanced electric field, as calculated in Section II.9.6.1, leads to an induced voltage on the collector prior to the arriving particles. Therefore, a grid is mounted very close to the collector plate, which acts as an equi-potential surface shielding the collector. In addition, one has to prevent the escape of secondary electrons. The secondary electrons are repelled back to the collector by supplying a negative voltage to the grid in connection to the shielding of the advanced electrical field. Further mechanical designs exist to improve the matching to a 50 Ω cable; the results of different types are compared, and the achievable time resolution is simulated e.g. in Refs. [172–174].

II.9.6.7.2 Time structure using secondary electrons

At many low energy proton LINACs, a device for the bunch structure observation referred to as **B**unch **S**tructure **M**onitor **BSM** is installed. The principle is based on the observation of secondary electrons liberated from a single wire intersecting the beam, as shown in Fig. II.9.140 and reviewed in Refs. [175, 176]. The beam hits a wire, which is typically held on a negative potential of -10 kV. By the related electric field, the liberated secondary electrons are accelerated toward a thin slit on the side of the vacuum chamber. Here, they pass a pair of plates, where an RF-field is applied with the same frequency as the accelerating RF or a higher harmonics. This field deflects the electrons, and the different arrival times are transformed via varying deflection angles to a difference in space, i.e. this deflector acts as a "time-to-space converter". (The same principle is used in a non-resonant way in an analogue oscilloscope.) After a drift of typically 0.5 m, the electrons are detected with a Faraday cup or a secondary electron multiplier with a small slit in front. (A secondary electron multiplier is the same as a photomultiplier but without a photo-cathode.) For a fixed slit position, the phase of the deflecting RF relative to the accelerating RF is changed electronically to transmit electrons representing different time slots of the beam bunches, to get a full image of the bunch structure; i.e. the bunch shape is obtained by a scanning method. To visualise the high temporal resolution of a BSM, Fig. II.9.138 depicts a measurement using a BSM and the comparable signals from a current transformer.

The resolution of this device is better than 1^o in phase, independent of the frequency of the RF,

- $Z_2 = Z_1 \Rightarrow \Gamma = 0$ the matching is perfect, no signal is reflected.
- $Z_2 = 0 \Rightarrow \Gamma = -1$ corresponding to a short circuit, the reflected signal has the same amplitude but opposite sign.
- $Z_2 = \infty \Rightarrow \Gamma = 1$, corresponding to an open circuit, the reflected signal comes back with the same amplitude and sign.

Another description of the matching is the so-called "Voltage Standing Wave Ratio" which is defined as

$$\text{VSWR} = \frac{Z_2}{Z_1} = \frac{1+\Gamma}{1-\Gamma} \quad . \tag{II.9.149}$$

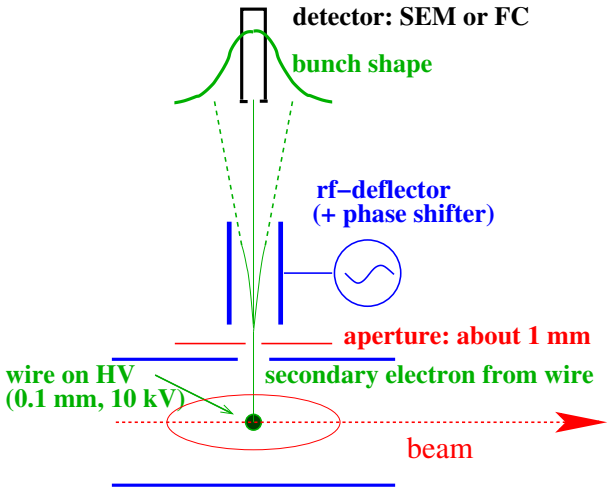

Fig. II.9.140: Principle of a deflector technique for bunch structure observation by a Bunch Shape Monitor. SEM means secondary electron multiplier.

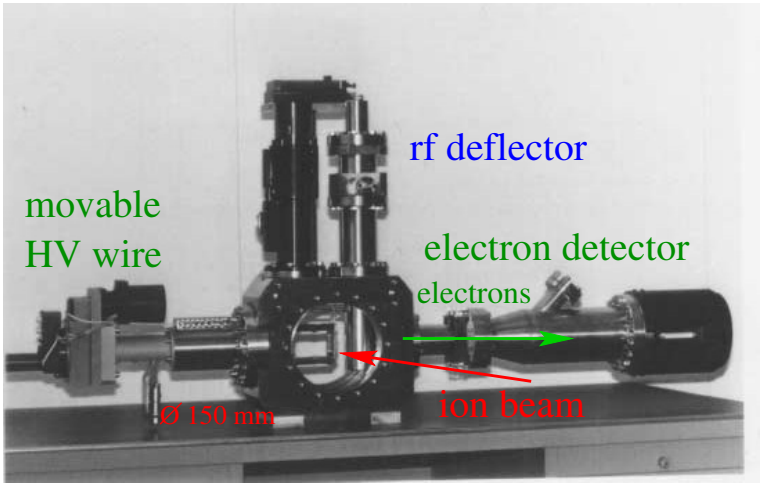

Fig. II.9.141: The BSM installed at CERN LINAC 2 [175]. The vacuum feed-through on the left side is the support for the high-voltage wire. The RF-deflector is installed on the vertical flange, and the detector is mounted on the right.

up to several hundred MHz. It is known that the emission of secondary electrons is a fast process with a time difference of less than 10 ps between the hit of the beam particle and the electron emission, i.e. much faster than the required resolution. The RF deflector is built as a resonator to get an electric field high enough for typically 100 mrad deflection to have an appropriate separation at the detector ~ 0.5 m apart. A constant dc-voltage applied to the deflector plates serves as an electrostatic lens to enable transverse focusing of the secondary electron beam. The HV-wire is movable so that the bunch shape can be measured for different horizontal locations, and it is possible to do a measurement with a high current beam by intercepting the beam edge with low power deposition.

II.9.6.8 Bunch structure for relativistic electron beams

The longitudinal diagnostics at electron accelerators are not performed by recording BPM signals, although it would be possible due to the relativistic velocities and, hence, the mainly transverse electric

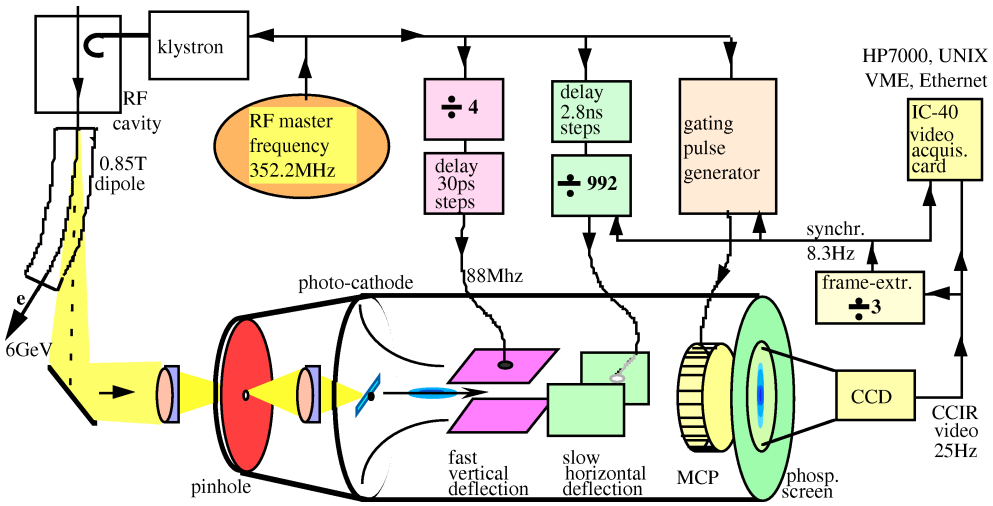

Fig. II.9.142: Principle of a streak camera used for bunch width determination at the electron synchrotron ESRF, from Ref. [178].

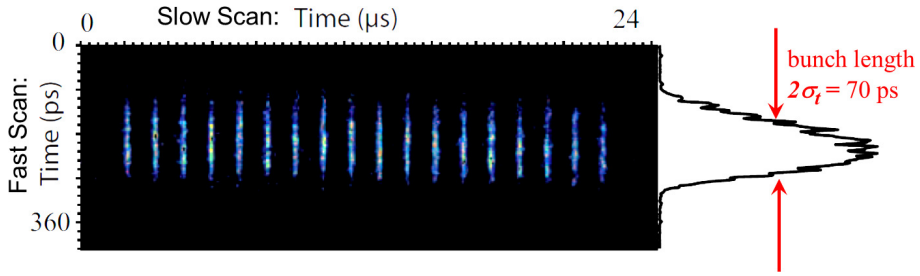

Fig. II.9.143: Bunch length measurement with a streak camera, using synchrotron light from individual bunches emitted by the passage through a dipole at SOLEIL [180]. The horizontal axis scaling is 24 μs full scale for the bunch repetition (slow scan direction), and the vertical axis is 360 ps full scale for the bunch structure (fast scan direction).

field. However, the bunch length, e.g. at a synchrotron light source, is typically several 10 ps, so even a BPM electronics bandwidth of several GHz is insufficient to reproduce the detailed bunch structure. However, the emission of synchrotron light at a dipole or preferably from an insertion device can be used as a representation for the bunch structure. A review of this technique is given in Ref. [177].

The principle of such a measurement is shown in Fig. II.9.142. It uses a streak camera as a commercially available device [179], which allows visible light observations with a time resolution down to typically 1 ps. The synchrotron light is focused and scraped by a pinhole onto the photo-cathode of a streak camera. The secondary electrons from the photo-cathode are accelerated and pass a fast deflector, driven by a frequency of 50 to 300 MHz, which are locked to the accelerating frequency for synchronisation. The general scheme is similar to the discussed "time-to-space converter" in Section II.9.6.7.2. After a certain drift space, the electrons are amplified by an MCP and converted to photons by a phosphor screen. With a standard digital camera, the image from the phosphor is recorded. The different arrival times of the synchrotron light, and, hence, the bunch structure is converted to a difference in space with a full scale of typically several 100 ps and a resolution in the ps range. A second, perpendicular pair of plates is driven with a much lower frequency to separate the images from the individual bunches.

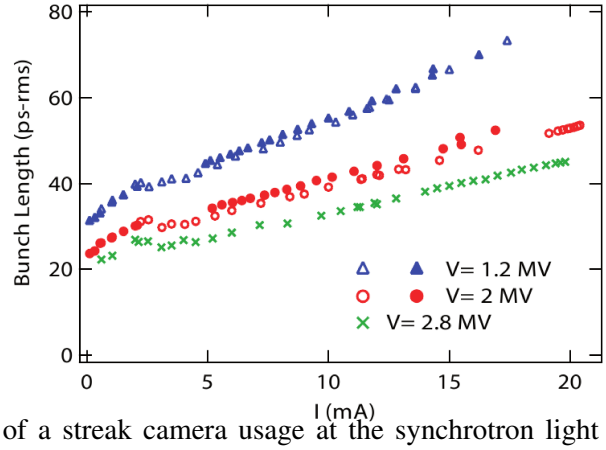

Fig. II.9.144: Example of a streak camera usage at the synchrotron light facility SOLEIL achieved from measurements like depicted in Fig II.9.143: For different accelerating voltages, the bunch length is recorded as a function of the beam current stored in the synchrotron, from Ref. [180].

Fig. II.9.143 depicted an example of a bunch length measurement performed with synchrotron radiation from a dipole [180]. The slow scan for separating the individual bunches is displayed on the horizontal axis. The vertical axis has a full scale of 360 ps, and the bunch width is only $\sigma \simeq 40$ ps, demonstrating the high resolution of such a system. Synchrotron radiation users need short bunches for time-resolved spectroscopy. A large voltage is applied to the synchrotron RF cavities to produce and maintain these short bunches. In Fig. II.9.144 the bunch width is plotted for different RF voltages. As displayed, the achievable bunch length depends on the stored electron current. Counteracting the RF bunching force, non-linear processes such as wake-fields and instabilities increase for higher currents. Effects such as head-tail oscillations or longitudinal bunch oscillation due to coupled bunch instabilities can be monitored by performing streak camera measurements, see e.g. Ref. [177].

II.9.6.9 Electro-optical bunch structure at linear light sources

At modern LINAC-based light sources, the process of free-electron lasing depends non-linearly on the temporal structure of the bunches. A typical bunch width is in the order of 100 fs with a non-Gaussian bunch structure, and significant shot-to-shot variations might occur. The time resolution of $\sim$ 1 ps concerning the light observation by the aforementioned streak camera is insufficient.

The technique of electro-optical sampling is suited for a time resolution down to some 10 fs. Electrons at LINAC-based light sources are accelerated to highly relativistic velocities leading to an enlarged and temporally compressed transverse electric field as described by Eq. II.9.137 and Section II.9.6.1. This electric field is detected by a birefringent crystal mounted typically 5 mm outside of the beam path, see Fig. II.9.145 (left). A GaP or ZnTe crystal of thickness less than 100 μm is installed in most cases. The underlying effect of electro-optical modulation is a change of the index of refraction between two orthogonal crystal planes depending on the external electric field which leads to a rotation of the polarisation of transmitted light [181]; this process is called electro-optical modulation. The rotation of polarisation, as caused by the time-dependent electric field of the electron bunch, can be probed by a co-propagating laser which is linear-polarised before the crystal. With the help of a subsequent analysing polariser, this is transferred to a time-dependent intensity modulation. A short laser pulse of typically 10 fs duration is used for the probing. At most installations, a Titanium-Sapphire (Ti:Sa) laser or Ytter-

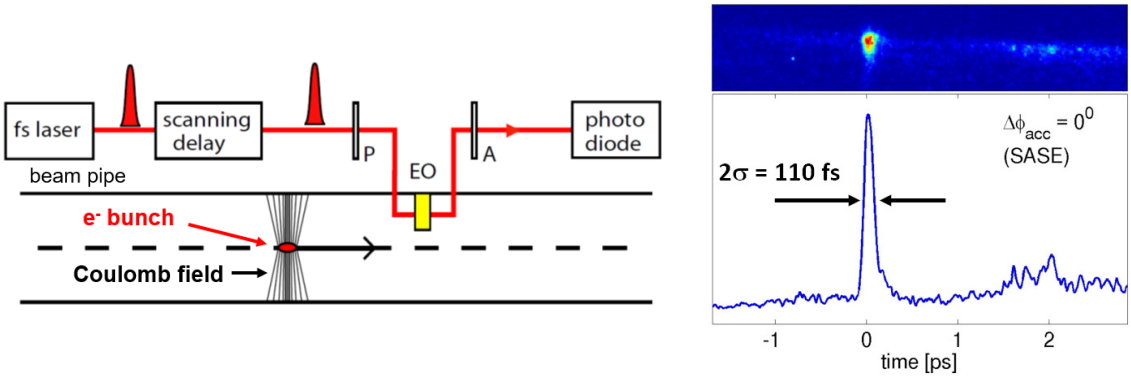

Fig. II.9.145: Left: Electro-optical scanning by a short laser pulse for relativistic electron beams (P: polariser, A: analyser for the polarisation, EO: electro-optical crystal), courtesy B. Steffen. Right: Single shot bunch structure measurement (camera image and projection) using EOTD at the LINAC FLASH at DESY [183].

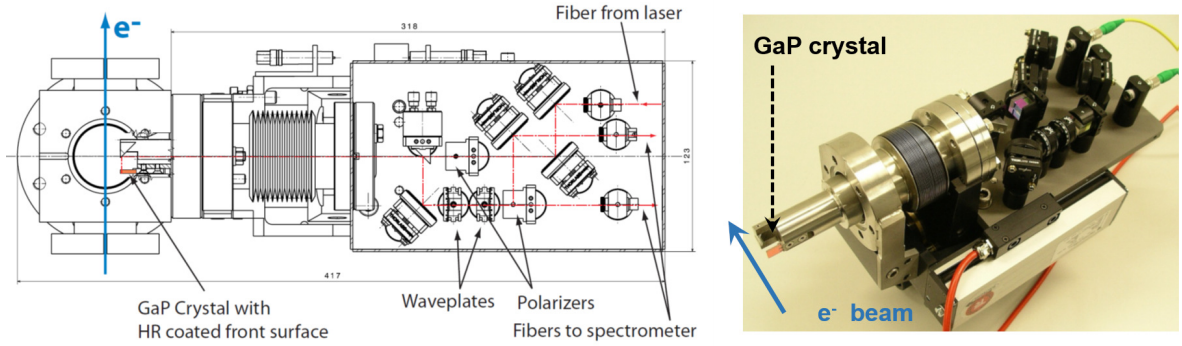

Fig. II.9.146: Birefringent crystal and optics for an electro-optical bunch shape monitor as installed at the PSI FEL [182].

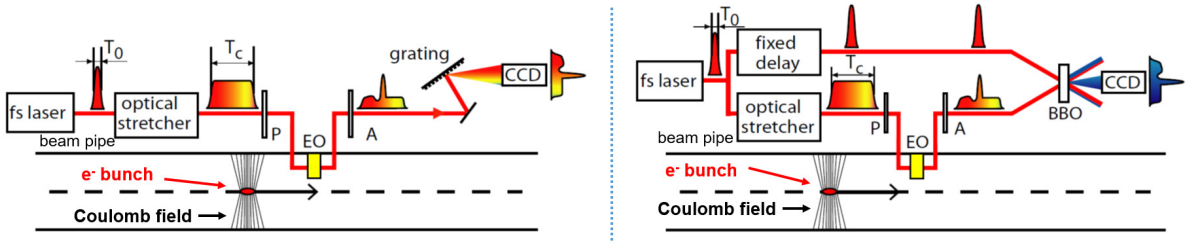

Fig. II.9.147: Left: Scheme of the electro-optical spectral decoding EOSD method. Right: Scheme of the electro-optical temporal decoding EOTD method, courtesy B. Steffen.

bium fibre laser creates the short pulse. In the basic installation, the arrival time between this laser pulse and the electron bunch is varied by an optical delay (i.e. varying path length of the laser light) to probe the temporal bunch structure as schematically depicted in Fig. II.9.145 (left). A photo of the beamline installation is presented in Fig. II.9.146. This configuration is a scanning method (the controllable laser delay is varied each shot and acts as the time axis) and is not suited to monitor shot-to-shot variations of the electron bunches. Therefore, this method is rarely installed at modern LINAC-based light sources.

To enable single shot observations, the setup is modified by two different methods as shown in

Fig. II.9.147. The first method is called **E**lectro-**O**ptical **S**pectral **D**ecoding **EOSD**: Generally, a laser pulse of finite duration is composed by light within a range of wavelengths. An optical stretcher [181] separates the different wavelengths in time by a colour-dependent optical path length in a dispersive element such as prisms, providing a correlation between the wavelength and the arrival time at the crystal. The electron bunch field temporally modifies the wavelength-dependent light in the electro-optical crystal. After passing the analysing polariser, the change in beam-induced polarisation is reflected in a wavelength-dependent intensity variation. An optical spectrometer transfers this colour modulation to a spatial profile, which is finally monitored by a camera.

The second method is referred to as **E**lectro-**O**ptical **T**emporal **D**ecoding **EOTD** and is based on two laser beams: The same method of beam-induced modulation is installed. However, the original laser beam is split before the optical stretching. Both laser beams are combined with an angle inside a non-linear crystal [181]. (Barium Boron Oxide BBO is often used for this purpose, providing a 2^{nd}-harmonics generation as often used for frequency doubling of a laser beam.) The modulation detection is performed by frequency mixing of both laser beams as the non-linear crystal emitting the sum frequency of both laser beams, i.e. acts as a single-shot correlation measurement. Owing to the non-coaxial propagation inside the crystal, the light of the sum frequency is emitted from different locations, leading to a spatial separation of the beam-induced intensity modulation. Finally, a camera can monitor the related image. A detailed comparison of both methods is described in Ref. [183]. The achievable time resolution of the EOSD method is better than 50 fs. In contrast, the achievable time resolution by the EOTD method is about 25 fs. However, EOTD has the disadvantage of a larger laser power requirement related to frequency mixing. A measurement of a single pulse of 100 fs duration at an FEL facility obtained by the EOTD method is shown in Fig. II.9.145 (right).

II.9.7 Beam loss detection

In a real accelerator, the transmission from the source to the target is never 100 %. To achieve optimal transmission, the fraction of lost beam particles must be controlled carefully. The lost beam particles cause some activation of the accelerator components by nuclear reactions. Moreover, the surrounding material can be destroyed by radiation and heating due to the particles' energy loss. The important nuclear physics processes leading to secondary particles are reviewed briefly. To detect the shower of secondary particle s, a large variety of **B**eam **L**oss **M**onitors **BLM** exists. Most of them are particle counters, detecting secondary reaction products. At nearly every high current accelerator facility, these monitors are installed for the protection of the accelerator components. The relatively cheap BLM instruments are mounted outside of the vacuum pipe at crucial locations as schematically depicted in Fig. II.9.148. Their signals serve as essential information to prevent unwanted loss during the operation, e.g., caused by malfunctions of components. A careful analysis of the location and time structure of possible losses has to be performed before the choice of the suitable types of beam loss monitors can be made; see Refs. [184–187] for a review. Beam loss monitors can be sensitive devices which detect even a tiny fraction of losses; therefore, they are also used for machine tuning. Two examples are discussed in the last part of this section.

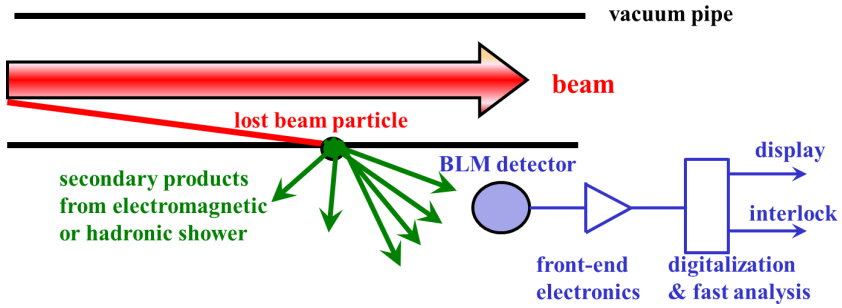

Fig. II.9.148: Schematic drawing of an installation of beam loss monitor outside of the vacuum pipe.

II.9.7.1 Secondary particle production

When a high energy particle hits the vacuum pipe or any other material, secondary particles are generated. The relevant processes are described e.g. in Refs. [188–190]. Here, only a brief overview is given:

- **Interaction of electrons**
  For electron energies above $\sim$ 100 MeV, Bremsstrahlung dominates the slow-down process in materials, as shown in Fig. II.9.21. The created high energy γ photons give rise to further particles via e^+e^- pair production. If the energy of the γ photons are high enough, other particles such as $\mu^\pm, \pi^\pm$... can also be produced, and an electro-magnetic shower is generated. Moreover, the nucleus can be excited to so-called giant resonances: This is a collective nuclear excitation, where the neutrons oscillate against the protons. The dipole mode of these giant resonances has a threshold of about 6 MeV for typical materials. The de-excitation proceeds with high probability via neutron emission as a (γ, n) reaction. For higher energies also (γ, p) and (γ, np) channels are open.
  When the electron is slowed down below $\sim$ 10 MeV, ionisation loss by electronic stopping dominates, resulting in soft X-rays, which are absorbed within a short distance.
- **Interaction of protons**
  Besides electronic stopping, as shown in Fig. II.9.20, nuclear interactions are possible. First, we define the term "thick target" as applicable if the interaction length is comparable to the range given by the electronic stopping. In these thick targets, the probability of a nuclear reaction rises to nearly 100 % for energies above 1 GeV, see Fig. II.9.149. Most of the final channels of these nuclear reactions include neutron emission. As an example, for the stopping of 1 GeV proton in copper or iron, $\sim$ 10 fast neutrons are liberated. The neutron yield scales approximately with E_{kin} for energies above 1 GeV. In addition, hadron showers (by the strong interaction at the quark level) are possible, resulting in various species of "elementary" particles.
- **Interaction of ions**
  In addition to the interactions of protons, an ionic projectile can be fragmented, or fission can be induced, leading to radioactive nuclei and fast proton and neutron emission. Simple scaling laws do not exist due to the complex nuclear physics involved.

Common to all interactions is the production of radioactive nuclei leading to an activation of the accelerator components. The surrounding material relatively quickly stops the emitted charged particles. However, the neutrons produced by most primary interactions can travel long distances. Therefore, some

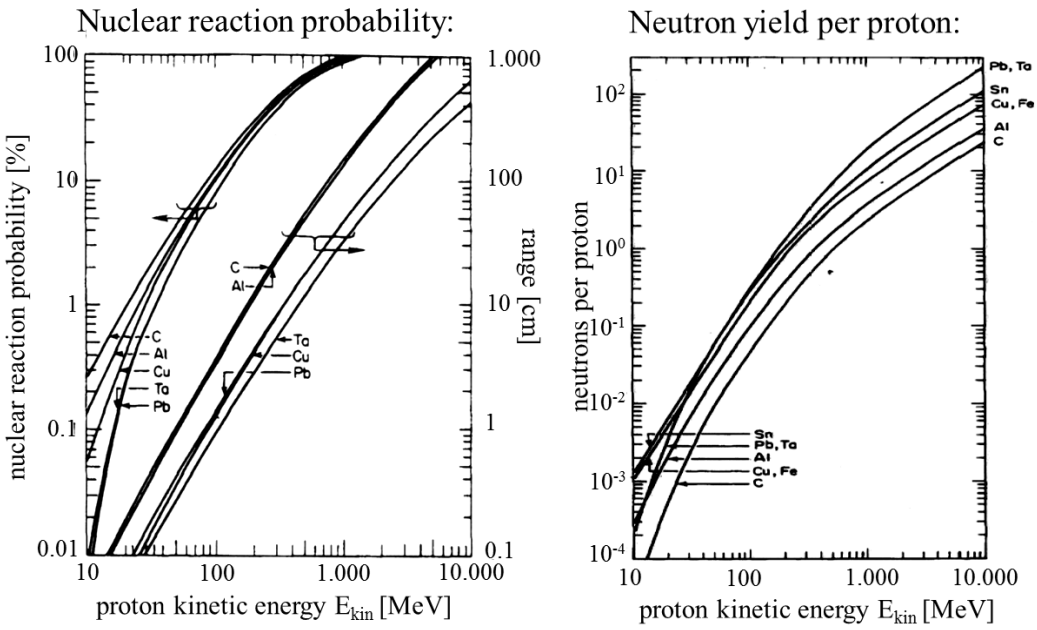

Fig. II.9.149: Left: The ranges of protons in various metals and the probability of an inelastic nuclear reaction within the range as a function of the proton energy, i.e within a thick target. Right: The total number of neutrons per proton incident on a thick target for various metals as a function of the proton energy, from Ref. [189].

of the beam loss monitors are sensitive to these neutrons. Except for the production of radioactive nuclei, all processes are fast, compared to the timescale of interest in accelerator physics, i.e. faster than $\sim$ 10 ns. In this sense, a beam loss monitor reacts instantaneously to particle losses. Due to the kinematics of the primary interaction, the secondary particles are emitted into a forward peaked angular distribution. This leads to a spatial resolution of the loss detection by the monitor position close to the loss point.

II.9.7.2 Types of beam loss monitors

Beam loss monitors localise the position and time of the lost beam particles. Their signals should be proportional to the amount of losses at this position. A high sensitivity is needed at locations where low losses are expected. A high dynamic range is required to deal with a sudden loss of a sizeable beam fraction. Depending on the application, a bunch-to-bunch resolution for a $\sim$ 10 ns time scale is needed, as well as up to 100 ms for slow detection. All loss monitors are installed outside the vacuum pipe, detecting mostly secondary particles. The particles can be neutrons, which are barely absorbed by the surrounding material, charged particles such as protons, electrons, positrons and muons or γ-rays. Figure II.9.150 shows a photo of some frequently used types as tested at the GSI synchrotron. An overview of the different BLM types is given in Refs. [185, 187].

II.9.7.2.1 Plastic scintillators

Plastic scintillators detect charged particles due to their electronic stopping, as discussed in Section II.9.2.9.1. In addition, γ-rays are detected, as they liberate electrons from the molecules via photo effect or Compton scattering; subsequently, those electrons generate than the optical photons via electronic stopping. Moreover, scintillators are sensitive to neutrons due to their elastic scattering on the

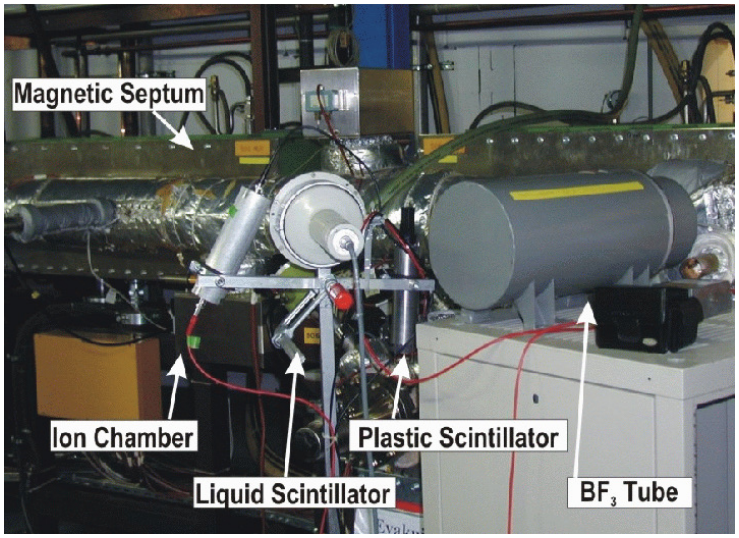

Fig. II.9.150: The tested beam loss detectors installed at the extraction from the GSI heavy ion synchrotron [191].

hydrogen atoms of the polymers [17]. Due to the elastic scattering process generated by the relativistic neutrons, a large momentum transfer to the hydrogen atoms of the macro-molecules is probable, which leads to a fast proton travelling through the scintillator material and finally generates the light emission by its electronic stopping.

The generated light is guided to a photo-multiplier, converted to electrons and amplified, see Fig. II.9.151 for a typical realisation. The readout of the resulting electronic signal can be performed by digitising the analogue voltage using a relatively small photo-multiplier gain, or a particle counting mode can be used for higher sensitivity and larger dynamic range. A typical output for the counting mode is depicted in Fig. II.9.151, showing analogue pulses of $\sim$ 10 ns duration. Due to the wide spectrum of incoming particle species and their related energies, the pulse height distribution is quite broad. (This should be compared to the narrow pulse height distribution of single energetic particles in Fig II.9.33.) In counting mode, the plastic scintillators have an extensive dynamic range, from single particle counting up to a count rate of 10^7 s^{-1}. In most cases, the scintillation monitors are located in crucial areas such injection or extraction area, or close to scrapers. The disadvantage is the low radiation hardness of the plastic materials due to the complex chemical composition of the polymers from the plastic matrix. A very rough number of the damage threshold is given by the dose $D = 1$ Mrad $= 10^4$ Gy; around this value, the light transmission is reduced by a factor $1/e = 0.37$. Typical sizes of plastic scintillators are cylindrical rods of 2 cm diameter and 10 cm length. Sometimes, long fibres of plastic or inorganic materials are used.

II.9.7.2.2 Liquid scintillator

A scintillator material within a liquid solvent of about 1 litre can also be used used [17]. The device is sensitive to charged particles, $e^{\pm}$, γ and neutrons by the same mechanisms discussed for plastic scintillators. A comparable pulse height distribution is observed. The pulse length of the scintillation process is about 1 order of magnitude longer, and therefore the dynamic range is a factor of 10 lower for the counting mode. Due to the microscopic light creation, discrimination between γ-rays and neutrons can

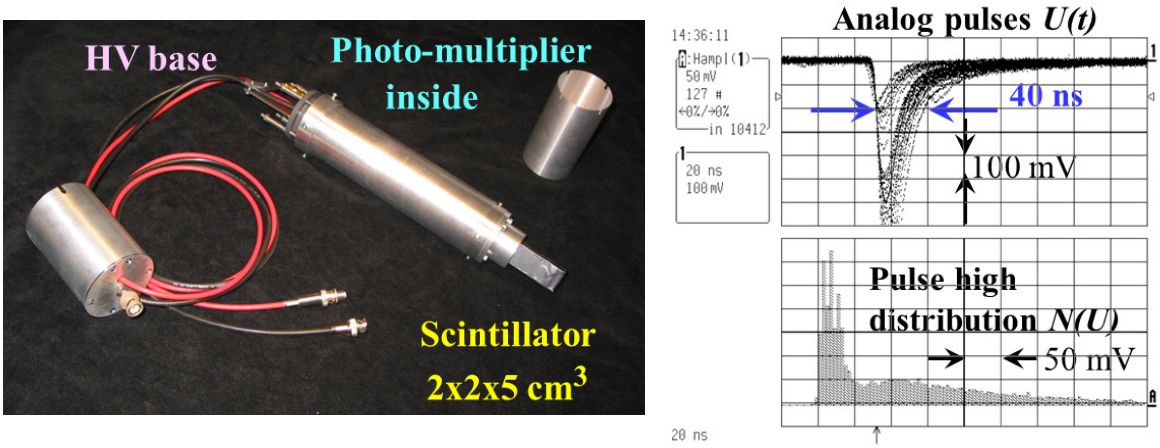

Fig. II.9.151: Left: Photo of a typical BLM based on a plastic scintillator connected to a photo-multiplier. Right: Typical pulses from a plastic scintillator (top, 100 mV/div and 20 ns/div) and their pulse height distribution (bottom, 50 mV/div) as measured at the GSI heavy ion synchrotron.

be performed using selected electronics, referred to as pulse shape discrimination [17]. The liquid is about a factor of 10 more radiation hard than the plastics due to the simpler chemical composition of the solvent.

II.9.7.2.3 PIN diode

Solid-state detectors can be used as particle counters. In the typically 100 μm thick depletion layer of the doped Si-crystal, electron-hole pairs are generated. For a minimum ionising particle (MIP), a charged proton at the minimum of its electronic stopping power, about 10^4 electron-hole pairs are generated. This signal has to be amplified by a charge-sensitive pre-amplifier and can then be counted. As depicted in Fig. II.9.152, two face-to-face mounted PIN diodes are operated in coincidence to count only the charged particles and to suppress the counting of low-energy photons emitted at electron accelerators by synchrotron radiation. These photons are absorbed in one PIN diode and do not arrive at the second. The detection efficiency is relatively low due to the small active area of typically 10×10 mm^2 and the 0.1 mm depletion depth. A device with two PIN diodes, including the amplifier and the counter, is commercially available [5] and installed at some synchrotron light sources.

II.9.7.2.4 Ionization chamber

Ionisation chambers **IC** [17] measure the number of secondary charges created in a gas volume; see also section II.9.2.9.2. Fig. II.9.153 shows a round ionisation chamber filled with Ar or N_2 gas. Typically, a sealed glass or metal tube contains $\sim$ 100...1000 cm^3 of gas between an outer high voltage electrode and an inner grounded readout electrode [192]. The output current is measured with a sensitive current-to-voltage or current-to-frequency converter [193]. The IC is not sensitive to neutrons and has a low detection efficiency for γ-rays; mainly charged hadrons and $e^{\pm}$ are detectable. By definition, the signal strength directly yields the absorbed dose in Gy. Because an inert, noble gas such as Ar or diatomic gases such as N_2 or air are used in the detection volume, the device is very radiation hard. The signal strength is orders of magnitude lower than for detectors in particle counting mode. In Fig. II.9.153, the scheme

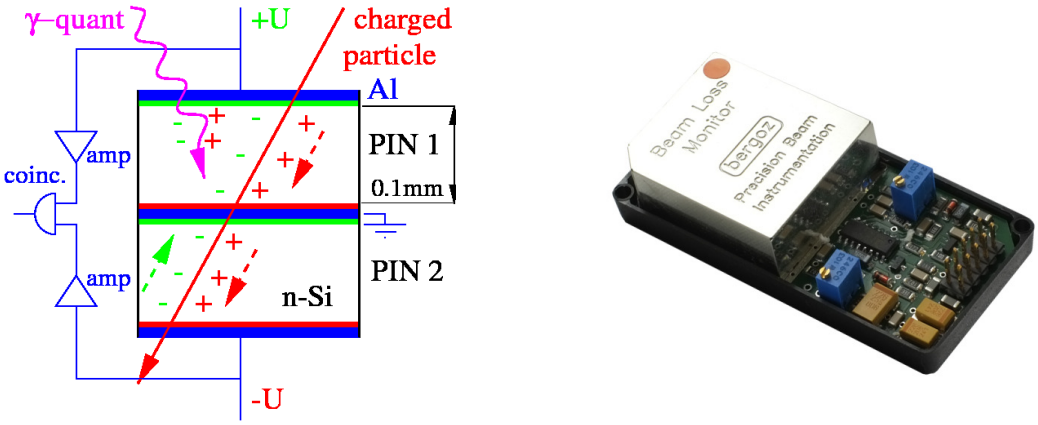

Fig. II.9.152: Schematic drawing of a two PIN diodes driven in coincidence and a photo of the device [5].

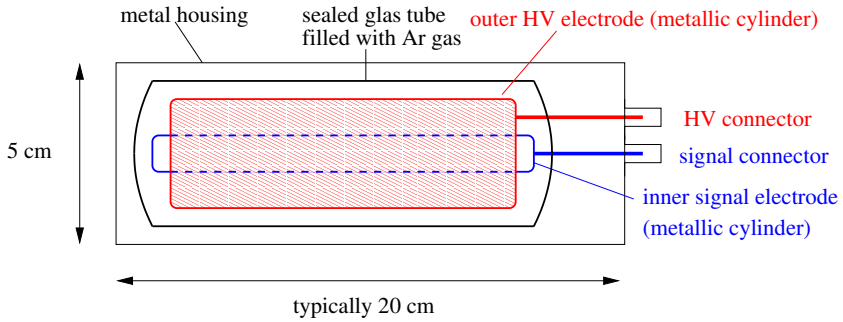

Fig. II.9.153: Schematic drawing of an ionisation chamber as used for beam loss detection.

Table II.9.15: Basic parameters for the so-called RHIC-type co-axial IC [192] and the planar LHC-type IC [194] for beam loss measurement.

Parameter	Co-axial IC	Planar IC
Outer length & diameter [cm]	20 & 6	50 & 9
Active gas volume [l]	0.11	1.5
Gas type & pressure [bar]	Ar at 1.1	N_2 at 1.1
Number of electrodes	2	61
Distance of electrodes [mm]	31.7, co-axial with $Ø_{inner} = 6.3$, $Ø_{outer} = 38$	5.7
Voltage [kV]	1	1.5
Reaction time [μs]	$\simeq 3$	$\simeq 0.3$
Overall dynamic range	10^6	10^8

of a co-axial IC is depicted. The IC does not react as fast as scintillators for this geometry because the gas ions, created by the radiation, need $\sim$ 10 μs to reach the electrode. This time constant leads to a convolution of the primary signal, which for most applications, is acceptable. Therefore, the digital electronics readout of the IC current is usually not faster than 1 ms. The essential parameters for such an IC are summarised in Table II.9.15. A typical installation of a co-axial IC at an accelerator beam line or synchrotron is depicted in Fig. II.9.154.

The detection threshold of an IC is proportional to the gas volume. The drift time of the gas ions and electrons should be shortened to achieve a fast reaction time, even for a large gas volume. It can

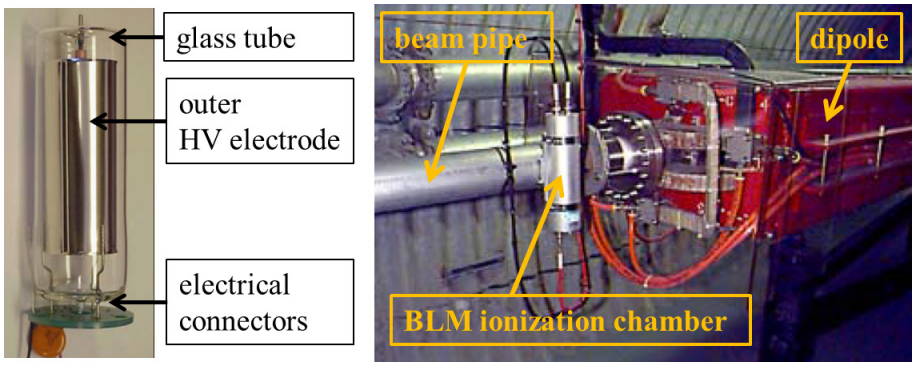

Fig. II.9.154: Left: Photo of a 15 cm long co-axial ionisation chamber used as a beam loss monitor. Right: The installation of such an ionisation chamber for beam loss detection in a transport line [192].

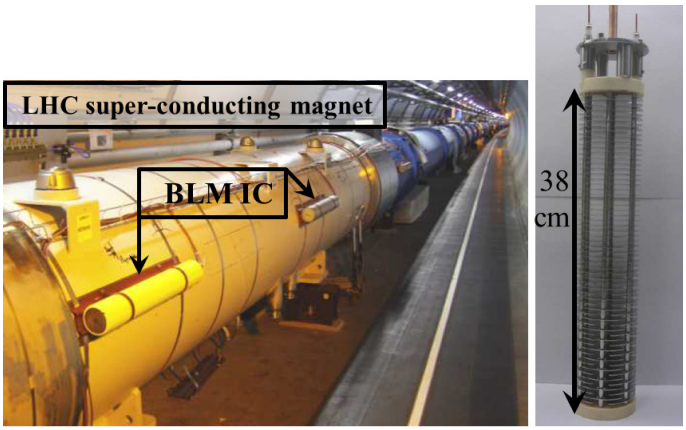

Fig. II.9.155: Photo of the installation of a 50 cm long ionisation chamber comprising 61 parallel plates at CERN LHC [194].

be realised by a parallel electrode arrangement with alternating biased and readout electrodes. Such an IC is shown in Fig. II.9.155 as installed at CERN's LHC and further facilities. About 4000 BLMs are installed along the 27 km long LHC, corresponding to an average distance of about 6 m. They serve as the main detectors for machine protection and can trigger a fast beam abortion. The design of ICs for LHC and relevant simulations concerning the response to various radiation species are discussed e.g. in Ref. [194].

A further type of IC is referred to as long, cable-based IC. It comprises an air-filled long co-axial cable of some cm diameter as regularly used for medium power transmission of RF signals, see Fig. II.9.156. Here, the air acts as the ionisation medium, and the cable can be 10 to 100 m long. The spatial resolution can be achieved by recording the signal's arrival time at both ends using particle counting technologies; a typical time resolution of 10 ns corresponds to a spatial resolution of 1.5 m. This detector is suited for loss location at long transfer lines by using only one single detector with two readout channels.

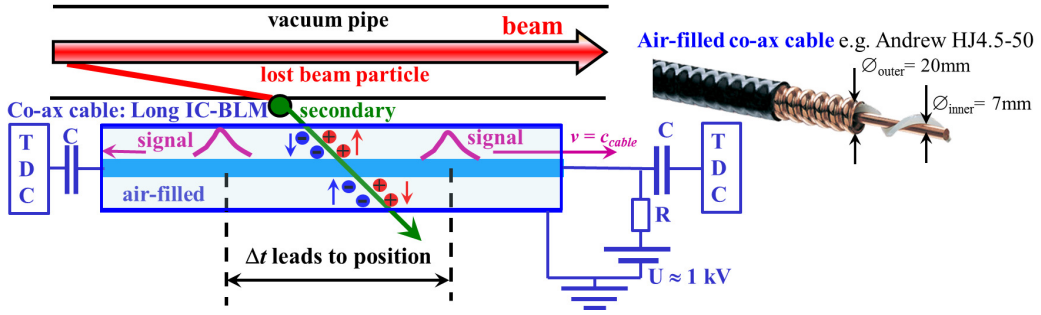

Fig. II.9.156: Scheme of a long, cable-based ionisation chamber installed along a beam line and a photo of a typically used RF-cable.

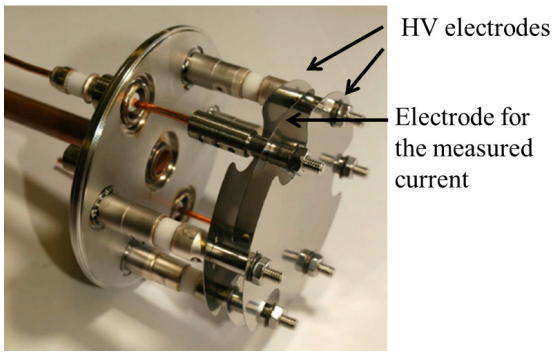

Fig. II.9.157: Photo of a three plate SEM beam loss monitor [195].

II.9.7.2.5 Secondary Electron Multiplier and Secondary Electron Monitor

An Aluminum Coated Electron Multiplier (ACEM) is an electron-multiplier where the photo-cathode is replaced by an aluminium surface. Secondary electrons are liberated by the interaction of the radiation and amplified by the dynodes. It offers a fast rise time and high dynamic range but a sensitivity much lower than for scintillators.

If the loss rate is very high, the current of secondary electrons from a surface is high enough to be measured directly. This can be realised by a secondary electron monitor with three plates installed in a small vacuum vessel [195]. The outer plates are biased by some +100 V, and the secondary electron current emitted from the central plate is measured by a trans-impedance amplifier or a current-to-frequency converter. The inner part of such a monitor is shown in Fig. II.9.157. Relevant simulations and tests of the response to different radiation are reported in Ref. [195].

II.9.7.2.6 Cherenkov light detectors

Inside an optical medium, the propagation velocity of light c_{medium} is reduced by the wavelength-dependent index of refraction $n(\lambda)$ to be $c_{\mathrm{medium}} = c/n(\lambda)$ where c is the velocity of light in vacuum. For typical cases, the index of refraction is constant within the optical wavelength interval used for the light detection. Cherenkov radiation is created when a charged particle moves with a velocity v faster than the material-dependent propagation velocity of light, i.e. if the condition

$$v > c_{\mathrm{medium}}/n \tag{II.9.150}$$

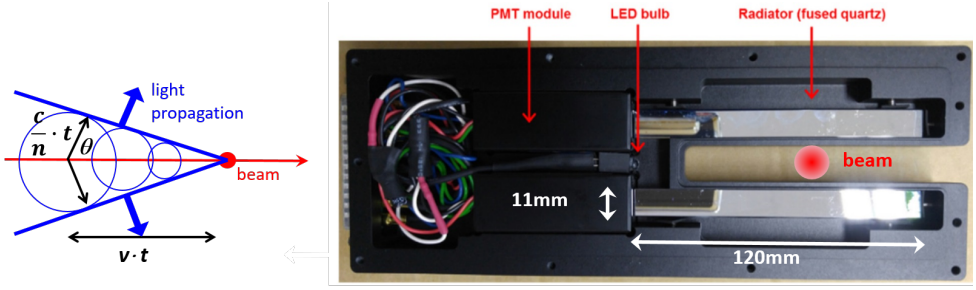

Fig. II.9.158: Left: Scheme of the Cherenkov wavefront for a charge moving with a velocity faster than the light propagation in the medium. Right: Example of the realisation at the PAL-XFEL [196] with quartz plates on top and bottom of the beam's vacuum pipe.

is fulfilled. The broadband light is emitted such that the electro-magnetic fields add up coherently as a wavefront with an opening angle θ of

$$\cos\theta = \frac{c}{v \cdot n} \tag{II.9.151}$$

as schematically depicted in Fig. II.9.158 (left). For mechanical objects, a comparable process is the wake-field created by the mechanical object moving in water or air faster than the sound-wave propagation. A noticeable amount of photons is emitted, which depends only on the particle velocity v, index of wavelength-dependent refraction $n(\lambda)$, and geometrical size of the radiator. The basics of Cherenkov radiation are discussed in Refs. [16–18]. In several applications, Quartz or fused silica in the shape of pads or rods are used providing an index of refraction in the order of $n \simeq 1.5$ in the optical wavelength range. Those materials have a low scintillation yield, typically with an emission band in the near UV range; optical filters can further suppress the scintillation. Those detectors are insensitive to other ionising radiations as generated by the synchrotron light or X-ray emission from close-by acceleration cavities. The light in the optical wavelength range is detected with photo-multipliers. An example of such an installation is depicted in Fig. II.9.158 (right) installed close to an undulator mounted directly on the vacuum chamber of an electron LINAC-based free electron laser [196]. Further recently realised examples are described in Refs. [197–199] where long optical fibres are installed; the spatial resolution is achieved by comparing the arrival time of the light signals at both ends of the fibres, converted to a distance by the known propagation velocity.

The main advantage of Cherenkov-based BLMs is related to the direct detection of the lost electrons, as they are still fast enough to generate Cherenkov light even after passing through the vacuum chamber. Due to the intrinsic low scintillation yield, other background from ionising radiation is suppressed. A fast observation down to a bunch-by-bunch time scale on the ns level is possible as Cherenkov light emission is an instantaneous process in contrary to scintillation (typical decay time of fluorescence level of $\simeq 100$ ns) and charge collection time of ionisation chambers (typically $\simeq 1$ μs). Hence, Cherenkov BLMs are frequently used at LINAC-based FEL facilities due to the short pulse operation.

II.9.7.2.7 Optical fibre

All discussed devices so far are particle counters. A different scheme uses material modifications by the absorbed dose, as reviewed in Ref. [200]. Optical fibres, e.g. used in telecommunication, can be

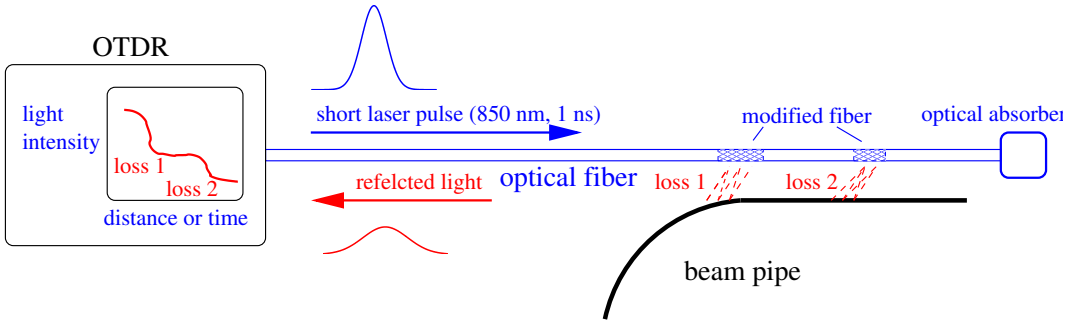

Fig. II.9.159: Principle of an OTDR beam loss detection with optical fibres.

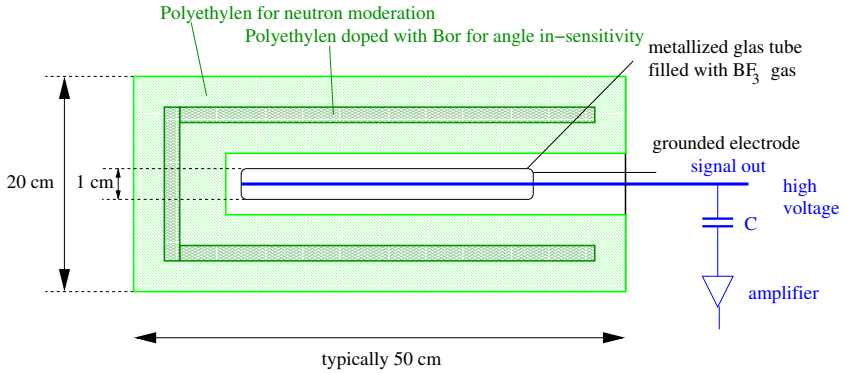

Fig. II.9.160: Scheme of a BF_3 proportional tube as used for beam loss detection. The proportional tube is filled with BF_3 gas surrounded by polyethylene to moderate the neutrons.

fabricated cheaply at nearly arbitrary length. A fibre installed close to the beam pipe can reach up to several km length [201]. Due to radiation damage, secondary particles modify this fibre by creating colour centres. This leads to a change in light transmission of the fibre and a noticeable amount of reflected light. As used in applications for telecommunication, the quality of fibre is tested by an optical time domain reflector (OTDR) ; see Fig. II.9.159: A $\sim$ 1 ns laser pulse is coupled to the fibre and travels along the fibre. If the fibre's optical properties are modified due to the radiation, part of the light is reflected. Its intensity, as well as the arrival time with respect to the input pulse, is measured. Due to the known velocity of light in the fibre of $\sim 0.66c$, the arrival time can be converted to a distance. This sensor arrangement can achieve a reasonable spatial resolution, and critical loss regions can be identified. An annealing process can partially repair the fibre, either by time or by heating the fibre to about 150 °C. Dedicated doping of the fibres makes them sensitive to different beam loss mechanisms. This monitor has a slow time response of more than 1 s due to the use of the OTDR.

Another method uses optical fibres as a scintillator, where the ionising particles create light during their passage [200]. With a photo-multiplier at each end of the fibre, the location of the interaction can be determined by comparing the arrival time. Not only scintillation but also Cherenkov light is detected as created by a charge travelling fast than the velocity of light inside the medium, see above.

II.9.7.2.8 BF_3 proportional tube

To measure only neutrons, a cylindrical proportional tube (typical diameter 10 mm and length 500 mm) filled with the gas BF_3 can be used [17]. Sometimes this detector is referred to as REM-Counter. For

thermal neutrons, the reaction ^{10}B+n $\rightarrow$ ^{7}Li + α has a high cross-section ($\sim$ 1 kbarn) and is exothermic with a Q-value (total kinetic energies of Li and α) of 2.3 MeV. Concentric layers of polyethylene surround the gas-filled tube with an outer diameter of $\sim$ 200 mm. The neutrons from the primary beam interaction are slowed down by elastic collisions with the hydrogen nuclei of the polyethylene. Special precautions are taken to achieve a flat detection efficiency as a function of the angle. Frequently these detectors are used at nuclear power plants for neutrons with an energy of up to 10 MeV, but the thermalisation yield of the neutrons can be extrapolated at least up to 100 MeV. In the traditional application, the glass tube is operated as a proportional tube. For this arrangement the count rate is limited to several 10^4 s^{-1} due to the time needed for recharging the inner wire of the proportional tube. Instead of the BF_3 working gas comparable types are used, but filled with ^{3}He, having a comparable cross-section for thermal neutron absorption by the reaction $^{3}_{2}$He + n $\rightarrow$ $^{3}_{1}$H + $^{1}_{1}$H [17].

II.9.7.2.9 Comparison of different beam loss monitors

Several BLM types were tested at the extraction septum magnets of the GSI synchrotron [191]. Figure II.9.161 (left) shows a typical example for a O^{8+} beam accelerated from 11.4 MeV/u to 800 MeV/u and then extracted slowly over 3 s; the maximum number of stored particles was 4×10^{10}. The signal as a function of time seen in the figure is displayed together with the signal for the synchrotron dc-transformer (top, arbitrary units) and a reference signal proportional to the extracted current measured at the experiment location (second plot, using a secondary electron monitor in arbitrary units, see Section II.9.2.9.3). The general feature is that the signals for the different loss monitors are showing the same time behaviour. This is not evident a priori due to the different detection mechanisms. This shows the predominant role of the "prompt" radiation (within a time scale of ms) whatever the type of secondary radiation is. The signals of all detectors are background-free, showing the minor role of permanent activation compared to the signals induced during the beam delivery. The choice of a BLM type is, therefore, mainly driven by the expected count rate.

The linearity of the different detectors can be seen in Fig. II.9.161 (right) shows the total counts for one spill as a function of the current detected at the experiment. The count-rate varies considerably: The plastic scintillator shows the maximum rate, about a factor of 30 more than the BF_3-tube, due to the detection of more categories of secondary particles species. The liquid scintillator shows a lower rate; the saturation for the highest rate is due to the slow integrating pre-amplifier. The signal strength of the IC is lower by a factor of 200 compared to the plastic scintillator. The dynamic range is highest for the plastic scintillator. The PIN diode is not shown here, but the count rate would have been about three orders of magnitude below the plastic scintillator.

Table II.9.16 shows a simplified comparison of the discussed BLMs. Based on the physical detection method, BLMs are sensitive to different types of radiation, and the signal strength varies by several orders of magnitude. The expected loss rate and secondary particle composition at a given accelerator facility is one criterium for the choice of a BLM type. Generally, detectors with counting capability (such as scintillator, PIN-diode, and Cherenkov counter) are more sensitive than integrating detectors (such as SEM, IC, and optical fibre). Moreover, particle counting offers an extensive dynamic range. However, the material used for scintillators, PIN-diode and Cherenkov counters might be damaged by ionising radiation relatively quickly, leading to a signal decrease preventing absolute dose measurements. The

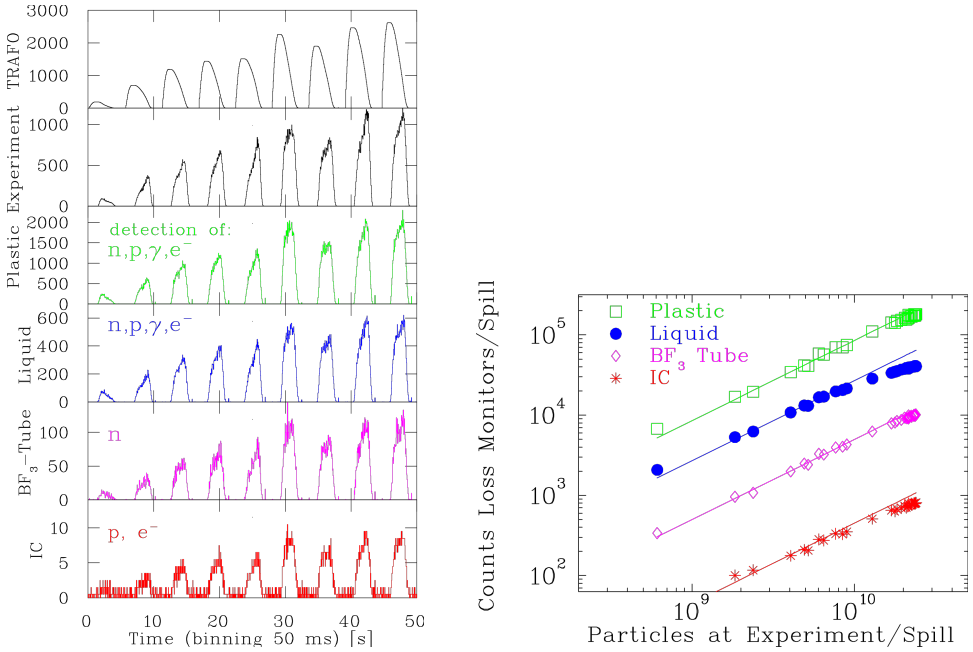

Fig. II.9.161: Left: Typical example from different beam loss monitors for an O^{8+} beam accelerated from 11 to 800 MeV/u for nine cycles with varying intensities up to 4×10^{10} particles per cycle [191]. Right: Linearity of the loss monitors as a function of the current for the same parameters. The lines are linear fits.

Table II.9.16: Simplified comparison of various beam loss monitors.

Physical property	Detected particles	Signal strength	Times response	Radiation tolerance	Main application
Plastic scint.	all ionising rad.	high	fast	low	machine experiments
Liquid scint.	all ionising rad.	high	fast	medium	machine experiments
PIN diode	charged part.	medium	fast	low	general purpose
Ionisation chamber	charged part.	medium	medium	high	protection, general purpose
SEM	charged part.	low	medium	high	protection at high rad. area
Cherenkov counter	primary beam	medium	ultra fast	low	fast protection
Opt. fibre OTDR	all ionising rad.	low	very slow	medium	loss location determination
BF_3 prop. tube	neutrons	low	slow	medium	prot. outside acc. tunnel

radiation hardness for ionisation chambers is much higher due to their simple detection scheme using inert gases. Moreover, ICs measure the absolute dose, enabling simpler algorithms to determine the fraction of beam loss. The time response for particle loss detection is another issue; particle counters react faster to shower irradiation than gas detectors. The fastest response is achieved with Cherenkov counters as they are based on prompt light emission. BF_3 proportional tubes are mainly used outside the acceleration tunnel to monitor the radiation level outside the radiation-protected area. The radiation damage determination of optical fibres based on OTDR measurements is mainly used to precisely localise critical loss locations. More information on signal strength, radiation hardness and applications can be found in Ref. [185].

II.9.7.3 Machine protection using beam loss detectors

The most frequent application of beam loss monitors is the protection of the accelerator components. The high energy stored in the beam can damage the surroundings when the projectiles hit materials. In particular, the vacuum pipe can be damaged by the temperature rise from the energy deposition of the particles, leading to a vacuum leakage. Moreover, other materials, such as electrical feed-throughs, the isolation of the magnet coils, or any electronic devices, can be destroyed due to the modification of the material by radiation. As discussed in Section II.9.7.1, the nuclear interaction leads to radioactive nuclei which have lifetimes of hours or more. Activation of the accelerator components is the result, preventing the access of persons into the accelerator tunnel, and maintenance is strongly hampered. As a general rule of thumb, the power dissipation from the beam losses should be below 1 W/m to enable "hands-on maintenance".

Another essential application of beam loss monitors is the quench protection of super-conducting magnets and cavities. Even a small amount of losses can heat the super-conducting material above the critical temperature causing a quench, i.e. a transition to normal conductivity. Loss monitors always control this dangerous situation. They create an interlock: as soon as a critical count rate or dose is reached, the beam is kicked out of the accelerator immediately. The design criteria of an interlock system are discussed in Refs. [185, 190, 193]. Last but not least, the reason for low losses is the protection of the environment and an efficient transfer of particles to the experiment. In the control room of most high current accelerator facilities, the loss rate at sensitive locations is monitored online to visualise the full functionality of the machine.

We discuss briefly two categories of losses:

- **Irregular or fast losses** occur because of a malfunction of an accelerator device, such as the power supplier of magnets or RF cavities, leading to a beam with wrong parameters and, subsequently, the loss of part or all beam particles. Moreover, misalignment of the device settings (e.g., the beam is not centred inside a quadrupole leading to steering, or wrong kinetic energy of the beam by a wrong RF cavity phase or amplitude) can result in a mismatch of the beam at the following stages of the accelerator, and part of the beam might be lost. Beam loss monitors localises these losses, warning the operator or triggering an interlock to stop the beam delivery.
- **Regular or slow losses** are known losses, e.g., at aperture limits of a collimator system or losses due to the finite lifetime of the beam in a synchrotron. Most of them are unavoidable, but an increase in the loss rate shows a malfunction. In addition, beam loss monitors can be used to find the appropriate parameters, e.g. for an emittance-reducing collimator.

By looking in particular at the first item, it is obvious that a beam loss monitor system should have a high sensitivity and an extensive dynamic range. The high sensitivity is needed to get a usable signal when only a tiny fraction of the beam is lost. Using scintillators or PIN diodes, single particle counting can be performed with a very low detection threshold. Detecting the lost particles directly gives a much higher sensitivity than looking at the lost fraction of the total signal by a current transformer. The high dynamic range is mainly needed for the detection of irregular losses because the losses at one location can sometimes vary by several orders of magnitude, e.g. due to a power failure of a magnet or cavity. The monitoring has to be operated over several orders of magnitude concerning the signal strength without

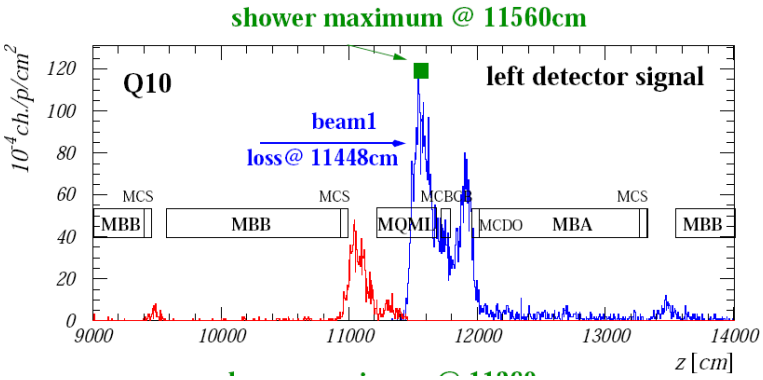

Fig. II.9.162: Simulation of a secondary particle distribution (hadron shower) due to a proton loss inside a quadrupole for the LHC and 7 TeV protons [202]. The maximum of the shower is about 1 m from the loss point.

changing the full-scale range to prevent the signal saturation for large losses. A particle counting mode delivers this high dynamic for rates ranging from 10 s^{-1} up to 10^7 s^{-1}. Close to a collimator, scintillators offer a high dynamic range, which is needed for the sensitive detection of the tails in the transverse particle distribution. For other regular losses, the required dynamic range can be lower due to the slower time variation. For the detection of those applications, ionisation chambers are often installed in this case.

Beam loss monitors are relatively cheap instruments and are installed outside the vacuum pipe, see Fig. II.9.150. At most facilities, they are mounted at many locations along the accelerator to have good spatial coverage. The required time resolution depends very much on the application: For resolving the properties of individual bunches, fast responding detectors (reaction time less than 100 ns), like scintillators or PIN diodes, are needed. Ionisation chambers are much slower having, in conjunction with the connected analogue and digital electronics, only $\sim$ 100 μs time response. However, ICs offer the direct determination of dose and are, therefore, often installed for machine projection systems.

The position of beam loss monitors should be well chosen. For highest sensitivity, the distribution of the secondary particles should have a maximum at this location. The secondary particle distribution is calculated using adequate simulation software for particle-matter interaction and secondary particle tracking. For high energies, the well-known code `GEANT4` [203] or `FLUKA` [204] are used. An example is shown in Fig. II.9.162 for the case of the LHC beam. An realistic assumption of the primary particle loss is needed. A loss of beam particles at a quadrupole is assumed in Fig. II.9.162. This is the most probable location because the beam has the largest width here.

II.9.7.4 Beam loss monitoring for alignment

Beam loss monitors have two main advantages, namely their large sensitivity and the fact that these monitors can be installed at many locations. For the alignment of the beam at critical positions having small beam pipes, several beam loss monitors can be mounted densely. An example of the slow extraction region at the GSI synchrotron is shown in Fig. II.9.163. Here, the septum elements, used to kick the beam, have small pipe diameters comparable to the actual beam size. If the angle at the input of the septum magnets is slightly wrong, part of the beam is lost there. Therefore, the angle kick at the first element

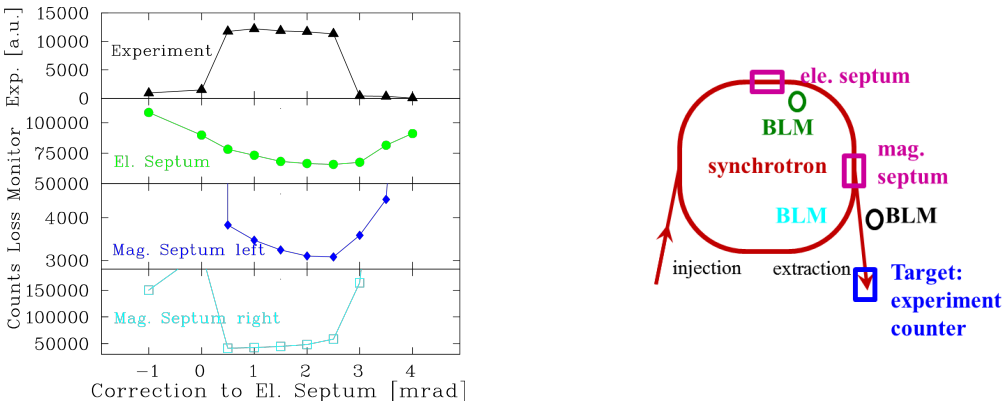

Fig. II.9.163: Left: Counts per spill from three loss monitor locations and the current at the experiment as a function of the angle electro-static septum at the GSI synchrotron [191]. Right: The location of the BLMs and target diagnostics related to the measurement.

(here the electro-static septum) has to be aligned carefully in small steps to find the minimal loss rate. Using beam loss monitors, the alignment procedure can be executed with higher sensitive input signals than by monitoring the transmitted current, as demonstrated by the top curve in Fig. II.9.163.

A stable beam stored inside a synchrotron serves as a second example. Here, the tune needs to be chosen carefully to avoid tune-resonances resulting in a transverse beam blow-up. The mechanical alignment and the settings of the various magnets are never in perfect agreement with theory; therefore, the optimal setting for the beam has to be found experimentally. The beam blow-up can be measured precisely by using a scraper close to the transverse beam tail inside the vacuum tube. A beam loss monitor mounted close to this scraper can determine the number of beam particles hitting this scraper. In Fig. II.9.164, the loss rate normalised to the circulating current is determined as a function of the machine tune. The tune is varied by changing the main quadrupoles slightly. At specific settings, the loss rate increases. A beam-optics aided alignment of all critical elements minimises the beam loss, and optimal storage is performed [205]. Figure II.9.165 shows the working diagram for a 2-dimensional tune scan with the loss rate recorded by a BLM plastic scintillator in counting mode [206]. As a first step, a scan was performed with a regular beam setting without closing an undulator. As expected, the highest loss rate is induced at a third-order resonance along the line $Q_y = 6\frac{2}{3}$. Moreover, a high loss occurred in case the horizontal and vertical tune had the non-integer value of $q_{x,y} = \frac{3}{4}$. The tune values $Q_x = 17.84$, and $Q_y = 6.72$ were chosen for regular operation, as indicated in the figure. A second scan was done to show the additional effect of a closed undulator, and the modification of the loss rate was recorded. In particular, a high loss rate is visible on a line which couples the horizontal and vertical tune fulfilling the condition $Q_x + 3Q_y = 60$ as excited by the undulator's higher-order field components. Since there is a relationship between the resonant beam excitation and those higher field components as the driving term of the resonance, such measurement can be used to characterise the undulator's field components. For the displayed case, the working point was shifted depending on the undulator setting to avoid this beam loss.

More advanced experiments can be realised. For example, to get information about the beam lifetime limitations due to the interaction between the individual beam particles by Coulomb-scattering (i.e. intra-beam interaction by multiple Coulomb scattering leading to a transverse or longitudinal beam

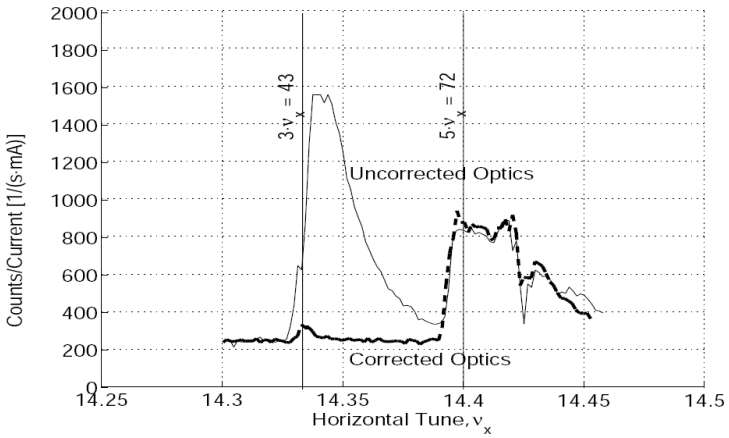

Fig. II.9.164: Tune scan at the ALS synchrotron light source [205]. The horizontal tune is varied for a fixed vertical tune, and the loss rate, as measured with a scintillator at a collimator, is plotted. By changing the setting of some quadrupoles, one resonance ($3 \cdot \nu_x$) can be suppressed.

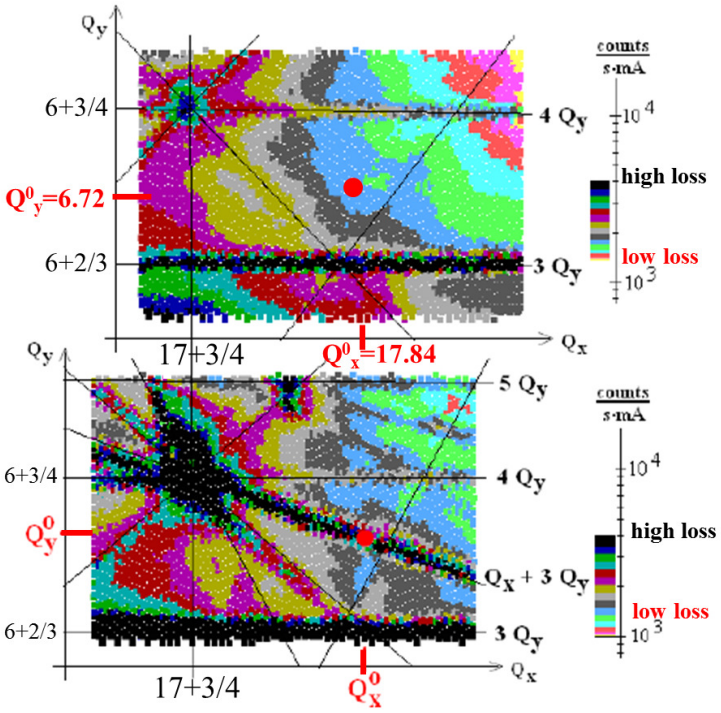

Fig. II.9.165: Loss rate at a plastic scintillator BLM for a two-dimensional tune scan at the BESSY synchrotron light source [206] without (top) and with (bottom) closed undulator. The horizontal Q_x and vertical Q_y tune is changed; in the case of the closed undulator (bottom), the coupling resonance fulfilling $Q_x + 3Q_y = 60$ is excited, leading to strong losses.

enlargement) or Touschek scattering (i.e. transfer of transverse particle momentum to the longitudinal plane by a single scattering process). A longitudinal increase of $\Delta p/p$ by Touschek scattering can be monitored by a scraper located at a dispersive region due to the coupling of $x = D \cdot \Delta p/p$, while at locations with $D = 0$ only the transverse effect is seen [206].

II.9.8 Summary

The functionality of various beam instruments is described, and their applicabilities for different beam parameters are mentioned. For daily accelerator operation, mainly current, position, and, to some extent, transverse profile measurements are executed. It is advantageous if the monitor is non-invasive for the beam, such as current transformers and BPMs, to enable a simultaneous measurement at several locations, archiving of beam parameters, and, if possible, for automated beam alignment by a feedback loop. We refer to Table II.9.1 in the introduction for using the individual instruments. Here, a brief summary is presented.

Current transformers of various types serve as non-invasive instruments but have a lower detection threshold.

For bunched beams, the transverse centre position can be recorded by BPMs. Due to their principle, BPMs are non-invasive but require a minimum beam current for precise position determination. The subsequent electronics influence the achievable position resolution: the spatial resolution can be balanced with respect to the observation duration (long-time observation results in an improved position resolution). BPMs are the most frequently used monitors for beam alignment and serve, in many cases, as the sensor for a feedback loop. By exciting the beam to coherent oscillations, important synchrotron parameters, like tune and chromaticity, are determined with BPMs.

Various techniques are applied for profile measurements, with scintillation or OTR screens being a favoured technique for the regular operation of transfer lines due to their reproduction of the 2-dimensional distribution. SEM-Grids and wire scanners are also often used due to their robustness and extensive dynamic range. A non-invasive technique for profile measurements is realized by an IPM for medium to high-intensity proton beams in transfer lines and synchrotrons. At electron synchrotrons, the anyhow available synchrotron light is used for transverse and longitudinal diagnostics.

More complex parameters can be determined at transfer lines behind a LINAC or cyclotron, particularly the transverse and longitudinal emittances. The related measurements are, in many cases, performed by experts during dedicated machine development times, which allow for more sophisticated instruments and methods. Advanced numerical methods are applied to achieve reliable results.

Bunch length measurement can be performed by recording the temporal structure of synchrotron light. However, extreme time resolution is required at LINAC-based light sources, which is realized by electro-optical modulation techniques. Those methods are based on detecting the electro-magnetic field accompanied by the relativistic charged particle. For non-relativistic velocities, the field is not an appropriate representation of the particle distribution; hence, a direct detection of the particles is required.

Most accelerator facilities are equipped with a large amount of beam loss monitors to supervise the correct accelerator functionality permanently and generate an interlock in case of any malfunction to prevent permanent activation or component destruction.

Last but not least, beam instrumentation and diagnostics should support accelerator development and operation for scientific and social benefit.

Acknowledgment

The large and complex field of beam diagnostics can only be covered by participating in the open discussions held in the community of accelerator physicists, where one gets in contact with new and exciting

physics and technologies. The valuable discussion with numerous colleagues is gratefully acknowledged. The GSI beam diagnostic group members were always open for discussion sharing their knowledge, and were willing to prepare many good figures. In particular, I have to express my thanks to Mohammed Almalki, Christoph Dorn, Tino Giacomini, Rainer Haseitl, Tobias Hoffmann, Wolfgang Kaufmann, Piotr Kowina, Andreas Reiter, Hannes Reeg, Thomas Sieber, Serban Udrea, and Beata Walasek-Höhne. In particular, the detailed discussion with Rahul Singh is warmly appreciated for his clear view of physics and technologies and for sharing many innovative ideas with me. Moreover, I thank many GSI colleagues for releasing important and meaningful data.

The careful and critical reading of the script and the intense discussion on all subjects by Andreas Peters (Heidelberg Ion Therapy Centre), Jeroen Belleman (CERN), Jun He (Chinese Academy of Science), and, recently, Carsten Welsch (University Liverpool and Cockcroft Institute) is gratefully acknowledged and led to important improvements.

Valuable comments by previous JUAS participants and further readers led to improvements in the description; I acknowledge the related discussion warmly. Further criticisms and comments are always welcome.

Last but not least, thanks to my wife Elisabeth Forck and my children for their understanding and patience during many long evenings I was working on this lecture.

II.9.9 Appendix A: Frequently used abbreviations

ac	alternating current
ACCT	alternating current current transformer
ADC	analogue-digital converter
amp	amplifier (electronic device)
BIF	beam induced fluorescence monitor
BLM	beam loss monitor
BPM	beam position monitor
BSM	bunch shape monitor
BTF	beam transfer function
BW	bandwidth for electrical devices
CCD	charged coupled device for a camera
dc	direct current
DCCT	direct current current transformer
CERN	centre européenne pour la recherche nucléaire
CMOS	complementary metal oxide semiconductor
DESY	deutsches Elektronen Synchrotron
DFT	discrete Fourier transformation
DTL	drift tube LINAC
DSO	digital signal oscilloscope
DSP	digital signal processor
EOM	electro-optical modulator
EOSD	electro-optical spectral decoding
EOTD	electro-optical temporal decoding
FCT	fast current transformer, identical to passive transformer
FEL	free electron laser
FT	Fourier transformation
FFT	fast Fourier transformation
FWHM	full width half maximum
Grid	identical to SEM-grid for profiles
GSI	Gesellschaft für Schwerionenforschung
Harp	identical to SEM-grid for profiles
HV	high voltage above ~ 1 kV
IC	ionization chamber
ICT	integrating current transformer
IF	intermediate frequency for a rf-mixer
IPM	ionization profile monitor, identical to RGM
IR	infrared light
LHC	large hadron collider at CERN
LINAC	linear accelerator
LO	local oscillator for rf-mixer
MCP	micro-channel plate
mw	micro-waves with 1 GHz $< f <$ 100 GHz
MWPC	multi-wire proportional chamber for profile measurement
NWA	network analyser

op-amp	operational amplifier (electronic chip device)
OTR	optical transition radiation for profiles
PHD	pulse height distribution for particle detectors
OTDR	optical time-domain reflectometer
PMT	photo-multiplier tube
pre-amp	first stage amplifier direct behind detector (fully equipped electronic device)
PU	pick-up used, e.g. as the detecting device for beam position monitoring
rf	radio frequency with 100 kHz $< f <$ 1 GHz
RFQ	radio frequency quadrupole LINAC
RGM	residual gas (profile) monitor, identical to IPM
SEEM	secondary electron emission monitor, identical to SEM
SEM	secondary electron (emission) monitor, identical to SEEM
SEM-grid	secondary electron emission grid for profiles, identical to harp
SLM	synchrotron light monitor, identical to synchrotron radiation monitor
SPA	spectrum analyser
SR	synchrotron radiation
SRM	synchrotron radiation monitor, identical to synchrotron light monitor
TDR	time-domain reflectometer or time-domain reflection
ToF	time-of-flight
UV	ultra-violet light
WCM	wall current monitor

II.9.10 Appendix B: Definition of statistical moments

This appendix complies the definition of the statistical moments of a 2-dimensional distribution as used for the emittance calculation in Section II.9.4.

Continuous case:

A 2-dimensional density distribution $\rho(x, x') \in \mathbb{R}$ with independent, real variables $x \in \mathbb{R}$ and $x' \in \mathbb{R}$ is given. The first moments $\mu \equiv \langle x \rangle \in \mathbb{R}$ and $\mu' \equiv \langle x' \rangle \in \mathbb{R}$ are called expectation values and are defined as

$$\mu \equiv \langle x \rangle = \frac{\int_{-\infty}^{\infty}\int_{-\infty}^{\infty} x \cdot \rho(x,x')\, dx'dx}{\int_{-\infty}^{\infty}\int_{-\infty}^{\infty} \rho(x,x')\, dxdx'} \quad \text{and} \quad \mu' \equiv \langle x' \rangle = \frac{\int_{-\infty}^{\infty}\int_{-\infty}^{\infty} x' \cdot \rho(x,x')\, dxdx'}{\int_{-\infty}^{\infty}\int_{-\infty}^{\infty} \rho(x,x')\, dxdx'} \quad . \tag{II.9.152}$$

The n^{th} central moments of a density distribution $\rho(x, x')$ is calculated via

$$\langle x^n \rangle = \frac{\int_{-\infty}^{\infty}\int_{-\infty}^{\infty} (x-\mu)^n \cdot \rho(x,x')\, dx'dx}{\int_{-\infty}^{\infty}\int_{-\infty}^{\infty} \rho(x,x')\, dxdx'} \quad \text{and} \quad \langle x'^n \rangle = \frac{\int_{-\infty}^{\infty}\int_{-\infty}^{\infty} (x'-\mu')^n \cdot \rho(x,x')\, dxdx'}{\int_{-\infty}^{\infty}\int_{-\infty}^{\infty} \rho(x,x')\, dxdx'} \quad . \tag{II.9.153}$$

Using the abbreviation $P(x) = \int \rho(x,x')\, dx'$ and $P'(x') = \int \rho(x,x')\, dx$ as in Fig. II.9.73 this is

equivalent to

$$\langle x^n \rangle = \frac{\int_{-\infty}^{\infty} (x-\mu)^n \cdot P(x)\, dx}{\int_{-\infty}^{\infty} P(x)\, dx} \quad \text{and} \quad \langle x'^n \rangle = \frac{\int_{-\infty}^{\infty} (x'-\mu')^n \cdot P'(x')\, dx'}{\int_{-\infty}^{\infty} P'(x')\, dx'} \tag{II.9.154}$$

The second moments with $n = 2$ are called variances. If the variance is positive, its square root is the standard deviation $\sigma_x = \sqrt{\langle x^2 \rangle}$ and $\sigma_{x'} = \sqrt{\langle x'^2 \rangle}$.
The mixed quantity $\langle xx' \rangle$ is called covariance and is defined as

$$\langle xx' \rangle = \frac{\int_{-\infty}^{\infty}\int_{-\infty}^{\infty} (x-\mu)\cdot(x'-\mu')\cdot\rho(x,x')\, dxdx'}{\int_{-\infty}^{\infty}\int_{-\infty}^{\infty} \rho(x,x')\, dxdx'} \quad . \tag{II.9.155}$$

Discrete case:
A real measurement leads to discrete values of the density distribution $\rho(x_i, x'_j)$ at discrete steps x_i and x'_j. The first moment is calculated for this case via

$$\mu \equiv \langle x \rangle = \frac{\sum_{i,j}\ x_i \cdot \rho(x_i, x'_j)}{\sum_{i,j}\ \rho(x_i, x'_j)} \quad \text{and} \quad \mu' \equiv \langle x' \rangle = \frac{\sum_{i,j}\ x'_j \cdot \rho(x_i, x'_j)}{\sum_{i,j}\ \rho(x_i, x'_j)} \quad . \tag{II.9.156}$$

The n^{th} central moment of the discrete distribution is

$$\langle x^n \rangle = \frac{\sum_{i,j}\ (x_i-\mu)^n \cdot \rho(x_i, x'_j)}{\sum_{i,j}\ \rho(x_i, x'_j)} \quad \text{and} \quad \langle x'^n \rangle = \frac{\sum_{i,j}\ \left(x'_j-\mu'\right)^n \cdot \rho(x_i, x'_j)}{\sum_{i,j}\ \rho(x_i, x'_j)} \quad . \tag{II.9.157}$$

The covariance is correspondingly

$$\langle xx' \rangle = \frac{\sum_{i,j}\ (x_i-\mu)\left(x'_j-\mu'\right)\cdot\rho(x_i, x'_j)}{\sum_{i,j}\ \rho(x_i, x'_j)} \quad . \tag{II.9.158}$$

II.9.11 Appendix C: Theorems of Fourier transformation

The Fourier transformation of a time-dependent function $f(t)$ is widely used to transform it into a frequency-dependent function $\tilde{f}(\omega)$. The technical application concerning the time-dependent function $f(t)$ is called time-domain processing, and its measurement typically uses an oscilloscope. The handling of the frequency-dependent function $\tilde{f}(\omega)$ is called frequency-domain processing, and the measurements typically use a spectrum analyzer. (The physically used frequency f is related to the angular frequency ω via $\omega = 2\pi f$.) The transformation from time-domain to frequency-domain is often executed to discuss electronic circuits, as the calculation methods might be simpler in one of the domains. The theorems below are extensively used for the discussion of BPMs in Section II.9.5.

Firstly, the essential mathematical theorems in terms of continuous functions and infinite time observation are complied. Secondly, the crucial modifications for the realistic technical case of signal sampling

with discrete time steps and finite observation time are given.

II.9.11.1 Theorems for continuous functions

Definition of Fourier transformation: Let $f(t) \in \mathbb{R}$ be a real, non-periodic and continuous function of the independent variable $t \in \mathbb{R}$ which is absolute integrable i.e. the integral $\int_{-\infty}^{\infty} |f(t)|dt < \infty$ exists and is convergent. Then the Fourier transformation $\tilde{f}(\omega)$ of $f(t)$ is defined as an integral transformation via

$$\tilde{f}(\omega) \equiv \int_{-\infty}^{\infty} f(t) \cdot e^{-i\omega t} dt \ . \tag{II.9.159}$$

The Fourier transformation is a complex function $\tilde{f}(\omega) \in \mathbb{C}$ of a real variable $\omega \in \mathbb{R}$. In a technical application the absolute value $A(\omega) = |\tilde{f}(\omega)|$ called amplitude or magnitude or the square $A^2(\omega) = |\tilde{f}(\omega)|^2$ called power is often displayed, as well as the phase $\tan\varphi(\omega) = \text{Im}\left(\tilde{f}(\omega)\right)/\text{Re}\left(\tilde{f}(\omega)\right)$ using the real and imaginary part of this complex function.

Definition of inverse Fourier transformation: For the frequency-domain function $\tilde{f}(\omega)$ the time-domain function $f(t)$ can be calculated via the inverse Fourier transformation

$$f(t) = \frac{1}{2\pi} \int_{-\infty}^{\infty} \tilde{f}(\omega) \cdot e^{i\omega t} d\omega \ . \tag{II.9.160}$$

which results in the original time-domain function $f(t)$.

No loss of information: As a direct corollary of the definition it can be stated: Starting from a time-domain function $f(t)$ and performing the Fourier transformation yielding $\tilde{f}(\omega)$ and then executing the inverse Fourier transformation, the original time-domain function $f(t)$ is obtained. In other words: Each time-domain function $f(t)$ defines an unique transformation $\tilde{f}(\omega)$ and vice versa. For the technical application, this means that a description can either be performed in time- or frequency-domain yielding equivalent results.

Linearity: Let $a, b \in \mathbb{R}$ being some real numbers and $f_1, f_2 \in \mathbb{R}$ two Fourier transformable functions then it is

$$\int_{-\infty}^{\infty} [af_1(t) + bf_2(t)] \cdot e^{-i\omega t} dt = a\tilde{f_1}(\omega) + b\tilde{f_2}(\omega) \tag{II.9.161}$$

hence, it is a linear transformation.

Time-shift theorem: Let $t_0 \in \mathbb{R}$ being a real number then it is

$$\int_{-\infty}^{\infty} f(t + t_0) \cdot e^{-i\omega t} dt = e^{-i\omega t_0} \cdot \tilde{f}(\omega) \tag{II.9.162}$$

i.e. the amplitude spectrum $A(\omega) = |\tilde{f}(\omega)|$ is equal to the un-shifted Fourier transformation while the phase is modified by the frequency dependent phase factor $\varphi(\omega) = \omega t_0$ with respect to the phase of the un-shifted function $\tilde{f}(\omega)$.

Frequency-shift theorem: Let $\omega_0 \in \mathbb{R}$ being a real number which is used as a harmonic modulation via $e^{i\omega_0 t}$ (technically called carrier frequency) of the original function $f(t)$ (technically called signal), then it is

$$\int_{-\infty}^{\infty} f(t)e^{i\omega_0 t} \cdot e^{-i\omega t}dt = \tilde{f}(\omega - \omega_0) \tag{II.9.163}$$

i.e. the original Fourier transformation is shifted by the modulation frequency ω_0. The effect of the modulation can be described as a replication of the signal transformation $\tilde{f}(\omega)$ (technically called base-band signal as centred around $\omega = 0$) to the modulation frequency as centred around $\omega = \omega_0$. This theorem is the basis for the technical application of frequency mixing, e.g. used for narrow-band position determination by BPMs as described in Section II.9.5.9.

Law of Similarity: Let $a \in \mathbb{R}$ being a real, non-zero ($a \neq 0$) number then it is

$$\int_{-\infty}^{\infty} f(t/a) \cdot e^{-i\omega t}dt = |a| \cdot \tilde{f}(a\omega) \tag{II.9.164}$$

i.e. a scaling law concerning the time or frequency range can be applied. Moreover, it can be stated that for a scalable time-domain function, the Fourier transformation can easily be given. For example, consider a Gaussian function as it can be stated as wider the time-domain function is, as narrower is the frequency-domain function.

Differentiation law: Let $f(t) \in \mathbb{R}$ be a function and the n^{th} derivative $f^{(n)}(t)$ exists and is Fourier transformable then it is

$$\int_{-\infty}^{\infty} f^{(n)}(t) \cdot e^{-i\omega t}dt = (i\omega)^n \cdot \tilde{f}(\omega) \tag{II.9.165}$$

i.e. the Fourier transformation of the n^{th} derivative is given by the product of the of $(i\omega)^n$ with the Fourier transformation of the original function. This theorem is used in Eq. II.9.78.

Parseval Formula: Let $f(t) \in \mathbb{R}$ be Fourier transformable and square-integrable then

$$\int_{-\infty}^{\infty} |f(t)|^2 dt = \frac{1}{2\pi} \int_{-\infty}^{\infty} |\tilde{f}(\omega)|^2 d\omega \tag{II.9.166}$$

i.e. there is a simple relation between the integrated time-domain function and the integrated frequency spectrum.

Law of convolution: The convolution of two absolute integrable functions $f_1(t), f_2(t) \in \mathbb{R}$ is defined as

$$f_1(t) * f_2(t) \equiv \int_{-\infty}^{\infty} f_1(\tau) \cdot f_2(t-\tau)\, d\tau \ . \tag{II.9.167}$$

The Fourier transformation of a time domain function $f(t) = f_1(t) * f_2(t)$ which is composed by the

convolution of two functions $f_1(t)$ and $f_2(t)$ can be expressed as

$$\tilde{f}(\omega) = \int_{-\infty}^{\infty} [\, f_1\,(t) * f_2\,(t)\,] \cdot e^{-i\omega t}\, dt = \tilde{f}_1(\omega) \cdot \tilde{f}_2(\omega) \tag{II.9.168}$$

i.e. the action of a time-domain convolution of two functions can be calculated in frequency-domain by the multiplication of the individual Fourier transformed functions. This theorem is often used as the modification of the input signal $f_1(t)$ by a serial electronics chain of action $f_2(t)$ (comprises e.g. of low and high pass filters) is calculated by the product of the elements' Fourier transformations; the resulting product function in frequency-domain is then inverse Fourier transformed to yield the final time-domain function $f_1(t) * f_2(t)$. This is widely used for the design of matched filters. Moreover, the theorem enables the choice to perform the filter calculation either in time-domain by convolution or in frequency-domain as there is a one-to-one correspondence between the two methods.

Non-Fourier transformable functions: As the function $f(t)$ must be absolute integrable in terms of an indefinite integral, it must have the property $f(t) \to 0$ for $t \to \infty$ and $t \to -\infty$. Hence, polynomials (like $f(t) = \sum_{k=0}^{n} a_i \cdot t^k$), exponential functions (like $f(t) = e^t$) and periodic functions (like $f(t) = \sin t$) are not Fourier transformable in this mathematical sense. However, the Fourier transformation can artificially be restored if those functions have non-zero values only within a finite interval $[t_{\min}, t_{\max}]$ and are zero outside of this interval; the method is referred to as windowing, see Eq. II.9.169. This is a realistic assumption as a physical quantity is always measured within a limited time duration starting at $t_{\min}$ and ending at $t_{\max}$. In this case, the frequency spectrum is modified, and the width depends on the choice of the duration $t_{\max} - t_{\min}$.

Windowing by integral kernel: The application of Fourier transformation can be extended by the insertion of a kernel or weight function $W(t)$ in the integral transformation as

$$\tilde{f}_W(\omega) \equiv \int_{-\infty}^{\infty} W(t) \cdot f(t) \cdot e^{-i\omega t} dt \tag{II.9.169}$$

which is called windowing. An example is the action of a rectangular window symmetric around $t = 0$ with $W(t) = 1$ for $t \in [-t_0, t_0]$ and $W(t) = 0$ for $t \notin [-t_0, t_0]$ as e.g. the case for a measurement within a limited time duration, see Fig. II.9.166. This procedure yields a convolution function in frequency-domain as $\tilde{W}(\omega) = 2 \cdot \frac{\sin \omega t_0}{\omega} = 2t_0 \cdot \mathrm{sinc}\,(\omega t_0)$, referred to as sinc-function $\mathrm{sinc}\,(x) \equiv \frac{\sin x}{x}$. The central lope of this function has a base width of $2\pi/t_0$. For a Fourier transformable function $f(t)$ the multiplication in time-domain by a transformable weight function $W(t)$ corresponds to a convolution in frequency-domain

$$\tilde{f}_W(\omega) = \tilde{W}(\omega) * \tilde{f}(\omega) \tag{II.9.170}$$

as given by the reversal of Eq. II.9.168.

Application for periodic signals: In the following the frequency spectrum for a train of bunches, e.g. stored in a synchrotron and depicted in Section II.9.5.2 is discussed. The train of bunches is represented by a Fourier transformable time-domain function $f(t)$. This function can be decomposed into two functions: Firstly, the single bunch function $f_{sb}(t)$ defined within one acceleration-period of length t_{acc} i.e.

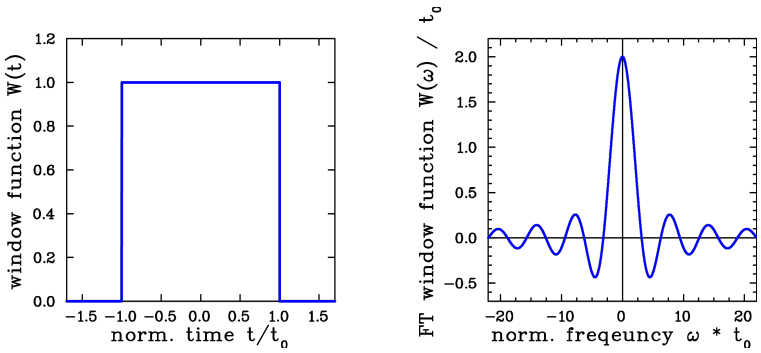

Fig. II.9.166: The window function $W(t)$ (see text) and its Fourier transformation $\tilde{W}(\omega) = 2t_0 \cdot \frac{\sin \omega t_0}{\omega t_0}$.

for $t \in [0, t_{acc}]$ and being identically zero outside of the acceleration-period $f_{sb}(t) = 0$ for $t \notin [0, t_{acc}]$. Secondly, a periodic function $f_\delta(t)$ with the periodicity of the acceleration-period as composed of a train of δ-functions as $f_\delta(t) = \sum_{n=-\infty}^{\infty} \delta(t - n \cdot t_{acc})$. The train of bunches $f(t)$ can be written as a convolution of both functions as

$$f(t) = f_{sb}(t) * f_\delta(t) \equiv \int_{-\infty}^{\infty} f_{sb}(\tau) \cdot f_\delta(t-\tau)\, d\tau = \sum_{n=-\infty}^{\infty} \int_{-\infty}^{\infty} f_{sb}(\tau) \cdot \delta(t-\tau-n \cdot t_{acc})\, d\tau \ . \quad \text{(II.9.171)}$$

The periodic expression $f_\delta(t)$ is called a Dirac Comb and it can be shown that the Fourier transformation is a Dirac Comb in frequency domain, i.e.

$$f_\delta(t) = \sum_{n=-\infty}^{\infty} \delta(t - n \cdot t_{acc}) \implies \tilde{f}_\delta(\omega) = \sum_{n=-\infty}^{\infty} \delta(\omega - n \cdot \omega_{acc}) \ . \quad \text{(II.9.172)}$$

This is true even though periodic functions cannot be Fourier transformed, and the mathematical argumentation uses the concept of Fourier series to approximate periodic functions. Using the law of convolution Eq. II.9.168 the frequency spectrum of the entire train of bunches can be written as

$$\tilde{f}(\omega) = \sum_{n=-\infty}^{\infty} \tilde{f}_{sb}(\omega) \cdot \delta(\omega - n \cdot \omega_{acc}) \ . \quad \text{(II.9.173)}$$

This shows that the spectrum is composed of lines at all harmonics of the acceleration frequency with an envelope related to the Fourier transformation of the single bunch as depicted in Fig. II.9.89 and II.9.90. In the case of a finite observation time, the formulas can be extended by a window function $W(t)$ and $\tilde{W}(\omega)$ according to Eqn. II.9.169 and II.9.170 leading to a finite width of the frequency lines, e.g. depicted in Fig. II.9.109.

II.9.11.2 Theorems for discrete sampling

In many technical applications, a continuous time domain function $f(t)$ defined in a finite time interval is digitized at equidistant time steps Δt. This is an approximation of $f(t)$ by a finite number of $N \in \mathbb{N}$ samples $x(0), x(1)...x(N-1)$. An example is the digitalization of the voltage from a BPM electrode by an **A**nalogue **D**igital **C**onverter **ADC** to enable the subsequent numerical treatment by digital signal

processing.

Discrete sampling and discrete Fourier transformation: Let us assume that a signal sequence of N elements $x(0), x(1)...x(N-1)$ is sampled equidistantly at with a frequency $f_{\text{sample}} = 1/\Delta t$. The **D**iscrete **F**ourier **T**ransformation **DFT** is defined in analogy to Eq. II.9.159 as

$$X(m) \equiv \sum_{n=0}^{N-1} x(n) \cdot e^{-i2\pi m \cdot n/N} \quad . \tag{II.9.174}$$

It is common to express time-domain quantities by lowercase letters (here $x(n)$) and the corresponding frequency-domain quantities by capital letters (here $X(m)$). As all samples have finite values $x(n) < \infty$ and the sampling of the N values is performed during finite duration of $N \cdot \Delta t$, the restriction of absolute integrability by the indefinite integral in the mathematical description above is now obsolete. (As an example, the DTF of a sine-wave recorded during a finite time can now be calculated.) The above mathematical theorems can be applied correspondingly, more details are described in textbooks on signal processing e.g. Ref. [151].

Inverse discrete Fourier transformation: The inverse DFT is called **IDFT** and is defined as

$$x(n) = \frac{1}{N} \sum_{m=0}^{N-1} X(m) \cdot e^{i2\pi m \cdot n/N} \quad . \tag{II.9.175}$$

DFT leakage and Nyquist-Shannon theorem: As there are only a finite number of samples N recorded with the frequency f_{sample}, the DFT is only given with steps of $f_{\text{ana}}(m) = \frac{m}{N} \cdot f_{\text{sample}}$ i.e. N equidistantly spaced frequency samples of $\Delta f_{\text{ana}} = \frac{1}{N} \cdot f_{\text{sample}}$ from zero up to half of the sample frequency $f_{\text{ana}}^{\text{max}} = \frac{f_{\text{sample}}}{2}$. Even in the case of a sine-wave recorded with finite time steps and finite duration the central lope of the frequency spectrum has a finite width, i.e. some of the power from the maximum "leaks" to the sides of the frequency spectrum. The minimum width (defined as the full width half maximum FWHM or technically expressed as 3 dB point) of the lope is given by the distance of two samples $\Delta f_{\text{ana}}^{\text{res}} = \frac{2}{N} f_{\text{sample}}$, i.e. the frequency resolution scales inversely proportional to the amount of non-zero samples; this is a consequence of the Nyquist-Shannon sampling theorem. The related resolution limit was discussed in the frame of tune measurement in Section II.9.5.12.1. The finite frequency resolution can also be understood in terms of a continuous function $f(t)$ and a weight function $W(t)$ as discussed in Eq. II.9.169 and the convolution in frequency domain given by Eq. II.9.170.

DFT windowing: The properties of the spectrum can be influenced by weights $w(n)$ to be inserted in the definition of the DFT in terms of a kernel or window in analogy to Eq. II.9.169 as

$$X_W(m) \equiv \sum_{n=0}^{N-1} w(n) \cdot x(n) \cdot e^{-i2\pi m \cdot n/N} \quad . \tag{II.9.176}$$

Various types of windows are used as optimized to the required spectral information, see e.g. Ref. [151].

DFT and FFT, zero-padding: The DFT can be calculated for any amount of samples N. The abbreviation **F**ast **F**ourier **T**ransformation **FFT** refers to a dedicated type of algorithm for the calculation which requires that the amount of samples is given by $N = 2^k$ with $k \in \mathbb{N}$. In this case, the calculation can

be executed much faster than for the general case, see e.g. Ref. [151]. If a real signal is sampled with $N \neq 2^k$ samples, additional zero-valued data can be appended to the data stream until the condition for the new amount of samples $N' = 2^k > N$ is reached; this is called zero-padding.

II.9.12 Appendix D: Relation between lattice parameters for synchrotrons

For the following description, we recall some basic formulas of accelerator optics in circular machines as given in textbook on accelerator physics. These relations are important for the discussion of tune, chromaticity, and lattice function measurements in Section II.9.5.12 and II.9.5.13. The relations are:

$$\frac{\Delta C}{C_0} = \alpha \frac{\Delta p}{p_0} \quad \text{Definition of momentum compaction factor} \tag{II.9.177}$$

$$\alpha = \frac{1}{\gamma_{tr}^2} \quad \text{Momentum compaction factor and } \gamma\text{-transition} \tag{II.9.178}$$

$$E_{tr} = \gamma_{tr} m_0 c^2 \quad \text{Definition of transition energy} \tag{II.9.179}$$

$$\frac{\Delta f}{f_0} = -\frac{\Delta T}{T_0} = -\eta \frac{\Delta p}{p_0} \quad \text{Definition of frequency dispersion or slip factor} \tag{II.9.180}$$

$$\eta = \frac{1}{\gamma_{tr}^2} - \frac{1}{\gamma_0^2} = \alpha - \frac{1}{\gamma_0^2} \quad \text{Frequency dispersion and } \gamma\text{-transition} \tag{II.9.181}$$

$$\frac{\Delta Q}{Q_0} = \xi \frac{\Delta p}{p_0} \quad \text{Definition of chromaticity} \tag{II.9.182}$$

$$f_s = \sqrt{\frac{1}{2\pi c^2} \cdot \frac{Ze}{Am_0} \cdot \frac{1}{\gamma_0 \beta_0^2} \cdot \frac{f_{rf}}{f_0} \cdot |\eta| \cdot U_{rf} \cdot \cos\varphi_0} \quad \text{Synchrotron frequency} \tag{II.9.183}$$

$$Q_s = \frac{f_s}{f_0} \quad \text{Synchrotron tune.} \tag{II.9.184}$$

with C_0 circumference of the synchrotron and c the velocity of light. The parameter of the reference particle with mass Am_0 and charge Z are: β_0 velocity, p_0 momentum, f_0 revolution frequency, T_0 revolution time, γ_0 relativistic factor and Q_0 the transverse tune. The particles are bunched by the accelerating frequency f_{rf} with amplitude U_{rf} and a phase φ_0 concerning the reference particle relative to the crest of f_{rf}. Δ... describes the width of the distribution for the corresponding parameter. The above parameters are normally used in terms of turn-by-turn quantities or in terms of a many-turn description.

The dispersion $D(s)$ is a lattice function which varies along the synchrotron and describes the transverse offset $x_D(s)$ in dependence on the longitudinal coordinate s as

$$x_D(s) = D(s) \frac{\Delta p}{p_0} \quad \text{Definition of dispersion function} \tag{II.9.185}$$

Dispersion has a local meaning as it is defined along the trajectory s of the reference particle within the accelerator.

References

[1] General readings on Beam Diagnostics

1. H. Schmickler (Ed.), *Beam Instrumentation for Particle Accelerators, Proc. CERN Accelerator School CAS*, **CERN-ACC-2020-0010** (2018).

2. V. Smaluk, *Particle Beam Diagnostics for Accelerators: Instruments and Methods,* VDM Verlag Dr. Müller, Saarbrücken 2009.
3. D. Brandt (Ed.), *Beam Diagnostics for Accelerators, Proc. CERN Accelerator School CAS,* Dourdan, **CERN-2009-005** (2009).
4. P. Strehl, *Beam Instrumentation and Diagnostics*, Springer-Verlag, Berlin 2006.
5. M.G. Minty and F. Zimmermann, *Measurement and Control of Charged Particle Beams,* Springer-Verlag, Berlin 2003.
6. S-I. Kurokawa, S.Y. Lee, E. Perevedentev, S. Turner (Eds.), *Proceeding of the School on Beam Measurement,* Proceeding Montreux, World Scientific Singapore (1999).
7. H. Koziol, *Beam Diagnostic for Acclerators, Proc. CERN Accelerator School CAS,* Uni. Jyväskylä, Finland, p. 565 **CERN 94-01**, http://schools.web.cern.ch/Schools/CAS/CAS_Proceedings.html (1993).
8. J.M. Month, S. Turner (Eds.), *Frontiers in Particle Beams; Observation, Diagnosis and Correction,* Proceeding Anacapri, Lecture Notes in Physics 343, Springer-Verlag, (1988).
9. These JUAS lecture notes are available at the JUAS INDICO web-site and www.gsi.de/work/fairgsi/linac_operations/ beam_instrumentation/ research_and_development_lobird/veroeffentlichungen.htm.

[2] Conferences

1. *Dedicated beam diagnostics conferences:*
   - *International:* International Beam Instrumentation Conference (IBIC)
     Beijing 2024, Saskatoon 2023, Krakow 2022, Pohang 2021 (online event), Santos 2020 (online event), Malmö 2019, Shanghai 2018, Grand Rapid 2017, Barcelona 2016, Melbourne 2015, Monterey 2014, Oxford 2013, Tsukuba 2012.
   - *Europe:* Diagnostics and Instrumentation at Particle Accelerators (DIPAC)
     Hamburg 2011, Basel 2009, Venice 2007, Lyon 2005, Mainz 2003, Genoble 2001, Chester 1999, Franscati 1997, Travemünde 1995, Montreux 1993.
   - *America:* Beam Instrumentation Workshop (BIW)
     Newport News 2012, Santa Fe 2010, Lake Tahoe 2008, Batavia 2006, Knoxville 2004, Brookhaven 2002, Cambridge (MA) 2000, Standford 1998, Argonne 1996, and earlier.

   Proceedings are available for IBIC, DIPAC (since 1999) and BIW (since 2008) on http://www.jacow.org.
2. *General accelerator conferences:*
   - *International:* International Particle Accelerator Conference (IPAC)
     Nashville 2024, Venice 2023, Bangkok 2022, Campinas 2021 (online event), Caen 2020 (shorted online event), Melbourn 2019, Vancouver 2018, Copenhagen 2017, Busan 2016, Richmond 2015, Dresden 2014, Shanghai 2013, New Orleans 2012, San Sebastian 2011, Kyoto 2010.
   - *Europe:* European Particle Accelerator Conference (EPAC)
     Genoa 2008, Edinburgh 2006, Lucerne 2004, Paris 2002, Vienna 2000, Stockholm 1998, Sitges 1996, London 1994, Berlin 1992, Nice 1990, Rome 1988.

– *America:* Particle Accelerator Conference (PAC)
Albuquerque 2022, Lansing 2019, Chicago 2016, Pasadena 2013, New York 2011, Vancouver 2009, Albuquerque 2007, Knoxville 2005, Portland 2003, Chicago 2001, and earlier.

Proceedings are available on http://www.jacow.org.

[3] M. Bai et al., *Nucl. Instrum. Meth.* **A 499**, 372 (2003).

[4] M. Arinaga et al., *Nucl. Instrum. Meth.* **A 499**, 100 (2003).

[5] Company Bergoz, www.bergoz.com

[6] D. Belohrad, *Proc. Diag. Instrum. Part. Acc. Conf. DIPAC 11,* Hamburg, p. 564 (2011).

[7] R.C. Webber, *Proc. Beam Instr. Workshop BIW 94,* Vancouver, p. 3 (1994).

[8] H. Reeg, *Proc. Diag. Instrum. Part. Acc. Conf. DIPAC 01,* Grenoble, p. 120 (2001).

[9] S. Hancock, M. Lindroos, S. Koscielniak, *Phys. Rev. Special Topic Accel. Beams,* **3**, 124202 (2000) and CERN-PS-2000-068-OP (2000) and http://cern.ch/tomography.

[10] S. Hancock, J.L. Sanchez Alvarez,
CERN PS/RF Note 2001-010, http://cern.ch/tomography.

[11] K. Unser, IEEE Trans. Nucl. Sci., NS-28, p. 2344 (1981).

[12] M. Krupa, A. Napieralski, *Int. Journal of Microelectronics and Computer Science (IJMCS)*, Vol. 4, p. 32 (2013).

[13] D. Belohrad et al., *Proc. Int. Beam Instrum. Conf. IBIC 2014*, Monterey, p. 553 (2014).

[14] S. Artinian et al., *Proc. Int. Part. Acc. Conf. IPAC 2013*, Shanghai, p. 476 (2013) and S. Artinian et al., *Proc. Int. Beam Instrum. Conf. IBIC 2012*, Tsukuba, p. 476 (2012).

[15] H. Choi et al., *Proc. Int. Beam Instrum. Conf. IBIC 2014*, Monterey, p. 553 (2014).

[16] W.R. Leo, *Techniques for Nuclear and Particle Physics Experiment,* Springer-Verlag Berlin (1994).

[17] G. F. Knoll, *Radiation Detection and Measurement*, John Wiley, New York (2010).

[18] J.D. Jackson, *Classical Electrodynamics*, John Wiley & Sons (1998).

[19] R.L. Workman et al. (Particle Data Group), Prog. Theor. Exp. Phys. 2022, 083C01 (2022) and 2023 update, Chapter 34, see also pdg.lbl.gov.

[20] F. Ziegler, J.P. Biersack *SRIM*, see *The stopping and Ranges of Ions in Solids*, Pergamon Press (1985) and www.SRIM.org.

[21] O. Tarasov, D. Bazin et al., *LISE++* and subroutine *GOBAL*, lise.nscl.msu.edu/lise.html.

[22] M.J. Berger et al. Code ESTAR, National Institute of Standards and Technology NIST, see http://physics.nist.gov/PhysRefData/Star/Text/ESTAR.html.

[23] E.J. Sternglass, *Phys. Rev.* **108**, 1 (1957).

[24] C. G. Drexler, R.D. DuBois, Phys. Rev **A 53**, 1630 (1996).

[25] R.W. Müller, P. Strehl, *Nucl. Instrum. Meth.* **A 415**, 305 (1998).

[26] A. F. D. Morgan, *Proc. DIPAC 05,* Lyon, p. 51 (2005).

[27] P. Finocchiaro et al., *Proc. Diag. Instrum. Part. Acc. Conf. DIPAC 97,* Frascati, p.53 (1997).

[28] P. Forck et al., *Proc. Diag. Instrum. Part. Acc. Conf. DIPAC 97,* Frascati, p. 165 (1997).

[29] P. Forck et al., *Proc. of Beam Instrum. Workshop BIW 96,* Argonne, p. 422 (1996).

[30] P. Lecoq, A. Getkin, M. Korzhik, *Inorganic Scintillators for Detector Systems,* Springer Verlag (2017).

[31] F. Sauli, *Prinziple of operation of multiwire and drift chambers,* CERN77-09 (1977).

[32] H. Reeg, *Proc. Diag. Instrum. Part. Acc. Conf. DIPAC 99,* Chester, p. 141 (1999).

[33] M. Sapinski, *Proc. of Beam Instrum. Workshop BIW 12,* Newport News, p. 245 (2012), corresponding code available at http://sapinski.web.cern.ch/sapinski/soft/pyTT.

[34] G. Ferioli, R. Jung, *Proc. Diag. Instrum. Part. Acc. Conf. DIPAC 97,* Frascati, p. 168 (1997).

[35] R. Jung, G. Ferioli, S. Hutchins *Proc. Diag. Instrum. Part. Acc. Conf. DIPAC 03,* Mainz, p. 28 (2003) and R. Jung, *Proc. Diag. Instrum. Part. Acc. Conf. DIPAC 93,* Montreux, p. 4 (1993).

[36] B. Walasek-Höhne et al., *Proc. Intern. Beam Instrum. Conf. IBIC 19,* Malmo, p. 242 (2019) and B. Walasek-Höhne et al., *Proc. Diag. Instrum. Part. Acc. Conf. DIPAC 11,* Hamburg, p. 553 (2011).

[37] E. Gütlich et al., *Proc. of Beam Instrum. Workshop BIW 08,* Lake Tahoe (2008) and E. Gütlich et al.,*Proc. Diag. Instrum. Part. Acc. Conf. DIPAC 11,* Hamburg, p. 179 (2011).

[38] A. Lieberwirth et al., *Nucl. Instrum. Meth.* **B 365**, 533 (2015), P. Forck et al., *Proc. Intern. Part. Acc. Conf. IPAC 14,* Dresden, p. 3482 (2014) and P. Forck et al., *Proc. Diag. Instrum. Part. Acc. Conf. DIPAC 11,* Hamburg, p. 170 (2011) and reference their in.

[39] G. Kube et al., *Proc. Part. Acc. Conf. PAC 12,* New Orleans, p. 2119 (2012).

[40] U. Iriso et al., *Diag. Instrum. Part. Acc. Conf. DIPAC 09,* Basel, p. 200 (2009).

[41] R. Ischebeck et al., *Proc. Intern. Beam Instrum. Conf. IBIC 14,* Monterey, p. 259 (2014) and R. Ischebeck et al., *Phys. Rev. Special Topic Accel. Beams* **18**, 082802 (2015).

[42] T.J. Shea et al., *Proc. Part. Acc. Conf. PAC 97,* Vancouver, p. 2215 (1997).

[43] R.Haseitl et al., *Proc. PCs at Part. Acc. Conf. PCaPAC 2008*, Ljubljana, p. 180 (2008).

[44] L. Wartski et al., J. Appl. Phys. **46**, 3644 (1975).

[45] J. Bosser et al., Nucl. Instrum. Meth. **A 238**, 45 (1985).

[46] C. Bovet et al. *Proc. Diag. Instrum. Part. Acc. Conf. DIPAC 99,* Chester, p. 90 (1999) and V.E. Scarpine et al., *Proc. Part. Acc. Conf. PAC 2007, Albuquerque*, p.2639 (2007).

[47] V.E. Scarpine et al., *Proc. Proc. of Beam Instrum. Workshop BIW 08*, Batavia, p.473 (2006).

[48] M.A. Tordeux and J. Papadacci, *Proc. Euro. Part. Acc. Conf. EPAC 00*, Vienna, p. 1818 (2000).

[49] P. Catravas et al., *Proc. Part. Acc. Conf. PAC 99, New York*, p. 2111 (1999).

[50] S. Wesch, B. Schmidt, *Proc. Diag. Instrum. Part. Acc. Conf. DIPAC 11,* Hamburg, p. 539 (2011).

[51] M. Plum, *Beam Instrum. Workshop, Knoxville, AIP Conf. Proc. 732*, p. 23 (2004).

[52] M. Benedikt et al., *Proc. Diag. Instrum. Part. Acc. Conf. DIPAC 01,* Grenoble, p. 189 (2001).

[53] C. Bovet et al., *Proc. Euro. Part. Acc. Conf. EPAC 98,* Stockholm, p. 1488 (1998).

[54] S. Burger et al., *Proc. Diagn. Instrum Part Acc. Conf. DIPAC 03*, Mainz, p. 122 (2003).

[55] J. Emery et al., *Proc. Int. Beam Instrum. Conf. IBIC 19*, Malmo, p. 392 (2019), R. Veness et al., *Proc. Int. Part. Acc. Conf. IPAC 17,* Copenhagen p. 412 (2017) and R. Veness et al. *Proc. Int.*

Beam Instrum. Conf. IBIC 15, Melbourne, p. 392 (2017).

[56] U. Raich, *Proc. Diag. Instrum. Part. Acc. Conf. DIPAC 05,* Lyon, p. 1 (2005).

[57] R.J. Colchester, R. Jung, *Proc. Part. Acc. Conf. PAC 97, Vancouver IEEE Trans. Nucl. Sci.,* Vol NS-32 p. 1917 (1985).

[58] C. Field, *Nucl. Instrum. Meth.,* A360, p. 467 (1995).

[59] G.L. Orlandi et al,. *Phys. Rev. Accel. Beams* **19**, 092802 (2016).

[60] T. Lensch et al., *Proc. Int. Beam Instrum. Conf. IBIC 19*, Malmo, p. 304 (2019).

[61] G.L. Orlandi et al,. *Phys. Rev. Accel. Beams* **23**, 042802 (2020).

[62] P. Forck, *Proc. Int. Part. Acc. Conf. IPAC 10,* Kyoto, p.1261 (2010) and P. Forck et al., *Proc. Diag. Instrum. Part. Acc. Conf. DIPAC 05,* Lyon, p. 221 (2005).

[63] T. Giacomini et al., *Beam Instrum. Workshop, Knoxville, AIP Conf. Proc. 732*, p. 286 (2004) and T. Giacomini et al. *Proc. Diag. Instrum. Part. Acc. Conf. DIPAC 05,* Lyon, p. 150 (2005).

[64] P. Forck, P. Strehl, *Proc. Diag. Instrum. Part. Acc. Conf. DIPAC 99,* Chester, p. 42 (1999) and P. Forck, A. Peters, P. Strehl, *Proc. Beam Instr. Workshop BIW 00,* Cambridge AIP 546, p. 606 (2000).

[65] R. Connolly et al., *Proc. Beam Instr. Workshop BIW 00,* Cambridge AIP 546, p. 330 (2000).

[66] K. Smith, Position-sensitive particle detection with microchannel-plate electron multiplier, *Experimental Methods in phys. science, Academic Press* Vol. 29A, p. 253 (1995).

[67] G. Ferioli et al., *Proc. Diag. Instrum. Part. Acc. Conf. DIPAC 01,* Grenoble, p. 201 (2001).

[68] D. Möhl, Stochastic cooling, in *CERN Acc. School,* CERN 95-06, p. 587 (1995) http://cas.web.cern.ch/cas/CAS_Proceedings.html.

[69] J. Bosser, Electron cooling, in *CERN Acc. School,* CERN 95-06, p. 673 (1995).

[70] V. Shiltsev, *Nucl. Instrum. Meth.* **A 986**, 164744 (2021) and V. Shiltsev, arXiv:2003.0972v3 (2020).

[71] M. Sapinski et al., *Proc. Int. Beam Instrum. Conf. IBIC 16*, Barcelona, p. 520 (2016).

[72] D. Vilsmeier, P. Forck, M. Sapinski, *Proc. Int. Beam Instrum. Conf. IBIC 17*, Grand Rapids, p. 355 (2017) and D. Vilsmeier, M. Sapinski, Code **Virtual-IPM** available at https:gitlab.com/IPMsim/Virtual-IPM.

[73] A. Allisy (Ed.), *Secondary Electron Spectra from charged Particle Interaction*, International Commission on Radiation Units and Measurement Report No. 55 (1996).

[74] K. Satou, H. Kuboki, T. Toyama, *Proc. Int. Beam Instrum. Conf. IBIC 16*, Barcelona, p. 811 (2016).

[75] J. Zagel et al., *Proc. Int. Beam Instrum. Conf. IBIC 14*, Monteray, p. 408 (2014) and V. Kashikhin et al., *IEEE Trans. Appl. Supercnductivity* 24, p. 0501004 (2014).

[76] D. Vilsmeier, M. Sapinski, R. Singh, *Phys. Rev. Accel. Beams* **22**, 052801 (2019).

[77] D. P. Sandoval et al., *Proc. Beam Instr. Workshop BIW 93,* Santa Fe, p. 273 (1993) and references their in.

[78] M.A. Plum et al., *Nucl. Instrum. Meth.* **A 492,** 74 (2002).

[79] P. Forck, A. Bank, *Proc. Euro. Part. Acc. Conf. EPAC 2002, Paris*, p. 1885 (2002) and A. Bank, P. Forck, *Proc. Diagn. Instrum Part Acc. Conf. DIPAC 03*, Mainz, p. 137 (2003).

[80] A. Variola, R. Jung, G. Ferioli, *Phys. Rev. Special Topic Accel. Beams* **10**, 122801 (2007), G. Burtin et al., *Proc. Euro. Part. Acc. Conf. EPAC 00, Vienna*, p. 256 (2000).

[81] G. Kube, *Proc. Diagn. Instrum Part Acc. Conf. DIPAC 07*, Venice, p. 6 (2007).

[82] M. Wilke, *Proc. Beam Instr. Workshop BIW 94,* Vancouver, p. 128 (1994).

[83] A. Hoffmann, F. Meot, *Nuncl. Instrum. Meth.* **203**. p. 483 (1982).

[84] G. Kube et al., *Proc. Diagn. Instrum Part Acc. Conf. DIPAC 05*, Lyon, p. 202 (2005).

[85] C. Bovet et al., *Proc. Part. Acc. Conf. PAC 91,* San Francisco, p. 1160 (1991).

[86] B.X. Yang et al., *Proc. Part. Acc. Conf. PAC 97,* Vancouver, p. 2215 (1997).

[87] M. Pont et al., *Proc. IPAC 11,* San Sebastian, p. 3023 (2011) and G. Benedetti et al., *Proc. IPAC 11,* San Sebastian, p. 2059 (2011).

[88] B.K. Scheidt, *Proc. DIPAC 05,* Lyon, p. 24 (2005).

[89] M.A. Tordeux et al., *Proc. DIPAC 07,* Venice, p. 180 (2007).

[90] G. Kube et al., *Proc. Diagn. Instrum Part Acc. Conf. DIPAC 07*, Venice, p. 6 (2007).

[91] C. Thomas et al., *Phys. Rev. Accel. Beams* **13**, 022805 (2010).

[92] M. Samadi et al., *Phys. Rev. Accel. Beams* **23**, 024801 (2020).

[93] T. Mitsuhashi, Beam size measurement by use of SR interferometers, in *Proceeding of the School on Beam measurement,* Montreux, p. 399 World Scientific Singapore (1999) and T. Mitsuhashi, *Proc. Beam Instr. Workshop BIW 2004,* Knoxville, AIP Conf. Proc. 732, p. 3 (2004).

[94] T. Naito, T. Misuhashi, *Phys. Rev. Accel. Beams* **9**, 122802 (2006).

[95] A.I. Novokshonov et al., *Proc. Int. Beam Instrum. Conf. IBIC 16*, Barcelona, p. 829 (2016) and A.I. Novokshonov et al., *Proc. Int. Part. Acc. Conf. IPAC 17*, Copenhagen, p. 117 (2017).

[96] L.Torino, U. Iriso, *Proc. Int. Beam Instrum. Conf. IBIC 16*, Barcelona, p. 589 (2016) and L.Torino, U. Iriso, *Proc. Int. Beam Instrum. Conf. IBIC 15*, Melbourne, p. 428 (2015).

[97] J.M. Stockli, *Proc. Beam Instr. Workshop BIW 06,* Batavia, AIP Conf. Proc. 868, p. 25 (2006).

[98] W. Hillert, *Transverse linear Beam Dynamics*, in H. Schmickler (Ed.), *Introduction to Particle Accelerators, Proc. CERN Accelerator School*, Chavannes de Bogis, p. 230 (2021) & references therein.

[99] H. Wiedemann, *Particle Accelerator Physics* Springer Verlag (2015)

[100] S.Y. Lee, *Accelerator Physics* World Scientistic (2007)

[101] M. Reiser, *Theory and Design of charged Particle Beams*, J. Wiley Publishing New York (1994).

[102] K.T. McDonald , D.P. Russell, *Methods of Emittance Measurement,* Proc. Anacapri, Lecture Notes in Physics 343, Springer-Verlag, p. 122 (1988).

[103] B. Cheymol et al., *Proc. Diag. Instrum. Part. Acc. Conf. DIPAC 09,* Basel, p. 316 (2009).

[104] M.W. Wang et al., *Proc. Int. Beam Instrum. Conf. IBIC 18,* Shanghai, p. 509 (2018).

[105] P. Ausset et al., *Proc. Diag. Instrum. Part. Acc. Conf. DIPAC 09,* Basel, p. 110 (2009).

[106] T. Ludwig et al., *Rev. Sci. Instrum.* **65**, 1462 (1994).

[107] B. Cheymol and A. Ponton, *Proc. High Brightness Hadron beam Conf. HB 16,* Malmo, p. 226 (2016).

[108] M. Dolinska et al., *Proc. Diag. Instrum. Part. Acc. Conf. DIPAC 99,* Chester, p. 161 (1999) and T. Hoffmann et al., *Proc. Beam Instr. Workshop BIW 00,* Cambridge AIP 546, p. 432 (2000).

[109] M. Crecenti, U. Raich, *Proc. Diag. Instrum. Part. Acc. Conf. DIPAC 95,* Travemünde, DESY M9507, p. 66 (1995).

[110] P. Forck et al., *Proc. Linear Accel. Conf. LINAC 00,* Monterey, p. 166 (2000).

[111] G. Penco et al., *Proc. Euro. Part. Acc. Conf. EPAC 08,* Genoa, p. 1236 (2008).

[112] M.E. Schulze et al., *Proc. Linear Accel. Conf. LINAC 00,* Monterey, p. 575 (2000).

[113] V.A. Dimov et al., *Proc. High Brightness Hadron Beam Conf. HB 16,* Malmö, p. 433 (2016) and references therein.

[114] C.B. McKee et al., *Nucl. Instrum. Meth.* **A 458,** 264 (1995).

[115] D. Stratakis et al., *Phys. Rev. Accel. Beams,* **9**, 112801 (2006).

[116] Q. Z. Xing et al., *Phys. Rev. Accel. Beams,* **21**, 072801 (2018).

[117] A. Wolski et al., *Phys. Rev. Accel. Beams,* **25**, 122803 (2022).

[118] R.E. Shafer, *Proc. Beam Instr. Workshop BIW 89,* Upton, p. 26 (1989)
available e.g. at www.bergoz.com/en/mx-bpmf (1989).

[119] S.R. Smith, *Proc. Beam Instr. Workshop BIW 96,* Argonne AIP 390, p. 50 (1996).

[120] P. Forck, P. Kowina, and D. Liakin, *Beam Position Monitors*, in D. Brandt (Ed.), *Beam Diagnostics for Accelerators, Proc. CERN Accelerator School CAS,* Dourdan, **CERN-2009-005**, p. 187 (2009).

[121] M. Wendt, *Proc. Diag. Instrum. Part. Acc. Conf. DIPAC 11,* Hamburg, p. 18 (2011).

[122] M. Wendth in H. Schmickler (Ed.), *Beam Instrumentation for Particle Accelerators, Proc. CERN Accelerator School CAS*, Tuusula, **CERN-ACC-2020-0010**, p. 355 (2018).

[123] G. Kube, M. Werner, *Proc. Diag. Instrum. Part. Acc. Conf. DIPAC 07,* Venice, p. 105 (2007).

[124] F. Stulle (Company Bergoz), private communication.

[125] J.M. Byrd, Bunched Beam Signals in the time and frequency domain, in *Proceeding of the School on Beam Measurement,* Montreux, p. 233 World Scientific Singapore (1999).

[126] J.F. Power et al., *Proc. Beam Instr. Workshop BIW 00,* Cambridge AIP 546, p. 535 (2000).

[127] B.G. Pine, *CARE-ABI Workshop Lüneburg 2006,* p. 28, see
https://mdi.desy.de/sites2009/site_mdi/content/e37820/e37935/e38711/e38712/
infoboxContent38753/LueneburgCARE-proc.pdf.

[128] R.E. Shafer, *Proc. Beam Instr. Workshop BIW 93,* Santa Fe, p. 303 (1993).

[129] C. Simon et al., *Proc. Int. Beam Instrum. Conf. IBIC 14,* Monterey, p. 303 (2014) and M. Almaki etal., *Proc. Int. Beam Instrum. Conf. IBIC 14,* Barcelona, p. 319 (2016).

[130] C. Boccard, *CARE-ABI Workshop Lüneburg 2006,* see
adweb.desy.de/mdi/CARE/Lueneburg/ABI-Lueneburg.htm (2006) and E. Calvo-Giraldo et al., *Proc. Diag. Instrum. Part. Acc. Conf. DIPAC 03*, Mainz, p. 187 (2003).

[131] N. Kurita et al., *Proc. Part. Acc. Conf. PAC 95,* Dallas, p. 2512 (1995).

[132] C.K. Ng et al, *Proc. Part. Acc. Conf. PAC 95,* Dallas, p. 2485 (1995).

[133] S. Varnasseri et al., *Proc. Diag. Instrum. Part. Acc. Conf. DIPAC 05,* Lyon, p. 90 (2005).

[134] A. A. Nosych et al., *Proc. Int. Beam Instr. Conf. IBIC 14,* Monterey, p. 298 (2014).

[135] P. Kowina et al., *Proc. Diag. Instrum. Part. Acc. Conf. DIPAC 05,*, Lyon, p. 114 (2005).

[136] Textbooks on micro-wave engineering, e.g., D.M. Pozar, *Microwave Engineering*, J. Wiley, New York (1998).

[137] D. Nölle, M. Wendt, *Proc. LINAC 04,* Lübeck, p. 435 (2004).

[138] D. Nölle et al., *Proc. LINAC 04,* Lübeck, p. 426 (2004).

[139] R. Lorenz, *Proc. Beam Instr. Workshop BIW 98,* Stanford AIP 451, p. 53 (1998).

[140] G. Vismara, *Proc. Beam Instr. Workshop BIW 00,* Cambridge AIP 546, p. 36 (2000) and G. Vismara, *Proc. Diag. Instrum. Part. Acc. Conf. DIPAC 99,* Chester, p. 11 (1999).

[141] M. Wendt, *Proc. Intern. Beam Instrum. Conf. IBIC 14,* Monterey, p. 468 (2014).

[142] R. Garoby, *Low Level R.F. Building Blocks*, in *CERN Acc. School,* CERN 93-03, p. 428 (1992).

[143] Company I-Tech, www.i-tech.si.

[144] J.M. Belleman, *Proc. Diag. Instrum. Part. Acc. Conf. DIPAC 05,* Lyon, p. 137 (2005).

[145] K. Unser, *Proc. Beam Instr. Workshop BIW 96,* Argonne AIP 390, p. 527 (1996) & www.bergoz.com.

[146] J. Belleman, *From Analog to Digital*, in D. Brandt (Ed.), *Beam Diagnostics for Accelerators, Proc. CERN Accelerator School CAS,* Dourdan, **CERN-2009-005**, p. 281 (2009).

[147] M. Gasior, *Analog to Digital Conversion in Beam Instrumentation Systems*, in H. Schmickler (Ed.), *Beam Instrumentation for Particle Accelerators, Proc. CERN Accelerator School CAS*, Tusula, **CERN-ACC-2020-0010**, p. 406 (2018).

[148] e.g. J. Serano, *Introduction to FPGA Design*, in D. Brandt (Ed.), *Proc. CAS on Digital Signal Processing*, Sigtuna, CERN 2008-003, p. 231 (2008).

[149] V. Schlott et al., *Proc. Euro. Part. Acc. Conf. EPAC 00,* Vienna p. 1809 (2000) and www.i-tech.si.

[150] e.g. T. Schilcher, *RF Applications in digital Signal Processing*, D. Brandt (Ed.), *Proc. CAS on Digital Signal Processing*, Sigtuna, CERN 2008-003, p. 249 (2008).

[151] See textbooks on Digital Signal Processing, e.g. R.G. Lyons, *Understanding Digital Signal Processing*, Prentice Hall Pearson Education, Boston (2011).

[152] R. Jones, *Proc. Beam Instr. Workshop BIW 10,* Santa Fe, p. 22 (2010), image: private communication.

[153] see e.g. J.D. Fox, E. Kikuzani, *Bunch Feedback System and Signal Processing*, in *Proceeding of the School on Beam Measurement,* Montreux, p. 579 World Scientific Singapore (1999).

[154] J. Wenninger , *Lattice Measurements*, in D. Brandt (Ed.), *Beam Diagnostics for Accelerators, Proc. CERN Accelerator School CAS,* Dourdan, **CERN-2009-005**, p. 361 (2009).

[155] J. Wenninger, *Linear Imperfections*, in H. Schmickler (Ed.) *Beam Instrumentation for Particle Accelerators, Proc. CERN Accelerator School CAS*, Tuusula, **CERN-ACC-2020-0010**, p. 241

(2018).

[156] R. Steinhagen, *Tune and Chromaticity Diagnsotics*, in D. Brandt (Ed.), *Beam Diagnostics for Accelerators, Proc. CERN Accelerator School CAS,* Dourdan, **CERN-2009-005**, p. 317 (2009).

[157] R. Jones, *Measuring Tune, Chromaticity and Coupling*, in H. Schmickler (Ed.), *Beam Instrumentation for Particle Accelerators, Proc. CERN Accelerator School CAS*, Tuusula, **CERN-ACC-2020-0010**, p. 222 (2018).

[158] R. Bartolini et al., *Proc. Euro. Part. Acc. Conf. EPAC 96,* Sitges, p. 1329 (1996) and R. Bartolini et al., CERN Sl/95-84 (1995).

[159] M. Wendt, *RF Measurement Techniques*, in H. Schmickler (Ed.), *Beam Instrumentation for Particle Accelerators, Proc. CERN Accelerator School CAS*, Tuusula, **CERN-ACC-2020-0010**, p. 147 (2018).

[160] D. Boussard, *Schottky noise and Beam Transfer Function Diagnostics*, in *CERN Acc. School,* CERN 95-06, p. 749 (1995).

[161] U. Rauch et al., *Proc. Diag. Instrum. Part. Acc. Conf. DIPAC 09,* Basel p. 324 (2009) and R. Singh et al., *Proc. High Brightness Hadron Beam Conf. HB 10*, Morschach, p. 226 (2010).

[162] J. Borer et al., *Proc. Euro. Part. Acc. Conf. EPAC 92,* Berlin, p. 1082 (1992) and P. Castro et al., *Proc. Part. Acc. Conf. PAC 93,* Washington, p. 2103 (1993).

[163] R. Tomas et al., *Phys. Rev. Accel. Beams,* **20**, 054801 (2017) and reference therein.

[164] H. Burkhardt (CERN), private communication.

[165] J.C. Dooling et al., *Proc. Linear Accel. Conf. LINAC 00,* Monterey, p. 193 (2000).

[166] F. Tecker, *Longitudinal Beam Dynamics in circular Accelerator*, in H. Schmickler (Ed.), *Introduction to Particle Accelerators, Proc. CERN Accelerator School*, Chavannes de Bogis, p. 748 (2021).

[167] H. Wollnik, *Optics of charged particles,* Academic Press (1987).

[168] P. Forck et al., *Proc. Diag. Instrum. Part. Acc. Conf. DIPAC 05,* Lyon, p. 48 (2005).

[169] B. Fellenz, J. Crisp, *Proc. of Beam Instrum. Workshop BIW 98,* Stanford, p. 446 (1998).

[170] W.R. Rawnsley et al., *Proc. Beam Instr. Workshop BIW 00,* Cambridge AIP 546, p. 547 (2000).

[171] M. Ferianis et al., *Proc. Diag. Instrum. Part. Acc. Conf. DIPAC 03,* Mainz,p.113 (2003).

[172] J.-P. Carniero et al., Int. J. Mod. Phys. A, vol. 34, no. 36, (2019).

[173] R. Singh, *Proc. Heavy Ion Accelerator Technology. HIAT 2022*, Darmstadt, p. 144 (2022), and R.Singh et al. *Proc. Int. Beam Instrum. Conf. IBIC 2022*, Krakow, p. 268 (2022).

[174] G. Rodrigues et al. *Proc. Int. Beam Instrum. Conf. IBIC 2022*, Krakow, p. 460 (2022).

[175] A.Feschenko, *Proc. Part. Acc. Conf. PAC 01,* Chicago, p. 517 (2001) and A. Feschenko, *Proc. Russian Part. Acc. Conf. RuPAC 12,* Saint Petersburg, p. 181 (2012).

[176] N. E. Vinogradov et al., *Nucl. Instrum. Meth.* **A 526**, p. 206 (2004).

[177] K. Scheidt, *Proc. Euro. Part. Acc. Conf. EPAC 00,* Vienna, p. 182 (2000).

[178] K. Scheidt, *Proc. Euro. Part. Acc. Conf. EPAC 96,* Sitges, p. 1624 (1996).

[179] e.g. Campany Hamamatsu, www.hamamatsu.com

[180] M. Labat et al., *Proc. Diagn. Instrum Part Acc. Conf. DIPAC 07*, Venice, p. 241 (2007).

[181] See textbooks on optics, e.g. E. Hecht, *Optics*, Pearson Addison-Wesley (2016).

[182] B. Steffen et al., *Proc. Diag. Instrum. Part. Acc. Conf. DIPAC 09*, Basel, p. 263 (2009).

[183] B. Steffen et al., *Phys. Rev. Accel. Beams* **12**, 032802 (2009).

[184] K. Wittenburg, *Proc. Euro. Part. Acc. Conf. EPAC 02,* Paris, p. 109 (2002).

[185] K. Wittenburg, *Beam Loss Monitors*, in H. Schmickler (Ed.), *Beam Instrumentation for Particle Accelerators, Proc. CERN Accelerator School*, Tuusula, **CERN-ACC-2020-0010**, p. 456 (2018).

[186] A. Zhukov, *Proc. Beam Instrumtation Workhsop BIW 10,* Santa Fe, p. 553 (2010).

[187] R.E. Shafer, *Proc. Beam Instr. Workshop BIW 02,* Brookhaven AIP 648, p. 44 (2002).

[188] A.H. Sullivan, *A Guide to Radiation and Radioactivity Level near high Energy Particle Accelerators*, Nuclear Technology Publishing, Ashford (1992).

[189] S. Roesler, M. Silari, R.H. Thomas, *Radiation effects and protection,* in *A.W. Chao, K.H. Mess, M. Tigner F. Zimmermann (Eds.), Handbook of Acceleration Physics and Engeneering, 1^{st} and 2^{nd} edition* World Scientific p. 767 (2013).

[190] P. Forck, *Machine and People Protection*, in H. Schmickler (Ed.), *Introduction to Particle Accelerators, Proc. CERN Accelerator School*, Chavannes de Bogis, p. 748 (2021) and references therein.

[191] P. Forck and T. Hoffmann, *Proc. Diag. Instrum. Part. Acc. Conf. DIPAC 01,* Grenoble, p. 129 (2001).

[192] R.E. Shafer et al., *Proc. intern. Conf. High Energy Acc.*, Batavia, p. 609 (1983) and D. Gassner et al., *Beam Instrum. Workshop BIW 00*, Cambridge, p. 392 (2000).

[193] B. Dehning, *Proc. Diag. Instrum. Part. Acc. Conf. DIPAC 05,*, Lyon, p. 117 (2005).

[194] E.B. Holzer et al., *Proc. Euro. Part. Acc. Conf. EPAC 08,* Genoa, p. 1134 (2008) and M. Stockner et al., *Proc. Diag. Instrum. Part. Acc. Conf. DIPAC 07,* Venice, p. 328 (2007).

[195] D. Kramer et al., *Proc. Diag. Instrum. Part. Acc. Conf. DIPAC 07,* Venice, p. 313 (2007) and D. Kramer *Design and Implementation of a Detector for High Flux mixed Radiation Fiels,* PhD Thesis Technical University of Liberec (2008).

[196] H. Yang and D.C. Shin, *Proc. Free Electron Laser Conf. FEL 17,* Santa Fe, p. 503 (2017).

[197] Y.I. Maltseva, et al., *Proc. Int. Beam Instrum. Conf. IBIC 19*, Malmo, p. 233 (2019).

[198] S. Benitez et al., *Proc. Int. Part. Acc. Conf. IPAC 21*, Campinas, p. 2640 (2021).

[199] A.S. Fisher et al., *IBIC 2022*, Krakow, p. 229 (2022) and A.S. Fisher et al., *Phys. Rev. Accel. Beams*, **23**, 082802 (2020).

[200] F. Wulf, M. Körfer, *Proc. Diag. Instrum. Part. Acc. Conf. DIPAC 09,* Basel, p.411 (2009).

[201] H. Henschel et al., *Proc. Diag. Instrum. Part. Acc. Conf. DIPAC 01,* Grenoble, p. 73 (2001), H. Henschel et al., *Proc. Beam Instr. Workshop BIW 00,* Cambridge (MA), p. 647 (2000).

[202] E. Gschwendtner et al., *Proc. Euro. Part. Acc. Conf. EPAC 02,* Paris, p. 1894 (2002).

[203] GEometry ANd Tracking simulation code GEANT4, see www.geant4.org

[204] FLUktuierende KAskaden simulation code FLUKA, see www.fluka.org

[205] D. Robin et al., *Proc. Euro. Part. Acc. Conf. EPAC 00,* Vienna, p. 136 (2000).

[206] P. Kuske, *Proc. Diag. Instrum. Part. Acc. Conf. DIPAC 01,* Grenoble, p. 31 (2001) and P. Kuske et al., *Proc. Part. Acc. Conf. PAC 01,* Chicago, p. 1656 (2001).

II.9.13 Exercises for Beam Instrumentation and Diagnostics

1 Calculation of beam currents and further properties

A facility is built of a LINAC and a synchrotron for protons or heavy ions.

1.1 LINAC

The average current is 0.1 mA of protons. The pulsed LINAC has a macro-pulse length of 1 ms and a macro-pulse period of 20 ms. The acceleration is done with a rf-frequency of 100 MHz. The particles are distributed 10 % in rf phase around the reference particle in longitudinal direction. The transverse beam size is $2x = 1$ cm assuming a rectangular shape .

Assumption for all parts of this exercise to simplify the calculations: Assume a homogeneous charge distribution with hard edges i.e. a rectangular shape. The beta-function β is constant everywhere and, hence, the transverse beam size $x = \sqrt{\beta \cdot \epsilon}$ changes only due to the variation of the emittance ϵ.

Calculate the pulse current, the number of particles within one macro-pulse and within one bunch. What is the particle density at $E_{\mathrm{kin}} = 10$ MeV kinetic energy? Compare this density to that of the residual gas assuming a pressure of $p = 10^{-7}$ mbar $= 10^{-5}$ Pa ($\simeq 10^{-7}$ torr). Calculate the average distances between the protons.

Hint: Use the ideal gas theorem $p = nk_{\mathrm{B}}T$, with n particle density, $T = 300$ K temperature and $k_{\mathrm{B}} = 1.4 \cdot 10^{-23}$ J/K the Boltzmann-constant.

Calculate the pulse current, the number of particles within one macro-pulse and within one bunch. What is the particle density at $E_{\mathrm{kin}} = 10$ MeV kinetic energy? Compare this density to that of the residual gas assuming a pressure of $p = 10^{-7}$ mbar $= 10^{-5}$ Pa ($\simeq 10^{-7}$ torr). Calculate the average distances between the protons.

Hint: Use the ideal gas theorem $p = nk_{\mathrm{B}}T$, with n particle density, $T = 300$ K temperature and $k_{\mathrm{B}} = 1.4 \cdot 10^{-23}$ J/K the Boltzmann-constant.

1.2 Synchrotron

With a kinetic energy of 10 MeV the particles are injected into a synchrotron with $L_{\mathrm{syn}} = 220$ m circumference using multi-turn injection of $t_{\mathrm{inj}} = 100$ μs length and 100 % efficiency. The final kinetic energy after acceleration is $E_{\mathrm{kin}} = 1$ GeV. How many particles are injected, what is the electrical current at injection and extraction? Give also the revolution frequency.

Due to the multi-turn injection, the horizontal emittance ϵ is enlarged by a factor of 25. Calculate the density at injection and extraction for a de-bunched beam, assuming the conservation of the normalized emittance $\epsilon_{\mathrm{norm}} = \frac{v_s}{c}\gamma\epsilon$ with v_s is the longitudinal velocity and γ the Lorentz factor. Compare the particle density to the residual gas density for a pressure of $p = 10^{-10}$ mbar. What are the average distances between the protons?

1.3 Extraction

a) Slow extraction: The stored particles are extracted within 10 s. Calculate the current and the mean distance between the particles in the transfer line. What is their density? Compare its density to the

residual gas density for a pressure of $p = 10^{-9}$ mbar.

b) Fast extraction: For a transfer to an other synchrotron, all particles are collected within one bunch of $t_{\mathrm{bunch}} = 100$ ns length. Give the current of this bunch within a transfer line; assume a rectangular bunch distribution for simplicity.

1.4 Changes for an ion accelerator

Assuming the same accelerator facility as above but for an Uranium beam. The kinetic energies are adopted by changing the unit from MeV to MeV/u (mass unit u= 938 MeV).

At the ion source U^{4+} is generated; at $E_{\mathrm{kin}} = 1$ MeV/u the ions are stripped to U^{28+}; additionally, at $E_{\mathrm{kin}} = 10$ MeV/u the ions are stripped to U^{70+} and after extraction at $E_{\mathrm{kin}} = 1$ GeV/u to the bare nuclei U^{92+}. For the LINAC the electrical current (in units of Ampere) stay the same as for protons.

What are the differences?

2 Methods of current measurements at proton accelerators

(from previous examination)

For the below-mentioned proton accelerators and beam parameters, an appropriate method for current measurement should be chosen; give the main argument for your choice:

a) Behind the ion source with an energy of 100 keV, a beam current of 100 mA and a pulse duration of 1 ms.

b) Behind the ion source with the same parameter as under **a)** but a current of 10 nA.

c) Behind a proton LINAC with an energy of 100 MeV, a beam current of 100 mA and a pulse duration of 1 ms.

d) The permanent monitoring during the 1 s long acceleration within a synchrotron from an energy of 100 MeV to 1 GeV and a current of the circulating beam of about 100 mA.

e) The circulating current within a synchrotron after acceleration and de-bunching (i.e. a continues current)

f) In a transport line behind a synchrotron where 10^{12} protons are extracted within 1 μs.

g) The same parameters as under **f)** but with a duration of 10 s using "slow extraction" mode.

3 Transformer for a pulsed LINAC

A macro-pulse of 1 ms length has to be measured by a current transformer with an allowed droop of 3 % and a upper cut-off frequency of $f_{\mathrm{high}} = 100$ kHz. (Why is this bandwidth needed?) The core has the size: inner radius $r_{\mathrm{i}} = 30$ mm and outer radius $r_{\mathrm{o}} = 60$ mm and length in beam direction of 4 cm. The permeability of the torus is $\mu_{\mathrm{r}} = 10^5$ and $\mu_0 = 4\pi \cdot 10^{-7}$ Vs/Am. Calculate the droop time τ_{droop} and the corresponding lower cut-off frequency f_{low}.

Passive transformer: The load resistor of a passive transformer is $R = 1$ kΩ, having a temperature of 300 K. The loss resistivity is $R_{\mathrm{L}} = 10\ \Omega$.

Calculate the required number of windings for the given droop, the sensitivity (meaning the current-to-voltage conversion [V/A], also called trans-impedance) and the detection threshold for a signal-to-noise of $S/N = 1$ for pure thermal contributions. Use the thermal noise voltage $U_{\mathrm{eff}} = \sqrt{4k_{\mathrm{B}}TR\Delta f}$ with Boltzmann-constant $k_{\mathrm{B}} = 1.4 \cdot 10^{-23}$ J/K, temperature $T = 300$ K and bandwidth $\Delta f = f_{\mathrm{high}} - f_{\mathrm{low}}$.

What is the corresponding minimal detectable beam current?

Active transformer: Calculate for the same properties of an active transformer of the same size with an open-loop gain of $A = 10^6$, a feedback resistor $R_\mathrm{f} = 1$ MΩ and the same loss resistivity $R_\mathrm{L} = 10\ \Omega$.

Fast passive transformer: Passive transformers are normally used for short bunch measurements as transferred between synchrotrons. They have a load resistor of $R = 50\ \Omega$ for smooth signal transmission. For an allowed droop of 3 % per μs and a bandwidth of 100 MHz calculate the same properties as above. Because the permeability is frequency dependent $\mu_\mathrm{r} \propto 1/f$ for $f > 100$ kHz, take an average value of $\mu_\mathrm{r} \simeq 10^3$.

4 Slow extraction current measurement

Assuming the stored number of particles from exercise 1 at a kinetic energy of 1 GeV/u and 1 s extraction time for proton ($1.25 \cdot 10^{12}$ stored) and Uranium ($1.8 \cdot 10^{10}$ stored) case. A current measurement is done with a 0.5 cm long ionization chamber, filled with Argon at atmospheric pressure. The energy loss of protons is

$$\frac{dE_\mathrm{p}}{\rho dx} = 0.00144 \frac{\mathrm{MeV}}{\mathrm{mg/cm^2}}.$$

The scaling for heavy ions in this energy range is $dE/dx \propto Z^2$. For Argon, the W-value is 26.3 eV, and the mass is 40 amu. (Avogadro-number $N_\mathrm{A} = 6.0 \cdot 10^{23}$ mol^{-1} and volume of 1 mol gas is $V_\mathrm{mol} = 22.4$ l.)

Calculate the secondary currents for both ions. (The nuclear charge of Uranium is $Z = 92$ and mass $A = 238$.)

Calculate the secondary current using a secondary electron monitor (SEM) with the energy loss in aluminium for protons of

$$\frac{dE_\mathrm{p}}{\rho dx} = 0.00177 \frac{\mathrm{MeV}}{\mathrm{mg/cm^2}}$$

and the secondary electron yield $Y = 27.4\ e^-$/(MeV/mg/cm^2). What is the secondary current for the proton beam? What is the secondary current for the Uranium beam using the scaling $dE/dx \propto Z^2$?

5 Beam power at a LINAC

Calculate the absorbed power for a beam delivered by a LINAC with proton or Uranium $^{238}\mathrm{U}^{28+}$ at $E_\mathrm{kin} = 10$ MeV/u stopped in a water cooled Faraday cup. The electrical macro-pulse current for both ions is $I_\mathrm{macro} = 2$ mA, and the pulse duration is $t_\mathrm{macro} = 1$ ms with a repetition rate of 50 Hz. What is the average power? What is the required flow of cooling water for a maximal increase of the water temperature of 60 ^{o}C. The specific heat of water is $c = 1$ cal/gK $= 4.2$ J/gK.

What is the peak power?

6 Material destruction for intense beams

A beam of 1 MeV/u Uranium $^{238}\mathrm{U}^{4+}$ with a macro-pulse current of $I_\mathrm{macro} = 10$ mA and duration of $t_\mathrm{macro} = 200\ \mu$s is stopped on a copper plate e.g., inside a Faraday Cup. The penetration depth is $R_\mathrm{Cu} = 9.5\ \mu$m. Assume a round beam of radius r with a constant beam density. Estimate the minimal possible beam spot to avoid melting of the stopper material. The required constants for copper are given

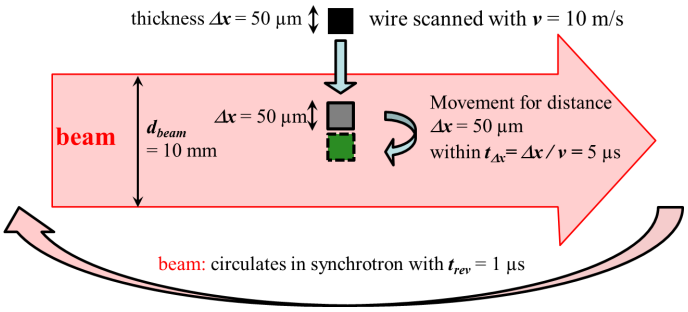

Fig. II.9.167: Simplified scheme of a flying wire measurement in a synchrotron.

in Table II.9.17.

What does change if such a beam hits a tungsten surface of a high-power Faraday cup? The range in tungsten is $R_{\mathrm{W}} = 7.4\ \mu$m; for further material constants see Table II.9.17.

What does change if the beam hit the vacuum pipe made of iron? The range in iron is $R_{\mathrm{Fe}} = 9.7\ \mu$m; other material constants are given in Table II.9.17.

Having a beam of radius $r_{\mathrm{beam}} = 5$ mm. What is the maximum allowed pulse length to avoid melting?

What is a rough scaling for the minimal radius as a function of beam energy?

Calculate the same properties for a 1 MeV proton beam. The ranges are $R_{\mathrm{Cu}} = 6.7\ \mu$m in copper, $R_{\mathrm{W}} = 5.38\ \mu$m in tungsten, and $R_{\mathrm{Fe}} = 6.4\ \mu$m i iron.

	Range R_{mat}	density ρ	melting T_{melt}	sp. heat c	melt. heat a_{melt}
Copper Cu	9.5 μm	8.96 g/cm^3	1083 ^{o}C	0.44 J/gK	210 J/g
Tungsten W	7.4 μm	19.25 g/cm^3	3380 ^{o}C	0.13 J/gK	192 J/g
Iron Fe	9.7 μm	7.87 g/cm^3	1535 ^{o}C	0.45 J/gK	275 J/g

Table II.9.17: Ranges of the ions and material constants required for the calculations: Range R for 1 MeV/u Uranium, density ρ, melting temperature T_{melt}, specific heat c and melting heat a_{melt}.

7 Transverse profile by flying wire scanner

In a synchrotron, a beam of protons or Uranium at an energy of $E_{\mathrm{kin}} = 1$ GeV/u is stored. A thin wire is scanned through the beam to monitor the transverse profile. The beam diameter is Ø 10 mm and the revolution time is $t_{\mathrm{rev}} = 1.0\ \mu$s. The wire is made of Graphite with $50 \times 50\ \mu$m cross section and scanned with a velocity of $v = 10$ m/s. The setup is schematically depicted in Fig. II.9.167.

The energy loss in Graphite of protons is $dE/dx = 4.29$ MeV/cm and for Uranium of mass 238 amu is $dE/dx = 35640$ MeV/cm.

The number of stored particles are for protons $N_{\mathrm{stored}} = 10^{12}$ and for Uranium $N_{\mathrm{stored}} = 10^9$.

Assumption to simplify the calculation: The beam and wire have a rectangular cross section, and the particles doesn't execute betatron oscillations.

Calculate the energy loss per passage of the ion through the wire and the calculate the ratio with respect to the ion's kinetic energy.

Calculate the average number of the ion's passages through the wire.

Hint: Calculate first the time it takes for the wire passage to pass a length of 50 μm (i.e. the wire

thickness)! What is the total energy loss for an individual ion after these passages? Do you think, the particles can be used for further acceleration inside the synchrotron?
What is the total thermal energy absorbed by the wire? Does the wire withstand the energy deposition without melting assuming a maximal power rating of 1 W/mm?
What happens, if not fully stripped Uranium is stored?

8 Signal estimation for an ionization profile monitor

8.1 LINAC

The transverse profile of a LINAC beam of $I = 1$ mA Ar^{10+} and pulse length $t_{\mathrm{macro}} = 1$ ms at energy $E_{\mathrm{kin}} = 1.4$ MeV/u should be measured with an ionization profile monitor. The length of the collecting strips are $l = 100$ mm. The residual gas contain 90 % N_2 and 10 % H_2 at a pressure of $p = 10^{-7}$ mbar. Give the resulting voltage after a current-to-voltage converter using a trans-impedance amplifier with a conversion of $Z_{\mathrm{trans}} = 10^8$ V/A $\equiv 0.1$ V/nA (referred to as trans-impedance).
Assumption: Take a rectangular beam cross section and assume that 10 % of the beam is covered by one strip.

The needed quantities are: Density at *normal* pressure for H_2 is $\rho_{\mathrm{H}} = 0.09 \cdot 10^{-3}$ g/cm^3 and for N_2 it is $\rho_{\mathrm{N}} = 1.25 \cdot 10^{-3}$ g/cm^3. The energy loss for H_2 is
$dE_{\mathrm{H}}/\rho dx = 66$ MeV/(mg/cm^2) and for N_2 it is $dE_{\mathrm{N}}/\rho dx = 22$ MeV/(mg/cm^2). As a first approximation, assume that the average energy for the production of one e^--ion pair is 36 eV.

8.2 Synchrotron

Assume, that the beam is injected to a synchrotron with 10 fold multi-turn efficiency with respect to the current. The residual gas contains now only H_2 and has a pressure of $p = 10^{-10}$ mbar. Calculate the current per strip for this case measured within $t_{\mathrm{meas}} = 1$ ms.

How one can get a higher secondary current without changing the vacuum pressure?

9 Signal estimation for broad-band BPM

The beam position in a proton synchrotron has to be measured by a linear-cut type BPM. The pick-up electrode has a length of $l = 20$ cm, a distance from the beam centre to the plates is $a = 10$ cm and a total capacity of $C = 100$ pF, as used for the calculation of Fig. 5.3 and 5.4 in the lecture notes. The beam has a velocity of $\beta = 50$ % and a bunch length of $\sigma = 100$ ns. For the position read-out, assume a linear response $U_\Delta/U_\Sigma = x/a$ as a function of displacement x. Calculate the transfer impedance Z_t of a half-cylindrical plate using a 1 MΩ termination. Give the sum voltage for a peak value of the beam current of $I_{\mathrm{beam}} = 1$ A. What is the difference voltage for a $x = 1$ mm displacement in this case? What are the corresponding values for U_Σ and U_Δ for a 50 Ω termination assuming $Z_t(50\Omega) = Z_{\mathrm{t}}(1\mathrm{M}\Omega)/20$, corresponding to a frequency of 1 MHz as shown in Fig. 5.3?

Remark: In principle, for the transfer impedance, the Fourier-transformation is required (Why?). For a Gaussian function in time with standard deviation σ_{t} the Fourier-transformation is a half-Gaussian function (for positive frequencies centred at $f = 0$) having a standard deviation $\sigma_{\mathrm{f}} = \frac{1}{2\pi\sigma_{\mathrm{t}}}$.

What is the thermal noise at the $R = 50$ Ω and $R = 1$ MΩ amplifier input-impedance for a bandwidth of $\Delta f = 100$ MHz? Use the thermal noise voltage $U_{\mathrm{eff}} = \sqrt{4k_{\mathrm{B}}TR\Delta f}$ with the temperature $T =$

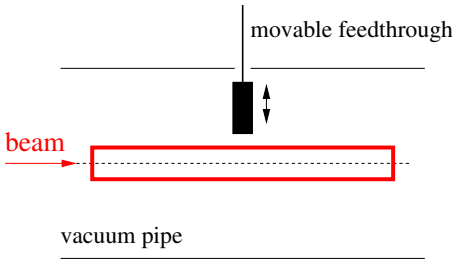

Fig. II.9.168: Scheme of a profile measurement at a synchrotron using a scraper.

300 K and Boltzmann-constant $k_\mathrm{B} = 1.4 \cdot 10^{-23}$ J/K. What is the minimal beam current for $x = 1$ mm displacement for a signal-to-noise ratio $S/N = 2$ using only this thermal noise? (For a real amplifier, the noise contribution is at least a factor 2 bigger.)

For longer bunches, the transfer impedance has a scaling $Z_\mathrm{t} \propto \omega$ for the 50 Ω termination. At which bunch length the position sensitivity of the 1 MΩ and the 50 Ω terminations are equal?

How can the position sensitivity be improved, and what is the main reason?

10 Profile measurement with a scraper

(from previous examination)

Inside a synchrotron the transverse beam profile is measured sometimes destructively using a scraper. It consist of a plate moved in the beam path, see Fig. II.9.168. For the profile determination the scraped position is drawn on the horizontal axis, i.e. its position is the independent variable. The time needed to pass the beam is orders of magnitude longer (typically 1 s) than the revolution time. During the measurement no refilling of the synchrotron occurs.

Discuss this method:

a) What is the primary *beam* quantity to be measured?

b) Propose a method to determine this quantity directly or indirectly and give the reason for your choice.

c) How is the beam *profile* generated from the measured primary signal and the scraper position? Make a principle drawing for the position dependence of the primary signal versus the position and the deduced profile.

d) Why it makes only sense to go up to the middle of the beam?

e) This method can also be used at a LINAC. What is the change of the primary signal as a function of the scraper position? What one has to do for getting the full transverse profile?

11 Beam energy measurement by time-of-flight

(from previous examination)

At a proton LINAC, the coarse final energy is known between 5 MeV and 10 MeV. The accelerator is operated with an rf-frequency of $f_\mathrm{acc} = 100$ MHz. The distance of the two BPMs used for the time-of-flight measurement is 4 m.

a) To what limits one has to know the energy to get an unique solution?

b) A third pick-up should be installed for the coarse energy determination. What is the maximal distance

to achieve a unique solution?

12 Beam diagnostics design for a proton facility

The task for the group work is the design of beam diagnostics for a proton facility built of a LINAC, a booster-synchrotron and a high energy synchrotron as depicted in Fig. II.9.169. The facility is outlined below, giving only the very basic parameters.

It is a realistic task to ask for actual facts and numbers required for an adequate layout of the beam instrumentation and diagnostics methods.

The basic parameters for the facility are:

1. The proton source is located on a high voltage platform with $U = 100$ kV, i.e. the protons' energy is $E_{\mathrm{kin}} = 100$ keV. The maximal current is $I = 50$ mA, but also lower currents down to $I = 100$ nA are sometimes needed for the commissioning of the facility.
2. A low energy LINAC (e.g. RFQ) is used for the acceleration to $E_{\mathrm{kin}} = 3$ MeV. It is driven in a pulsed mode with maximal pulse length of $t_{\mathrm{pulse}} = 1$ ms and $f_{\mathrm{rep}} = 1$ Hz repetition rate. The accelerating frequency is $f_{\mathrm{acc}} = 300$ MHz. The transverse beam size is in the order of $\sigma = 0.5$ cm (one standard deviation). The bunch length is $\sigma_{\mathrm{bunch}} = 10^o$ of the acceleration frequency (one standard deviation).
3. In the second part of the LINAC the particles are accelerated to $E_{\mathrm{kin}} = 100$ MeV. The transverse beam size is in the order of $\sigma = 0.3$ cm; the bunch length is $\sigma_{\mathrm{bunch}} = 10^o$ of the acceleration frequency (one standard deviation).
4. The $E_{\mathrm{kin}} = 100$ MeV proton beam is injected in a synchrotron of $l = 200$ m circumference which delivers a maximal final kinetic energy of $E_{\mathrm{kin}} = 1$ GeV. A time of $t_{\mathrm{cycle}} = 1$ s is needed for acceleration from 100 MeV to 1 GeV. The acceleration frequency is in between 2.57 MHz $< f_{\mathrm{acc}} < 5.25$ MHz resulting in 4 circulating bunches. The beam velocity at injection is $v/c = 43$ % and at extraction it is $v/c = 87$ % which corresponds to a time for one revolution from $t_{\mathrm{rev}} = 1.6$ μs to $t_{\mathrm{rev}} = 0.76$ μs. The bunch length is $\sigma_{\mathrm{bunch}} = 20^o$ of the acceleration frequency (one standard deviation). The beam size varies from injection to extraction from $\sigma = 0.5$ to 0.3 cm. The horizontal and vertical tunes are $Q_x = 4.28$ and $Q_y = 3.22$, respectively. At maximum 10^{12} protons can be stored in this synchrotron.
5. The beam is extracted towards the High Energy Beam Transport HEBT line of 300 m length. Three different target location are foreseen to be delivered with beam, either by slow extraction within 1 s or by single-turn extraction within 0.76 μs to a fixed target as well as a transfer to a 2^{nd} synchrotron.
6. The beam can be injected to a second synchrotron of 2200 m length for further acceleration from 1 GeV to 100 GeV. The protons from the 1^{st} synchrotron are injected by a so called "bunch-to-bucket" transfer i.e. 10 successive fillings are used to accumulate 10^{13} protons in the 2^{nd} synchrotron before acceleration is started. The acceleration takes $t_{\mathrm{cycle}} = 1$ s and then the beam is extracted to a target. The resulting bunch length is $\sigma_{\mathrm{bunch}} = 20^o$ of the acceleration frequency (one standard deviation). The tunes are $Q_x = 20.28$ and $Q_y = 18.22$, respectively.

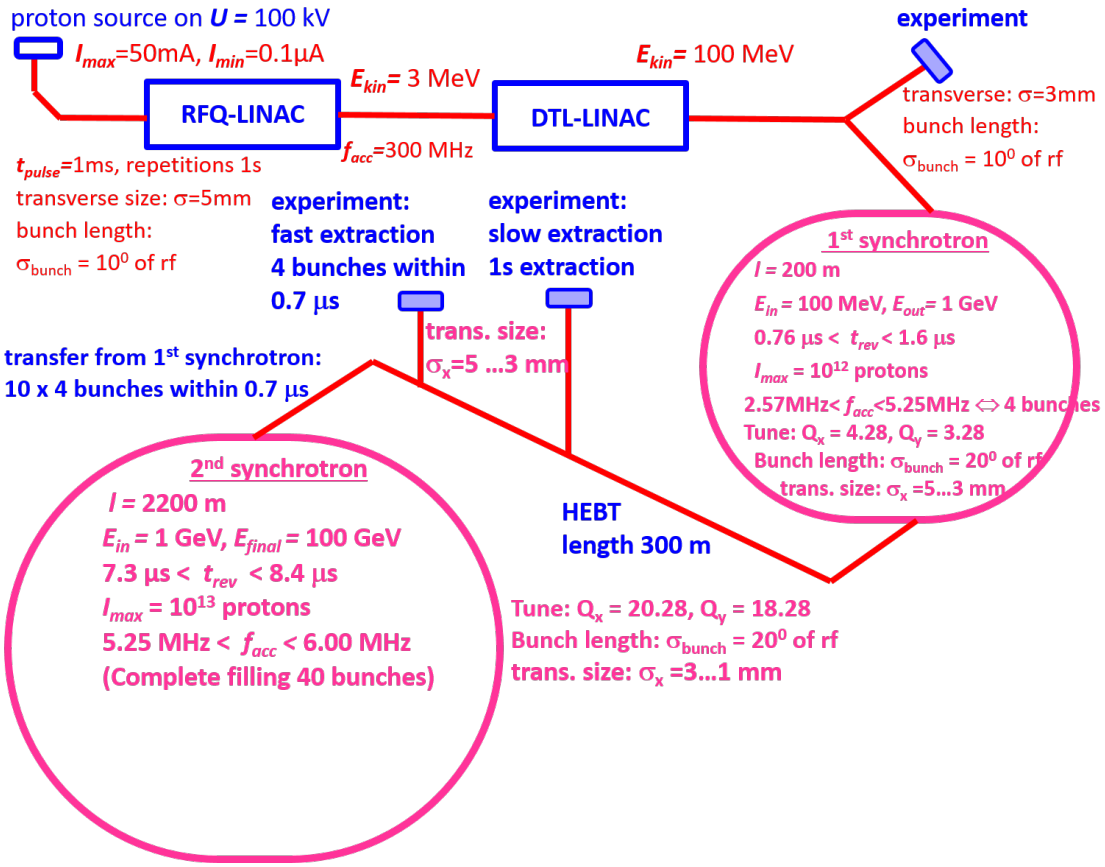

Fig. II.9.169: The simplified facility for beam diagnostics design.

13 Beam diagnostics design for a LINAC FEL facility

The task for this group work is to discuss the beam instrumentation for an electron LINAC, which is used as a light source of coherent X-rays referred to as Free Electron Laser depicted in Fig. II.9.170. The light is generated in a long undulator, and the coherence is based on the SASE process; SASE stands for Self Amplified Spontaneous Emission. The simplified facility is oriented on the SwissFEL at Paul Scherrer Institute (PSI) in Switzerland.

Tow modes of operation should be assumed:

1. Single-bunch operation where only one bunch is generated
2. Bunch train of 100 bunches separated 50 ns.

The related pulse structure is generated by the pulsing of the laser beam, which illuminates the photo-cathode. The charge per bunch is $Q_{\mathrm{bunch}} = 100$ pC. The repetition rate is 100 Hz.

The simplified facility comprises:

1. The electron source, the so-called rf-gun, is equipped with a photo-cathode illuminated by a short, intensive laser beam. The photo-cathode is installed an rf-cavity operated with $f_{\mathrm{acc}} = 1$ GHz. The kinetic energy of the electrons out of the rf-gun is $E_{\mathrm{kin}} = 7$ MeV.
2. After a drift for transverse focusing, longitudinal matching, and beam diagnostics, the beam is injected into a first LINAC. The LINAC is operated with a frequency of $f_{\mathrm{acc}} = 1$ GHz. The final

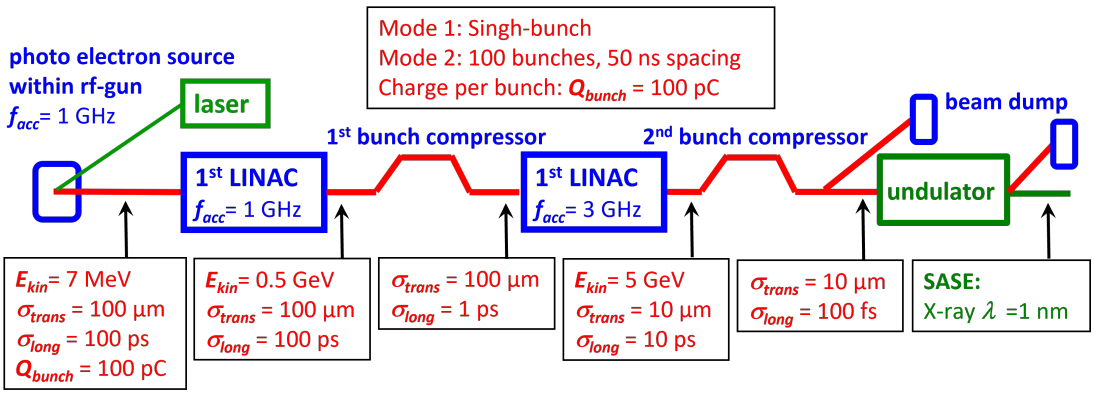

Fig. II.9.170: Simplified electron LINAC FEL facility for beam diagnostics design.

energy is $E_{\mathrm{kin}} = 500$ MeV. The typical transverse beam size is $\sigma_{\mathrm{trans}} = 100$ μm, and the bunch length is $\sigma_{\mathrm{long}} = 100$ ps.

3. A first bunch compressor shorten the bunch to $\sigma_{\mathrm{long}} = 1$ ps. (The bunch compressor uses the variation of path lengths for electrons with different energies such that the electrons reach the input of the subsequent LINAC with a compressed time spread, i.e. a short bunch length.)
4. The second LINAC operates at $f_{\mathrm{acc}} = 3$ GHz and accelerates to $E_{\mathrm{kin}} = 5$ GeV. The transverse beam size $\sigma_{\mathrm{trans}} = 10$ μm.
5. A second bunch compressor shorten the bunch to $\sigma_{\mathrm{long}} = 100$ fs.
6. The beam is then sent to a beam dump or a 30 m long undulator. The SASE light in the soft X-ray range ($\lambda = 1$ nm) is emitted from the undulator. Behind this undulator, the electron beam is bent toward a second beam dump.

II.9.14 Solution for Exercises for Beam Instrumentation and Diagnostics

1 Calculation of current and further properties

1.1 LINAC

Pulse current: $I_{\mathrm{pulse}} = \frac{t_{\mathrm{rep}}}{t_{\mathrm{pulse}}} = \frac{20\ \mathrm{ms}}{1\ \mathrm{ms}} \cdot I_{\mathrm{dc}} = 2$ mA.

Number of particles within one macro-pulse: $N_{\mathrm{pulse}} = \frac{I_{\mathrm{pulse}} \cdot t_{\mathrm{pulse}}}{e} = 1.25 \cdot 10^{13}$.

Number of particles within one bunch: $N_{\mathrm{bunch}} = \frac{t_{\mathrm{bunch}}}{t_{\mathrm{pulse}}} \cdot N_{\mathrm{pulse}} = \frac{10\ \mathrm{ns}}{1\ \mathrm{ms}} \cdot 1.25 \cdot 10^{13} = 1.25 \cdot 10^{8}$.

Velocity at 10 MeV: $E_{\mathrm{kin}} = 1/2 mc^2 \beta^2 \Leftrightarrow \beta = \sqrt{\frac{2E_{\mathrm{kin}}}{mc^2}} = 0.146$.

Bunch length in time: $t_{\mathrm{bunch}} = 0.1/f_{\mathrm{rf}} = 1$ ns.

Bunch length in space: $l_{\mathrm{bunch}} = \beta c t_{\mathrm{bunch}} = 4.4$ cm.

Density within the bunch for a rectangular shape of $2x = 1$ cm edge length:

$\rho_{\mathrm{bunch}} = \frac{N_{\mathrm{bunch}}}{(2x)^2 l_{\mathrm{bunch}}} = 2.84 \cdot 10^{7}\ \mathrm{cm}^{-3}$.

$\Rightarrow$ average distance $\langle d \rangle = \sqrt[3]{1/\rho_{\mathrm{bunch}}} = 30$ µm.

Residual gas density: $n_{\mathrm{gas}} = \frac{p}{k_B T} = 2.4 \cdot 10^{9}\ \mathrm{cm}^{-3}$.

1.2 Synchrotron

Revolution time at injection: $t_{\mathrm{inj}} = \frac{L_{\mathrm{syn}}}{\beta c} = 5.0$ µs $\Leftrightarrow f_{\mathrm{rev}} = 200$ kHz.

Revolution time at extraction: $E_{\text{kin}} = mc^2(\gamma - 1) \Leftrightarrow \gamma = 2.066 \Leftrightarrow \beta = \frac{\sqrt{\gamma^2-1}}{\gamma} = 0.875$.
$\Rightarrow t_{\text{rev}} = 0.84$ µs $\Leftrightarrow f_{\text{rev}} = 1.12$ MHz.
Multi-turn injection within 100 µs: $I_{\text{inj}} = \frac{100\ \mu s}{t_{\text{rev}}} \cdot I_{\text{pulse}} = 40$ mA and $N_{\text{inj}} = 1.25 \cdot 10^{12}$.
After acceleration: $I_{\text{final}} = \frac{\beta_{\text{final}}}{\beta_{\text{inj}}} \cdot I_{\text{inj}} = 239$ mA.
Beam size due to multi-turn injection: $x_{\text{inj}} = \sqrt{\epsilon} \cdot x_{\text{LINAC}} = 5 \cdot x_{\text{LINAC}}$ and $y_{\text{inj}} = y_{\text{LINAC}}$
$\Rightarrow$ density $\rho_{\text{inj}} = \frac{N_{\text{inj}}}{\pi x_{\text{inj}} y_{\text{inj}} L_{\text{syn}}} = 1.45 \cdot 10^7$ cm^{-3}.
$\Rightarrow \langle d \rangle = \sqrt[3]{1/\rho_{\text{inj}}} = 41$ µm.
Emittance shrinkage during acceleration: $\epsilon_{\text{extr}} = \frac{\beta_{\text{inj}}\gamma_{\text{inj}}}{\beta_{\text{extr}}\gamma_{\text{extr}}} \cdot \epsilon_{\text{inj}} = 0.081\epsilon_{\text{inj}}$
Related beam size shrinkage in horizontal direction $x_{\text{extr}} = \sqrt{\epsilon_{\text{extr}}/\epsilon_{\text{inj}}} \cdot x_{\text{inj}} = 0.71$ cm and vertical direction $y_{\text{extr}} = \sqrt{\epsilon_{\text{extr}}/\epsilon_{\text{inj}}} \cdot y_{\text{inj}} = 0.14$ cm.
Density at extraction with emittance shrinkage in both directions:
$\rho_{\text{extr}} = \frac{\rho_{\text{inj}}}{0.081} = 1.79 \cdot 10^8$ cm^{-3}.
$\Rightarrow$ average distance $\langle d \rangle = \sqrt[3]{1/\rho_{\text{extr}}} = 18$ µm.
Residual gas density: $n_{\text{gas}} = \frac{p}{k_B T} = 2.7 \cdot 10^6$ cm^{-3}.

1.3 Extraction

a) Slow extraction:

Current in transfer line: $I_{\text{trans}} = \frac{t_{\text{rev}}}{t_{\text{extr}}} \cdot I_{\text{final}} = 20$ nA.
Total length of current string: $L_{\text{string}} = \beta_{\text{extr}} c \cdot t_{\text{extr}} = 2.6 \cdot 10^9$ m
$\Rightarrow$ density: $\rho = \frac{N_{\text{inj}}}{\pi x_{\text{extr}} \cdot y_{\text{extr}} \cdot L_{\text{string}}} = 16$ cm^{-3}
$\Rightarrow$ average distance $\langle d \rangle = \sqrt[3]{1/\rho_{\text{extr}}} = 4.0$ mm.
Residual gas density: $n_{\text{gas}} = \frac{p}{k_{\text{B}} T} = 2.7 \cdot 10^7$ cm^{-3}.

b) Fast extraction:

Current: $I_{\text{bunch}} = \frac{t_{\text{rev}}}{t_{\text{bunch}}} \cdot I_{\text{extr}} = 2.0$ A.
Bunching to $t_{\text{bunch}} = 100$ ns leads to a bunch length of $l_{\text{bunch}} = \beta_{\text{extr}} c t_{\text{bunch}} = 26.3$ m
$\Rightarrow$ density: $\rho_{\text{bunch}} = \frac{L_{\text{syn}}}{l_{\text{bunch}}} \cdot \rho_{\text{extr}} = 1.5 \cdot 10^9$ cm^{-3}.
$\Rightarrow$ average distance $\langle d \rangle = \sqrt[3]{1/\rho_{\text{bunch}}} = 9$ µm.

Table of results

	LINAC 10 MeV	Synchrotron inj. 10 MeV	Synchrotron extr. 1 GeV	Extraction slow	Extraction fast
beam current I	2 mA	40 mA	240 mA	20 nA	2.0 A
beam velocity β [% of c]	15	15	88	88	88
protons per bunch	$1.3 \cdot 10^8$	$1.3 \cdot 10^{12}$	$1.3 \cdot 10^{12}$	$1.3 \cdot 10^{12}$	$1.3 \cdot 10^{12}$
bunch duration t_{bunch}	1 ns	(5 µs)	(840 ns)	(10 s)	100 ns
bunch length l_{bunch}	4.4 cm	(220 m)	(220 m)	$(3 \cdot 10^9$ m)	26 m
horizontal size $2x$ [cm]	1	5	1.4	1.4	1.4
vertical size $2y$ [cm]	1	1	0.3	0.3	0.3
average distance $\langle d \rangle$ [µm]	30	41	18	4000	9
beam density ρ_{beam} [cm^{-3}]	$3.6 \cdot 10^7$	$1.5 \cdot 10^7$	$1.8 \cdot 10^8$	$1.6 \cdot 10^1$	$1.5 \cdot 10^9$
vacuum pressure p [mbar]	10^{-7}	10^{-10}	10^{-10}	10^{-9}	10^{-9}
res. gas density ρ_{gas} [cm^{-3}]	$2.7 \cdot 10^9$	$2.7 \cdot 10^6$	$2.7 \cdot 10^6$	$2.7 \cdot 10^7$	$2.7 \cdot 10^7$

1.4 Changes for an ion accelerator

Current up to 1 MeV/u with $q = 4$: $I_{\mathrm{pulse}} = 2$ mA $\Rightarrow N_{\mathrm{pulse}} = \frac{I_{\mathrm{pulse}} \cdot t_{\mathrm{pulse}}}{4e} = 3.1 \cdot 10^{12}$
Current for 1 MeV/u to 10 MeV/u with $q = 28$: $I_{\mathrm{pulse}} = 2$ mA $\Rightarrow N_{\mathrm{pulse}} = \frac{I_{\mathrm{pulse}} \cdot t_{\mathrm{pulse}}}{28e} = 4.5 \cdot 10^{11}$
Current at 10 MeV/u with $q = 70$: $I_{\mathrm{pulse}} = 2$ mA $\Rightarrow N_{\mathrm{pulse}} = \frac{I_{\mathrm{pulse}} \cdot t_{\mathrm{pulse}}}{70e} = 1.8 \cdot 10^{11}$
Injection into the synchrotron $q = 70$: $I_{\mathrm{pulse}} = 2$ mA $\Rightarrow N_{\mathrm{inj}} = \frac{0.1\ ms}{1\ \mathrm{ms}} \cdot N_{\mathrm{pulse}} = 1.8 \cdot 10^{10}$.

2 Methods of current measurements at proton accelerators

a) Faraday Cup or active transformer, the beam power is sufficient low for a Faraday Cup, and the beam current sufficient high for a transformer
b) Faraday Cup, the current is too low for a transformer
c) Active transformer due to the high beam power
d) DCCT for a permanent monitoring, other possibility using a FCT and integrating the bunch signal
e) DCCT as the only choice
f) Passive transformer, well suited for a bunched beam detection, Faraday Cup not possible because the beam energy is above pion production threshold
g) Ionization chamber

3 Transformer for a pulsed LINAC

Droop of a transformer:

$$U(t) = I_{\mathrm{beam}} \frac{R}{N} \cdot e^{-t/\tau_{\mathrm{droop}}} = U_0 \cdot e^{-t/\tau_{\mathrm{droop}}} \quad .$$

For a 3% droop within 1 ms:

$$\frac{U(t)}{U_0} = e^{-1\ \mathrm{ms}/\tau_{\mathrm{droop}}} = 0.97 \quad \Leftrightarrow \quad \tau_{\mathrm{droop}} = 32.8\mathrm{ms} \quad .$$

The lower cut-off frequency is $f_{\mathrm{low}} = \frac{1}{2\pi \cdot \tau_{\mathrm{droop}}} = 4.85$ Hz.

The bandwidth of 100 kHz is required to monitor the changes in the pulse current on a 10 µs time scale, e.g. given by the ion source fluctuation.

Passive transformer:

The droop is determined by the inductance L and the resistors R and R_{L}:

$\tau_{\mathrm{droop}} = \frac{L}{R+R_{\mathrm{L}}} \Leftrightarrow L = 33.13$ Hy.

The inductance of a given core is: $L = \frac{\mu_0\mu_{\mathrm{r}}}{2\pi} \cdot lN^2 \cdot \ln\frac{r_{\mathrm{o}}}{r_{\mathrm{i}}} \Leftrightarrow N = \sqrt{\frac{2\pi L}{\mu_0\mu_{\mathrm{r}} l \cdot \ln r_0/r_{\mathrm{i}}}} = 244.5 \simeq 250.$

Sensitivity: $S = \frac{U}{I_{\mathrm{beam}}} = \frac{R}{N} = 4$ V/A (here $\tau_{\mathrm{droop}} \gg t$).

Signal-to-noise: $U_{\mathrm{noise}} = \sqrt{4k_{\mathrm{B}}T(R_{\mathrm{L}}+R)\Delta f} = 1.3$ µV

$\Rightarrow$ for S-to-N=1: $I_{\mathrm{beam}}^{\text{S-to-N=1}} = \frac{1}{S} \cdot U_{\mathrm{noise}} = \frac{N}{R} \cdot U_{\mathrm{noise}} = 0.315$ µA.

Active transformer:

$\tau_{\mathrm{droop}} = \frac{L}{R_{\mathrm{L}}}$ for $R_{\mathrm{f}}/A \ll R_{\mathrm{L}} \Rightarrow L = 0.315$ Hy.

The number of windings is $N = \sqrt{\frac{2\pi L}{\mu_0\mu_{\mathrm{r}} l \cdot \ln r_0/r_{\mathrm{i}}}} = 25.$

Sensitivity: $S = \frac{R_{\mathrm{f}}}{N} = 4.2 \cdot 10^4$ V/A.

The noise voltage is $U_{\mathrm{noise}} = \sqrt{4k_{\mathrm{B}}T(R_{\mathrm{L}}+R_{\mathrm{f}}/A)\Delta f} = 0.135$ µV and

the noise current $I_{\mathrm{noise}} = \frac{A}{R_{\mathrm{f}}} \cdot U_{\mathrm{noise}} = 0.14$ µA.

The corresponding beam current for S-to-N=1 $\Rightarrow I_{\mathrm{beam}}^{\text{S-to-N=1}} = I_{\mathrm{noise}}/N = 6$ nA i.e. a factor 50 lower than for the passive case. This 6 nA threshold concerns only the amplifier input contribution, which is indeed lower than other limiting factors, like Barkhausen noise and magnetostriction.

Fast passive transformer:

3 % droop within 1 µs: $\frac{U(t)}{U_0} = e^{-1\mu s/\tau_{\mathrm{droop}}} = 0.97 \Leftrightarrow \tau_{\mathrm{droop}} = 32.8$ µs

$\Rightarrow f_{\mathrm{low}} = \frac{1}{2\pi\cdot\tau_{\mathrm{droop}}} = 4.9$ kHz.

Inductance L: $\tau_{\mathrm{droop}} = \frac{L}{R+R_{\mathrm{L}}} \Leftrightarrow L = 1.97$ mHy.

The number of windings for $\mu_{\mathrm{r}} = 10^3$: $N = 19 \simeq 20.$

Sensitivity: $S = \frac{U}{I_{\mathrm{beam}}} = \frac{R}{N} = 2.65$ V/A.

Signal-to-noise: $U_{\mathrm{noise}} = 9.09$ µV $\Rightarrow$ for S-to-N=1: $I_{\mathrm{beam}}^{\text{S-to-N=1}} = \frac{1}{S} \cdot U_{\mathrm{noise}} = 3.8$ µA. Due to the wide bandwidth, the minimal detectable beam current is larger than for the case of an active transformer discussed above.

4 Slow extraction current measurement

Density of the Ar filling: $\rho = \frac{N_{\mathrm{A}}\cdot 40\ \mathrm{g}}{22.4\ \mathrm{l}} = 1.79$ mg/cm^3.

Energy loss of protons for a path length of $\Delta x = 0.5$ cm:

$\Delta E_{\mathrm{p}} = \frac{dE}{\rho dx} \cdot \rho \cdot \Delta x = 1289$ eV per proton.

Number of secondary e^-: $N_{\mathrm{e}} = \frac{\Delta E}{26.3\ \mathrm{eV}} = 49\ e^-$/ion.

For the extraction of $N_{\mathrm{i}} = 1.25 \cdot 10^{12}$ ions/s it is $N_{\mathrm{e}}^{\mathrm{tot}} = N_{\mathrm{i}} \cdot N_{\mathrm{e}} = 6.13 \cdot 10^{13}\ e^-$/s,

the corresponding current is: $I_{\mathrm{e}} = e \cdot N_{\mathrm{e}}^{\mathrm{tot}} = 9.77 \cdot 10^{-6}$ A $\simeq 10$ µA.

For Uranium: $\Delta E_{\mathrm{u}} = (92)^2 \cdot \Delta E_{\mathrm{p}} = 10.9$ MeV.

Number of secondary e^-: $N_{\mathrm{e}} = 4.14 \cdot 10^5\ e^-$/ion,

the e^--rate for the Uranium case is: $N_{\mathrm{e}}^{\mathrm{tot}} = N_{\mathrm{i}} \cdot N_{\mathrm{e}} = 7.45 \cdot 10^{15}\ e^-$/s,

the corresponding current is: $I_{\mathrm{e}} = 1.19$ mA. This value is in the range of IC saturation current!

For the SEM and protons: $N_\mathrm{e} = 0.048\ e^-$/ion $\Rightarrow I_\mathrm{e} = 9.69 \cdot 10^{-9}$ A $\simeq 10$ nA.
For Uranium: $N_\mathrm{e} = 406\ e^-$/ion $\Rightarrow I_\mathrm{e} = 1.18 \cdot 10^{-6}$ A $\simeq 1$ µA.

5 Beam power at a LINAC

The macro-pulse current is: $I_\mathrm{macro} = 2$ mA,
the average current is $I_\mathrm{aver} = \frac{1\ \mathrm{ms}}{20\ \mathrm{ms}} \cdot I_\mathrm{macro} = 100$ µA.
With $I = \frac{qeN}{t}$ the corresponding average rate is:
protons: $N_\mathrm{p} = 6.25 \cdot 10^{14}$ 1/s and
Uranium: $N_\mathrm{U} = 2.23 \cdot 10^{13}$ 1/s.
The absorbed average power is $P^\mathrm{aver} = eN \cdot E_\mathrm{kin} \cdot A$, A mass of ions
$\Rightarrow P_\mathrm{p}^\mathrm{aver} = 1.0$ kW and $P_\mathrm{U}^\mathrm{aver} = 8.5$ kW.
The *peak* power is higher than the average value by the factor $\frac{20\ \mathrm{ms}}{1\ \mathrm{ms}}$
$\Rightarrow P_\mathrm{p}^\mathrm{peak} = 20$ kW and $P_\mathrm{U}^\mathrm{peak} = 170$ kW.
The average power has to be transported by the flow of cooling water:
$P_\mathrm{water} = \frac{dV}{dt} \cdot \rho c \cdot \Delta T$
($\frac{dV}{dt}$ is the flow, ρ the density, c the heat capacitance and $\Delta T = 60$ K the temperature increase.)
Protons: $P_\mathrm{water} = P_\mathrm{p}^\mathrm{aver} \Rightarrow \frac{dV}{dt} = 3.97$ cm^3/s $= 0.23$ l/min
Uranium: $P_\mathrm{water} = P_\mathrm{U}^\mathrm{aver} \Rightarrow \frac{dV}{dt} = 33.7$ cm^3/s $= 2.0$ l/min.

6 Material destruction for intense beams

Power within a macro-pulse of an ion of mass $A = 238$: $P_\mathrm{macro} = \frac{I_\mathrm{macro}}{q} \cdot E_\mathrm{kin} \cdot A = 595$ kW
Energy within the macro-pulse: $W_\mathrm{macro} = P_\mathrm{macro} \cdot t_\mathrm{macro} = 119$ J.
The specific energy for heating the metal to the melting temperature is $Q_\mathrm{heat} = \rho c(T_\mathrm{melt} - T_0)$ and the specific energy to melt the metal is $Q_\mathrm{melt} = \rho \cdot a_\mathrm{melt}$. The total specific energy is the sum for heating and melting $Q_\mathrm{tot} = Q_\mathrm{heat} + Q_\mathrm{melt}$

	Cu	Fe	W
Q_heat [kJ/cm^3]	3.1	5.3	8.4
Q_melt [kJ/cm^3]	1.9	2.2	3.7
Q_tot [kJ/cm^3]	5.0	7.5	12.1

The beam is stopped in a volume $V = \pi r_\mathrm{min}^2 \cdot R_\mathrm{mat}$ (assuming a round beam with constant density as a first approximation). The minimum beam radius to prevent melting is $r_\mathrm{min} = \sqrt{\frac{W_\mathrm{macro}}{Q_\mathrm{tot} \cdot \pi \cdot R_\mathrm{mat}}}$, with the material dependent ranges R_mat of Uranium ions (i.e. $R_\mathrm{Cu} = 9.5$ µm, $R_\mathrm{Fe} = 9.7$ µm, $R_\mathrm{W} = 7.4$ µm):

	Cu	Fe	W
r_min [mm]	25.6	22.7	20.5

Having now a beam with $r_\mathrm{beam} = 5$ mm the maximal allowed beam energy
$W_\mathrm{macro} = \pi r_\mathrm{beam}^2 \cdot Q_\mathrm{tot} \cdot R_\mathrm{mat}$ is:

	Cu	Fe	W
W_macro [J]	4.6	5.7	7.0

and the time is $t_{\mathrm{pulse}} = \frac{W_{\mathrm{macro}}}{P_{\mathrm{macro}}}$

	Cu	Fe	W
t_{pulse} [µs]	7.6	9.6	11.8

The estimation above assumes a constant beam density; for a Gaussian distribution the central part of the beam spot is heated stronger. For a save operation of an accelerator, the above given value for t_{pulse} have to be about a factor 2 or 3 lower.

The penetration depth R (or range) of ions in material scales approximately with $R_{\mathrm{mat}} \propto E_{\mathrm{kin}}^{1.75}$
$\Rightarrow r_{\mathrm{min}} \propto \sqrt{E_{\mathrm{kin}}/R} \propto E_{\mathrm{kin}}^{-0.375}$, i.e. for high beam energies the temperature increase is lower.
The corresponding values for a 1 MeV proton beam of 10 mA current and 200 µs duration are
$P_{\mathrm{macro}} = 10$ kW and $W_{\mathrm{macro}} = 2$ J.
The minimum radius is:

	Cu	Fe	W
r_{min} [mm]	3.9	3.6	3.1

To prevent melting assuming a beam radius of 5 mm it is:

	Cu	Fe	W
W_{macro} [J]	3.2	3.8	5.1
t_{pulse} [µs]	319	378	511

Contrary to the Uranium case, no destruction is expected for the full beam duration.

7 Transverse profile by flying wire scanner

The energy loss per passage of the wire with thickness $\Delta x = 50$ µm as given by $\Delta E_{\mathrm{pass}} = \frac{dE}{dx} \cdot \Delta x$ is for the two ions:

	p	U
ΔE_{pass} [MeV]	0.021	178
$\Delta E_{\mathrm{pass}}/E_{\mathrm{kin}}$	$2.1 \cdot 10^{-5}$	$7.5 \cdot 10^{-4}$

$\Rightarrow$ even after 2 passages the Uranium is out of the typical longitudinal acceptance of about $(\Delta E/E)_{\mathrm{accept}} \simeq 10^{-3}$ and they will be lost. For the proton case the particles energy loss is below the acceptance value and they will be stored.
Kinematics of the "flying wire":
total time to pass the beam: $t_{\mathrm{tot}} = \frac{d_{\mathrm{beam}}}{v} = 1$ ms
time to move by *one* wire thickness $\Delta x = 50$ µm: $t_{\Delta x} = \frac{\Delta x}{v} = 5.0$ µs
number of passages of particles through the wire: $N_{\mathrm{pass}} = \frac{t_{\Delta x}}{t_{\mathrm{rev}}} = 5.0$ with $t_{\mathrm{rev}} = 1.0$ µs, i.e. 5 passes through the wire.
Using the number of stored particle N_{stored} (protons $N_{\mathrm{stored}} = 10^{12}$ and Uranium $N_{\mathrm{stored}} = 10^{9}$)
the total energy is: $W = e \cdot \Delta E_{\mathrm{pass}} \cdot N_{\mathrm{pass}} \cdot N_{\mathrm{stored}}$,
the total power: $P = \frac{W}{t_{\mathrm{tot}}}$,
and the power per mm: $P_{\mathrm{mm}} = \frac{P}{10\ \mathrm{mm}}$. It follows for both ions:

	p	U
W [J]	0.017	0.142
P [W]	17	142
P_{mm} [W/mm]	1.7	14.2

$\Rightarrow$ For protons the heating of the wire is just above the safty-border of 1 W/mm ($\Rightarrow$ a more realistic calculation is required).
$\Rightarrow$ For Uranium the wire melts; note, that 10^{-3} less Uranium ions are stored.

If not fully striped ions are stored, than they change their charge state according to an energy-dependence distribution, i.e. a noticeable fraction of ions is lost after the next dipole due to the non-matched charge state.

8 Signal estimation for a ionization profile monitor

Target thickness of H_2: $x_{\mathrm{H}} = \rho_{\mathrm{H}} \cdot \frac{p}{p_{\mathrm{norm}}} \cdot l = 9.0 \cdot 10^{-11}$ mg/cm^2
(p vacuum pressure, $l = 100$ mm monitor length)
Target thickness of N_2: $x_{\mathrm{N}} = \rho_{\mathrm{N}} \cdot \frac{p}{p_{\mathrm{norm}}} \cdot l = 1.25 \cdot 10^{-9}$ mg/cm^2
Energy loss per ion in H_2: $E_{\mathrm{H}} = \frac{dE}{\rho_{\mathrm{H}} dx} \cdot x_{\mathrm{H}} = 5.94$ meV
Energy loss per ion in N_2: $E_{\mathrm{N}} = \frac{dE}{\rho_{\mathrm{N}} dx} \cdot x_{\mathrm{N}} = 27.5$ meV
Number of ions per pulse: $N_{\mathrm{macro}} = \frac{I}{qe} \cdot t_{\mathrm{macro}} = 6.25 \cdot 10^{11}$.
Total energy loss within the monitor per pulse:
for H_2: $E_{\mathrm{H}}^{\mathrm{tot}} = N_{\mathrm{macro}} \cdot E_{\mathrm{H}} = 3.71 \cdot 10^9$ eV
for N_2: $E_{\mathrm{N}}^{\mathrm{tot}} = N_{\mathrm{macro}} \cdot E_{\mathrm{N}} = 17.2 \cdot 10^9$ eV.
Numbers of e^--ion pairs $N^{\mathrm{pair}} = \frac{E^{\mathrm{tot}}}{W}$, with $W = 36$ eV:
for H_2: $N_{\mathrm{H}}^{\mathrm{tot}} = 1.0 \cdot 10^8$
for N_2: $N_{\mathrm{N}}^{\mathrm{tot}} = 4.8 \cdot 10^8$.

For the case of the LINAC: 90 % N_2 and 10 % H_2 it is:
$I_{\mathrm{sec}} = e \left(0.1 N_{\mathrm{H}}^{\mathrm{pair}} + 0.9 N_{N}^{\mathrm{pair}} \right) / t_{\mathrm{macro}} = 70.4$ nA
10 % of the beam is covered by one strip $\Rightarrow I_{\mathrm{sec}}^{\mathrm{strip}} = 7.04$ nA
$\Rightarrow U_{\mathrm{sec}}^{\mathrm{strip}} = 0.704$ V after I/U-conversion.
(Current down to 1 nA can be measured with sensitive pre-amplifiers even in the electronically noisy environment close to an accelerator.)
For the case of the synchrotron: Target thickness $x_{\mathrm{H}} = 9.0 \cdot 10^{-14}$ mg/cm^2 and $p = 10^{-10}$ mbar
$\Rightarrow N_{\mathrm{H}}^{\mathrm{pair}} = 1.0 \cdot 10^6$
$\Rightarrow I_{\mathrm{sec}} = 0.16$ nA and per strip $I_{\mathrm{sec}}^{\mathrm{strip}} = 16$ pA. This cannot be converted by an I/U-converter and a MCP as a "pre-amplifier" with up to 10^6 fold amplification is required.

9 Signal estimation for broad-band BPM

Transfer impedance for 1 MΩ: $Z_t = \frac{1}{2\beta c C} \cdot \frac{A}{\pi a} = \frac{l}{\beta c C} = 6.7\ \Omega$, with area $A = \pi a l$.
Sum voltage for $I_{\mathrm{beam}} = 1$ A: $U_{\Sigma I_{\mathrm{beam}}} = 1$ A:

$$U_\Delta = Z_\perp \cdot x \cdot I_{\mathrm{beam}} = \frac{x}{a} \cdot Z_t \cdot I_{\mathrm{beam}} \Rightarrow U_\Delta(x = 1\ \mathrm{mm}) = 67\ \mathrm{mV}.$$

With $Z_\perp = \frac{Z_t}{a}$:

$$t \cdot I_{\mathrm{beam}}.$$

For 50 Ω termination and $Z_t(50\Omega) = Z_t(1\mathrm{M}\Omega)/20$:} Sum voltage for $I_{\mathrm{beam}} = 1$ A : $U_\Sigma = 2Z_t \cdot I_{\mathrm{beam}} = 0.67$ V and difference voltage $U_\Delta(x = 1\mathrm{mm}) = 3.3$ mV.
The thermal noise voltage is given by:
$R = 1\mathrm{M}\Omega$: $U_{\mathrm{eff}}(R = 1\mathrm{M}\Omega) = \sqrt{4k_{\mathrm{B}}TR\Delta f} = 1.3$ mV
$R = 50\ \Omega$: $U_{\mathrm{eff}}(R = 50\ \Omega) = \sqrt{4k_{\mathrm{B}}TR\Delta f} = 9.3\mu$V

The minimum beam current for $S/N = 2$ is:
$R = 1$ MΩ: $U_\Delta = 2 \cdot U_{\mathrm{eff}}(R = 1\mathrm{M}\Omega) = 2.7$ mV $\Rightarrow I_{\mathrm{beam}} = \frac{a}{x}\frac{1}{Z_t(1M\Omega)} \cdot U_\Delta = 40$ mA.
$R = 50\Omega$: $U_\Delta = 2 \cdot U_{\mathrm{eff}}(R = 50\Omega) = 18.4\ \mu$V $\Rightarrow I_{\mathrm{beam}} = \frac{a}{x}\frac{1}{Z_t(50\Omega)} \cdot U_\Delta = 5.5$ mA.
The scaling of Z_t for 50 Ω is given by $U_\Delta \propto \omega \propto 1/\sigma_{\mathrm{t}}$
$\Rightarrow$ 50 Ω has a better S/N for bunches shorter than 720 ns.
By a narrow-band analysis the band-width Δf is much lower (typically 10 kHz for the narrow-band case instead of 100 MHz in the broad-band case) and therefore the thermal noise voltage via $U_{\mathrm{eff}} \propto \sqrt{\Delta f}$ (i.e. the noise contribution is about a factor 100 lower).

Remark concerning the value of minimal current I_{beam} for termination with $R = 1$ MΩ:
The minimal values of $I_{\mathrm{beam}} = 40$ mA calculated above is unrealistically high due to the fact that the BPM's capacitance of $C = 100$ pF together with the resistor $R = 1$ MΩ form a low-pass filter with the cut-off frequency $f_{\mathrm{cut}} = (2\pi RC)^{-1} = 1.6$ kHz. High frequencies $f \gg 10$ kHz will therefore be damped. A more realistic value for the minimal beam current related to that effect is $I_{\mathrm{beam}} \simeq 1$ mA. For the estimation of this value the noise of an amplifier is taken into account as well. Generally, the amplifiers contribution is characterized by the so called noise figure $F = U_{\mathrm{eff}}(\mathrm{amplifier})/U_{\mathrm{eff}}(\mathrm{thermal})$, which describes the ratio between the real amplifier noise $U_{\mathrm{eff}}(\mathrm{amplifier})$ with respect to the thermal noise $U_{\mathrm{eff}}(\mathrm{thermal})$ at a corresponding resistor and temperature. Typical values for a low-noise amplifier are $F \geq 2$.

10 Profile Measurement with a scraper

a) The primary signal is the loss of stored beam particles.

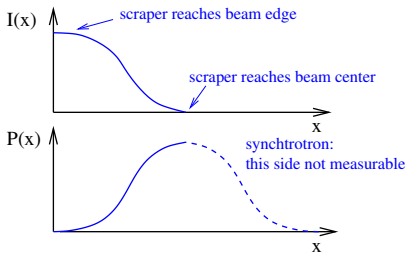

Fig. II.9.171: The circulating current $I(x)$ and the calculated beam profile $P(x)$ as a function of the scraper position x in the case of a synchrotron.

b) One could measure the fraction of lost particles either by determine the current hitting the scraper (i.e. the scraper acts like a Faraday cup) or with a beam loss monitor outside of the beam pipe. These methods

have the disadvantage of low signal strength, because no refilling occur. Therefore it is more suitable to measure the remaining circulating current inside the synchrotron with a dc-transformer (be aware that the scraper movement last typically 1 s, while the revolution time is typically 1 µs). This later method is proposed due to the larger signal strength.

c) Because the remaining circulating current $I(x)$ as a function of scraper position x is determined, the profile $P(x)$ is given by the negative derivative $P(x) = -\frac{dI(x)}{dx}$.

d) The movement of the scraper is slow compared to the revolution time. Due to the betatron oscillation the beam particles reach after a few turns the side of the scraper in any case. If their beatatron amplitudes are larger than the scraper position, they are lost. When the scraper reaches the middle of the beam path, no particles are circulating any more.

e) In a transport-line of a LINAC new particles are passing the scraper location. Therefore, the argument of item **d)** is not valid. For recording the full beam profile, the scraper has to transverse the full beam profile.

11 Beam energy measurement by time-of-flight

Non-relativistic formulas can be used for the given energies.

For the lower boundary of $E = 5$ MeV it is:

$\beta = \sqrt{\frac{2E}{mc^2}} = 0.103$, time required for $L = 4$ m distance $T = \frac{L}{\beta c} = 129$ ns, number of bunches N between the pick-ups $N = T \cdot f_{\mathrm{rf}} \simeq 13$ for 100 MHz rf.

For the upper boundary of $E = 10$ MeV it is:

$\beta = \sqrt{\frac{2E}{mc^2}} = 0.146$, time required for $L = 4$ m distance $T = \frac{L}{\beta c} = 91$ ns, number of bunches N between the pick-ups $N = T \cdot f_{\mathrm{rf}} \simeq 9$.

a) The error propagation of $\Delta\beta/\beta$ as a function of number of bunches N between the pick-ups is given by $\frac{\partial \beta c}{\partial N} = \frac{\partial}{\partial N}\left(\frac{L}{NT + t_{\mathrm{scope}}}\right) \simeq -\frac{L}{N^2 T}$ due to $T \gg t_{\mathrm{scope}}$, with T equals the total time to travel the distance L between the pick-ups.

The error of the energy reading is $\frac{\Delta E}{E} = 2\frac{\Delta\beta}{\beta} = 2\frac{\Delta N}{N}$.

For a unique solution $\Delta N = 1$ and therefore:

Lower boundary $E = 5$ MeV $\Rightarrow \frac{\Delta E}{E} = \frac{2}{N} = 15$ % with $N = 13$.

Upper boundary $E = 10$ MeV $\Rightarrow \frac{\Delta E}{E} = \frac{2}{N} = 22$ % with $N = 9$.

b) The third pick-up should be installed within the distance between two successive bunches:

Lower boundary $E = 5$ MeV: $d_{\mathrm{bunch}} = \frac{\beta c}{f_{\mathrm{rf}}} = 31$ cm.

Upper boundary $E = 10$ MeV: $d_{\mathrm{bunch}} = \frac{\beta c}{f_{\mathrm{rf}}} = 44$ cm.

The lower boundary $E = 5$ MeV gives the shorter distance and, hence, the third pick-up should be installed less than 31 cm apart from the first one.

12 Beam diagnostics design for a proton facility

This exercise is meant as a group work where the beam instrumentation and their diagnostics applications should be discussed. No unique answer for the layout of beam instrumentation and its usage for diagnostics is expected. The layout of the proton heavy ion LINAC and synchrotron at GSI can serve as a guideline and are depicted below. The devices and their usage is discussed in the lecture and the preceding sections.

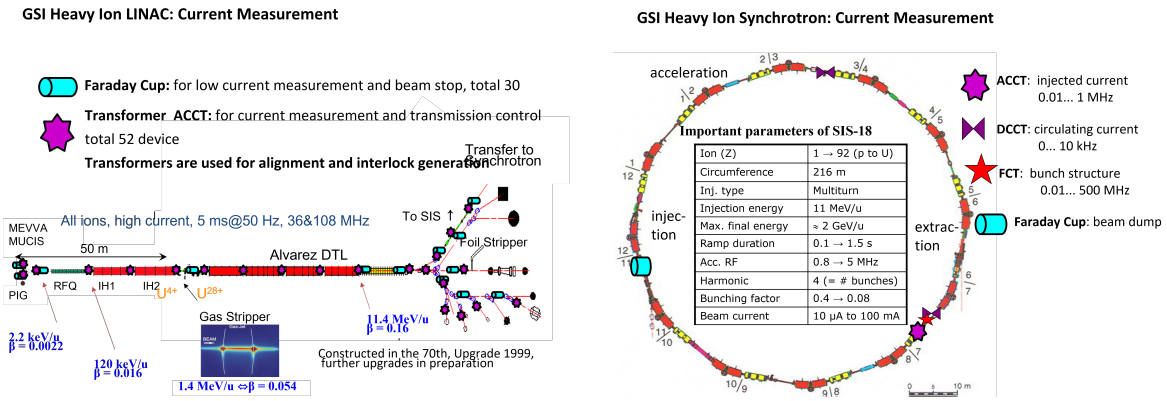

Fig. II.9.172: The instrumentation for beam current measurement at the GSI facility.

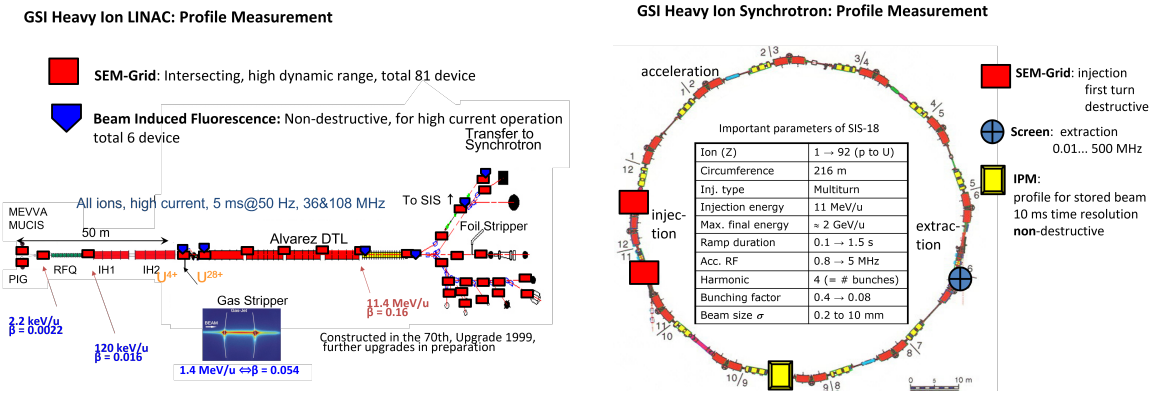

Fig. II.9.173: The instrumentation for beam profile measurement at the GSI facility.

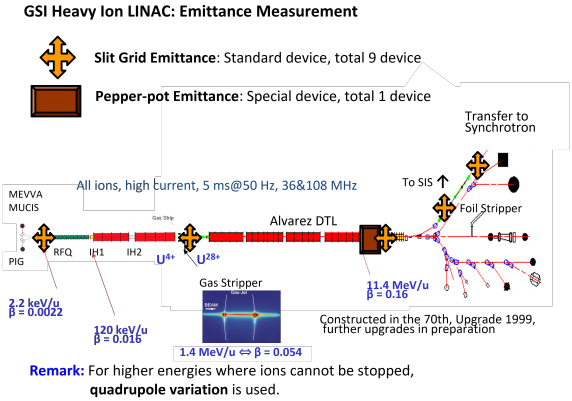

Fig. II.9.174: The instrumentation for beam emittance measurement at the GSI facility. At the high beam transport lines, quadrupole scans are performed using scintillation screens or SEM-grid are detectors. Within the synchrotron, the emittance can be deduced from the profile measurement at one location.

Bunch shape measurement: For longitudinal bunch shape measurements at the LINAC, Fast Faraday Cups and Bunch Shape Monitor based on secondary electron emission is used. At the synchrotron and high energy beam transport, the sum signal of BPMs is used as the bunch length is sufficient for broadband electronics observation.

Beam loss monitors: BLMs are installed in the synchrotron at about 30 positions in regular distributions

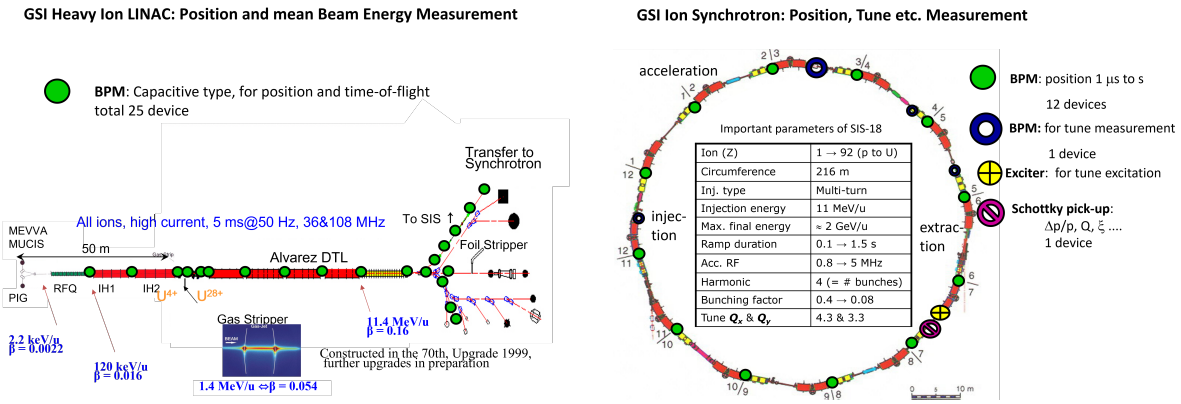

Fig. II.9.175: The instrumentation with BPM and pick-up at the GSI facility.

and, in addition at possible acceptance limitations such as scrapers, septa and rf cavities.

13 Beam diagnostics design for a LINAC FEL facility

This exercise is meant as a group work where the beam instrumentation and their diagnostics applications should be discussed. The answers can be oriented on the following publications for the SwissFEL at PSI and the references therein:

- V. Schlott et al., *Proc. Int. Beam Instr. Conf. IBIC 15,* Melbourne, p. 12 (2015) https://accelconf.web.cern.ch/IBIC2015/papers/mobla03.pdf and the related invited talk https://accelconf.web.cern.ch/IBIC2015/talks/mobla03_talk.pdf.
- V. Schlott et al., *Proc. Int. Beam Instr. Conf. IBIC 17,* Grand Rapids, p. 104 (2017), https://accelconf.web.cern.ch/ibic2017/papers/mopwc03.pdf and doi:10.18429/JACoW-IBIC2017-MOPWC03.